Universiteit Antwerpen

Faculteit Wetenschappen

Departement Fysica

Measurement of the Brout-Englert-Higgs boson decaying to two W bosons in the fully leptonic final state with the CMS detector at the Large Hadron Collider

---

Meting van het Brout-Englert-Higgs boson via het vervalkanaal naar twee W bosonen in de volledig leptonische eindtoestand met de CMS detector bij de Large Hadron Collider

Proefschrift voorgelegd tot het behalen van de graad van

doctor in de Wetenschappen: Fysica

aan de Universiteit Antwerpen

te verdedigen door

Sten Luyckx

Promotor:

Prof. Dr. Nick van Remortel

Antwerpen, 2014

Preface

At the microscopic level, the laws of nature can be formulated in terms of fundamental elementary particles. Years of research and increasingly powerful accelerators led to the development of the Standard Model (SM), a quantum field theory based on symmetry principles, that successfully describes the dynamics of the elementary particles and the fundamental interactions. The SM describes matter as composed of twelve elementary particles, the fermions, that interact by exchanging vector bosons, the carriers of the fundamental interactions: the electromagnetic, the strong and the weak forces.

Despite its success in predicting experimental results with high precision, the Standard Model is far from being completely understood. Without even mentioning the gravitational interaction, there are a lot of questions to be answered. What is the theoretical explanation of many Standard Model parameters? Why are there just three replicated generations of elementary particles? Why do certain particles have masses and some don't? And since all particles should be massless because of the conserved fundamental symmetries, responsible for the existence of the three main interactions, where is this mass coming from? This last problem is the so-called electroweak symmetry breaking problem. In 1964 Brout, Englert, Higgs, Guralnik, Hagen and Kibble proposed a neat solution to tackle this problem. In their proposed mechanism, the mass of a particle arises from its interaction with an additional field, the Brout-Englert-Higgs (BEH) field. The fundamental quantum associated with this field, the so-called BEH boson or, in short Higgs boson[1], is the particle physicists were looking for in the last few decades. The study of the electroweak symmetry, the Brout-Englert-Higgs mechanism and thereby the study of the Higgs boson, the signature of this theory, are considered as one of the most important topics of modern physics.

The largest and most powerful accelerator to date is the Large Hadron Collider (LHC) at the European Organization for Nuclear Research (CERN) in Geneva. It is a proton-proton collider designed to work at a center of mass energy of $\sqrt{s}$ =14 TeV with

[1]The name of the particle has grown historically within the community. Modern nomenclature adopts the term *scalar boson* or *Standard Model scalar*.

a peak instantaneous luminosity of 10^{34} cm^{-2} s^{-1}. It is circulating proton beams since 2009. The LHC is surrounded by four main experiments, including the Compact Muon Solenoid (CMS) experiment, where the research covered by this thesis was conducted. The main short term goal of the CMS experiment is the discovery of this Higgs boson by studying the remnants of proton-proton collisions. Since the production of the Higgs boson is a very rare process and the Higgs boson decays to different particle final states depending on its theoretically unpredictable mass, the CMS experiment is designed to have a maximal sensitivity to all these final states. The CMS experiment has collected 6.1 fb^{-1} at a center-of-mass energy of 7 TeV in 2011 and 23.3 fb^{-1} at a center-of-mass energy of 8 TeV in 2012.

Finally, on the fourth of July 2012, both the ATLAS and CMS collaborations claimed the observation of a Higgs-like boson with a mass of 125 GeV, which led to the awarding of the Nobel Prize to F. Englert and P. Higgs for *the theoretical discovery of a mechanism that contributes to our understanding of the origin of mass of subatomic particles, and which recently was confirmed through the discovery of the predicted fundamental particle, by the ATLAS and CMS experiments at CERN's Large Hadron Collider.*

One of the important analyses that contributed to the discovery of the Higgs boson is presented here: the measurement of the BEH boson decaying to two W bosons in the fully leptonic final state ($\mathrm{H} \to \mathrm{W}^+\,\mathrm{W}^- \to 2\ell\,2\nu$) with the CMS detector at the Large Hadron Collider. The analysis is presented with the full 2011 and 2012 dataset. Henceforth, the particle will be named the Higgs boson and the mechanism the Brout-Englert-Higgs mechanism.

In the first Chapter an introduction on the Standard Model of particle physics is given, with an emphasis on the Brout-Englert-Higgs mechanism. An overview of Higgs boson production at the LHC is given, the pre-LHC Higgs boson search results are covered and the observation of a Higgs-like boson at the LHC is discussed in more detail. Chapters 2 and 3 describe the characteristics of the LHC and the CMS detector. The methods used in CMS to reconstruct all the particles relevant to this analysis are discussed in Chapter 4. From Chapter 5 onwards this thesis focuses on the final state of the Higgs boson decaying to two W bosons and their respective decay to two leptons and two neutrinos. The signal topology and its main backgrounds are covered, followed by a common preselection strategy, to optimize the signal versus background ratio. Next, Chapter 6 provides the estimation of all the different backgrounds in more detail with a first comparison to the data at an intermediate selection level as a cross-check. Chapter 7 covers the final signal extraction strategy and the systematics related to this analysis.

The statistical interpretation of this search is discussed in Chapter 8. Lastly, Chapter 9 covers the study of the spin-parity properties of the newly found scalar.

The results presented in this thesis are published in several papers and public CMS notes as the amount of available collision data increased. In chronologic order:

- CMS Collaboration, *Search for the Standard Model Higgs boson decaying to a W pair in the fully leptonic final state in pp collisions at* $\sqrt{s} = 8\ TeV$, CERN Report No. CMS-PAS-HIG-12-017 (2012);
- CMS Collaboration, *Observation of a new boson at a mass of 125 GeV with the CMS experiment at the LHC*, Phys.Lett. **B716**, 30 (2012);
- CMS Collaboration, *Evidence for a particle decaying to* W^+W^- *in the fully leptonic final state in a Standard Model Higgs boson search in pp collisions at the LHC*, CERN Report No. CMS-PAS-HIG-12-042 (2012);
- CMS Collaboration, *Measurement of* W^+W^- *and ZZ production cross sections in pp collisions at* $\sqrt{s} = 8\ TeV$, Phys.Lett. **B721**, 190 (2013);
- CMS Collaboration, *Update on the search for the Standard Model Higgs boson in pp collisions at the LHC decaying to* W^+W^- *in the fully leptonic final state*, CERN Report No. CMS-PAS-HIG-13-003 (2013);
- CMS Collaboration, *Search for a Standard-Model-like Higgs boson with a mass in the range 145 to 1000 GeV at the LHC*, Eur.Phys.J. **C73**, 2469 (2013);
- CMS Collaboration, *Observation of a new boson with mass near 125 GeV in pp collisions at* $\sqrt{s} = 7$ *and 8 TeV*, JHEP **1306**, 81 (2013);
- CMS Collaboration, *Measurement of Higgs boson production and properties in the WW decay channel with leptonic final states*, JHEP **1401**, 096 (2014).

The last paper contains the results based on the full 2011 and 2012 dataset as presented in this thesis.

Contents

"For more than three decades, the Higgs has been physicists' version of King Arthur's Holy Grail, Ponce de Leon's Fountain of Youth, Captain Ahab's Moby Dick. It's been an obsession, a fixation, an addiction to an idea that almost every expert believed just had to be true."

— T. Siegfried, former editor in chief of Science News, 2012

Chapter 1.

The Standard Model Higgs boson

In this first chapter the basic concepts of the Standard Model are introduced. The electroweak symmetry breaking and the Brout-Englert-Higgs mechanism are described. The theory limits on the Higgs boson mass as well as the pre-LHC experimental search results for the scalar boson are discussed. A description of the general strategy for the search for the Higgs boson at a proton-proton collider as the LHC is given, followed by the latest search results at the LHC.

Natural units are used throughout the whole work ($\hbar = c = 1$), unless specified.

1.1. The Standard Model

The experimental knowledge of elementary particles and their interactions is currently best described by the *Standard Model* (SM) [1, 2]. It is a quantum field theory[1] (QFT) based on symmetry principles: it includes the QFT of the electroweak interactions (Glashow-Weinberg-Salam model, GWS) and of the strong interaction (quantum chromodynamics, QCD). The keystone of the theory is the electroweak symmetry breaking, via the Brout-Englert-Higgs mechanism, giving rise to the mass of the vector bosons and predicting the existence of the Higgs boson. The theory predicts three of the four fundamental forces: the strong, the weak and the electromagnetic (EM) force. The fourth interaction, gravity, is much weaker than the other three forces and is not yet accommodated in a unified theory with the other three. It is however not relevant at the energies and distances typical in current particle physics laboratory experiments, so it will not be covered in this work.

[1] For an introduction to QFT see [1].

Table 1.1.: The spin-1/2 fermions and their mass grouped by their charge and generation [3].

Fermions	$1^{st.}$ gen. | mass		$2^{st.}$ gen. | mass		$3^{st.}$ gen. | mass		charge (Q)	Interactions
Quarks	u	$\sim$2 MeV	c	$\sim$1.3 GeV	t	$\sim$173.5 GeV	2/3	All
	d	$\sim$5 MeV	s	$\sim$95 MeV	b	$\sim$4.2 GeV	-1/3	
Leptons	ν_e	$\sim$0	ν_μ	$\sim$0	ν_τ	$\sim$0	0	Weak
	e	$\sim$511 keV	μ	$\sim$105.7 MeV	τ	$\sim$1776.2 MeV	-1	Weak, EM

Ordinary matter is described by the SM as being composed of twelve elementary particles, the *fermions*, all having a spin 1/2. They appear in nature in two distinct groups, *leptons* and *quarks*, and in three families or generations that behave almost identically under the fundamental interactions. The leptons consist of electrons (e), muons (μ), taus (τ) and their associated neutrinos (ν_e, ν_μ and ν_τ). They interact via the weak and, if charged, the electromagnetic force. Next, the quarks are labeled as up (u), down (d), charm (c), strange (s), top (t) and bottom (b); they can also interact with the strong force. A summary of the fermions including characteristics such as charge and observed mass is shown in Table 1.1. It should be noted here that everything around us in our daily life is built up by just u-quarks, d-quarks and electrons. The building blocks of matter, atoms, are composed of protons, neutrons and electrons. The protons and neutrons are the quark aggregates uud and udd, respectively (see Section 1.1.2). Lastly it should be noted that an anti-particle exists for each of these fermions with opposite quantum numbers, but with exactly the same mass and coupling as its counterpart.

The interactions between the particles are described in terms of the exchange of *vector bosons*. These are spin-1 particles and are the carriers of the fundamental interactions. The carrier of the EM force is the photon (denoted as A or γ). It is massless, electrically neutral, and does not interact via the weak or the strong force. The carriers of the weak interactions are the W and Z bosons. The W bosons are massive, have +1 or -1 electric charge, and interact via the weak force, but do not interact via the strong force. The Z boson is massive, electrically neutral, and interacts via the weak force, but does not interact via the electromagnetic force or the strong force. Finally, the carriers of the strong force are the gluons (denoted as g). They are massless, electrically neutral, and do not interact via the weak force, but do interact via the strong force. There are eight different types of gluons carrying eight different types of color charges. The interactions are summarized together with their carriers mass, charge and interaction range in Table 1.2.

Table 1.2.: The fundamental forces described by the SM with their carriers, the spin-1 bosons. The carriers mass, electric charge and the interaction range are also given [3].

Interaction	boson | mass		electric charge	range [m]
EM	photon (A or γ)	$< 10^{-18}$ eV	0	∞
Weak	Z	$\sim$91.2 GeV	0	10^{-18}
	$W^{\mp}$	$\sim$80.4 GeV	-1, $+1$	
Strong	gluons (g)	0	0	10^{-15}

1.1.1. Gauge symmetry

The Standard Model is a quantum field theory, where every particle is described by a field $\psi(x)$ in four dimensional space-time (x), and globally obeying the symmetries of special relativity: spatial translation, spatial rotations, and boosts of the reference frame. The kinematics and dynamics of all the particles are described by a Lagrangian density constructed by postulating the set of fundamental (local gauge) symmetries that exists in nature[2]. All interactions between the particles are fully described by the different terms of the SM Lagrangian [1].

The Standard Model is built on the fundamental postulate that the dynamics of all particles are determined by an underlying local gauge symmetry. This symmetry refers to the invariance of the Lagrangian under a local gauge group transformation, where the fields, describing particles, transform as follows:

$$\psi(x) \rightarrow \psi'(x) = U\psi(x) = e^{i\alpha^a(x)T^a}\psi(x) \tag{1.1}$$

where T^a are the generating matrices (generators) of a particular continuous group, $\alpha^a(x)$ the parameters which can be physically interpreted as coupling strengths, and a the indices that run over all of the generators of the fundamental representation of the particular group. The quantum-mechanical observables, which depend only on $|\psi|^2$ are invariant under equation (1.1), whereas a Lagrangian in general is not. By imposing local gauge invariance, additional gauge fields have to be introduced to make the Lagrangian invariant. These additional gauge fields describe the particles mediating the forces that determine the dynamics. This principle will be illustrated with the $U(1)$ gauge symmetry group.

[2]The requirement of a global gauge symmetry in the Lagrangian of a theory accounts for conservation of charges, via Noether's theorem, allowing for the introduction of new fields and interactions in the theory. Local gauge invariance implies the existence of gauge fields that mediate the interactions.

$U(1)$ gauge symmetry group: quantum electrodynamics

Quantum electrodynamics (QED) [1] describes the dynamics of electromagnetically charged particles. A charged particle with mass m and charge Q is described by the four-component Dirac spinor $\psi(x)$. For a free fermion of mass m the associated Dirac Lagrangian is

$$\mathcal{L}_{Dirac}^{free} = \overline{\psi}(i\gamma^\mu \partial_\mu - m)\psi \tag{1.2}$$

where $\overline{\psi} = \psi^\dagger \gamma^0$, γ^μ are the Dirac matrices[3] and μ are indices running from 0 to 3, representing the four space-time coordinates. By postulating a local $U(1)$ gauge invariance on the charged particle fields ψ, it can be illustrated that the addition of a gauge field A, describing the photon, is required, as well as a term describing the interaction between the photon and the charged Dirac particle [1].

Consider the following $U(1)$ local gauge transformation on the Dirac field:

$$\psi \to \psi' = e^{i\alpha(x)q}\psi \ . \tag{1.3}$$

The function $\alpha(x)$ is a real phase and depends on the space-time position (the symmetry transformation is called *local*) and q is a small real number. Then the mass term of the Lagrangian (1.2) is invariant under this local gauge transformation, but the first term is clearly not, due to the extra term $\partial_\mu \alpha(x)$ in the derivative transformation:

$$\partial_\mu \psi \to e^{i\alpha(x)q}\partial_\mu \psi + iqe^{i\alpha(x)q}\psi \partial_\mu \alpha(x) \ . \tag{1.4}$$

To make the theory invariant under the gauge symmetry, the usual space-time derivative ∂_μ must be replaced by a modified derivative D_μ, that transforms covariantly under phase transformations, that is, like ψ itself:

$$D_\mu \psi \to e^{i\alpha(x)q} D_\mu \psi \ . \tag{1.5}$$

[3]The Weyl representation of the γ matrices is used, corresponding to $\gamma^0 = \begin{pmatrix} 0 & I_2 \\ I_2 & 0 \end{pmatrix}$, $\gamma^i = \begin{pmatrix} 0 & \sigma^i \\ -\sigma^i & 0 \end{pmatrix}$ and $\gamma^5 = \begin{pmatrix} -I_2 & 0 \\ 0 & I_2 \end{pmatrix}$; where $I_2 = \mathrm{diag}(1,1)$ and σ^i are the Pauli matrices.

To form this covariant derivative D_μ, one must introduce the vector field A_μ such that the unwanted term in (1.4) is canceled. This is accomplished by:

$$D_\mu \equiv \partial_\mu - iq\mathrm{A}_\mu \tag{1.6}$$

where A_μ transforms as

$$\mathrm{A}_\mu \to \mathrm{A}'_\mu = \mathrm{A}_\mu + \frac{1}{q}\partial_\mu \alpha \ . \tag{1.7}$$

It is clear that D_μ satisfies (1.5), making it possible to obtain a Lagrangian that is invariant under the $U(1)$ local gauge transformation by replacing ∂_μ by D_μ:

$$\begin{aligned} \mathcal{L} &= i\overline{\psi}\gamma^\mu D_\mu \psi - m\overline{\psi}\psi & (1.8)\\ &= \overline{\psi}(i\gamma^\mu \partial_\mu - m)\psi + q\overline{\psi}\gamma^\mu \psi \mathrm{A}_\mu \ . & (1.9) \end{aligned}$$

The extra term in the Lagrangian compared to $\mathcal{L}^{free}_{Dirac}$ (1.2) expresses the coupling between the fermion field and the new vector field. In order to have a full description of the dynamics of the fields, a kinetic term for the gauge field has to be added which has to be invariant under Equation (1.7), thus it must be a function of the Maxwell tensor $\mathrm{F}_{\mu\nu}$, written in a covariant way. The term $\mathrm{F}_{\mu\nu} = [D_\mu, D_\nu]\mathrm{A} = \partial_\mu \mathrm{A}_\nu - \partial_\nu \mathrm{A}_\mu$ is invariant under the local gauge transformation and therefore the kinetic term for the gauge field A,

$$\mathcal{L}^{Maxwell}_{\mathrm{A}} = -\frac{1}{4}\mathrm{F}_{\mu\nu}\mathrm{F}^{\mu\nu} \ , \tag{1.10}$$

is also gauge invariant.

Lastly, it is important to note that a hypothetical mass term for the gauge field A,

$$\mathcal{L}^{mass}_{\mathrm{A}} = -\frac{1}{2}m^2_{\mathrm{A}}\mathrm{A}_\mu \mathrm{A}^\mu \ , \tag{1.11}$$

is not gauge invariant, and therefore the gauge field A must be massless in this theory (as can be seen by explicitly substituting A_μ by A'_μ from (1.7) in (1.11)).

To summarize, postulating local $U(1)$ gauge invariance is equivalent to adding a spin-1 massless field to the description of the system. The theory of free charged particles is transformed into the theory of quantum electrodynamics, which describes the interactions between charged particles mediated by the massless photon with a coupling strength

equal to the charge -q. The final Lagrangian describing QED is

$$\begin{aligned} \mathcal{L}_{QED} &= \overline{\psi}(i\partial_\mu\gamma^\mu - m)\psi - \frac{1}{4}\mathrm{F}_{\mu\nu}\mathrm{F}^{\mu\nu} + q\overline{\psi}\gamma^\mu\mathrm{A}_\mu\psi \\ &= \mathcal{L}_{Dirac} + \mathcal{L}_{Maxwell} + \mathcal{L}_{Int} \end{aligned} \tag{1.12}$$

where $\mathcal{L}_{Dirac}$ describes the kinetic energy and mass of the fermion field, $\mathcal{L}_{Maxwell}$ the kinetic energy of the gauge field and $\mathcal{L}_{Int}$ the interaction between both fields.

1.1.2. The SM gauge group

The gauge symmetry group of the Standard Model is $SU(3)_c \otimes SU(2)_L \otimes U(1)_Y$. The subgroup $SU(3)_c$ describes the strong interactions between quarks and gluons, while the subgroup $SU(2)_L \otimes U(1)_Y$ describes the electroweak interactions. The concept of charge from the electric charge described by the $U(1)$ local gauge symmetry can be extended to all of the above subgroups of the Standard Model gauge group. The main difference between the $SU(N)$ case and the $U(1)$ case, beside the required number of $N^2 - 1$ gauge fields instead of one, is its non-abelian nature, leading to self-interacting gauge fields [1]. The idea of these non-abelian gauge symmetries was formalized by Yang and Mills [4].

$SU(3)_c$: the strong interaction

The strong force in the Standard Model is determined by the particular properties of the $SU(3)_c$ part of the Standard Model gauge group, which is governed by quantum chromodynamics (QCD) [5, 6]. The quarks are charged under the strong force and transform as a triplet under the $SU(3)_c$ gauge transformation, while the leptons are colorless singlets. The eight introduced gauge fields describe eight spin-1 bosons and are called gluons. Gluons are massless, carry a color charge (hence the subgroup subscript c) and couple to quarks and themselves. The particular mathematical properties of the $SU(3)_c$ group, the color charges of the quarks and gluons, and the number of observed fermion generations are responsible for the fact that the strong coupling constantly decreases as the energy scale of the interaction increases.

This property has two very important phenomenological consequences. First of all, as the energy scale of a particular interaction increases, the coupling constant will vanish. This phenomenon is called *asymptotic freedom* [6][4]. In this case the coupling constant

[4]It should be noted that the effect was already observed by G. 't Hooft in 1972, but he did not publish.

is small enough to allow for calculations in perturbative series (Feynman diagrams). Secondly, quarks and gluons behave as free particles as long as the typical energy involved is high enough. At low energies the particles form bound states of quarks and gluons. This is called *confinement*. As a consequence, quarks and gluons have only been observed as color singlets into bound states called *hadrons*, which can be split up in $q\bar{q}$ pairs, called *mesons*, and $qqq/\bar{q}\bar{q}\bar{q}$ aggregates, called *baryons*. The best-known are the proton (uud) and the neutron (udd). Confinement is also responsible for the rich jet structures and hadron spectra observed at collider experiments. When a $q\bar{q}$ pair is created in high energy collisions from e.g. a Z boson decay $Z \to q\bar{q}$, the boosted quarks will loose energy by radiation (of gluons and photons) and will combine with another $q\bar{q}$ created out of the vacuum. This produces a cascade of mesons and baryons, leading to so-called *jets*. The process is called *fragmentation*. *Hadronization* is the process of forming low energy quark-antiquark pairs or quark triplets that finally bind into hadronic states.

$SU(2)_L \otimes U(1)_Y$: the electroweak interaction

The $SU(2)_L \otimes U(1)_Y$ groups are associated to the electroweak interaction, which is the unified description of electromagnetism and the weak interaction [7–9]. The long-range electromagnetic interaction is mediated by the massless photon, while the short-range weak force carriers are the massive W^+, W^- and Z bosons. However, these are different from the $SU(2)_L$ and $U(1)_Y$ gauge bosons. The $SU(2)_L$ gauge bosons only couple to the left-handed components ψ_L, hence the subscript L, of the fermion fields, leading to the observed parity-violation characteristic of the weak interactions. Using the Weyl spinor representation one can split ψ:

$$\psi = \psi_L + \psi_R = \begin{pmatrix} \varphi_L \\ 0 \end{pmatrix} + \begin{pmatrix} 0 \\ \varphi_R \end{pmatrix} . \tag{1.13}$$

The two-component objects ψ_L and ψ_R are referred to as left-handed and right-handed Weyl spinors respectively, and are obtained from the spinor ψ through the projection operators

$$\psi_L = P_L\psi = \frac{1}{2}(1-\gamma^5)\psi \quad \text{and} \quad \psi_R = P_R\psi = \frac{1}{2}(1+\gamma^5)\psi \ . \tag{1.14}$$

The left- or right-handedness of the spinors is also called *chirality*. The left-handed projections of the fermion fields form the following $SU(2)_L$ doublets:

$$\mathrm{f}_L \quad = \quad \begin{pmatrix} \nu_\mathrm{e} \\ \mathrm{e} \end{pmatrix}_L , \quad \begin{pmatrix} \nu_\mu \\ \mu \end{pmatrix}_L , \quad \begin{pmatrix} \nu_\tau \\ \tau \end{pmatrix}_L , \quad \begin{pmatrix} \mathrm{u} \\ \mathrm{d} \end{pmatrix}_L , \quad \begin{pmatrix} \mathrm{c} \\ \mathrm{s} \end{pmatrix}_L , \quad \begin{pmatrix} \mathrm{t} \\ \mathrm{b} \end{pmatrix}_L \tag{1.15}$$

while the right-handed components are $SU(3)_L$ singlets:

$$\mathrm{f}_R \quad = \quad \mathrm{e}_R , \quad \mu_R , \quad \tau_R , \quad \mathrm{u}_R , \quad \mathrm{d}_R , \quad \mathrm{c}_R , \quad \mathrm{s}_R , \quad \mathrm{t}_R , \quad \mathrm{b}_R \tag{1.16}$$

The three generators of $SU(2)_L$ are T_i and called the *weak-isospin*. The charge $T = \frac{1}{2}$ is associated to each doublet. Neutrinos and 'up'-quarks possess a third isospin component $T_3 = \frac{1}{2}$, whereas leptons and 'down'-quarks have $T_3 = -\frac{1}{2}$. Experimentally it is found that the weak isospin is different for left- and right-handed particles. Left-handed fermions transform as isospin doublets, while right-handed ones are singlets of 0 weak isospin, and therefore do not interact with gauge bosons.

The remaining $U(1)_Y$ gauge boson, with the generator Y called *hypercharge*, couples to both the left-handed and the right-handed components. Thus the $U(1)_Y$ symmetry with the hypercharge Y is not the usual symmetry of electromagnetism with the electric charge Q, as the $SU(2)_L$ doublets describing the fermions would need to have the same charge. However this is not the case since the two components of the doublets have different electric charge. For this reason, the $SU(2)_L$ and $U(1)_Y$ can not be considered separately and the $U(1)_{em}$ symmetry group associated with electromagnetism is hidden inside the $SU(2)_L \otimes U(1)_Y$ gauge group, as will be seen shortly. The hypercharge is non-zero for all fermions except for the right-handed neutrinos. Since right-handed neutrinos do not couple to any of the introduced interactions, they do not form a part of this theory. An overview table with all the quantum numbers of the fermions is given in Table 1.3.

The gauge fields associated with the generators of the $SU(2)_L \otimes U(1)_Y$ gauge group are denoted by W^1_μ, W^2_μ, W^3_μ and B_μ. They can be transformed into the fields describing the observed electroweak bosons as follows:

$$\begin{aligned} \mathrm{W}^\pm_\mu &= \frac{1}{\sqrt{2}}(\mathrm{W}^1_\mu \mp i\mathrm{W}^2_\mu) \\ \begin{pmatrix} \mathrm{A}_\mu \\ \mathrm{Z}_\mu \end{pmatrix} &= \begin{pmatrix} \cos\theta_\mathrm{W} & \sin\theta_\mathrm{W} \\ -\sin\theta_\mathrm{W} & \cos\theta_\mathrm{W} \end{pmatrix} = \begin{pmatrix} \mathrm{B}_\mu \\ \mathrm{W}^3_\mu \end{pmatrix} \end{aligned} \tag{1.17}$$

Table 1.3.: The quantum numbers summarized for the leptons ℓ and the quarks q: weak isospin (T, T_3), hypercharge (Y) and electric charge (Q). For simplicity the 'up'- and 'down'-type quarks are noted as q^u and q^d, respectively [2].

Field	T	T_3	Q	Y
ν_L	1/2	1/2	0	-1
ℓ_L	1/2	-1/2	-1	-1
ℓ_R	0	0	-1	-2
q^u_L	1/2	1/2	2/3	1/3
q^d_L	1/2	-1/2	-1/3	1/3
q^u_R	0	0	2/3	4/3
q^d_R	0	0	-1/3	-2/3

where θ_W is the weak mixing angle, quantifying the degree of mixing of the $SU(2)_L$ gauge fields and the $U(1)_Y$ gauge field in the observed photon and the Z boson. The weak mixing angle is a free parameter of the Standard Model and is measured to be approximately 30° [10]. The relation between the electric charge, the hypercharge and the weak isospin is given by the Gell-Mann-Nishijima formula [11–13]:

$$Q = T_3 + \frac{Y}{2}. \tag{1.18}$$

Two important observations can be made. First of all, an explicit mass term for the electroweak bosons would violate the gauge symmetry. Secondly, an explicit mass term for the fermions:

$$\mathcal{L}^{mass}_{fermion} = m\overline{\psi}\psi = m(\overline{\psi}_R\psi_L + \overline{\psi}_L\psi_R) \tag{1.19}$$

would couple left- and right-handed fermions, doublet and singlet members, respectively, and therefore would similarly violate the $SU(2)_L$ gauge symmetry. This presents us with a serious problem, as the W^+, W^- and Z bosons as well as fermions are experimentally measured to be massive, while explicit mass terms in the Lagrangian are not allowed. This problem is referred to as the *mass problem*.

1.1.3. Mass generation via spontaneous symmetry breaking

In the previous section we have built a theory of interacting fermions and vector fields by requiring gauge invariance. Nevertheless the masses of the gauge bosons in such theories all vanished in order for the Lagrangian to stay symmetric under such gauge

transformations. We will now dynamically generate massive bosons by spontaneously breaking the original invariance.

When a system is invariant under a given global symmetry but the ground state is not, the *Nambu-Goldstone theorem* applies. The symmetry is in this case said to be *spontaneously broken*. In this case the theorem states that there must exist one massless boson for each continuous global symmetry which is broken by the choice of a specific ground state. This theorem, first guessed by Nambu [14] and then formalized by Goldstone [15, 16] is of crucial importance in several physical contexts, ranging from solid state physics, to fluid dynamics to particle physics. The new appeared scalar fields are referred to as Goldstone bosons. A canonical example is that of a ferromagnetic system. Above the Curie temperature T_C, the system shows a $SO(3)$ rotational symmetry, with all the dipoles randomly oriented in the three-dimensional space, yielding a null overall magnetization. For $T < T_C$ all the dipoles are aligned in an arbitrary direction (spontaneous magnetization), reaching the configuration of minimum energy, and the rotational symmetry is hidden.

When the Nambu-Goldstone theorem is applied to local gauge symmetry, the Goldstone bosons are absorbed by the longitudinal degrees of freedom or polarization states of the vector bosons, allowing to provide them with a mass. This idea is called the *Brout-Englert-Higgs mechanism* and was discovered independently by Brout and Englert [17]; Higgs [18]; and Guralnik, Hagen and Kibble [19].

In the Standard Model an external field is needed to break the electroweak gauge symmetry, called the *Brout-Englert-Higgs field*. The goal is to generate the masses for the three gauge bosons W^+, W^- and Z, without generating a photon mass, what requires a minimum of three degrees of freedom. The most economical choice is a complex isospin $SU(2)$ doublet of scalar fields with hypercharge $Y = 1$ (that holds four fields and thus four degrees of freedom):

$$\phi = \begin{pmatrix} \phi^+ \\ \phi^0 \end{pmatrix} \quad \text{with} \quad \begin{aligned} \phi^+ &\equiv (\phi_1 + i\phi_2)/\sqrt{2} \ , \\ \phi^0 &\equiv (\phi_3 + i\phi_4)/\sqrt{2} \ . \end{aligned} \tag{1.20}$$

Since the doublet has no color charge the $SU(3)_c$ sector will be unaffected. The Lagrangian describing the scalar sector is the following:

$$\mathcal{L} = (D^\mu \phi)^\dagger (D_\mu \phi) - \mathrm{V}(\phi, \phi^\dagger) \quad \text{with} \quad \mathrm{V}(\phi, \phi^\dagger) = \mu^2 \phi^\dagger \phi + \lambda (\phi^\dagger \phi)^2 \ . \tag{1.21}$$

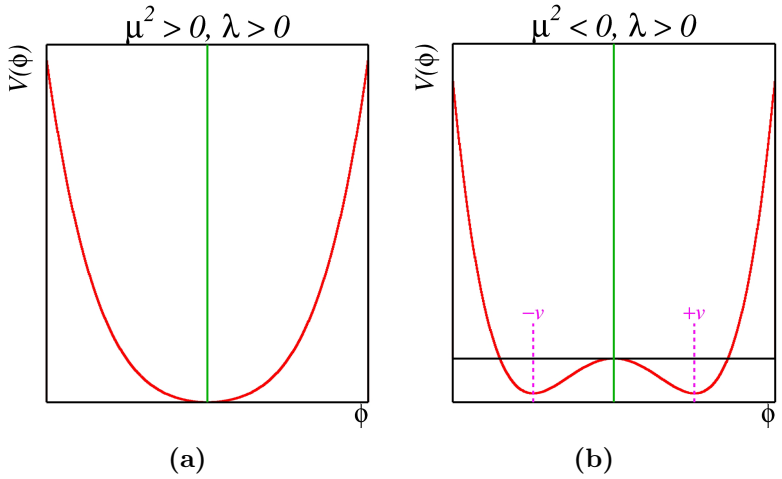

Figure 1.1.: The form of the Higgs potential $V(\phi, \phi^\dagger)$ for $\lambda > 0$ depending on the sign of μ^2 in function of ϕ: (a) μ^2 positive and (b) μ^2 negative [20].

The potential $V(\phi, \phi^\dagger)$ can have different properties depending on the values of its parameters, μ^2 and λ. In order to have a physical potential that grows asymptotically with the fields, λ must be positive[5], while μ^2 can either be positive or negative, leading to two different scenarios as shown in Figure 1.1. For $\mu^2 > 0$ the scalar potential has a global minimum at $\phi = 0$, which would not break the electroweak gauge symmetry. However for $\mu^2 < 0$ the potential has an infinite number of minima lying on a circle in a complex two dimensional space described by:

$$\phi^\dagger\phi = \frac{1}{2}(\phi_1^2 + \phi_2^2 + \phi_3^2 + \phi_4^2) = -\frac{\mu^2}{2\lambda} \equiv \frac{1}{2}v^2 \tag{1.22}$$

where v is the vacuum expectation value of the field ϕ. A particular choice of the vacuum state on this hypersphere will spontaneously break the original $SU(2)$ gauge symmetry. The typical choice for the minimum is

$$\phi_0 = \frac{1}{\sqrt{2}}\begin{pmatrix} 0 \\ v \end{pmatrix} . \tag{1.23}$$

The choice ϕ_0 with $T = 1/2$, $T_3 = -1/2$ and $Y = 1$ breaks both $SU(2)_L$ and $U(1)_Y$ gauge symmetries, but since ϕ_0 is neutral, the $U(1)_{em}$ symmetry with generator:

[5]The Hamiltonian has to be bound from below.

$$Q = T_3 + \frac{Y}{2} \tag{1.24}$$

remains unbroken as

$$Q\phi_0 = 0, \tag{1.25}$$

so that

$$\phi_0 \to \phi_0' = e^{i\alpha(x)Q}\phi_0 = \phi_0 \tag{1.26}$$

for any value of $\alpha(x)$. As a consequence the vacuum state is invariant under the $U(1)_{em}$ transformation and the photon remains massless. Out of the four generators of $SU(2)_L \otimes U(1)_Y$, T_i and Y, only the combination Q obeys the relation (1.25). The remaining three break the local gauge symmetry and thus generate massive gauge bosons through the Higgs mechanism. Looking at it from another perspective, due to the conservation of the electric charge, only neutral scalars are allowed to acquire vacuum expectation values. For this reason the vacuum (1.23) was chosen so that the charged complex field ϕ^+ of (1.20) does not acquire the vacuum expectation value.

Reparameterizing the Higgs field by expanding the Lagrangian (1.21) around this chosen vacuum ϕ_0 as

$$\phi(x) = \frac{1}{\sqrt{2}} \begin{pmatrix} 0 \\ v + \mathrm{H}(x) \end{pmatrix} \tag{1.27}$$

one finds [21]:

$$\begin{aligned}
\mathcal{L}_{Higgs} &= \left\{ \frac{1}{2}\partial_\mu \mathrm{H} \partial^\mu \mathrm{H} - \frac{1}{2} 2v^2 \lambda \mathrm{H}^2 \right\} + \left\{ -\frac{1}{3!} 6v\lambda \mathrm{H}^3 - \frac{1}{4!} 6\lambda \mathrm{H}^4 \right\} \\
&+ \left\{ \frac{1}{2}\frac{v^2 g^2}{4} \mathrm{W}_\mu^{-\dagger} \mathrm{W}^{-\mu} + \frac{1}{2}\frac{v^2 g^2}{4} \mathrm{W}_\mu^{+\dagger} \mathrm{W}^{+\mu} \right\} \\
&+ \left\{ \frac{1}{2}\frac{v^2(g^2+g'^2)}{4} \left(\frac{g\mathrm{W}_\mu^3 - g'\mathrm{B}^\mu}{\sqrt{g^2+g'^2}} \right)^2 + 0 \left(\frac{g'\mathrm{W}_\mu^3 + g\mathrm{B}^\mu}{\sqrt{g^2+g'^2}} \right)^2 \right\} \\
&+ \left\{ \frac{1}{4}(2v\mathrm{H} + \mathrm{H}^2) \left[g^2 \mathrm{W}_\mu^- \mathrm{W}^{+\mu} + \frac{1}{2}(g^2+g'^2) \left(\frac{\mathrm{W}_\mu^3 - g'\mathrm{B}_\mu}{\sqrt{g^2+g'^2}} \right)^2 \right] \right\} ,
\end{aligned} \tag{1.28}$$

where g and g' represent the coupling constant of $SU(2)_L$ and $U(1)_Y$, respectively. The first line originates from the expansion of the potential $\mathrm{V}(\phi, \phi^\dagger)$ and contains the kinetic term of the Higgs boson, its mass term and its self-interaction terms. The mass of the Higgs boson is $m_\mathrm{H} = v\sqrt{2\lambda}$ and is not predicted by the theory, as λ is a free parameter. In the second line, originating from the kinetic term $(D_\mu\phi)^\dagger (D^\mu\phi)$, one can identify the $\mathrm{W}^\pm$ vector bosons in the linear combination of the gauge bosons W^1_μ and W^2_μ). Through the process of spontaneous symmetry breaking they now have acquired mass:

$$m_\mathrm{W} = \frac{1}{2}vg \quad \text{with} \quad \mathrm{W}^\pm_\mu = \frac{1}{\sqrt{2}}(\mathrm{W}^1_\mu \mp i\mathrm{W}^2_\mu) \ . \tag{1.29}$$

Next the third line contains the mass terms for the observed Z and γ vector bosons[6]. Since the first linear combination of the gauge fields W^3 and B_μ has a non-zero mass term, it is interpreted as the massive Z boson. The second combination of the fields is massless and orthogonal to the first one. This results in:

$$m_\mathrm{Z} = \tfrac{1}{2}v\sqrt{g^2 + g'^2} \qquad \text{with} \quad \mathrm{Z}_\mu = \frac{g\mathrm{W}^3_\mu - g'\mathrm{B}^\mu}{\sqrt{g^2 + g'^2}} \tag{1.30}$$

$$m_\mathrm{A} = 0 \qquad \text{with} \quad \mathrm{A}_\mu = \frac{g'\mathrm{W}^3_\mu + g\mathrm{B}^\mu}{\sqrt{g^2 + g'^2}} \ . \tag{1.31}$$

The mixing of the gauge fields W^3 and B_μ can be interpreted as a rotation of the parameter θ_W, the weak mixing angle, where

$$\cos\theta_\mathrm{W} = \frac{g}{\sqrt{g^2 + g'^2}} \quad \text{and} \quad \sin\theta_\mathrm{W} = \frac{g'}{\sqrt{g^2 + g'^2}} \ , \tag{1.32}$$

resulting in the following relation between the weak boson masses:

$$m_\mathrm{Z} = \frac{m_\mathrm{W}}{\cos\theta_\mathrm{W}} \ . \tag{1.33}$$

Lastly, the fourth line of the Lagrangian (1.28) contains the cubic and quartic couplings of the Higgs boson to the weak gauge bosons. The coupling of a single Higgs boson to a

[6]The factor $\sqrt{g^2 + g'^2}$ is introduced to normalize the combinations of the gauge fields $g\mathrm{W}^3_\mu - g'\mathrm{B}^\mu$ and $g'\mathrm{W}^3_\mu + g\mathrm{B}^\mu$.

pair of W or Z bosons is proportional to m_{W} and m_{Z}, respectively:

$$\begin{aligned} g_{\mathrm{HWW}} &= g m_{\mathrm{W}} \\ g_{\mathrm{HZZ}} &= \frac{g}{2\cos\theta_{\mathrm{W}}} m_{\mathrm{Z}} \ . \end{aligned} \tag{1.34}$$

Using these relations, it is possible to derive the ratio of the branching ratios of the Higgs boson into a pair of vector bosons (valid at tree level[7]) :

$$\frac{BR(\mathrm{H}\to\mathrm{W^+W^-})}{BR(\mathrm{H}\to\mathrm{ZZ})} = \left(\frac{g_{\mathrm{HWW}}}{g_{\mathrm{HZZ}}}\right)^2 = 4\cos^2\theta_{\mathrm{W}}\frac{m_{\mathrm{W}}^2}{m_{\mathrm{Z}}^2} \simeq 2.7 \ . \tag{1.35}$$

This relation is called the *custodial symmetry* relation.

The electroweak part of the full Standard Model Lagrangian $\mathcal{L}_{SM} = \mathcal{L}_{GWS} + \mathcal{L}_{QCD} + \mathcal{L}_{Higgs}$, where GWS stands for the Glashow-Weinberg-Salam model of the electroweak unification, can now be expressed in terms of the physical fields:

$$\begin{aligned} \mathcal{L}_{GWS} &= \mathcal{L}_{NC} + \mathcal{L}_{CC} \\ &= \left\{ e J_\mu^{em} \mathrm{A}^\mu + \frac{g}{\cos\theta_{\mathrm{W}}} J_\mu^{\mathrm{Z}} \mathrm{Z}^\mu \right\} + \left\{ \frac{g}{\sqrt{2}} (J_\mu^+ \mathrm{W}^{+\mu} + J_\mu^- \mathrm{W}^{-\mu}) \right\} \end{aligned} \tag{1.36}$$

for the neutral current (NC) and charged current (CC) interactions, respectively. In this Lagrangian the electromagnetic coupling constant e has been introduced, identifying the coupling of the photon field A with the $\mathrm{W^+}$ and $\mathrm{W^-}$ fields as:

$$e = g\sin\theta_{\mathrm{W}} \ . \tag{1.37}$$

The following currents have also been defined:

$$\begin{aligned} J_\mu^{em} &= Q\bar{f}\gamma_\mu f \\ J_\mu^{\mathrm{Z}} &= \frac{1}{2}\bar{f}\gamma_\mu(c_{\mathrm{V}} - c_{\mathrm{A}}\gamma_5) f \quad \text{with} \quad c_{\mathrm{V}} = T_3 - 2Q\sin^2\theta_{\mathrm{W}} \ , \ c_{\mathrm{A}} = T_3 \\ J_\mu^+ &= \frac{1}{2}\bar{\nu}\gamma_\mu(1-\gamma_5) e \ . \end{aligned} \tag{1.38}$$

[7] At leading order; the diagrams do not contain any loops of particles that would enter at higher orders of the perturbation theory.

Fermion masses

Recall from Equation (1.11) that explicit mass terms for the fermion were excluded by the gauge invariance. An attractive feature of the Standard Model is that the same Higgs doublet which generates the W^+, W^- and Z masses, is sufficient to give masses to the leptons and quarks. For example, to generate mass for each lepton generation,

$$\begin{pmatrix} \nu_\ell \\ \ell \end{pmatrix} , \tag{1.39}$$

the following Lagrangian can be added [2]:

$$\mathcal{L}_{\ell,Yukawa} = -G_\ell \left[\begin{pmatrix} \bar{\nu_\ell}, & \bar{\ell} \end{pmatrix}_L \begin{pmatrix} \phi^+ \\ \phi^0 \end{pmatrix} \ell_R + \bar{\ell}_R \begin{pmatrix} \phi^-, & \bar{\phi^0} \end{pmatrix} \begin{pmatrix} \nu_\ell \\ \ell \end{pmatrix}_L \right] . \tag{1.40}$$

The Higgs doublet has exactly the required $SU(2)_L \otimes U(1)_Y$ quantum numbers to couple to $\bar{\ell}_L \ell_R$. After spontaneously breaking the symmetry and substituting the expansion around the chosen vacuum ϕ_0 (1.27) into (1.40) the Lagrangian becomes

$$\begin{aligned} \mathcal{L}_{\ell,Yukawa} &= -\frac{G_\ell}{\sqrt{2}} \left[v(\bar{\ell}_L \ell_R + \bar{\ell}_R \ell_L) + (\bar{\ell}_L \ell_R + \bar{\ell}_R \ell_L)\mathrm{H} \right] \\ &= -\frac{G_\ell}{\sqrt{2}} \left[v\bar{\ell}\ell + \bar{\ell}\ell\mathrm{H} \right] . \end{aligned} \tag{1.41}$$

The coupling G_ℓ, called the Yukawa coupling, can now be chosen so that

$$m_\ell = \frac{G_\ell v}{\sqrt{2}} \tag{1.42}$$

to generate the required lepton mass term. This results in the following Yukawa Lagrangian for each lepton generation ℓ:

$$\mathcal{L}_{\ell,Yukawa} = -m_\ell \left[\bar{\ell}\ell + \frac{1}{v}\bar{\ell}\ell\mathrm{H} \right] . \tag{1.43}$$

A few important remarks can be made. First, one should keep in mind that the actual mass of the leptons is not predicted, as G_ℓ is arbitrary. Secondly, the neutrinos ν_ℓ remain massless with this method. The quarks masses are generated in a similar way, but to generate a mass for the upper member of a quark doublet, a transformed doublet has to be constructed [2]. In addition the weak eigenstates need to mix to obtain the

mass eigenstates. Next, due to the spontaneous symmetry breaking, an interaction term couples the Higgs scalar to the fermions. The coupling is m/v where m is the mass of the particle and v is measured from experiment [10], $v \approx 246$ GeV. As a result the couplings to the fermions are in general very small (only the top quark has a big coupling, close to 1). Generally, the heavier the particle, the higher its coupling to the Higgs boson.

Spin and parity quantum numbers of the Higgs boson

Now that the Higgs boson has been introduced through the theory we can recap its quantum numbers. The Standard Model Higgs boson is a spin-0 particle ($J = 0$) and is invariant under parity (P), charge conjugation (C) and time reversal (T) transformations. This is often denoted as $J^{PC} = 0^{++}$. First of all the Higgs boson is a scalar particle, and thus has spin 0, as it has has been constructed from a potential (1.21) that is invariant under the transformation $\phi \rightarrow -\phi$. It is also the only scalar particle in the SM, hence it transforms even under parity. For the charge conjugation, one can look at one possible decay, in specific the decay to two photons. Since a photon has $C = -1$, the charge conjugation of the Higgs boson is even as $(-1)^2 = +1$. Next, since the SM theory is CPT invariant, it follows that the time reversal T is also even. On the other hand, if the Higgs boson held any conserved parity quantum number that was odd, the Lagrangian (1.28) could not have the self-interacting term H^3. This has the consequence that all the quantum numbers have to be even.

1.2. History of the Standard Model and the Higgs boson

After covering the theoretical deduction of spontaneous symmetry breaking and the Higgs mechanism, it is appropriate to put the search for the Higgs boson in a global context through a brief outline of the history of the Standard Model and the Higgs boson.

In the early 1960's particle physicists tried to construct a theory describing the interactions of leptons, some of them even attempted to unify the electromagnetic and the weak interactions. However a repeated key problem was the incorporation of a description of the masses of the particles in a gauge invariant way.

The mechanism of using spontaneous symmetry breaking to generate masses was first proposed by Philip W. Anderson in 1962 [22], although he did elaborate an explicit relativistic model. The relativistic model was developed in 1964 by three groups indepen-

dently: Robert Brout and François Englert [17]; Peter Higgs [18]; and Gerald Guralnik, Carl R. Hagen and Tom Kibble [19]. At the time this work was largely ignored and did not generate significant interest, despite it now being called the *Brout-Englert-Higgs mechanism*.

Only in 1967 the idea was picked up independently by Steven Weinberg and Abdus Salam for their construction of the Standard Model electroweak theory [8, 9]. By spontaneously breaking the $SU(2) \otimes U(1)$ group used by Sheldon Glashow in 1961 to describe the leptonic electroweak interactions [7], they were able to generate the interactions needed for their theory.

Theoretical interest finally ramped up by 1971 after Gerard 't Hooft and Martinus Veltman showed that Yang-Mills gauge theories, on which the electroweak theory was based, can be renormalized [23]. This was the key to prove that the electroweak theory could produce a viable and physically meaningful description of nature. By this time, theorists were exploring various alternative spontaneously broken gauge theories for the electroweak interactions and for other interactions.

Experimentally the verdict fell in 1973 through the discovery of neutral current interactions by the Gargamelle bubble chamber experiment at CERN [24], providing evidence in favor of the electroweak theory. Later on in 1978 parity violation measurements in inelastic electron scattering on deuterium and hydrogen targets at the Stanford linear accelerator measured the weak mixing angle θ_{W} to an accuracy of 15 % [25], essentially predicting the masses of the W and Z bosons. Based on these predictions, in 1983 the UA1 and UA2 experiments unambiguously verified the Standard Model through the observation of the W and Z bosons [26, 27].

At this point, the final piece of the puzzle is the Higgs boson itself. Both direct searches as indirect searches, through the measurements of the various parameters of the electroweak theory leading to constraints on the Higgs boson, were performed. Direct searches were performed at the Large Electron-Positron Collider (LEP) between 1989 and 2000 at CERN and at the Tevatron between 2001 and 2011. The results of these searches will be discussed in Section 1.4. After the decommissioning of the LEP collider, the construction of the Large Hadron Collider (LHC) started, which began full operation in 2010. One of the main purposes of the LHC is to provide the definitive answer on the existence of the Higgs boson. This answer will complete the half-century story of the Higgs boson. The results of this thesis contribute as an important part of this final answer. The search for the Higgs boson at the LHC will be covered in Section 1.5.

1.3. Theory bounds on the Higgs boson mass

Although the mass of the Higgs boson is a free parameter in the Standard Model theory, both lower and upper limits can be set on theoretical grounds. A first upper constraint is obtained considering the weak boson scattering process $\mathrm{W}_L\mathrm{W}_L \to \mathrm{W}_L\mathrm{W}_L$ (i.e. the scattering of longitudinally polarized W bosons) [28]. Without the existence of the Higgs boson, the amplitude of the scattering process would be proportional to the center-of-mass energy, diverging at high enough energies and thus violating unitarity at the unitarity bound $\sqrt{s} \simeq \Lambda_U = 1.2$ TeV. By also including the diagrams involving the exchange of a Higgs boson among the W_L, allowing for a cancellation of the bad high energy behavior at an energy scale $\sqrt{s} \sim m_{\mathrm{H}}$, unitarity can be restored as long as the Higgs boson is not too heavy. This unitarity bound can be expressed as

$$m_{\mathrm{H}} \leq \sqrt{\frac{8\sqrt{2}\pi}{3\mathrm{G}_F}} \sim 1 \text{ TeV} \tag{1.44}$$

with $\mathrm{G}_F = 1.1664 \times 10^{-5}$ $(\mathrm{GeV})^{-2}$ the Fermi constant. Now one may argue that the cancellation should take place before the unitarity bound is reached, in which case an upper limit on the Higgs mass of

$$m_{\mathrm{H}} \leq \sqrt{\frac{4\sqrt{2}\pi}{3\mathrm{G}_F}} \simeq 700 \text{ GeV} \tag{1.45}$$

can be derived, by considering all other possible final states such as $\mathrm{Z}_L\mathrm{Z}_L$, $\mathrm{Z}_L\mathrm{H}$ and HH. It should be noted that this is perturbative unitarity rather than unitarity so the bound cannot be taken strictly. It does not mean that the Higgs mass has to be below the upper bound, non-perturbative effects could restore unitarity for Higgs masses above the bound. Instead it underlines the fact that at high energies the theory becomes strongly coupled and the perturbative approach is not valid anymore. In summary, one learns from unitarity that the Higgs is lighter than about 700 GeV or that new physics must appear below $\Lambda_U = 1.2$ TeV. In the former the Higgs cancellation is the special case in which the new physics is the Higgs itself.

A more restricting set of bounds on the Higgs boson mass depends on the energy scale Λ up to which the SM is valid, i.e. the scale up to which no new interactions or particles are expected. The bounds arise from the evolution of the self-coupling constant

λ, the so-called Higgs quartic coupling, with energy (λ from (1.21)). Only a summary of the running calculation will be given, the details can be found in References [29, 30].

For the first bound, the Higgs potential (1.21), is affected by radiative corrections involving the mass of fermions and bosons and depending on the renormalization scale. These corrections could modify the shape of the Higgs potential so that the absolute minimum no longer exists and no stable spontaneous symmetry breaking occurs. This is avoided by requiring the λ coefficient to be positive and large enough to avoid instability up to a certain scale Λ and implies a lower bound on m_{H}. This is called the *stability bound*. A second limit can be imposed as the evolution of the coupling constant with energy presents a singularity (Landau pole) for some energy value at high energies. The perturbativity of the theory can be preserved by considering the SM as an effective theory up to a certain energy scale Λ[8]. This requirement is called the *triviality bound* and imposes an upper limit to the Higgs boson mass, depending on Λ itself.

The theoretical constraints on m_{H}, due to the triviality and stability bounds, as a function of the energy scale Λ are shown in Figure 1.2. If one expects that the Standard Model is the ultimate theory up to the Planck scale ($\Lambda = 10^{19}$ GeV), only a very narrow range of possibilities for the Higgs boson mass is allowed around 175 GeV. On the other hand, if the SM is only an effective theory up to $\Lambda = 1$ TeV then masses between 50 and 500 GeV are allowed by theoretical constraints.

1.4. Pre-LHC Higgs boson search results

Experimental bounds on the Higgs boson mass are provided by measurements at different experiments. Both direct and indirect searches have been performed.

Direct searches at LEP and Tevatron

The first direct search was performed at the LEP (Large Electron Positron) collider between 1989 and 2000 at CERN. The combined $\mathrm{e^+e^-}$ collision data of the four LEP experiments (ALEPH, DELPHI, L3 and OPAL), corresponding to 2.5 $\mathrm{fb^{-1}}$, at a center-of-mass energy between 90 and 209 GeV led to no evidence of the Higgs boson [32]. The non-observation of a statistically significant excess of signal candidates on top of the

[8] At this scale, the SM might break down due to new physics appearing.

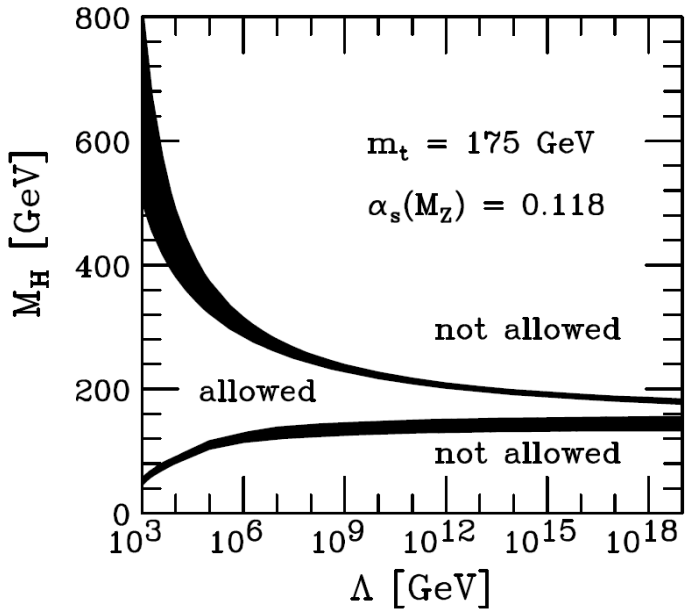

Figure 1.2.: The upper and lower theoretical limits on the Higgs mass as a function of the energy scale Λ up to which the Standard Model is valid, due to the triviality and stability requirements, respectively, on the running of the Higgs self-coupling λ. The shaded area indicates the theoretical uncertainties in the calculation of the bounds. [31].

known Standard Model backgrounds led to an experimental lower limit on the SM Higgs boson mass of 114.4 GeV at a confidence level (CL) of 95 %.

The second direct search was performed at the Tevatron accelerator at Fermilab between 2001 and 2011[9]. The search combines the results of the proton-antiproton ($p\overline{p}$) collision data of up to 10.0 fb^{-1} of the CDF and D0 experiments at a center-of-mass energy of $\sqrt{s}$ =1.96 TeV [33]. The Tevatron experiments have excluded the presence of a SM Higgs boson between $90 < m_H < 109$ GeV and $149 < m_H < 182$ GeV at a confidence level of 95 %. A mild excess is found at low masses between 115 and 140 GeV, that is interpreted as an indication for the presence of a new particle consistent with the Standard Model Higgs boson. The size of the excess corresponds to a significance of 3 standard deviations, meaning that their is only a 1/370 chance that the excess is produced by background fluctuations [33].

The ratios of the 95 % confidence level observed and expected (for the background-only hypothesis) limits to the SM cross section in function of the Higgs mass is shown in

[9]There was also a first run period of the Tevatron between 1987 and 1996. This period was omitted, due to the limited luminosity, with a sensitivity to a SM Higgs production cross section of only a factor 50 above that of the SM prediction.

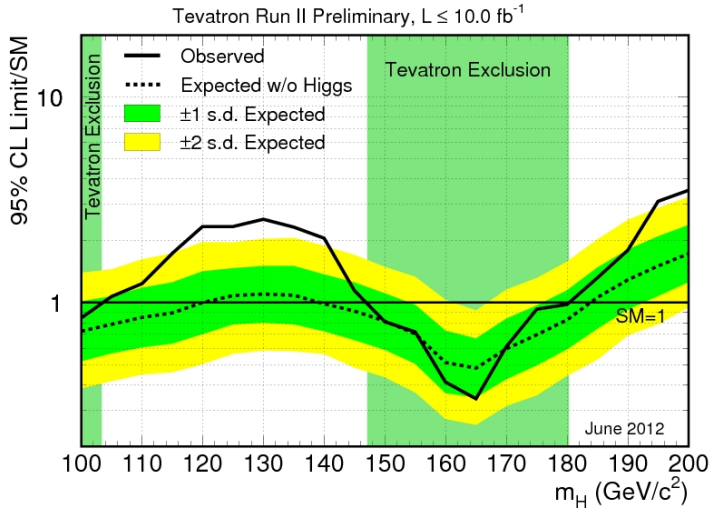

Figure 1.3.: Observed and median expected (for the background-only hypothesis) 95 % CL upper production limits expressed as multiples of the SM cross section as a function of Higgs boson mass for the combined CDF and D0 searches. The dark- and light-shaded bands indicate, respectively, the one and two standard deviation probability regions in which the limits are expected to fluctuate in the absence of signal. The Tevatron exclusion range is highlighted [33].

Figure 1.3. The green and yellow bands represent the 1σ and 2σ probability intervals around the expected limit due to the experimental and theoretical uncertainties. The plot reads as follows: if the (observed) value on the vertical axis is x, then a Higgs boson with a mass m_{H} produced with a rate of x times the rate predicted by the Standard Model is excluded at the 95 % confidence level. This means that Higgs masses for which the observed limit is below 1 are excluded under the hypothesis that the Standard Model is valid. When an excess of events is observed, the observed limit goes up, as can be seen in the region from 115 to 140 GeV where the observed limit sticks out by $\sim 3\sigma$.

Indirect constraints

Next to the direct searches, one can indirectly constrain the Higgs mass within the Standard Model framework, by using precision measurements of the fundamental parameters ($\mathrm{m_Z}$, $\mathrm{m_W}$, $\mathrm{m_{top}}$, etc.), measured at various experiments [34]. These parameters are sensitive to the presence of the Higgs boson through higher-order virtual-loop corrections, where the value of the Higgs mass enters logarithmically [35].

Using the latest measurements of all the fundamental parameters up to 2010, the fit results in a best fitted value of $m_{\mathrm{H}} = 84^{+30}_{-23}$ GeV and an upper limit of 159 GeV at the

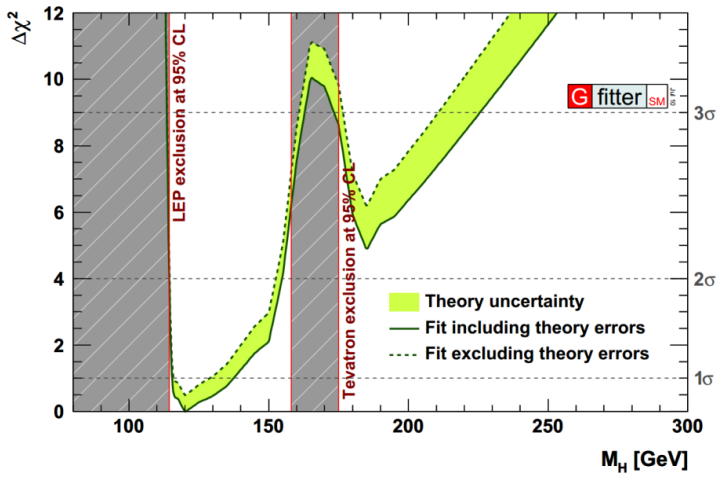

Figure 1.4.: $\Delta\chi^2$ as a function of the Higgs boson mass for a fit including the direct Higgs search results from LEP and Tevatron (up to the collision data of 2010). The solid (dashed) line represent the results when including (ignoring) the theoretical errors [37].

95 % confidence level for the SM Higgs boson mass. Combining the indirect constraints with the direct search results of LEP and Tevatron (with collision data up to 2010) results in a best fitted value of $m_{\mathrm{H}} = 121^{+17}_{-6}$ GeV and an upper limit of 155 GeV at the 95 % confidence level. The corresponding profile curve of the $\Delta\chi^2$ estimator in function of the Higgs mass for the latter fit is shown in Figure 1.4. More recent combinations exist, see [36], but as they include the direct search results from the LHC, they are not covered in this introduction.

1.5. Higgs boson production at the LHC

In this section the production mechanisms of the SM Higgs boson and its different decay modes at the LHC are covered. Afterwards the observation of a new boson at the LHC, published on the fourth of July 2012, is discussed.

1.5.1. Higgs boson production and decay modes

The cross section and rates for various processes in proton-proton collisions are shown as a function of the center-of-mass energy in Figure 1.5. The cross section for the production of a Standard Model Higgs boson with a mass between 150 and 500 GeV is 10-11 orders of magnitude smaller than the total cross section at the LHC center-of-mass energies of

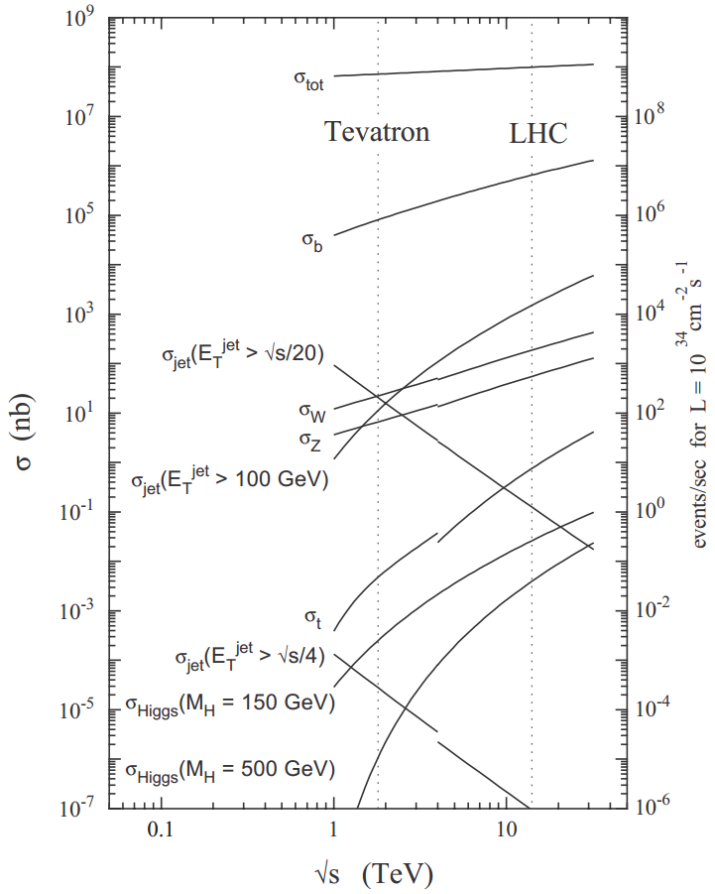

Figure 1.5.: Cross section and rates (for a luminosity of 1×10^{34} cm^{-2} s^{-1}) for various processes in proton-(anti) proton collisions, as a function of the center-of-mass energy [38].

$\sqrt{s} = 7$ TeV and $\sqrt{s} = 8$ TeV. The rarity of such events shows the challenging nature of the search for the Higgs boson.

The cross sections of the different Higgs boson production mechanisms for a proton-proton collider, like the LHC, are shown in Figure 1.6 for a center-of-mass energy of $\sqrt{s} = 7$ TeV [39] and $\sqrt{s} = 8$ TeV [40], which are the energies at which the LHC operated in 2011 and 2012, respectively. The leading-order Feynman diagrams of these Higgs boson production mechanisms are shown in Figure 1.7 and are:

- *Gluon-gluon fusion* ($\mathrm{gg} \to \mathrm{H}$): the dominating production process over the entire mass range accessible at the LHC [41]. The Higgs boson is produced from two initial state gluons mediated by virtual heavy fermions that couple to the Higgs boson. The t-quark loop will be dominating as it is so massive compared to the other fermions (see Section 1.1.3).

- *Vector boson fusion* (VBF, $qq \to qqH$): a production process at about one order of magnitude smaller than gluon fusion, where the Higgs boson is produced from the fusion of two weak bosons radiated off the incoming quarks, leaving a distinct signature of two high energy quarks following closely the direction of the incoming protons.

- *Associated production with a vector boson* or *Higgs-strahlung* ($q\overline{q}' \to WH$, $q\overline{q} \to ZH$): The Higgs boson is produced in association with a W/Z boson at a rate that is roughly another order of magnitude smaller than VBF at Higgs boson masses between 140 and 200 GeV.

- *Associated production with top quarks* ($gg \to t\bar{t}H$, $q\overline{q} \to t\bar{t}H$): The Higgs boson is produced in association with a top quark and an anti-top quark, at a rate that is roughly another order of magnitude smaller than Higgs-strahlung.

Once the Higgs boson is produced, it will decay in one of its possible *decay channels*. At tree level it can decay to a pair of W bosons, a pair of Z bosons, or a pair of massive fermions, and via radiative loop diagrams it can decay to a pair of photons, a pair of gluons, or a photon and a Z boson [42]. The branching ratios of the decay channels are strongly dependent on the Higgs mass, as shown in Figure 1.8:

- $\boldsymbol{m_H > 170}$ **GeV**: The high mass region is dominated by the decay to two massive vector bosons (W or Z). Since they are unstable, the final state would be composed of leptons and quark jets.

- $\boldsymbol{m_H < 150}$ **GeV**: The low mass region is dominated by the decay to a fermion pair. Since the Higgs coupling to fermions is proportional to their mass, the decays to $b\overline{b}$ and $\tau\tau$ have the highest branching ratios.

- $\boldsymbol{150 < m_H < 170}$ **GeV**: In the intermediate mass region both the fermionic and bosonic contributions are important, although the region is dominated by the decay to a pair of W bosons.

It is also important to note that any Higgs decays that contain jets (especially light jets) in the final state are almost useless for a search at a proton-proton collider, given the huge QCD background. As a consequence the rarer states containing leptons or photons in the final states are the most important channels to study. A good example is the $H \to \gamma\gamma$ channel which has a small branching ratio, but can be fairly easily distinguished from $\gamma\gamma$ pairs produced in QCD processes.

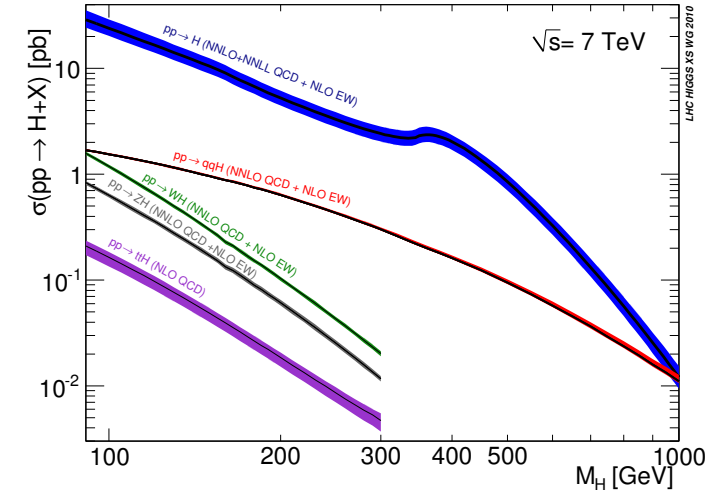

(a)

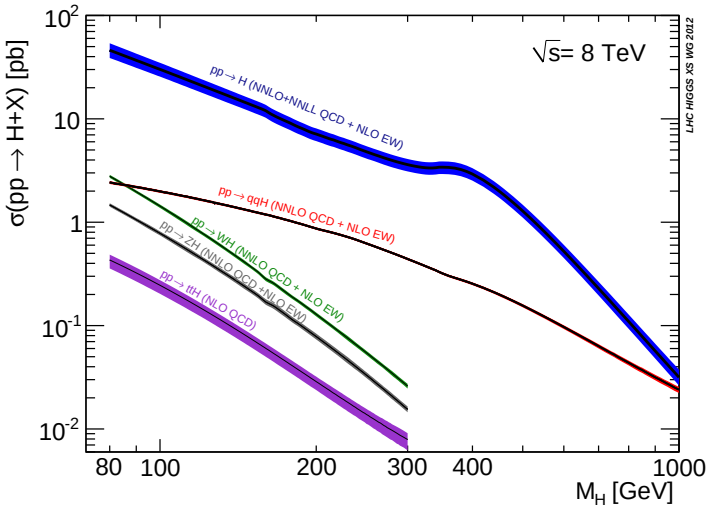

(b)

Figure 1.6.: Cross sections of the different Higgs production mechanisms as a function of the Higgs mass at (a) $\sqrt{s} = 7$ TeV and (b) $\sqrt{s} = 8$ TeV [39, 40].

The most important decay channels at the LHC are:

- $\mathbf{H \to \gamma\gamma}$: one of the most important channels for the discovery of the Higgs boson at masses below 140 GeV. Despite the low branching ratio, the signal-to-background ratio is rather good. The signal signature is two energetic isolated photons which can be well identified experimentally. The main background is an irreducible one, i.e. another SM process that leads to the same particles in the final state: the QCD double photon production $\mathrm{pp} \to \gamma\gamma$. Other *instrumental* backgrounds, i.e. to detector specific features like particle misidentification, can be reduced to an

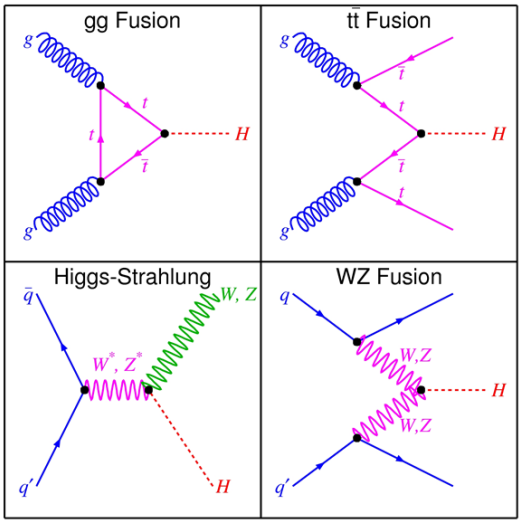

(a)

Figure 1.7.: Feynman diagrams of the LO production processes of the Higgs boson at the LHC [20].

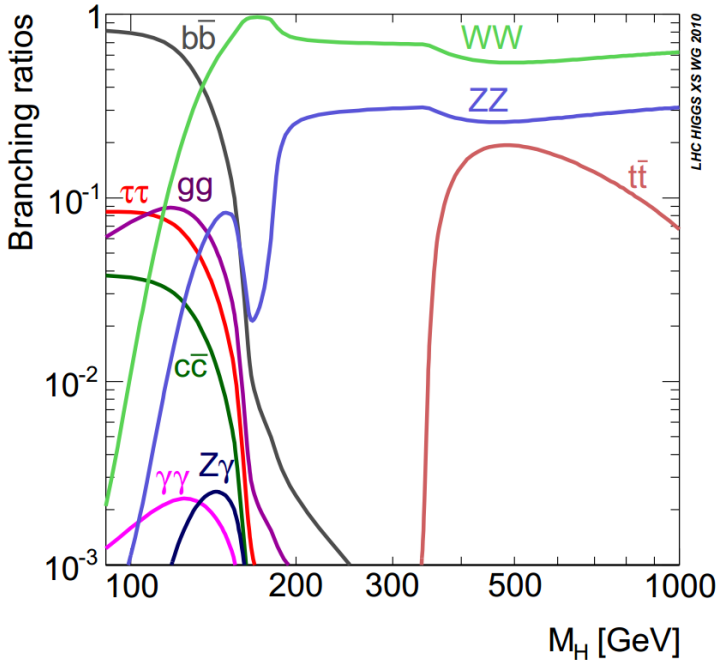

Figure 1.8.: Higgs branching ratios as a function of the Higgs mass [39]. The $s\bar{s}$ and $\mu\bar{\mu}$ decay channels are not shown in this figure as they are very small, but can be found in Reference [43] on page 112.

acceptable level by applying proper selection criteria to the reconstructed physical objects. The Higgs boson can be detected as a narrow resonance peak above the broader background.

- $\mathbf{H \to ZZ \to 4\ell}$: another very important channel for the discovery of the Higgs boson due to its very clean signature with four isolated leptons in the final state. Furthermore, it has a very good signal-to-background ratio. The irreducible background is the non-resonant double Z production $pp \to \mathrm{ZZ} \to \ell^+\ell^-\ell^+\ell^-$. Again some instrumental backgrounds can be reduced by applying proper selection criteria to the reconstructed physical objects. The Higgs boson would be revealed by the presence of a resonance peak above a small continuous background. The Higgs discovery in the ZZ channel is possible with an integrated luminosity of around 10 fb^{-1} in the whole mass range between 120 and 500 GeV, apart for a small region around $m_\mathrm{H} \sim 165$ GeV. This latter region is dominated by non-resonant double Z production and is affected by a relatively low Higgs branching ratio to ZZ as can be seen in Figure 1.8.

- $\mathbf{H \to W^+ W^- \to 2\ell\, 2\nu}$: the discovery channel in the intermediate mass region, $2\mathrm{m_W} < m_\mathrm{H} < 2\mathrm{m_Z}$ as the Higgs branching ratio to $\mathrm{W^+ W^-}$ is close to one. The signature is two charged leptons and missing energy. Due to the neutrinos in the final state, the mass peak can not be reconstructed. As a consequence the analysis is a counting analysis (the analysis is sensitive to the final number of events), which requires the accurate knowledge of all the possible backgrounds. The main backgrounds are the non-resonant double W production $pp \to \mathrm{W^+ W^-} \to 2\ell\, 2\nu$, $t\bar{t}$ and $\mathrm{W} + \mathrm{jets}$. Due to the very large branching ratio in both the high and low mass regions, the analysis is sensitive in the mass range 100-600 GeV. This channel is the subject of this thesis and will be extensively described in the following chapters.

Two more channels are important for a low mass Higgs discovery as they can significantly enhance the significance of a possible excess in the $\mathrm{H} \to \gamma\gamma$ or $\mathrm{H} \to \mathrm{ZZ}$ analyses. They are $\mathbf{H \to \tau^+\tau^-}$ for $m_\mathrm{H} \lesssim 150$ GeV and $\mathbf{H \to b\bar{b}}$ for $m_\mathrm{H} \lesssim 135$ GeV. The latter channel exploits the associated production with vector bosons ($\mathrm{V} = \{\mathrm{W^\pm}, \mathrm{Z}\}$) decaying to leptons: $pp \to \mathrm{H}(\to \mathrm{b\bar{b}})\,\mathrm{V}(\to \ell\ell, \ell\nu, \nu\nu)$. The mass resolution of both channels is however very poor (of the order of 10-20 GeV). Yet, they are the sensitive channels allowing to probe the decay of a Higgs boson to leptons, an important characteristic to prove that a found Higgs-like particle is the Standard Model Higgs boson.

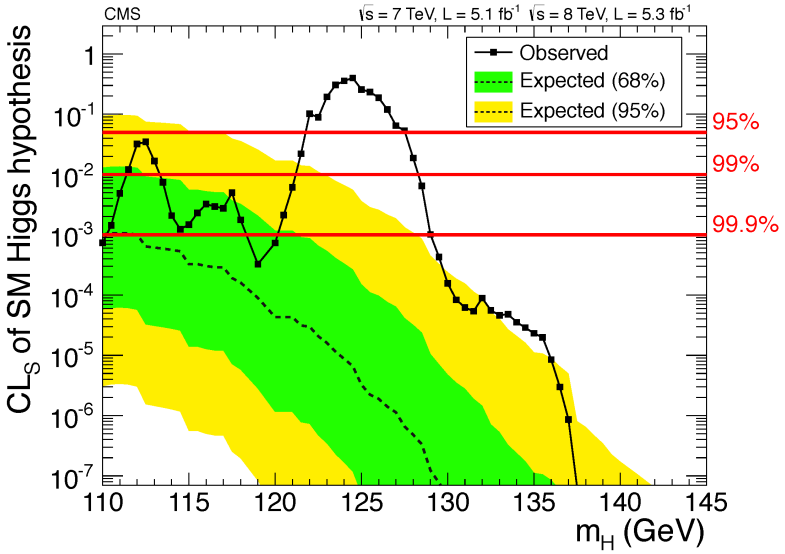

(a)

Figure 1.9.: The CL_s values for the SM Higgs boson hypothesis as a function of the Higgs boson mass in the range 110-145 GeV. The background-only expectations are represented by their median (dashed line) and by the 68 % and 95 % CL bands [44].

1.5.2. Observation of a Higgs-like boson

On the fourth of July 2012, the ATLAS and CMS collaborations each individually announced the observation of a new boson in the light of their search for the Higgs boson at the LHC [44, 45]. The search result consists of the combination of the five decay modes: $\gamma\gamma$, ZZ, W^+W^-, $\tau^+\tau^-$ and $b\bar{b}$ [10], with an integrated luminosity of around 5 fb^{-1} at $\sqrt{s} = 7$ TeV and around 5 fb^{-1} at $\sqrt{s} = 8$ TeV. This corresponds to the full 2011 dataset along with $\sim 1/4$ of the final 2012 dataset. CMS reported an excess of events above the expected background with a significance, the probability of background fluctuations to reproduce the observed excess, of 5.0 standard deviations at a mass near 125 GeV, signaling the production of a new particle. This excess was confirmed by the ATLAS collaboration which found a significance of 5.9 standard deviations, corresponding to a background fluctuation probability of 1.7×10^{-9} around the same mass [45]. The CMS combined limit on the Higgs cross section as a function of the Higgs mass is shown in Figure 1.9. The observed limit is clearly weaker than the expected limit for the background-only hypothesis around 125 GeV. More details can be found in the corresponding observation papers of both experiments in References [44, 45].

[10] It should be noted that not all subchannels of these decay modes are combined. For a detailed list see [45] and [44] for ATLAS and CMS, respectively.

During 2013 the analyses have been updated to include the full 2011 and 2012 datasets. The observed mass peaks near 125 GeV with the full dataset in the diphoton invariant mass distribution and the four-lepton invariant mass distribution, in the $\gamma\gamma$ and ZZ analyses, respectively, are shown in Figure 1.10. The former is shown for the ATLAS collaboration, while the latter is shown for CMS. Both distributions clearly show a mass peak that is compatible with the Higgs boson. The signature of a Higgs-like boson has been found in all five decay modes, $\gamma\gamma$, ZZ, $\mathrm{W^+W^-}$, $\tau^+\tau^-$ and $\mathrm{b\overline{b}}$ for CMS [46] and in the four decay modes, $\gamma\gamma$, ZZ, $\mathrm{W^+W^-}$, $\tau^+\tau^-$ for ATLAS [47]. The signature is currently statistically compatible with the Standard Model. This compatibility is quantified as the *signal strength* (μ or the best fit value for $\sigma/\sigma_{\mathrm{SM}}$) and is shown in Figure 1.11. The signal strength of the separate decay modes, as the combined signal strength, is for each experiment compatible with the Standard Model.

Lastly it is important to note that the decay to two photons indicates that the new particle is a boson with its spin different from one, as the Landau-Yang theorem forbids the direct decay of an on-shell spin-1 particle into a pair of photons [48, 49]. All these results are consistent, within uncertainties, with expectations for a Standard Model Higgs boson.

The double confirmation on the observation of a Higgs-like boson led in 2013 to the awarding of the Nobel Prize to François Englert and Peter Higgs, for the theoretical discovery of a mechanism that contributes to our understanding of the origin of mass of subatomic particles, and which recently was confirmed through the discovery of the predicted fundamental particle, by the ATLAS and CMS experiments at CERN's Large Hadron Collider. Englert's co-author of the proposed mechanism paper, Robert Brout, passed away in 2012. Thanks to Brout's and Englert's affiliation to the ULB, Belgium gained its first Nobel Prize in Physics.

The work in this thesis covers the $\mathrm{H} \to \mathrm{W^+W^-} \to 2\ell\,2\nu$ channel, a subchannel of the $\mathrm{H} \to \mathrm{W^+W^-}$ decay channel, which contributed to the observation on the fourth of July 2012 for the CMS experiment. The results for the full 2011 and 2012 dataset will be covered.

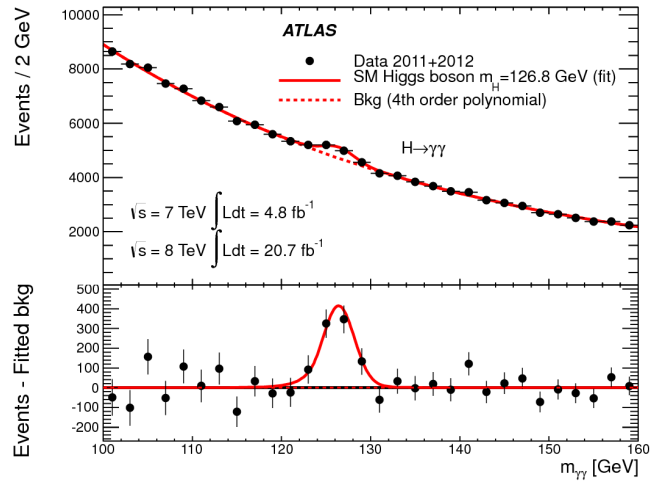

(a)

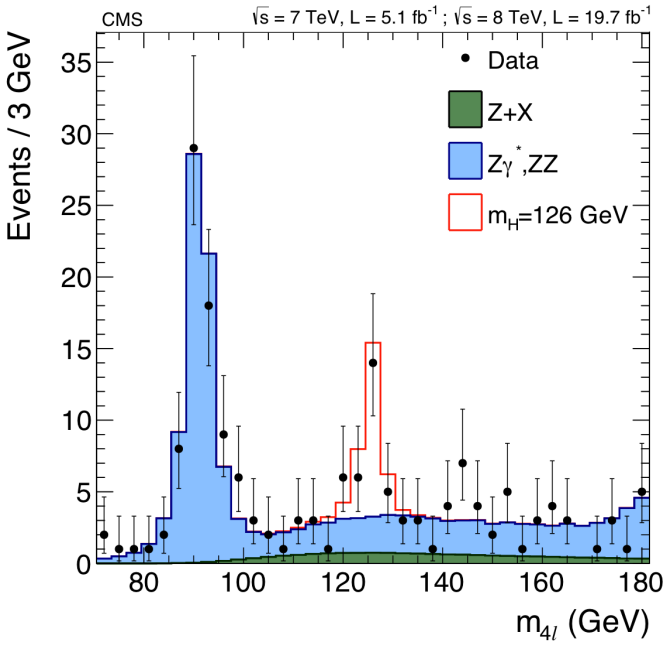

(b)

Figure 1.10.: (a) Diphoton ($\gamma\gamma$) invariant mass distribution for the full ATLAS data of 2011 and 2012 (black points with error bars). The solid red line shows the fit result for signal plus background, while the dashed red line shows only the background fit [50].
(b) Distribution of the four-lepton invariant mass for the sum of the 4e, 4μ and $2e2\mu$ channels for the full CMS data of 2011 and 2012. Points with error bars represent the data, shaded histograms represent the backgrounds, and the unshaded histogram the signal expectation for a mass hypothesis of 126 GeV. Signal and ZZ background are normalized to the SM expectation, Z + X background to the estimation from data [51].

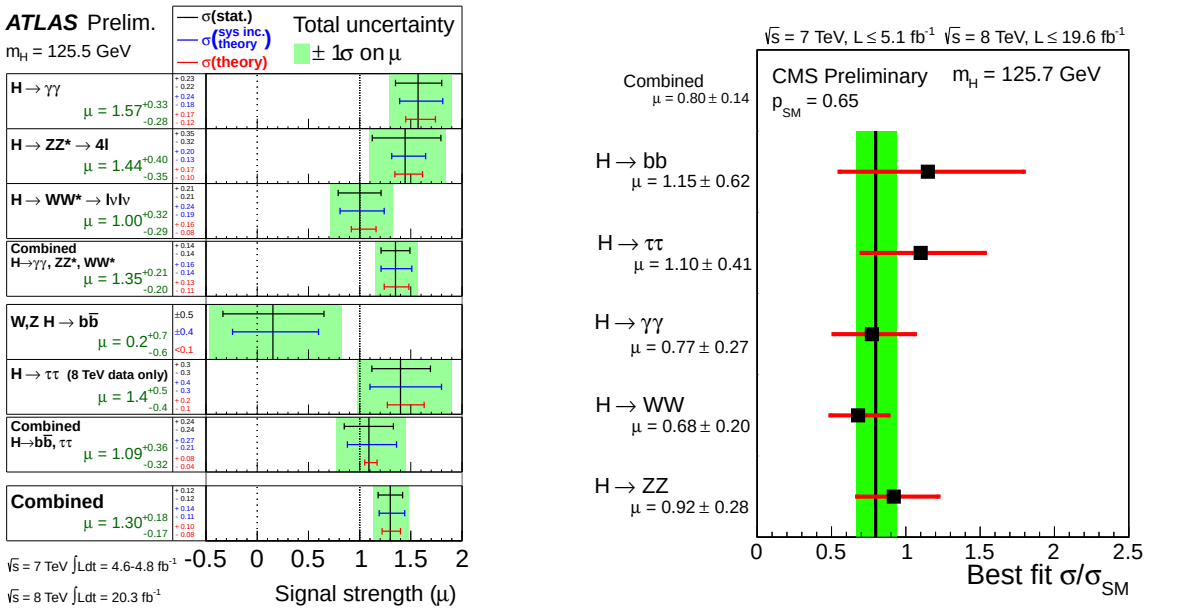

(a) (b)

Figure 1.11.: The measured signal strengths of the observed Higgs-like boson, normalized to the SM expectations, for the individual final states and (various) combined for (a) ATLAS, (b) CMS. In (a) the best-fit values are shown by the solid vertical lines, while the total $\pm 1\sigma$ uncertainties are indicated by green shaded bands. In (b) the best-fit values are shown by squares with error bars indicating the total $\pm 1\sigma$ uncertainties, while the combined signal strength is shown by a solid vertical line with a green shaded band indicating the total $\pm 1\sigma$ uncertainty [46, 47].

Chapter 2.

The Large Hadron Collider

The analysis of the outcome of proton-proton (p-p) collisions at high energies allows to study and verify several aspects of the Standard Model. These collisions are produced in accelerators, machines that are capable of accelerating particles to a very high center-of-mass energy and colliding them head-to-head at certain interaction points. The result of each collision is recorded by a cluster of specific sub-detectors that is set up around each interaction point.

Today, the world's largest and most powerful particle accelerator is the Large Hadron Collider (LHC) at CERN[1] in Geneva, Switzerland. It is a machine designed to open up the door to the unprecedented TeV energy range looking for answers to open key questions in particle physics such as the Brout-Englert-Higgs mechanism and new physics.

2.1. Layout and Design

The LHC [52] is a circular proton-proton accelerator housed in the tunnel of the former e^+e^- LEP accelerator [53]. The tunnel has a circumference of 27 km and is located underground at a depth between 45 m and 170 m across the French-Swiss border. The LHC consists of two different rings (beam pipes), in which the counter-rotating beams of protons can be accelerated to an energy of 7 TeV. As a result, the machine can produce proton-proton collisions at a center-of-mass energy of $\sqrt{s}$ =14 TeV. Next to protons, the LHC is also capable of accelerating Pb ions up to an energy of 2.76 TeV/nucleon resulting in heavy ion collisions at $\sqrt{s}$ =1.15 PeV. The plans for the LHC were approved in 1995 and the first protons circulated within the LHC in 2008.

[1] Conseil Europeén pour la Recherche Nucléaire.

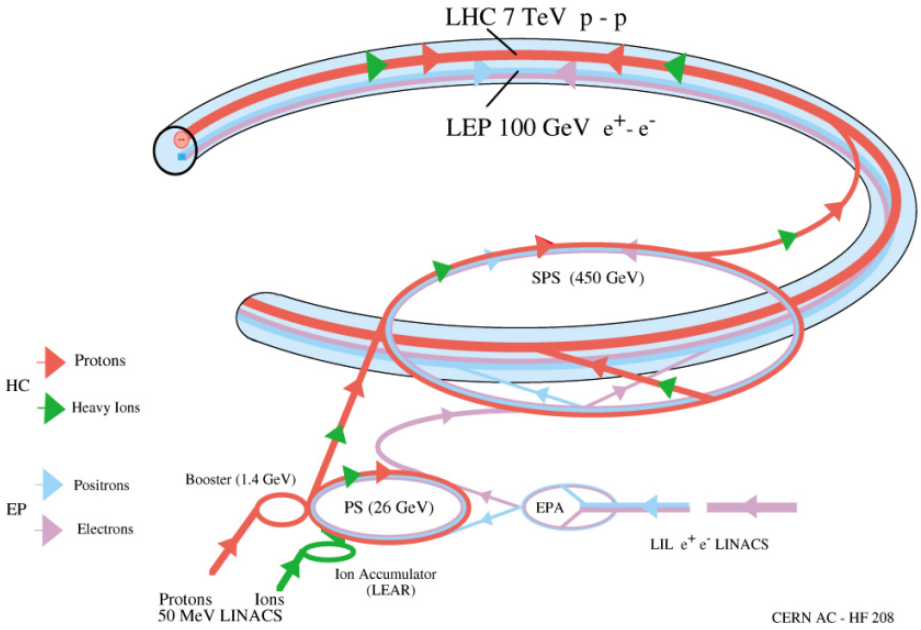

Figure 2.1.: The LHC injection complex for proton-proton or Pb-Pb collisions.

Injection

Protons are not just created or directly injected in the LHC. There is a whole series of accelerators to set up the beams for the LHC. The accelerator park is shown in Figure 2.1. Protons are first obtained out of the ionization of hydrogen in a strong electric field. These protons are accelerated to an energy of 50 MeV in the Linear Accelerator (LINAC) before they are injected in the Proton-Synchrotron-Booster (PSB) and accelerated to 1.4 GeV. In a next step, the protons are injected in the Proton Synchrotron (PS) where the proton beams are divided into small bunches of 1.15×10^{11} protons each and accelerated to 25 GeV. Next, the bunches are injected in the Super-Proton-Synchrotron (SPS) where they reach an energy of 450 GeV. Finally these proton bunches are inserted at two different locations in the LHC, one for each of the two beam pipes that hold counter-rotating proton bunches. The LHC accelerates these bunches to the nominal energy. Once this energy is reached, a few machine parameters are tweaked so that collisions at certain interaction points are achieved. With a maximum of 2808 bunches per beam with a minimal time of 25 ns between two bunches, a peak crossing rate of 40 MHz can be reached. When the machine is fully filled and at nominal energy, the beams have a circulating beam current of 0.582 A and the total energy per beam equals 362 MJ. At a certain point, when the beam is deteriorated, the beam is dumped (see Figure 2.3 for the dumping location) and the whole process starts over.

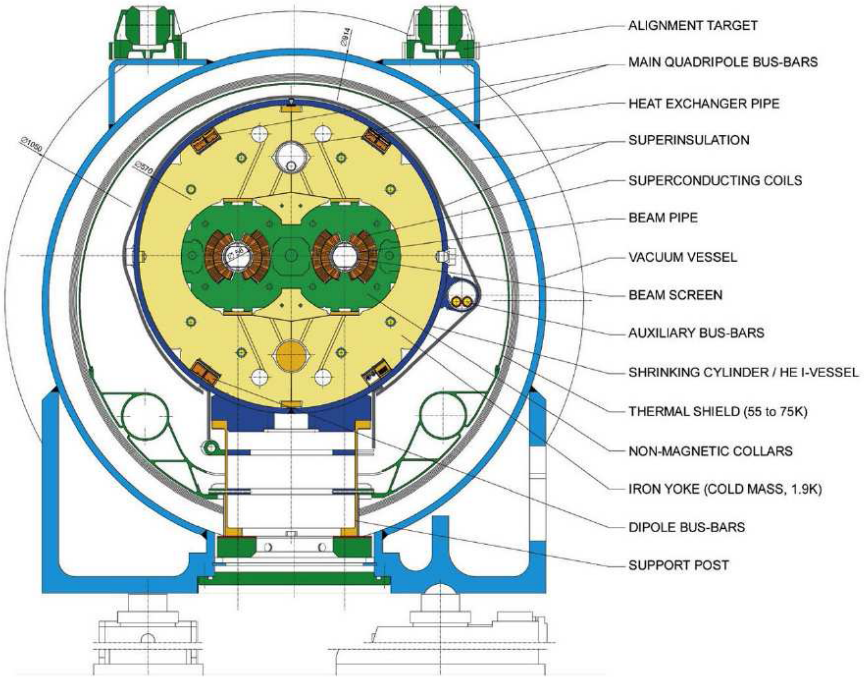

Figure 2.2.: Transverse view of the beam pipe and the magnets concealed in the holding cooling vessel.

Superconducting magnets

The limiting factor to reach high-energy circular proton beams is to maintain the strong magnetic field needed to keep the trajectory of the protons constrained to the two LHC beam pipes. Since the LHC accelerates opposite-rotating proton beams in two adjacent beam pipes, one requires an opposite magnetic field in each of these two pipes. This results in two very strong magnets, closely spaced, with a different (opposite) magnetic field. In order to meet these stringent conditions, there was a need for new state-of-the-art magnet technology.

The LHC uses thousands of magnets of different varieties and sizes to direct the beams around the accelerator. There are 1232 dipole magnets with a length of 14.3 m that are cooled down to 1.9 K with super-fluid helium to bring them in a superconduction state. This state enables the generation of the needed 8.3 T fields to bend the beam trajectories around the accelerator at the nominal beam energy of 7 TeV. The other magnets are mostly quadrupoles and octopoles that are used to control the protons trajectory or to focus the beams at the interaction points. A transverse view of the beam pipe and dipole magnets together with its holding cooling vessel is shown in Figure 2.2.

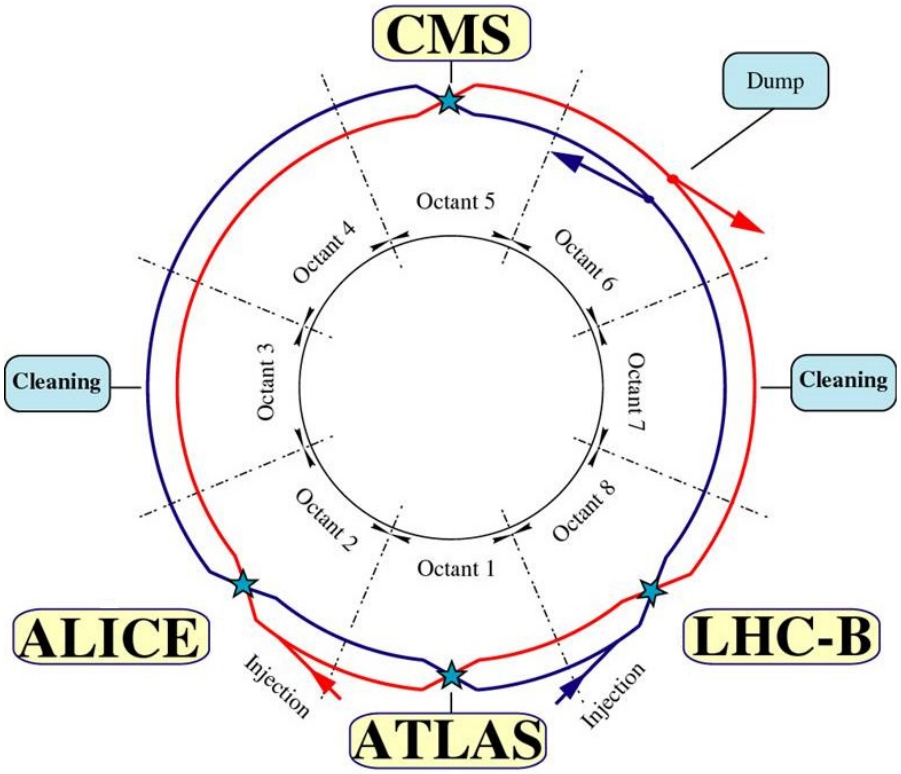

Figure 2.3.: Schematic layout of the LHC: the two opposite beams are shown in red (clockwise) and blue (anti-clockwise). The four experiments ALICE, ATLAS, LHCb and CMS are located at the four collision points.

Layout

The vacuum beam pipes of the counter-rotating proton beams cross in four interactions points as shown in Figure 2.3. Around these points, four experiments can be found: CMS (Compact Muon Solonoid) [54], ATLAS (A Toroidal LHC ApparatuS) [55], ALICE (A Large Ion Collider Experiment) [56] and LHCb (LHC Beauty experiment) [57]. The experiments are shown in Figure 2.4. CMS and ATLAS are very similar in scope, they are multipurpose detectors designed to probe new physics as well as performing precision measurements. On the short term, the primary goal of these experiments is to investigate the nature of the electroweak symmetry breaking mechanism. On the long term, they will be searching for new physics in the TeV energy scale. ALICE was specifically built to study heavy ion collisions to get a greater understanding of the quark-gluon plasma[2]. LHCb was designed to study flavor physics and CP-violation in general.

[2]This plasma is the hot dense medium produced during the heavy-ion collisions.

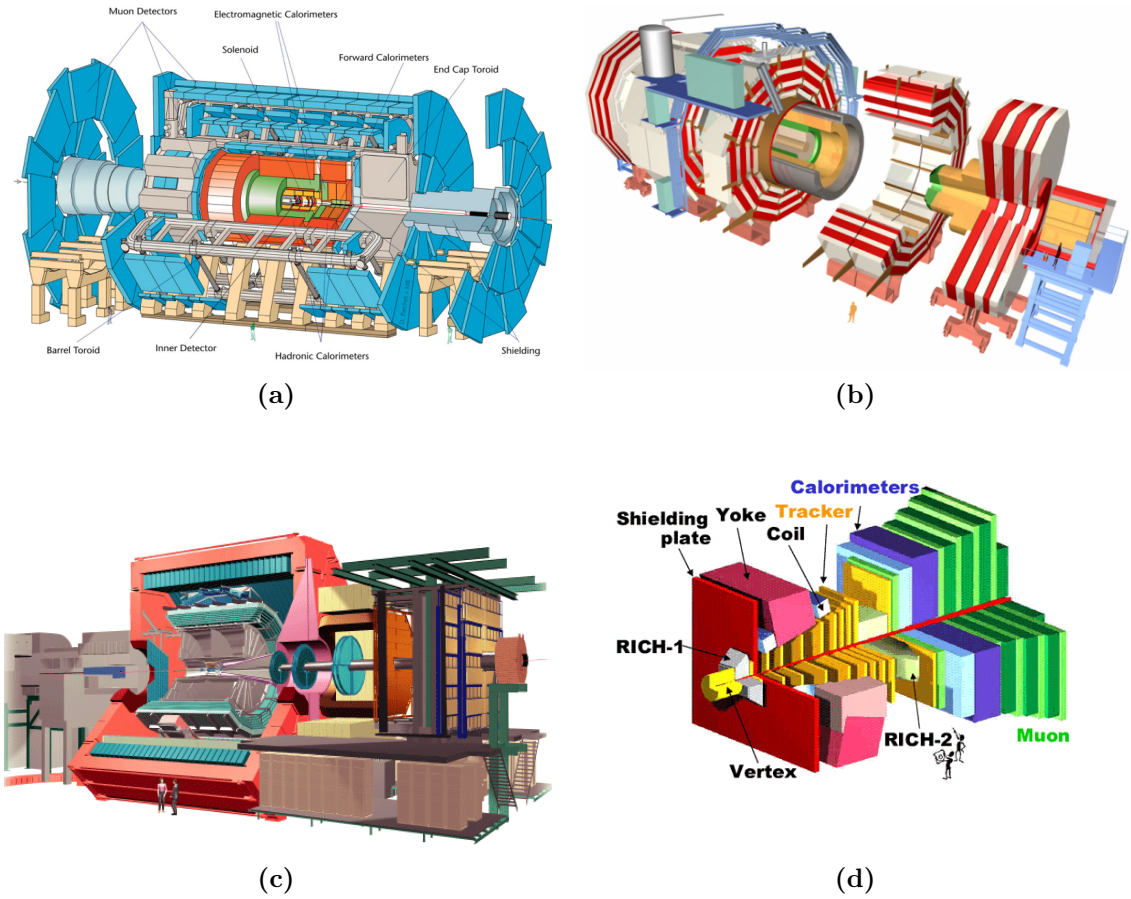

Figure 2.4.: The four major experiments at the LHC: (a) ATLAS, (b) CMS, (c) ALICE and (d) LHCb.

Luminosity

The instantaneous luminosity L is an important parameter to describe the performance of an accelerator. It gives the number of events generated per second $N_{events} = L\,\sigma_{events}$ where σ_{events} is the cross section of the events under study. Under the assumption of two identical colliding beams, the instantaneous luminosity can be written as

$$L = f\,n_b\frac{N_b^2}{A} \tag{2.1}$$

where f is the revolution frequency (fixed by the speed of light and the length of the LHC), n_b is the number of proton bunches, N_b is the number of protons in each bunch and A is the effective overlap area of the two colliding beams (in the direction transverse to the beam). The design instantaneous luminosity of the LHC is $L = 10^{34}\ \mathrm{cm}^{-2}\,\mathrm{s}^{-1}$

achieved with $n_b = 2808$ bunches containing $N_b = 1.15 \times 10^{11}$ protons per bunch. The amount of statistics collected is expressed in units of integrated luminosity, $\mathcal{L} = \int L\, dt$.

2.2. Run periods

The first beams circulated the LHC on September 10th, 2008. Only a few days later, the LHC had to cease operations due to an accident that happened on the 19th. An electrical fault led to the loss of large quantities of liquid Helium which was vented through the LHC tunnel. The expanding Helium dealt significant damage to the magnets and other accelerator infrastructure in sector three and four (see Figure 2.3). It took over a year to repair the LHC and fit in extra safety measures to prevent this type of incidents in the future. Despite the addition of infrastructure improvements, it was decided to run the LHC at a significant lower energy and luminosity than its design parameters. The LHC restarted in November 2009 and the first collisions of 450 GeV proton beams at a center-of-mass energy of $\sqrt{s}$ =900 GeV were recorded by the experiments.

In March 2010 the LHC produced the first ever collisions at $\sqrt{s}$ =7 TeV, a milestone in particle physics, operating only at half of its design energy. This was the start of a long data taking period in 2010 and 2011 at $\sqrt{s}$ =7 TeV. The number of bunches was slowly increased from 50 to 368 bunches in 2010 to a maximum of 1380 bunches in 2011. The instantaneous luminosity was also gradually increased from 8 $\times 10^{26}$ cm^{-2} s^{-1} at the start of 2010 to 2 $\times 10^{32}$ cm^{-2} s^{-1} at the end of 2010 to a final peak luminosity of 0.4 $\times 10^{34}$ cm^{-2} s^{-1} [58, 59] in 2011.

In order to optimize the sensitivity for Higgs boson discovery, it was decided to increase the beam energies for the 2012 data run. Collisions at $\sqrt{s}$ =8 TeV were achieved with a peak luminosity of 0.7 $\times 10^{34}$ cm^{-2} s^{-1}. The total integrated luminosities recorded by the CMS experiment are 44.2 pb^{-1} in 2010, 6.1 fb^{-1} in 2011 and 23.3 fb^{-1} in 2012 and are shown in Figure 2.5. Currently the LHC entered its first long shutdown period. The machine is being prepared to run collisions at $\sqrt{s}$ =13 TeV starting in 2015.

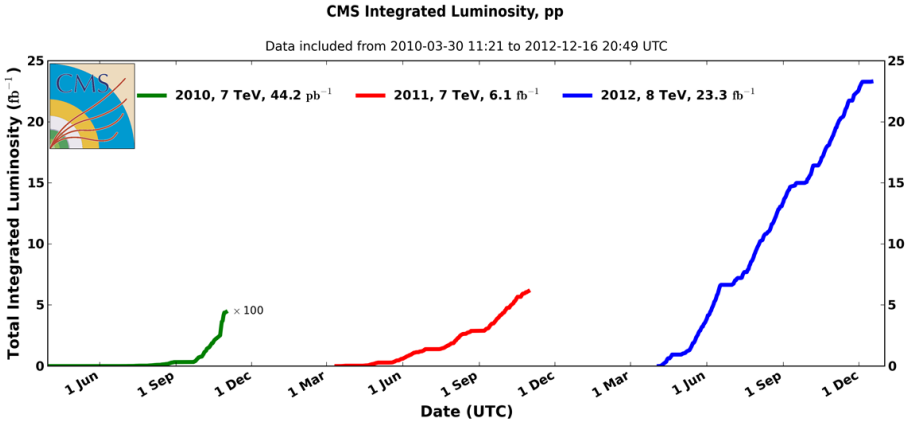

Figure 2.5.: Cumulative luminosity versus day delivered to CMS during stable beams and for p-p collisions. Data-taking from 2010 (green) multiplied by 100, 2011 (red) and 2012 (blue) are shown [60].

2.3. Pile-up

The beam intensities in the LHC are so high that when they cross at the interaction point, the probability to have more than one proton-proton collision becomes significant. This effect is called *pile-up* (PU) and the number of collisions per crossing are called *pile-up events*.

The number of inelastic proton-proton interactions in a bunch crossing follows a Poisson distribution:

$$P(n) = \frac{(L\,\sigma_{events})^n}{n!} e^{-L\,\sigma_{events}} \tag{2.2}$$

where L is the instantaneous luminosity and σ_{events} the cross section of the events under study. Since the instantaneous luminosity increased all along the data-taking from 2010 to 2012 (see Figure 2.5), the number of pile-up events increased from 1 to 35 pile-up events. This increase can be seen in Figure 2.6. The average numbers of pile-up events in the 2011 and 2012 data are approximately 9 and 21, respectively. The pile-up has an impact on the object reconstruction in the CMS detector and on the event selection procedure as will be discussed in Chapter 4 and 5, respectively.

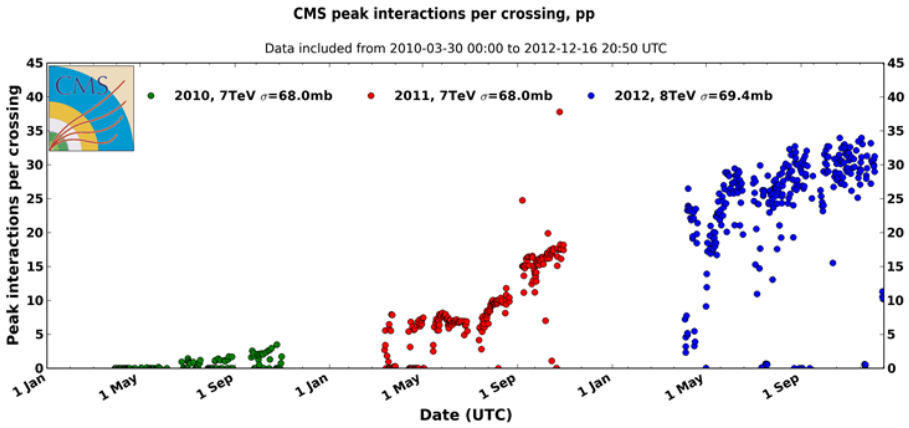

Figure 2.6.: Peak interactions per crossing versus time for proton-proton collisions, each point represents a new fill of the beams. (including special runs) Data-taking from 2010 (green), 2011 (red) and 2012 (blue) are shown [60].

Chapter 3.

The Compact Muon Solenoid

3.1. Introduction

The Compact Muon Solenoid (CMS) detector [54] is one of the two multi-purpose detectors of the LHC (see Chapter 2). The detector is located at the LHC interaction Point 5, about 100 m underground close to the French village of Cessy. It has a length of 21.6 m, a diameter of 14.6 m and a total weight of 12500 tonnes.

A lot of experimental challenges have to be met to cope with the extreme LHC conditions. At the design luminosity of $L = 10^{34}\ \mathrm{cm}^{-2}\,\mathrm{s}^{-1}$, the detector will observe an event rate of approximately 10^9 inelastic proton-proton collisions per second. An online data reduction process (trigger) needs to reduce this rate to about 100 events/s to allow storage and subsequent analysis. The short time of 25 ns between two bunch crossings has a major impact on the design of the read-out and trigger systems. At the design luminosity, a mean of 20 pile-up events (see Section 2.3) are superimposed on the event of interest arising from the same bunch crossing due to the high beam intensities and high center-of-mass energy. This implies that each 25 ns around 1000 charged particles emerge from the interaction point and the products of an interaction under study may be confused with those of a pile-up event. The problem becomes even more challenging when the response time of a detector element and its electronic signal is longer than 25 ns. Furthermore, the large flux of particles leads to high radiation levels requiring radiation-hard hardware.

Lastly, to meet the LHC physics goals, it is mandatory to have an excellent detector performance, which can be summarized as follows: [54]

- Good muon identification and momentum resolution over a wide phase space
- Good charged particle momentum resolution and reconstruction efficiency close to the interaction point
- Good electromagnetic energy resolution and high calorimeter granularity
- Good missing transverse energy (MET or $E_{\mathrm{T}}^{\mathrm{miss}}$) detection efficiency requiring a large hermetic geometric coverage.

The design of CMS, described in the following sections, meets all the above requirements. The coordinate system used in CMS is a right-handed system, with the origin centered at the nominal collision point inside the experiment, the y-axis pointing vertically upward, the x-axis pointing radially inward toward the center of the LHC and the z-axis pointing along the anticlockwise-beam direction. The azimuthal angle ϕ is measured from the x-axis in the xy plane and the polar angle θ is measured from the positive z-axis. Pseudorapidity is defined as $\eta = -\ln\tan\theta/2$. The momentum and energy transverse to the beam direction, denoted by p_{T} and E_{T} respectively, are computed form the x and y components.

General overview

The main detector layout is driven by the choice of the magnetic field configuration needed for the measurement of the momentum of the muons. Large bending power is needed to precisely measure the momentum of high-energy charged particles. Since this forces the choice of superconducting magnet technology, a superconducting solenoid was chosen in the case of CMS.

The overall layout of the CMS detector is shown in Figure 3.1. It is a cylindrical structure with a central barrel closed by two endcaps. In order to maximize the acceptance for the products of the proton-proton collisions, the detector is almost hermetic, it is only limited by the beam pipe that follows the axis of the cylinder. At the heart of CMS, a 13 m long, 6 m diameter superconducting solenoid that generates a 3.8 T field is located. Inside the solenoid, closest to the interaction point are the pixel detector and the silicon tracker. It is the first layer which encounters the products of a collision and which reconstructs the trajectories of the charged particles without significantly affecting their momenta. The high magnetic field of the solenoid bends these particles making it possible to deduct their momenta by studying their trajectory. The second layer, still

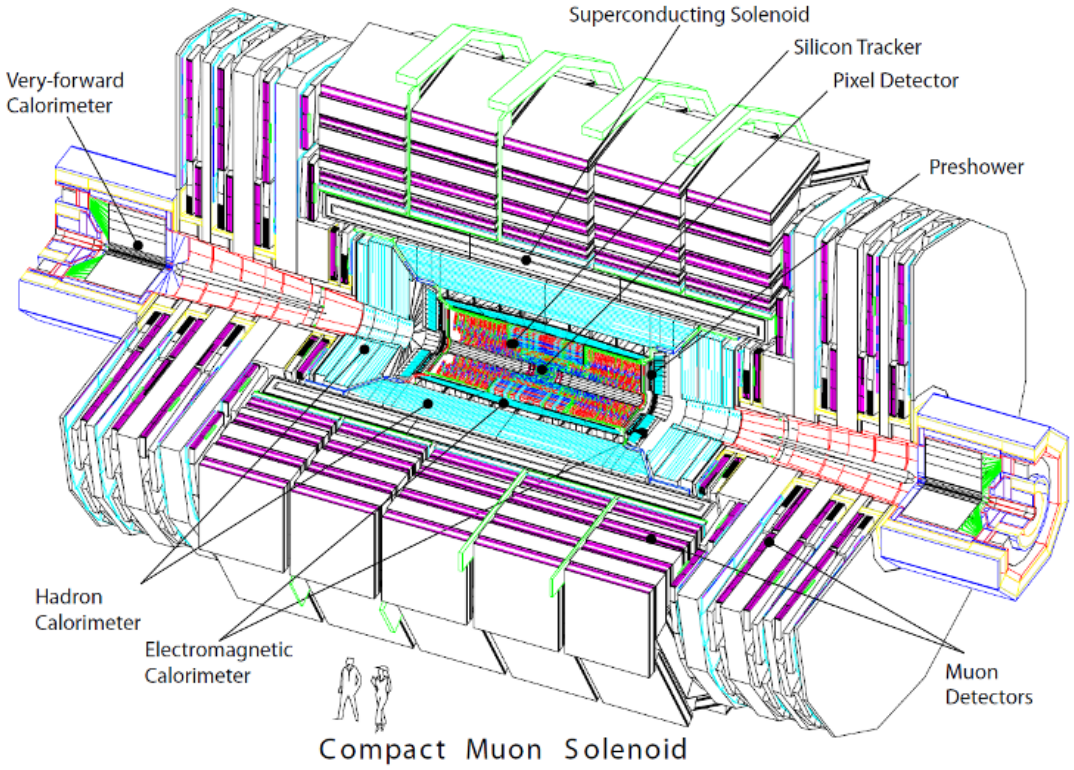

Figure 3.1.: Perspective view of the CMS detector [54].

inside the solenoid, is the electromagnetic calorimeter (ECAL) which measures the energy deposited by particles that initiate electromagnetic showers when they interact with matter, such as electrons, protons and photons. In the next layer, the last one inside the solenoid, the hadron calorimeter (HCAL) is located which measures the energy deposited from particles that passed the ECAL and initiate hadronic showers when they interact with matter such as protons, neutrons and pions. Outside the solenoid interspersed with the iron return yoke is the muon system. The hermetic layers of muon chambers in the barrel and endcap of the CMS detector take care of the reconstruction of the muon charge and momentum.

It is important to note that the design of the CMS experiment is carefully optimized to reach the overall most-efficient, highest precision measurement of all kind of particles. The tracker is the most inner layer since it is used to reconstruct the interaction vertices and the particle trajectories with a minimal of interference and without destroying them. Next in line are the electromagnetic and the hadron calorimeters which measure the energy of the particles in a destructive way. First particles like electrons and photons are absorbed in the electromagnetic calorimeter, while particles like protons, neutrons and pions penetrate through the electromagnetic part and are absorbed in the hadron

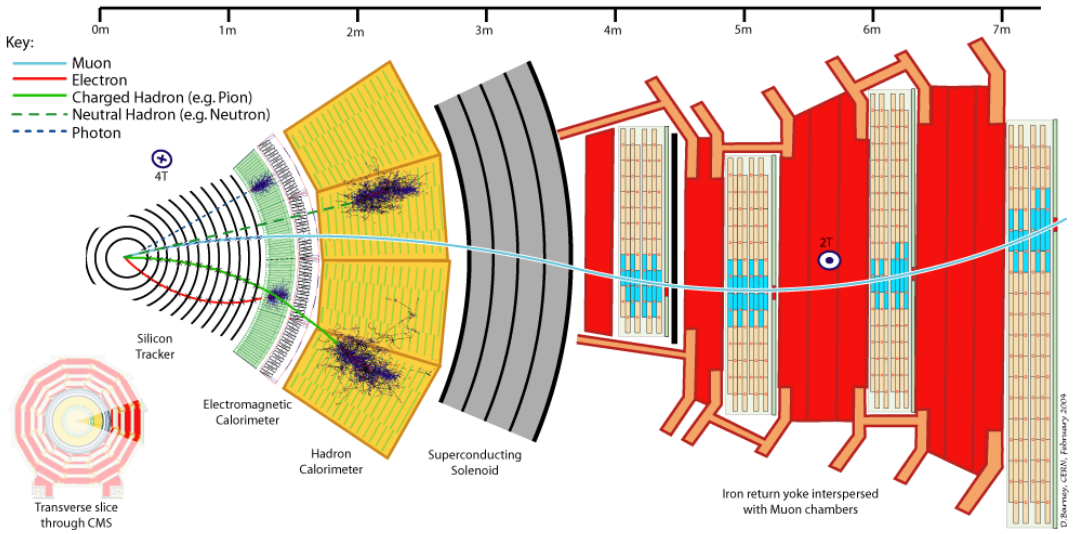

Figure 3.2.: Transverse slice through the CMS detector showing particle-detector interactions. Figure courtesy of Dave Barney for CERN.

calorimeter. Since muons are minimum-ionizing particles, they survive all the previous layers and leave their tracks in the large muon chambers. A transverse slice through the CMS detector with the particle-detector interactions of some key particles is shown in Figure 3.2.

Lastly, some particles like neutrinos remain undetected (due to their weakly interacting nature). Although the initial energy and momentum is conserved in a collision, most of the proton remnants trajectories are not covered by the detector, but are lost in the beam pipe. This makes it impossible to use the 3-momentum conservation law to calculate the total 3-momentum of the neutrinos that are not leaving a signal in the detector. However in the transverse plane the total transverse momentum is conserved. The imbalance of energy measured in the transverse plane, equal to the total transverse momentum of the undetected particles, is denoted by $E_{\mathrm{T}}^{\mathrm{miss}}$. Particles escaping detection through the beam pipe have low transverse momenta and do not contribute significantly to $E_{\mathrm{T}}^{\mathrm{miss}}$. This quantity can be used to indirectly detect weak interacting particles like neutrinos.

3.2. Tracking system

The tracking system of CMS [54] is designed to precisely and efficiently measure the trajectories of charged particles emerging from the LHC collisions in a pseudorapidity range of $|\eta| < 2.5$. In addition, it is necessary to accurately reconstruct secondary vertices

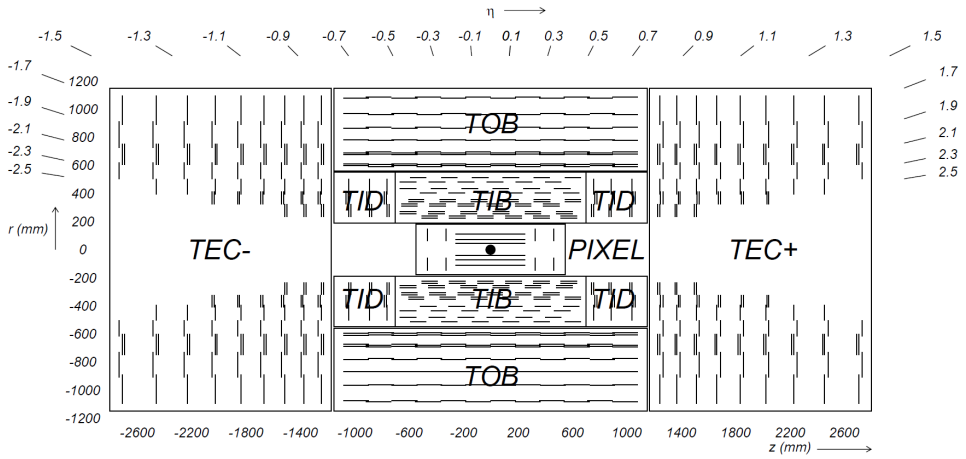

Figure 3.3.: Schematic cross section through the CMS tracker. Each line represents a detector module. Double lines indicate back-to-back stereo modules that deliver stereo hits [54].

to identify the decays of long-lived heavy particles and to distinguish the vertices of different pile-up events. The tracking system is the closest detector layer to the interaction point and has a length of 5.8 m, a diameter of 2.5 m and is completely embedded in the homogeneous 3.8 T magnetic field of the CMS solenoid.

The detector requires a high granularity and a fast response time due to the short time between two bunch crossings and the presence of the pile-up events. These features imply a high density of read-out electronics which is only possible if the system is cooled down. This is however in direct conflict with the aim to keep the amount of material used in the detector to a minimum. This is to avoid the introduction of additional interactions that in turn produce charged particles that contaminate the original collision remnants. In addition, the detector has to cope with an intense particle flux, causing severe radiation damage to the tracking system over time. This requires a radiation-hard detector with the goal of an expected lifetime of 10 years. As a result of all these stringent requirements, the whole tracker design is entirely based on silicon detector technology.

A schematic cross section through the CMS tracker is shown in Figure 3.3. The tracker consists of two sub-systems, the pixel detector and the silicon strip tracker. The most inner one is the *pixel detector* (PIXEL). It consists of three cylindric barrel layers, located at the respective radii of 4.4, 7.3 and 10.2 cm, surrounding the interaction point and two endcap disks that close the PIXEL cylinder. To keep the detector occupancy, i.e. the percentage of pixels hit by all particles, to a maximum of 1 %, a total of 66 million 100×150 µm^2 pixels cover an area of about 1 m^2.

The second sub-system is the *silicon strip tracker*. It consists of four subsystems: the Tracker Inner Barrel (TIB), the Tracker Outer Barrel (TOB), the Tracker Inner Disk (TID) and the Tracker Outer Disks (TEC). The TIB is composed of four layers and covers a radius from 20 to 55 cm. The TOB is composed of six layers and covers the larger radius from 55 to 116 cm. Both first layers of the TIB and the TOB contain *stereo modules*.[1] The TID and TEC are rings, with respectively 3 and 9 ring layers, closing off the TIB and TOB cylindric layers. Stereo modules are also installed in the first two layers of the TID and in layer 1, 2 and 5 of the TEC. Since the silicon strip tracker is further away from the interaction point, the particle flux is lower. This allows for bigger cell sizes, starting at 10 cm $\times$ 80 µm for the TIB to even 25 cm $\times$ 180 µm for the outer sections of the tracker. The overall achieved resolution approaches 35 µm in the $r \times \phi$ plane and 270 µm in the z-direction.

Figure 3.4 shows the outstanding tracker performance for single muons with a transverse momenta of 1, 10 and 100 GeV. A p_{T} resolution of 1-2 % can be reached for 100 GeV muon tracks up to $|\eta| \approx 1.6$. The resolution of the transverse impact parameter with respect to the primary vertex reaches a precision of 20 µm at $|\eta| \approx 0.5$ and increases to 70 µm at the edge of the tracker system.

3.3. Electromagnetic calorimeter

The Electromagnetic calorimeter (ECAL) [54] is a hermetic, homogeneous calorimeter that surrounds the tracking volume. The design has been driven by the requirement of an excellent energy resolution due to its crucial role in the physics program of CMS.

The ECAL consists of 61200 lead tungstate ($PbWO_4$) crystals mounted in the central barrel, closed by 7324 crystals in each of the two endcaps. The barrel (EB) has a radius of 129 cm and covers a pseudorapidity range of $|\eta| < 1.479$. The endcaps (EE) cover $1.479 < |\eta| < 3.0$. A preshower detector (ES but further called PS), consisting of two layers, is placed in front of the endcap crystals to identify neutral pions (through $\pi^0 \to \gamma\gamma$ decays) within $1.653 < |\eta| < 2.6$. It also improves the identification of electrons against minimum-ionizing particles. The scintillated light is collected by Avalanche Photo-diodes (APDs) in the barrel and Vacuum Photo-diodes (VPDs) in the endcaps. The longitudinal cross section is shown in Figure 3.5.

[1] Stereo modules contain two series of silicon strips pointing to opposite directions to increase the $r \times \phi$ resolution.

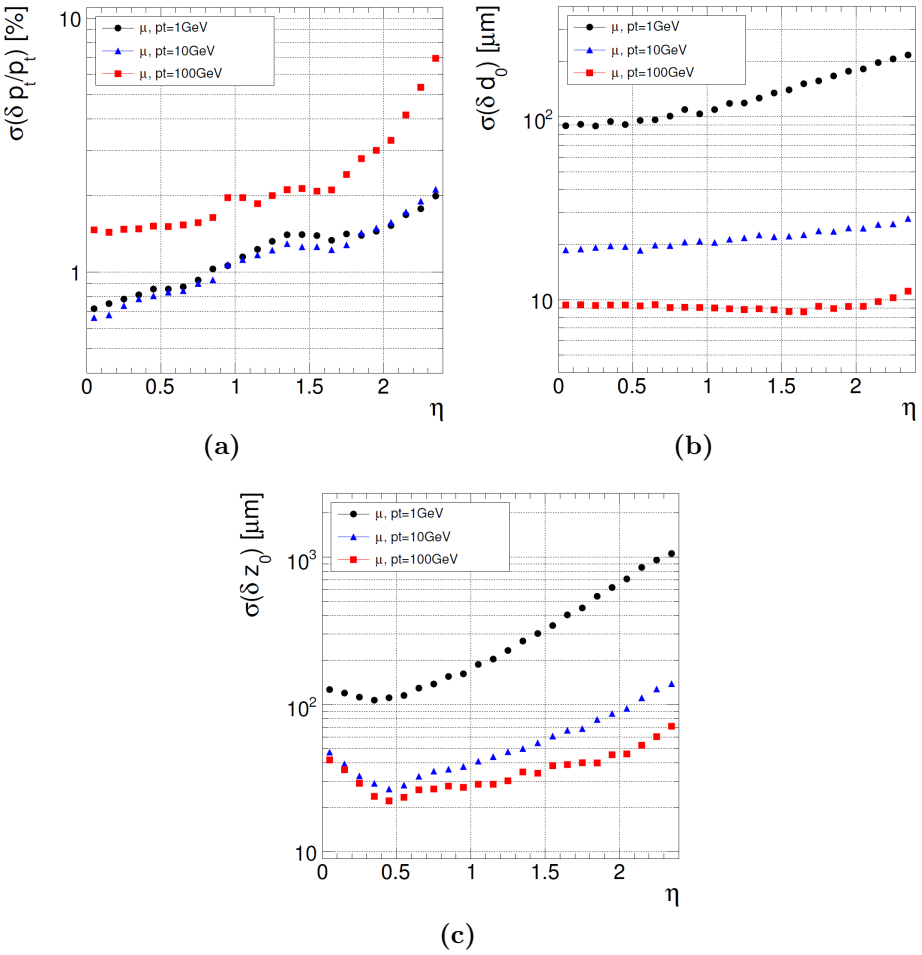

Figure 3.4.: Resolution of several track parameters for single muons with a p_T of 1, 10 and 100 GeV: (a) transverse momentum, (b) transverse impact parameter and (c) longitudinal impact parameter [54].

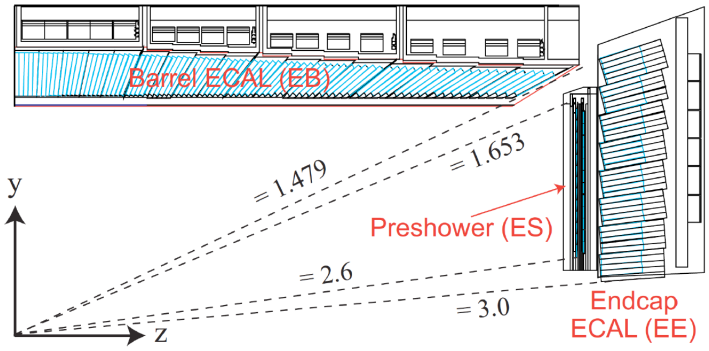

Figure 3.5.: Longitudinal cross section of the electromagnetic calorimeter [54].

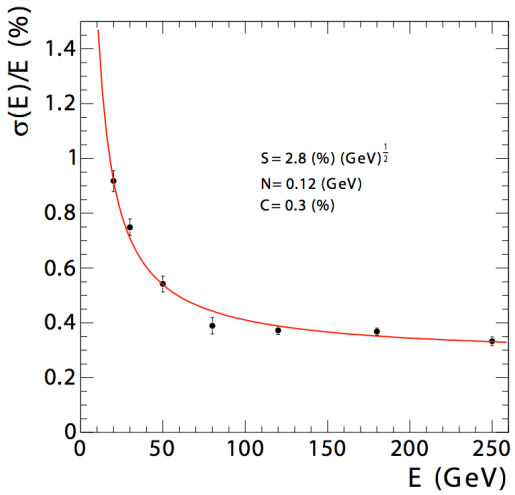

Figure 3.6.: ECAL energy resolution parametrized as a function of energy, following (3.1) of section 3.3 [54].

The characteristics of the $PbWO_4$ crystals made them an appropriate choice. The lead tungstate scintillating crystals have a short radiation length of 0.89 cm and a small Moliere radius of 2.2 cm resulting in a fine granularity and a compact calorimeter. They are also fast, 80 % of the light is emitted within the 25 ns between two bunch crossings. They are also radiation hard up to 10 Mrad. This allowed for a compact calorimeter inside the solenoid that is fast, has a fine granularity and is radiation resistant.

The energy resolution (measured with electron test beams) can be parameterized as a function of energy (in GeV):

$$\left(\frac{\sigma(E)}{E}\right)^2 = \left(\frac{S}{\sqrt{E}}\right)^2 + \left(\frac{N}{E}\right)^2 + C \tag{3.1}$$

with $S = 2.8$ %, $N = 12$ % and $C = 0.3$ % and is shown in Figure 3.6. In this formula, S is a stochastic term depending on the event characteristics, in particular on electromagnetic shower development. The second term, N is the noice term originating from electronics and pile-up. The last term C is a constant term that depends on the non-uniformity of the longitudinal light collection, on the energy leakage from the rear face of the crystals and on the accuracy of the detector inter-calibration constants. Accounting for all contributions, the ECAL energy resolution is below 1 % at all energies going to even less than 0.4 % at higher energies (see Figure 3.6).

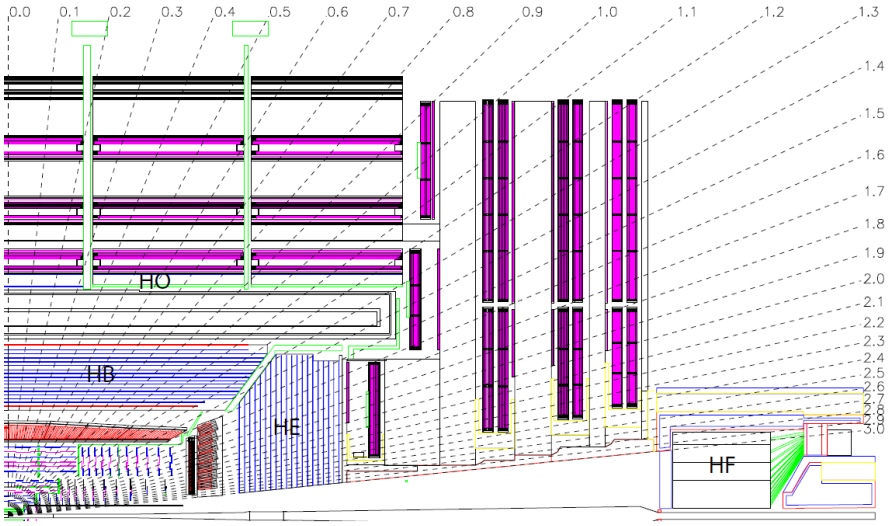

Figure 3.7.: Longitudinal cross section of one quarter of the hadron calorimeter. The abbreviations are specified in the text [54].

3.4. Hadron calorimeter

The hadron calorimeter (HCAL) [54] is a hermetic sub-detector installed between the ECAL and the magnet coil covering the large pseudorapidity range of $|\eta| < 5.2$. The calorimeter absorbs the particles that survive the ECAL material, except muons and weakly interacting particles, and is particularly important for the measurement of jets. Moreover the HCAL provides an important part of the $E_{\mathrm{T}}^{\mathrm{miss}}$ measurement, since hadrons contribute in p-p collisions to a significant fraction of the total produced particles and thus of the total deposited energy.

The hadron calorimeter consists of four sub-detectors: the hadron barrel (HB), the hadron endcaps (HEs), the hadron outer barrel (HO) and the hadron forward calorimeters (HF). A longitudinal cross section of the hadronic calorimeter layout is shown in Figure 3.7.

The HB and HE are hermetically joined with the barrel covering $|\eta| < 1.4$ and the endcaps covering the overlapping range $1.3 < |\eta| < 3.0$. The design of the HCAL maximizes material inside the magnet coil in terms of interaction lengths. Brass is the absorber material as it has a reasonable short interaction length, it is easy to machine and it is non-magnetic. To maximize the amount of absorber, a tile/fiber structure was used to minimize the amount of space devoted to the active medium. The tile/fiber consists of plastic scintillator tiles that are read out by embedded wavelength-shifting fibers. Layers of 5 cm brass absorber are alternated with 4 mm of plastic scintillator.

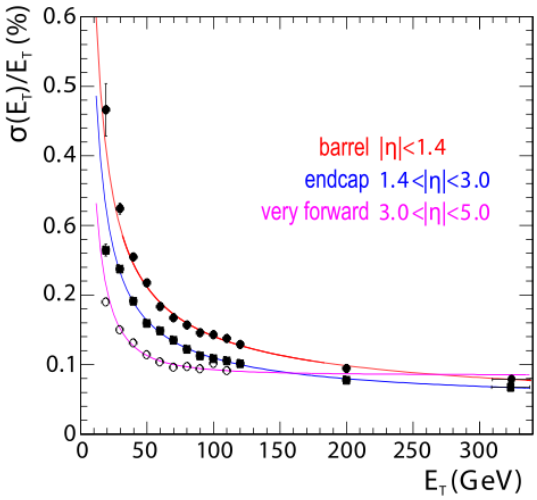

Figure 3.8.: HCAL jet transverse energy resolution as a function of the transverse energy for barrel, endcap and forwards jets [54].

The HO is an additional absorber placed outside the magnet coil since in the central pseudorapidity range, the combined stopping power of the ECAL and the HB does not provide a sufficient containment of the hadron showers. The HO consists of a layer of scintillators and the magnet coil acts as an extra absorber layer. It covers the same pseudorapidity range as the HB. To be able to measure energetic forward jets, forward HF calorimeters are installed. These forward calorimeters are located 11.2 m from the interaction point and cover the pseudorapidity range $2.9 < |\eta| < 5.2$. The HF has to survive an even higher particle flux, therefore it was chosen to use a Čerenkov detector with quartz fibers.

The HCAL performance is illustrated in Figure 3.8 by studying the resolution of the reconstructed jet transverse energy. The resolution is shown for the barrel, the endcap and the forward calorimeter. The resolution is about 30-50 % for low transverse energies but it improves to 10 % for higher transverse energies.

3.5. The Muon System

The Muon System [54] is located in the outer layer of the CMS experiment. As it is implied by the middle name of the experiment, the detection of muons is of central importance to CMS. Muons with high transverse momenta play a special role in the

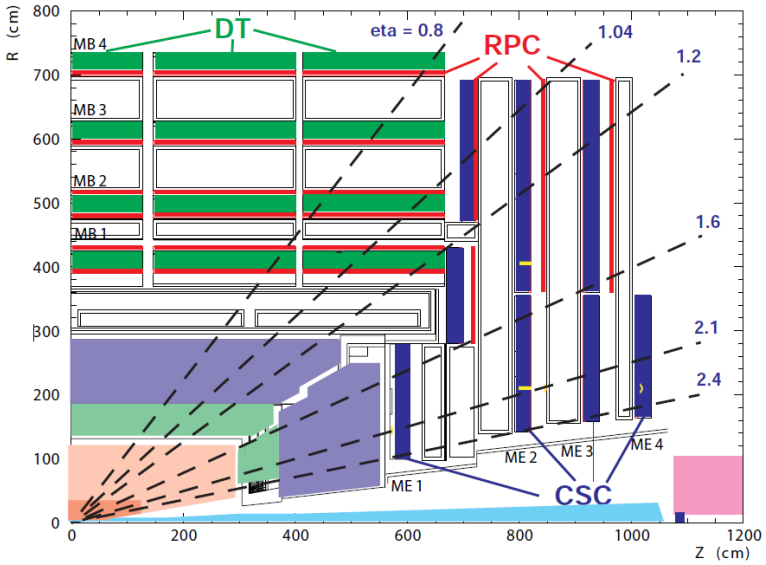

Figure 3.9.: Longitudinal cross section of one of quarter of the Muon System. The abbreviations are specified in the text [54].

Higgs and new physics searches since they are the cleanest signature of new undetected mass resonances that decay leptonically.

The muon system provides three functions: muon identification, muon momentum measurement and muon triggering. The presence of the 3.8 T solenoid field make the last two points possible. CMS uses three different types of gaseous particle detectors to measure and reconstruct the tracks of the muons. The muon system consists of a cylindrical muon barrel (MB) and two muon endcaps (ME) covering the pseudorapidity range of $|\eta| < 2.4$. A transverse cross section is shown in Figure 3.9.

The first type of gaseous chambers are *drift tubes* (DTs). These chambers cover the pseudorapidity range $|\eta| < 1.2$, have a length of 2.5 m and a cross section of 4.2×1.3 cm. The chambers with aluminum based walls are filled with Ar/CO_2 gas and have a stainless steel wire as an anode. The DTs are installed in the muon barrel (see Figure 3.9), the central part of the detector, since the muon rate is low enough to use this cost-effective technology, the magnetic field is uniform and the neutron-induced background is small. The second type of gaseous chambers are *cathode strip chambers* (CSCs). A CSC has a trapezoidal shape and consists of six cathode strips alternated with gas gaps. The chambers are placed in the MEs where the muon rate is higher and the magnetic field is non-uniform and large. They cover the pseudorapidity range $0.9 < |\eta| < 2.4$ and provide muon identification with a fast response time and adequate radiation hardness. The DTs and CSCs provide a similar spatial resolution of ≈ 100 µm. The third type of gaseous

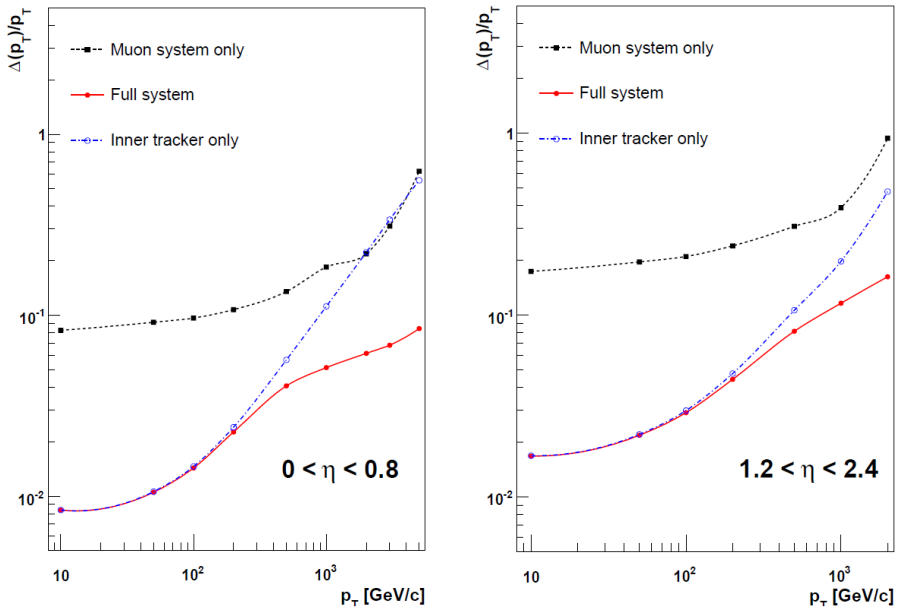

Figure 3.10.: The muon transverse-momentum resolution as a function of the transverse-momentum p_{T} using the muon system only, the inner tracking only and both in the pseudorapidity range: (a) $|\eta| < 0.8$ and (b) $1.2 < |\eta| < 2.4$ [54].

chambers are *resistive plate chambers* (RPCs). These chambers form a dedicated trigger system to secure an excellent performance of the muon triggers. The chambers are placed both in the MB as in the MEs. The RPCs cover the pseudorapidity range $|\eta| < 1.6$ providing a good time resolution but a worse resolution for the position than the DT and CSC chambers.

The performance of the muon system is illustrated in Figure 3.10. The muon transverse-momentum p_{T} resolutions are shown in function of p_{T}, using only the muon system, only the tracking and both together for the two pseudorapidity ranges $|\eta| < 0.8$ and $1.2 < |\eta| < 2.4$. The muon system provides a resolution of about 9 % for small η values below transverse momenta of 200 GeV while the resolution increases to 15-40 % at energies of 1 TeV. The combination of the muon system and the inner tracking system significantly decreases the uncertainty on the muon momenta at high transverse momenta, where the curvature induced by the magnetic field on the muon trajectories is small implying the need of a larger lever-arm.

3.6. Trigger system

The LHC provides a rate of 10^9 interactions every second, a bunch crossing every 25 ns, at its design luminosity of $L = 10^{34}$ cm^{-2} s^{-1}. This corresponds with a crossing frequency of 40 MHz. At the design luminosity, a mean of 20 pile-up events will also lead to a high detector occupancy. No technology is capable of reading out the millions of channels and storing the huge amounts of data produced at this frequency. The maximum that can be archived by the computer farm is only 300 Hz, meaning that the rate has to be reduced by a factor of 10^6. CMS uses a very efficient two-step trigger system [54] to reduce the rate. The first step is the hardware-based *Level-1 trigger* (L1) relying on custom-built electronics to reduce the event rate to 100 kHz. The second step is a software-based *high level trigger* (HLT) relying on commercial processors in a computer farm to bring the rate down to the final 300 Hz.

The architecture of the L1 trigger follows three basic steps and is shown in Figure 3.11. At a local level, the trigger primitive generators (TPGs) use fast-readout information from the muon system (track segments in the chambers) and the calorimeters (energy deposits) to form primitive objects. In the next step, regional triggers (RT) combine the TPG information using pattern logic to form a ranked list of particle candidates (such as electrons, muons, photons and jets) based on the quality of the deposits. Finally the various regional trigger outputs are combined in a global calorimeter/muon trigger (GT) to determine the highest-ranked particles. If these particles fulfill some characteristic requirements and if certain general detector criteria are met, the event is accepted. The GT is also able to correlate these particles to identify characteristic interaction final states. The result of the GT is communicated to all CMS sub-detectors through the timing, trigger and control (TTC) system to initiate the full readout of the detectors.

The L1 trigger has to analyze every LHC bunch crossing since it acts as the first selection layer. It takes however 3.2 µs for data to transit from the front-end electronics to the housing of the L1 logic, to make the keep-or-reject decision and for the information to return back to the detector front-end electronics. This means that the 40 MHz readout stream has to be pipelined in readout electronic memory buffers awaiting the trigger decision to minimize the dead-time between two registered events. To minimize this transit time, the L1 hardware is partially housed on the detector itself and partially in the underground control room at a distance of 90 m of the detector.

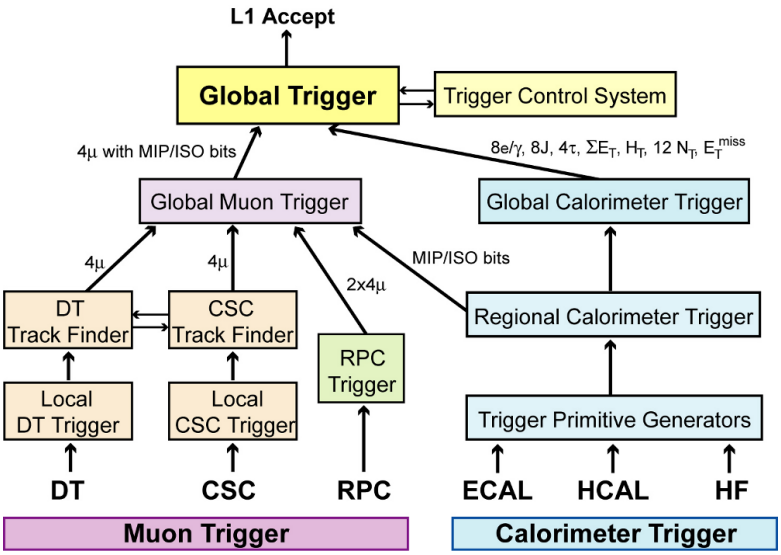

Figure 3.11.: Architecture of the Level-1 trigger [54].

If an event is accepted by the L1 trigger, all the sub-detector data that was pipelined is sent to the HLT farm which is located above the ground. The high level trigger farm consists of a computer farm of thousands of CPUs that perform more dedicated pattern recognition based on more accurate object reconstruction. The muon and the calorimeter data are used to construct more elaborated objects than the L1 objects and tracker information is added to get a more complete picture of the event. Again a decision is made ending up with a event rate of 300 Hz that is written to storage discs for offline analysis.

3.7. Beam monitoring system

A beam monitoring system [54] is installed to both monitor and protect CMS from the LHC beam conditions and radiation near the experiment. Some of the subsystems are able to initiate a LHC beam abort or a CMS control abort to protect the experiment. A part of these subsystems is also used for triggering purposes since they have time resolutions below 25 ns, the time between two bunch crossings.

Two *beam pick-up timing for the experiments* (BPTXs) devices are located around the beam pipe at a distance of 175 m from the interaction point on both sides of CMS. A BPTX detector provides precise information on the bunch structure and timing of the incoming beam with a time resolution below 0.2 ns. This information is used by the L1

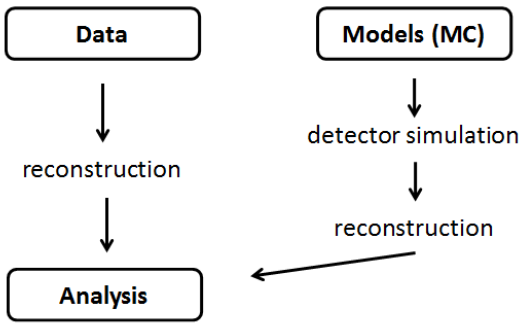

Figure 3.12.: Different steps that data and Monte Carlo Models undergo during their processing in the CMS software framework before an analysis can start.

trigger to gate its decision by the bunch crossing timing. It consists of two standard LHC beam position monitors each composed of four electrostatic button electrodes positioned symmetrically around the beam pipe. They are installed around each LHC experiment.

Two *beam scintillator counters* (BSCs) are installed at each side of CMS at 11 m from the interaction point to provide hit and coincidence rates. They are sensitive in the pseudorapidity range $3.23 < |\eta| < 4.65$. Each BSC consists of 16 scintillator tiles with a time resolution of 3 ns and are mounted on the inner surface of the HF detectors. The BSC elements have an average minimum-ionizing-particle detection efficiency of 95.7 %. They can be used by the L1 trigger to ensure an inelastic p-p interaction has occurred or to veto against backgrounds from accidental interactions of the beams with residual beam-pipe gas or with the beam-pipe wall that produce out-of-time signals.

3.8. CMS software and grid computing

To be able to perform physics analyses, the CMS collaboration needs more than just a custom-built detector. Without a proper simulation of the interaction between the collision products and the detector hardware, one is not able to understand the detector response and interpret the measured data. Simulation requires a lot of processing power, detector parts have to be calibrated, electronical noise has to be understood and there is need for both online and offline data quality management. Only a unified framework of both hard- and software can handle with all aspects of a multi-purpose experiment in a user friendly way. The path data and Monte Carlo models follow through the framework is shown schematically in Figure 3.12, more details can be found in this section.

CMSSW

The CMS collaboration developed its own custom software framework called *CMS Software* (CMSSW) [54] capable of reconstructing and storing all the data produced by the read-out electronics. It is an object oriented framework written in the C++ programming language. All the sub-systems of CMS have their own collections of classes and objects to process their specific data. All systems are linked together through Python based configuration modules that can execute a full software cycle.

The main task of the software framework is to process the digital detector signals coming from the read-out electronics and to transform them into physical objects such as electrons and jets that can be used for statistical analyses. This transformation occurs in steps where the information of all different sub-systems is combined to form the complete reconstructed picture of a bunch crossing. The reconstruction of the particles, including their energy, momentum and trajectory is achieved through advanced algorithms, combining the information of the different sub-systems. The reconstruction of various objects will be described in the next chapter. For a detailed description see Reference [61].

CMMSW is optimized to work closely together with the ROOT software package [62]. ROOT is a C++ analysis package used to statistically analyze data and visualize results. For this reason, the final CMS data is stored in ROOT compatible objects after it has been processed through the CMSSW framework.

Simulation of the detector response

For the LHC experiments, simulation is made out of two distinct steps: the simulation of specific physics processes that can occur in p-p collision and the simulation of the passage of the final state particles through the experimental apparatus. The first step is handled by Monte Carlo event generators, which involve theoretical input and are independent of the experiment[2]. The second step, the simulation of the detector response, uses the output of the first step as input and simulates the passage of particles through the detector from the interaction point all the way to the outer shell of the detector. Finally, one applies the same object reconstruction algorithms on both the simulated as the real data with the help of the CMSSW framework.

[2]References to the used Monte Carlo event generators will be given in Section 5.3.2.

Despite that the detector simulation is different for every experiment, general codes exist to simulate any detector since an experimental apparatus can be modeled in terms of elementary geometrical objects and the physics processes covering the interaction of particles with matter. These codes are also called *Monte Carlo radiation transportation codes*. In case of CMS the GEANT4 package [63] is used.

After the geometry of the detector has been implemented in detail, the code takes the four-momenta of a particle as input and propagates it through the detector while simulating all possible physical interactions resulting in energy deposits in various sub-detectors. This is done one-by-one for all particles coming from a p-p collision. It should be noted that the package is also able to simulate *secondary particle* production, originating from interactions between particles and the detector material. This is followed by the simulation of the electronics processing and digitization of the deposits including the simulation of the trigger decisions. At this point, the simulated output is similar to that of real data, so that the same reconstruction algorithms can be applied on both of them. Note that the simulation of all detector components is compared and adjusted to real data, based on dedicated test beam campaigns prior to the assembly of CMS and with well-understood physics processes that use recorded during nominal running of the experiment.

Data Quality Management

It is important to be sure that the detector performance stays fully understood during all the data taking and that the simulation is as close to reality as possible. Data quality management (DQM) occurs both online, during data taking itself, as offline. During the data taking physicists are on shift to make sure that all the sub-detectors are running optimal, as in the correct operation temperature, pressure, magnet field,... If there are problems with certain sub-systems, the data will be flagged for further offline investigations.

The offline DQM is split up in two parts, DQM of the data and DQM of the simulated Monte Carlo. The DQM of the simulated data has been shortly described at the end of the previous paragraph. For the data, one looks at simple well-understood collision events (such as $Z \rightarrow 2e$) checking that the detector is responding and aligned correctly. When there are no beams in the LHC, CMS can also trigger on cosmic rays, which are again simple signatures that can be used for the same task. All these measurements are combined and used to create calibration maps for various sub-detectors. These maps are

regularly updated to make sure the description is as correct as possible. Data of bad quality due to problems with certain sub-detectors are removed after investigation.

Data tiers

CMS uses a number of different data formats with varying degrees of detail, size and refinement to store its data in its various stages. The various stages in the reconstruction process with the addition of specific calibrations of sub-detectors eventually convert the raw online data into higher-level physics objects.

Event information from each step of the reconstruction chain is grouped in *data tiers*. The three most important data tiers are:

- **RAW**: the online HLT farm creates RAW data events containing the full detector data, the L1 trigger result, the result of the HLT selections and some higher-level objects created during the HLT processing
- **RECO**: containing reconstructed hit/cluster data and reconstructed objects (tracks, vertices, jets, electrons, ...)
- **AOD**: compact version of RECO, containing mainly reconstructed objects (tracks, vertices, jets, electrons, ...) with a minimum of localized hit information

The AOD tier is the smallest one in size containing the least amount of detector information. To perform the physics analysisi, the AOD data format is used.

Grid computing

CERN does not have the computing resources to process the huge amounts of data on site. It relies on a distributed computing infrastructure called the *Worldwide LHC Computing Grid* (WLCG or Grid) arranged in a tier system. It gives a community of over 8000 physicists near real-time access to LHC data and it runs more than one million jobs per day.

The primary tier, *tier 0*, is the CERN Data Center, a 1450 m^2 server farm located in CERN. All of the data from the LHC passes through this central hub, forming the first point of contact between the experiments and the Grid. It however only provides less than 20 % of the total computing capacity of the Grid. The CERN Data Center is

responsible for the safe keeping of all RAW data and it performs the first reconstruction stages of RAW data to more meaningful physics information.

The RAW data and the reconstructed data is distributed to the *tier 1* centers. They consist of 11 major computer farms large enough to store the LHC data. They are responsible for storing a proportional share of the RAW and reconstructed data. They perform large-scale reprocessing of the data and they store the corresponding outputs. A dedicated high-bandwidth network called the *LHC Optical Private Network* (LHCOPN) connects CERN to each of the 11 major tier 1 centers around the world through 10 gigabytes per second optical-fiber links.

The next tier consists of the *tier 2* centers. They are smaller computer clusters located at national laboratories and universities. This tier allows the various institutions to perform data analysis locally in their nearest tier 2 center. The Belgian CMS community uses a national tier 2 center located at the computer center of the ULB and UCL.

Chapter 4.

Object reconstruction

This chapter covers the reconstruction of the physical objects needed to perform the $\mathrm{H} \to \mathrm{W}^+\,\mathrm{W}^- \to 2\ell\,2\nu$ analysis discussed in this thesis. First the reconstruction of the charged particle tracks and of the vertices will be covered. Then the CMS Particle Flow event reconstruction is introduced, which uses the tracks, vertices and the energy deposits in the calorimeters to reconstruct the physical final state objects such as electrons, muons, jets and missing transverse energy ($E_{\mathrm{T}}^{\mathrm{miss}}$). Each final state object relevant to the analysis will be discussed further in detail. The chapter will end with an introduction to the B-tagging algorithm which helps in reducing the top-induced background.

4.1. Tracks

The charged particle trajectories, called *tracks*, are one of the most fundamental objects to reconstruct. They play a crucial role in any physics analysis as they will finally be identified as for example electrons, muons, hadrons, taus and jets.

At the end of the reconstruction chain, a track inside CMS is defined mainly by five parameters:

- The transverse momentum p_{T}
- The angle θ of the momentum vector at the point of origin of the track (related to the pseudorapidity $\eta = -\ln\tan\frac{\theta}{2}$)
- The azimuthal angle ϕ of the momentum vector

- The transverse impact parameter d_{xy} with respect to the nominal interaction point located at the center of CMS
- The longitudinal impact parameter d_z with respect to the nominal interaction point located at the center of CMS

The track reconstruction algorithm can be decomposed in seven logical parts described below. More details can be found in References [64–66]. Lastly the tracking performance is discussed.

Local hit reconstruction

In a first local step, adjacent deposits of charges in the pixel or strip detector are clustered in *hits*. To each hit one attributes its position in the $\eta \times \phi$ plane, the tracker layer, and the uncertainty on its position.

Seed generation

The generation of seeds is the major starting point of the pattern recognition. A seed should constrain all five track parameters and is the basis for the fitting algorithm that follows in the next step. A seed is formed by the association of a pair or a triplet of tracker hits in the innermost layers of the tracking system. The innermost layers are chosen since the occupancy rate is low, leading to a lower uncertainty in the position determination, and in addition the amount of traversed material is low, lowering the probability that particles lose energy. In order to constrain the momentum of pixel hit pairs, one needs an additional assumption on the reconstructed location of the interaction point. Triplet hits are better defined but less common than hit pairs resulting in higher purities at the expense of a lower efficiency.

Pattern recognition

Once the seeds are determined, the pattern recognition can be initialized. The pattern recognition is based on a combinatorial Kalman filter method [67, 68] and is called the Combinatorial Track Finder (CTF) algorithm.

The algorithm starts from the trajectory of a seed and searches from the inside layers of the tracker outwards for a hit in the next tracker layer. The trajectory is extrapolated

to the next layer according to the equations of motion of a charged particle in a constant magnetic field, accounting for multiple scattering and energy loss in the traversed material. On each layer, when a compatible hit is found, the track parameters of the trajectory are updated by the Kalman filter, improving the precision of the trajectory. When no hit is found in a layer, one further trajectory extrapolation is calculated, accounting for the possibility that a track did not leave a hit in a certain layer. The fake hit is called an invalid hit.

The procedure is repeated until either the outermost layer of the tracker is reached or a stopping condition is satisfied. In order not to bias the results, all trajectory candidates are determined in parallel. The algorithm is configurable through several parameters such as the minimum number of hits per track, the minimum transverse momentum and the maximum number of consecutive invalid hits.

Ambiguity resolution

Ambiguities can arise when a given track may be reconstructed from different seeds, or because a seed may result in more than one trajectory candidate. These ambiguities have to be resolved in order to avoid the double counting of tracks. A resolution criteria is introduced based on the fraction of hits which are shared between two trajectories to decide if a track is removed (details in [65]).

Final track fitting

Each trajectory now holds a collection of hits and an estimate of the track parameters. However the full information was only available at the last hit of the trajectory and the estimate can be biased by the constraints applied during the seeding stage. For this reason the whole collection of hits is re-fitted using a least-squares approach, implemented as a combination of a standard Kalman filter and smoother, obtaining a final estimate of the track parameters for every trajectory.

Iterative tracking

To optimize the complete track reconstruction, the CTF algorithm is repeated multiple times. Each iteration uses a smaller subset of input hits, by removing the hits attached to reconstructed tracks in the previous iteration. At each iteration the parameters of

the CTF algorithm are adapted to maximize the performance. In addition, the track collection is cleaned, according to the compatibility of the tracks with the location of the interaction point. The first two iterations are sufficient to reconstruct high p_{T} tracks, while up to six iterations are used to reconstruct low p_{T} tracks. This iterative approach allows the reconstruction of tracks with a p_{T} as low as 150 MeV.

Quality filtering

Secondary charged particles can be created by the interaction of a particle with the tracker material. This becomes problematic at high luminosity and results in an even higher number of combinatorial possibilities resulting in fake tracks. Extra quality cuts are applied to the final track collection to lower the track fake rate while maintaining a high reconstruction efficiency.

The quality cuts are based on the basic track parameters as the track p_{T}, η, d_{xy}, d_z, the track χ^2 per degree of freedom and the transverse (longitudinal) compatibility, defined as $d_{xy}/\delta_{d_{xy}}$ (d_z/δ_{d_z}), with the interaction point region. The optimal cut values depend on the number of crossed layers in the tracker. The cuts are more strict if the amount of hit layers is small. In contrast, a track with hits in 10 layers can be kept without having to check the quality cuts.

Tracking performance

The performance of the CMS tracking system has been studied extensively throughout its design, commissioning and data taking phases at center-of-mass energies of 0.9, 2.36 and 7 TeV [69, 70]. The measurement of the basic track parameter distributions, the reconstruction efficiencies and the detector resolutions are crucial to understand the detector and to validate the implemented simulation and track reconstruction algorithms.

For the $\sqrt{s} = 7$ TeV study, CMS used LHC Minimum Bias[1] data acquired during the first proton-proton collisions at 7 TeV to compare the performance of the track reconstruction to that of simulated models [70]. Figure 4.1 shows the main track distributions (transverse momentum p_{T}, pseudorapidity η, transverse impact parameter d_{xy} and longitudinal impact parameter d_z) comparing the data (black dots) with the simulation of the Pythia8 Tune 1 model [71] (blue histogram). A good agreement between data

[1]Minimum Bias events are recorded by generally loose and generic triggers with respect to the final state topology, thus sampling the visible p-p cross section in an unbiased way.

and Monte Carlo (MC) model is achieved. Next, Figure 4.2 illustrates the transverse and longitudinal impact parameter resolutions as a function of the track p_{T} and η. Only central tracks ($|\eta| < 0.4$) were used in the resolution versus track p_{T} figures. Three different values of track p_{T} (1, 3 and 8 GeV) are shown in the resolution versus track η figures. The agreement between the measured and simulated resolutions is overall within 2-3 %, except for a 10 % discrepancy for higher momenta and pseudorapidity tracks. The longitudinal and transverse impact parameter resolutions increase for higher track momenta since the charged particles are less deflected by multiple scattering while traversing the material of the beam pipe. Both impact parameter resolutions get worse for higher $|\eta|$ values since such particles have to traverse larger amounts of material.

The basic behavior of the inner tracking system and its reconstruction software is clearly well understood and falls within the excellent expected design performance.

4.2. Vertices

When all the tracks of a collision are reconstructed, the fitting of the positions of the vertices (and uncertainties) can start [72]. Two kind of vertices exist, *primary* and *secondary* vertices. A primary vertex is the location of the interaction point of a proton-proton interaction. At high luminosities there can be several primary vertices per bunch-crossing. Secondary vertices arise when long-lived particles originating from the primary vertex decay or interact inside the detector volume.

The Deterministic Annealing (DA) clustering algorithm [73] is used to reconstruct all vertices present in a collision. The clustering algorithm searches for a collection of vertex candidates and associates a set of reconstructed tracks to each vertex. The z-coordinate of the tracks is one of the main inputs of the clustering algorithm.

The vertex with the largest summed squared-p_{T} of the associated tracks is chosen as the event primary vertex. Since there is typically only one signal vertex next to a large number of inelastic collisions per bunch crossing, this leads to an efficiency for reconstructing and selecting the correct[2] vertex up to 99 % for $\mathrm{t\bar{t}H}$ events. For low multiplicity events like $\mathrm{H} \to \gamma\gamma$ it can go down to 76 % [72].

[2]within 500 µm in z of the true signal vertex

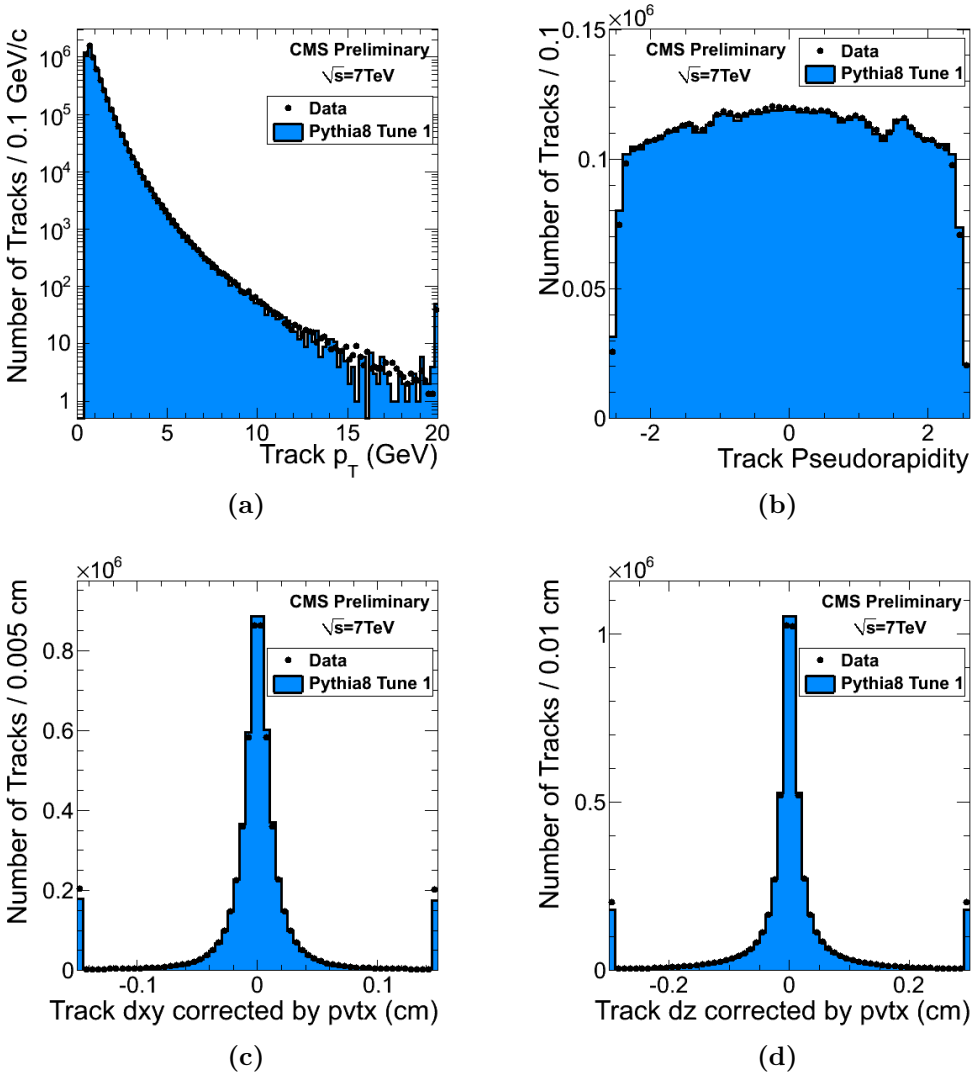

Figure 4.1.: Comparison of $\sqrt{s} = 7$ TeV Minimum Bias data (black points) and MC simulation (blue histogram) for the following track parameters: (a) transverse momentum p_{T}, (b) pseudorapidity η, (c) transverse impact parameter d_{xy} and (d) longitudinal impact parameter d_z [70].

4.3. Particle Flow event reconstruction

The *Particle-flow (PF) event reconstruction* [74–76] aims at reconstructing and identifying all stable particles in the event, i.e., electrons, muons, photons, charged hadrons and neutral hadrons, exploiting maximally the information of all CMS sub-detectors towards an optimal determination of their direction, energy and type. This concept is visualized in Figure 4.3. The algorithm produces a list of individual particles as if it came from a Monte Carlo event generator. This list can then be used to build jets, to determine

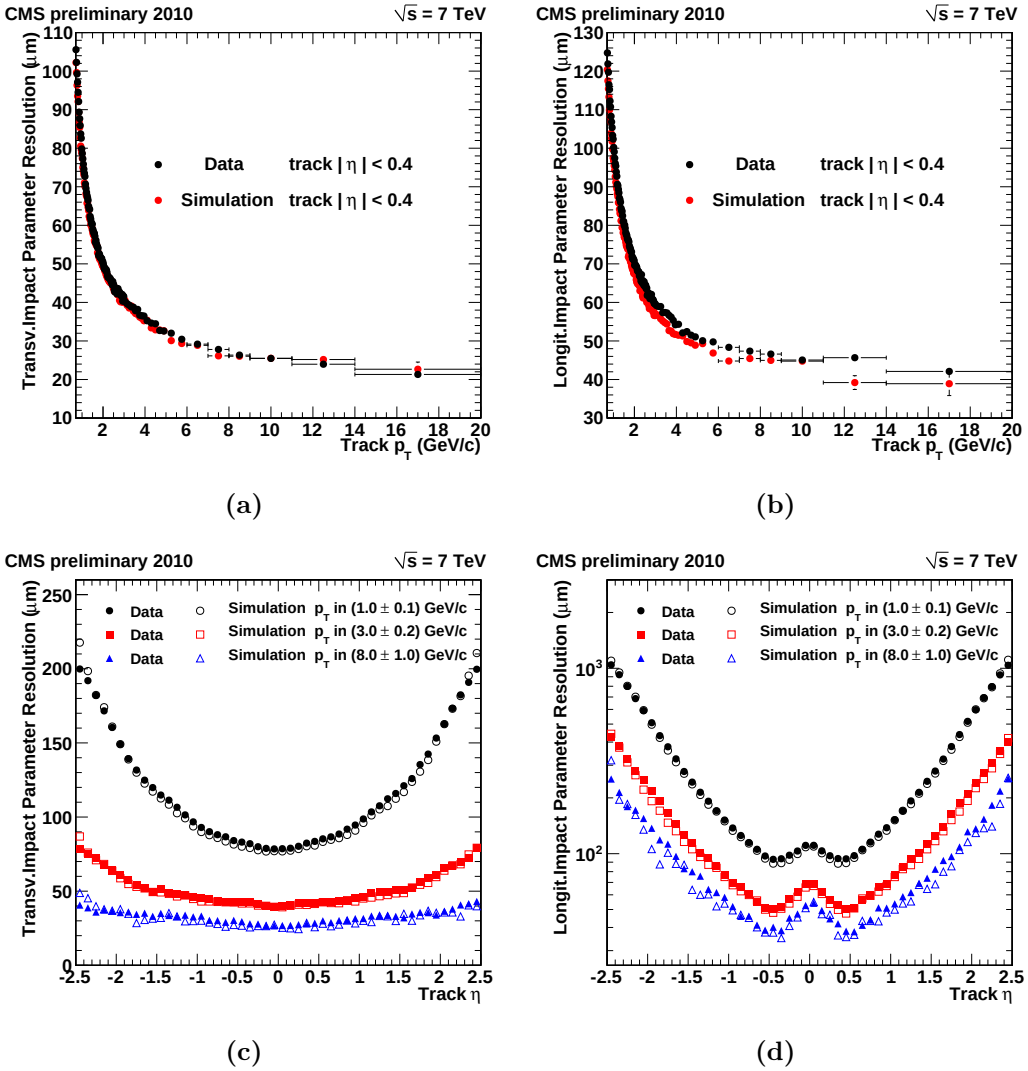

Figure 4.2.: Track resolution distributions comparing $\sqrt{s} = 7$ TeV Minimum Bias data to the detector simulations. Average transverse (a,c) and longitudinal (b,d) impact parameters are shown in function of the track transverse momentum p_{T} and the track pseudorapidity η. Figures (a,b) show the resolution for central tracks ($|\eta| < 0.4$) and figures (c,d) show three different track p_{T} values (1, 3, 8 GeV) [70].

the missing transverse energy $E_{\mathrm{T}}^{\mathrm{miss}}$, to reconstruct and identify taus from their decay products, to quantify charged lepton isolation with respect to other particles, to tag b-jets, etc.

As mentioned above, a combination of all the information from the CMS sub-detectors is needed. The three types of building bricks or *fundamental elements* of the PF event reconstruction are: charged particle tracks, calorimeter clusters and muon track segments[3].

[3]geometrically matched hits within each DT and CSC (Section 4.7).

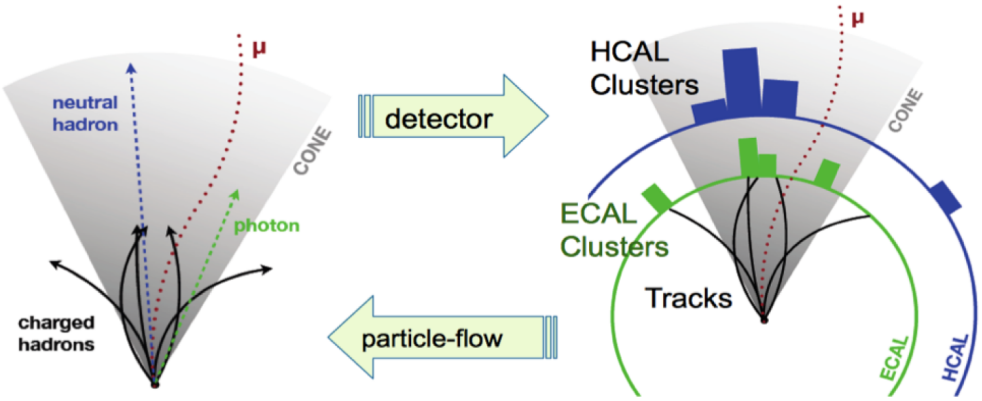

Figure 4.3.: The particle-flow concept.

All these elements must therefore be delivered with a high efficiency and a low fake rate. These requirements led to the development of the advanced iterative tracking (see Section 4.1) and clustering algorithms (covered below). These elements are then topologically linked into *blocks* by a linking algorithm. The blocks are interpreted by the core of the particle-flow algorithm which identifies and reconstructs the final list of particles..

The use of the PF event reconstruction is only possible thanks to the excellent performance of the CMS detector. The large silicon tracker can be used to reconstruct particle-tracks with a good precision and a low fake rate down to very low momenta. This is needed to build up jets, since even high momenta jets consist of a large fraction of low momenta particles (see Section 4.4). Furthermore, the homogeneous ECAL has a high granularity allowing the distinction of photons from charged particles. In contrast, the HCAL has a much lower granularity than the ECAL, causing the neutral and the charged hadrons to end up in the same cluster. However, due to its excellent energy resolution, it can still be used to isolate neutral hadrons by measuring the energy-excess of a charged-hadron cluster compared to its associated tracks.

Calorimeter clustering algorithm

There are four purposes to use a *clustering algorithm* in the calorimeters:

- Detect and measure the energy and direction of neutral hadrons and photons
- Separate these neutral hadrons from the energy deposits from charged hadrons

- Identify electrons and all accompanying Bremsstrahlung photons (emitted while crossing the tracker material)
- Complement the energy measurement of charged hadrons which have poorly determined track parameters (due to low-quality or high-p_{T} tracks)

For these purposes a specific clustering algorithm was developed that acts on each sub-detector separately: ECAL barrel, ECAL endcap, ECAL preshower (PS), HCAL barrel and HCAL endcap. No clustering is performed in the HF, each HF cell gives rise to one cluster.

The algorithm consists of three steps. First, calorimeter cells with an energy above a certain threshold are identified as *Cluster Seeds*. Second, *Topological Clusters* are formed by aggregating cells with at least one side in common with a cell already in the cluster, when the energy in the candidate cell is at least two standard deviations larger than the expected electronic noise (i.e. 80 MeV in the ECAL barrel, up to 300 MeV in the ECAL endcap and 800 MeV in the HCAL). Thirdly, a *particle-flow cluster* is now assigned for every cluster seed in a topological cluster. The energies and positions of the particle-flow clusters are determined in an iterative way. The total energy of the topological cluster is shared between all particle-flow clusters proportional to $e^{-d_{ij}^2/R^2}$, where d_{ij} is the distance between particle-flow cluster i and cell j. Then the position of the particle-flow cluster is recomputed as the center-of-gravity of the five or nine central cells. This process is iterated until the locations of the particle-flow clusters are stable. For the ECAL an extra correction to the particle-flow cluster location is added to compensate for the tilted crystals.

Linking algorithm

A given particle is generally expected to give rise to several particle-flow elements in the various CMS sub-detectors: one charged particle track, and/or several calorimeter clusters, and/or one muon track segment. These elements must now somehow be connected to each other to fully reconstruct each single particle, while taking care of any possible double counting from different detectors. The *linking algorithm* is performed for each pair of elements in the event and defines a distance between any two linked elements to quantify the quality of the link. *Blocks* of elements, linked directly or indirectly, can now be produced by the algorithm.

Due to the high granularity of the CMS detector, the blocks typically contain only a few elements, resulting in simple inputs for the particle reconstruction and identification algorithm. The advantage is that even for very complex events, only the number of blocks will increase and in general the number of elements in each block will remain the same, leaving the performance of the algorithm independent from the event complexity.

More specifically to create a link between a charged particle track and a calorimeter cluster, the track is first extrapolated from the outermost hit in the tracker to the calorimeters. For the ECAL and the HCAL the propagation is carried out at a depth corresponding to the maximum depth of a shower profile. For the PS it is just propagated to its two layers. The track is linked to the cluster when the propagated track is within the cluster boundaries. The cluster envelope can be enlarged by one cell in each direction to account for the uncertainty on the position of the shower maximum, multiple scattering for low-p_{T} charged particles, the presence of gaps between calorimeter cells and cracks between calorimeter modules. The link distance is defined as the distance in the (η,ϕ) plane between the extrapolated track and the cluster position. In addition, one can collect all the Bremsstrahlung photons coming from electrons with this technique. At each intersection between an electron-track and the tracker layers, the tangent to the electron-track is propagated to the ECAL with the same linking procedure.

Similarly, two calorimeter clusters between HCAL and ECAL, or PS and ECAL, are linked if the cluster position in the more granular calorimeter (PS or ECAL) is within the cluster envelope in the less granular one (ECAL or HCAL). As above, the envelope is allowed to be slightly enlarged and the link distance is defined in the (η,ϕ) plane as the distance between the two cluster positions.

Lastly a charged particle track in the tracker can be linked with a muon track segment in the muon system. Both tracks are linked when a global fit between the two results in an acceptable χ^2 and one speaks of *global muons*. When a muon track segment can be fitted with multiple tracker tracks, only the global muon track with the smallest χ^2 is retained. The link distance is defined as the χ^2 value rather than the distance in the (η,ϕ) plane as before.

Particle identification and reconstruction

The *particle identification and reconstruction* step builds the list of individual particles of the event with the particle-flow blocks as input. The final list of reconstructed particles

gives a full global description of the event. This section will briefly outline the steps taken to arrive to each *particle-flow object*. The general objects (jets, transverse missing energy $E_{\mathrm{T}}^{\mathrm{miss}}$, electrons and muons) are covered in specific sections in this chapter.

The procedure goes as follows: If a certain block contains global muons, their momenta are compared to that determined by the central tracker. A global muon is called a *particle-flow muon* if the deviation is less than three standard deviations and the corresponding track is removed from the block.

Next the electrons follow. Electrons tend to leave short tracks behind in the tracker and lose energy in the tracker layers by Bremsstrahlung. For this reason, the tracks are sent to a pre-identification stage which exploits the tracker as a pre-shower. The pre-identified electron tracks are then refit in an attempt to follow their trajectories all the way to the ECAL (see [74]). A final identification is performed with a combination of a number of tracking and calorimetric variables. Each identified electron is called a *particle-flow electron* and the corresponding track and ECAL clusters (including the ECAL clusters identified as Bremsstrahlung photons) are removed from the block.

At this point in the process a block contains mainly neutral hadrons, charged hadrons and photons. To identify neutral hadrons, the energy of the particle-flow cluster is compared to the linked momentum of the track (or the sum of the momenta of the tracks). An excess on top of the charged hadron energy can then be identified as a neutral hadron. This is of course only possible if the cluster energies are calibrated (see [74]).

Several tracks can be linked to the multiple ECAL or HCAL clusters. For multiple HCAL clusters, only the closest link is preserved. For multiple ECAL clusters the closest link is also kept, but the extra links are not yet rejected. The extra links should be ignored if they arise from overlapping photons to allow photon detection, but if they are caused by fluctuations in the hadronic shower they should be preserved to avoid double counting of the hadron energy. To take this decision, the ECAL clusters under consideration are ordered according to their link distance to the closest track. The ordered list is scanned and the corresponding link is kept as long as the total calibrated calorimetric energy (HCAL + the considered ECAL at this point) remains smaller than the total charged particle momentum.

A few situations can arise now. If the total calibrated calorimetric energy is still smaller than the total track momentum by more than three standard deviations, a relaxed search for muons and for fake tracks is performed. Next the tracks are ordered by

their measured p_{T} uncertainty and they are progressively removed from the block until the total momentum is equal to the calorimeter energy or until all tracks with an p_{T} uncertainty above 1 GeV have been removed. (Less than 0.3 per mil tracks go through this procedure) Each of the remaining tracks in the block gives rise to a *particle-flow charged hadron*.

In the opposite situation, when the total calibrated calorimetric energy exceeds the total track momentum, with a relative difference bigger than the calorimeter resolution, the excess gives rise to *particle-flow photons* and *particle-flow neutral hadrons*. Generally if the excess is bigger than the total ECAL energy, a photon is identified and the remaining part of the excess is attributed to a neutral hadron. Otherwise it is only attributed to a photon. The precedence of the photons is justified by the observation that in jets roughly 25 % of the energy is carried by photons, while neutral hadrons leave only 3 % of the jet energy in the ECAL.

The remaining ECAL and HCAL clusters in the block, either originally not linked to any tracks or for which the link was removed during the procedure, give respectively rise to *particle-flow photons* and *particle-flow neutral hadrons*.

The final list of all the particle-flow objects can now be passed to a jet algorithm to build the *particle-flow jets*. The *particle-flow missing transverse energy* $E_{\mathrm{T}}^{\mathrm{miss}}$ also arises as the missing energy in the transverse plane after adding the contributions of all the found particle-flow objects. Both topics are covered in more detail in Section 4.4 and Section 4.5, respectively.

For the present analysis, the muons and electrons are reconstructed with alternative algorithms than the PF algorithm, partially due to historical reasons, but also due to resolution reasons for the electron. More details can be found in the electron and muon section, Section 4.6 and 4.7 respectively. Although different reconstruction algorithms are used, every lepton used in this analysis will be required to be also reconstructed with the PF algorithm, meaning that the reconstructed lepton has to have a compatible PF lepton. This has the logical consequence that the PF muons and the PF electrons are replaced by the alternative reconstructed ones in the calculation of the PF $E_{\mathrm{T}}^{\mathrm{miss}}$.

4.4. Jets

A jet is defined as a collimated spray of particles, originating from a parton that appears in the final state of the collision. Quarks give rise to a collection of collimated hadrons, which are detected as a narrow cone of particles. The basic constituents of jets are charged hadrons, neutral hadrons and photons. The typical jet energy fractions are respectively 65 %, 10 % and 25 %. In this analysis, particles are reconstructed with the CMS particle-flow algorithm (see Section 4.3), whereafter the *Anti-k_{T} clustering algorithm* [77] is used to group the particles coming from the same quark together in a jet.

The Anti-k_{T} algorithm reconstructs the parton shower backwards. The procedure goes as follows. For any input particle i and any pair of input particles (i, j) one computes the distances d_i and d_{ij} in the event:

$$d_i = \frac{1}{p_{\mathrm{T}i}^2} \tag{4.1}$$

$$d_{ij} = \min\left(\frac{1}{p_{\mathrm{T}i}^2}, \frac{1}{p_{\mathrm{T}j}^2}\right) \frac{\Delta\phi^2 \Delta\eta^2}{R^2} \tag{4.2}$$

with R a cone size parameter. Both distances are compared and if d_i is the smallest, the particle i is called a jet and removed from the list of input particles. In contrast, when d_{ij} is the smallest, the particles i and j are combined to form a new particle with $p_T = \sum_i p_{\mathrm{T}i}$, $\eta = \frac{1}{p_{\mathrm{T}}} \sum_i p_{\mathrm{T}i}\eta_i$ and $\phi = \frac{1}{p_{\mathrm{T}}} \sum_i p_{\mathrm{T}i}\phi_i$. The original particles i and j are removed from the list. This procedure is repeated until no particles are left. The procedure is very safe since it ensures that hard particles are first combined with soft ones and that collinear particles are combined together before they are moved into jets. The present study uses the anti-k_{T} algorithm with a cone of $R = 0.5$.

In comparison to the particle-flow method, a more simple method can be used as input to the jet algorithm. *Calorimeter jets* are jets that are reconstructed by only using the energy deposits in the ECAL and the HCAL. Towers are formed by combining a HCAL cell and an array of ECAL crystals. These towers can be used as input to the jet algorithm above. The comparison of the jet energy resolution for both methods is shown in Figure 4.4. Since 65 % of the jet energy fraction consists of charged particles (charged hadrons), the addition of the tracker in the particle-flow algorithm strongly improves the energy resolution of the PF jets compared to the calorimeter jets. A comparison of the

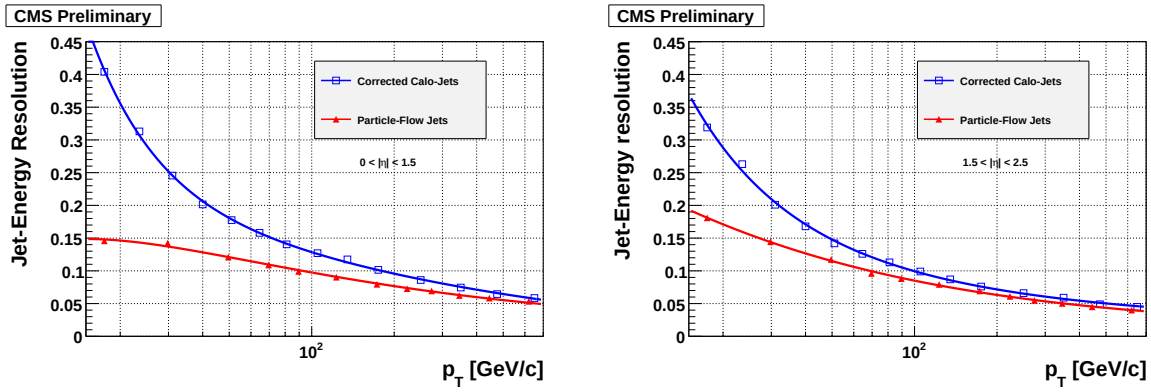

(a) (b)

Figure 4.4.: Jet-energy resolutions as a function of p_{T} for corrected calo-jets (open squares) and for particle-flow jets (upwards triangles) in (a) the barrel and (b) the end-caps. The resolution curves are fit to the sum of a constant term, a stochastic term and a noise term [74].

p_{T} resolution is shown in Figure 4.5 where the $(p_{\mathrm{T}}^{\mathrm{rec}} - p_{\mathrm{T}}^{\mathrm{gen}})/p_{\mathrm{T}}^{\mathrm{gen}}$ distribution for PF-jets is clearly narrower and less biased than the calo-jets one and are then used in the present thesis.

Jet energy corrections

When the jets are reconstructed, several detector corrections to the jet energy have to be applied to each jet. These are split up into three levels.

The *Level 1 correction* is discussed first. With the presence of pile-up, the momenta of jets are overestimated due to the contamination of particles originating from secondary interactions. Particles from a pile-up vertex can get clustered, along with other genuine particles, to form a jet that will therefore have a sensibly higher energy than the original jet originating purely from the hard interaction.

This offset to the jet energy gets very significant with the current pile-up conditions. The contribution from the pile-up is estimated by the *L1Fastjet* method. This method relies on the definition of a jet area [78]. The jet area can be interpreted as a measure of the jet susceptibility of being contaminated by uniformly distributed soft particles. One generates a grid of infinitely soft particles in a given $|\eta|$ range and the soft particles that get clustered within a given jet i form the jet area A_i. If a jet is purely arising from a pile-up interaction, the contamination level is $p_{\mathrm{T}\,jet}/A$. The density of pile-up

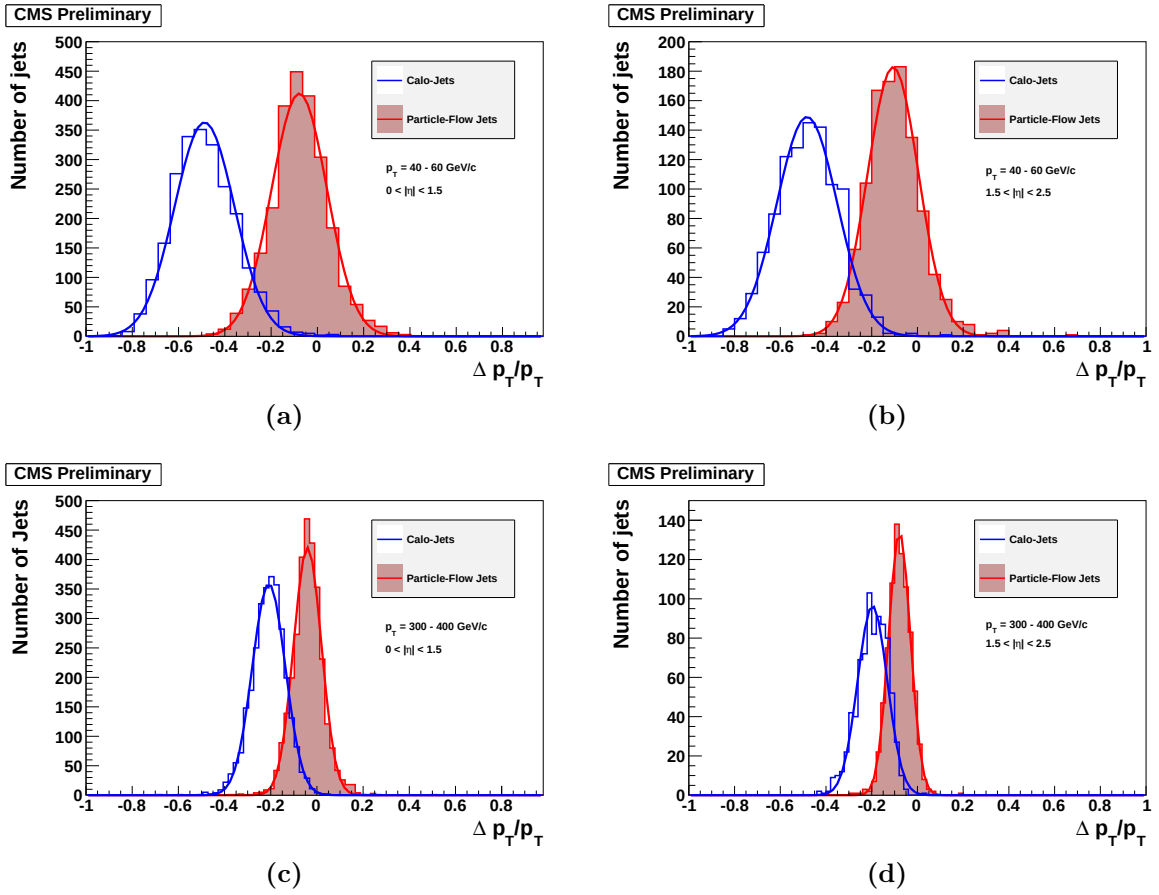

Figure 4.5.: Distributions of $(p_{\mathrm{T}}^{\mathrm{rec}} - p_{\mathrm{T}}^{\mathrm{gen}})/p_{\mathrm{T}}^{\mathrm{gen}}$: for $p_{\mathrm{T}}^{\mathrm{gen}}$ between 40 and 60 GeV (a,b) and between 300 and 400 GeV (c,d), as obtained from calo-jets (open histogram) and from particle-flow jets (solid histogram) pointing to the barrel (a,c) and to the end-caps (b,d). A Gaussian is used to fit the distributions [74].

contamination per event ρ (GeV/Area) is computed as

$$\rho = \mathrm{median}\left[\frac{p_{\mathrm{T}i}}{A_i}\right] \tag{4.3}$$

where i runs over all the jets in the event within a given region set by the user. The median is used, instead of the average, to make sure that the pile-up density ρ is less sensitive to genuine high-p_{T} non-pile-up jets and low-area jets. For each event, the momentum of jet i can be corrected as:

$$p_{\mathrm{T}i}^{\mathrm{corr}} = p_{\mathrm{T}i} - \rho A_i \tag{4.4}$$

where ρ is estimated for every event and is common for every jet of that event.

On top of the L1 correction, the *Level 2 correction* [79] is applied. The goal of the L2 correction is to uniformize the jet detector response in pseudorapidity η with respect to a reference control region. The barrel is chosen as control region since it provides the most precise response of the detector due to the higher granularity than the endcap and due to its uniform region. The correction is calculated by using the *Tag and Probe* technique, instead of relying on simulation. One uses a physical process, abundantly produced at the LHC, with a perfectly balanced final state in the transverse region, in this case di-jet events. If one jet is reconstructed in the barrel (the *tag*), one can probe the energy of the other jet (the *probe*) and map the imbalance as a function of pseudorapidity. From this jet imbalance, the correction factors as function of η can easily be derived [79].

On top of the previous two corrections, the *Level 3 correction* [79] corrects the variation of the jet response in respect to the momentum of the jet. A physical process producing one jet and another object needs to be used. The latter must have a good momentum resolution and the momentum determination should not be dependent on the hadronic calorimeter. CMS uses for example the $\mathrm{Z} + \text{jet}$ process, as one can use the $\mathrm{Z} \to \mu\mu$ decay to exploit the excellent muon chamber performance of CMS [79].

Figure 4.6 shows the total jet correction factor in function of η for both calo-jets as PF-jets. One can derive that PF-jets are already much better calibrated before the L2 correction is applied, as they use more detector information. On top of that, the p_{T} correction is almost negligible for PF-jets but very significant for calo-jets. This is another reason why this thesis uses the PF-jets.

Identifying and removing pure pile-up jets

In addition to the Level 1 correction, which corrects the contribution of pile-up to the energy of a jet, one has to reject entire jets coming purely from pile-up events. A combinatorial background arises from low-p_{T} originating from pile-up interactions which get clustered into high-p_{T} jets. This results in modified properties of hard jets by particles from pile-up interactions. A multivariate selection is applied to separate jets coming from the primary interaction and those constructed due to energy deposits associated with pile-up interactions.

Jets purely coming from pile-up events are identified by a multivariate analysis (MVA) technique based on the Boosted Decision Tree (BDT) [81] method. A discriminant is built [82] based on the following variables:

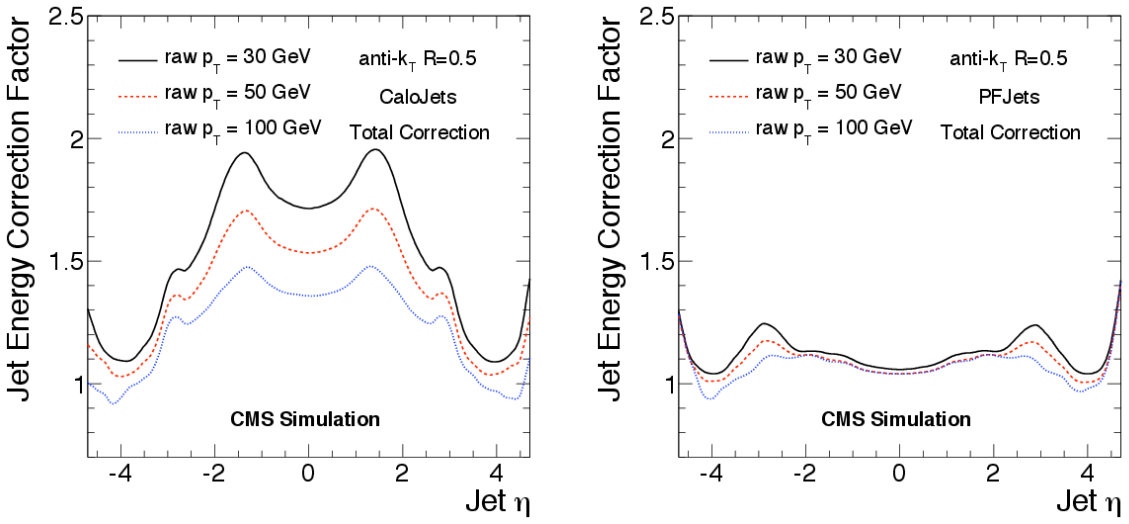

(a) **(b)**

Figure 4.6.: Total jet energy correction factor (L2+L3) derived from simulation for (a) calo-jets and (b) PF-jets at $\sqrt{s} = 7$ TeV as a function of jet η for three different values of uncorrected jet p_{T} [80].

- the number of vertices in the event
- the jet kinematics (p_{T}, η, ϕ)
- the compatibility of the jet to the hard interaction vertex based on the charged constituents
- the neutral and charged constituents multiplicities
- several jet shape properties (jet radius weighted by the relative p_{T} contribution of the constituents and the p_{T} fraction in rings around the jet axis).

The identification takes advantage of the difference in shape of the energy deposit in a jet cone. Jets from pile-up are soft, so they need to be overlaid with others to pass the jet p_{T} threshold. Therefore, the energy deposit of pile-up jets are more spread than the one from hard interactions. Among the three working points defined in reference [82], the loose one is used in the analysis as the jet identification (jetID) criteria. If a jet does not pass this jetID criteria, the jet is rejected from the event.

To cross-check this method, Z + jet events were selected in the first part of 2012 data (corresponding to $\approx$ 800 pb^{-1}) and compared with Drell-Yan Monte Carlo. The selection is requiring two opposite sign, same flavor, well isolated and identified electrons

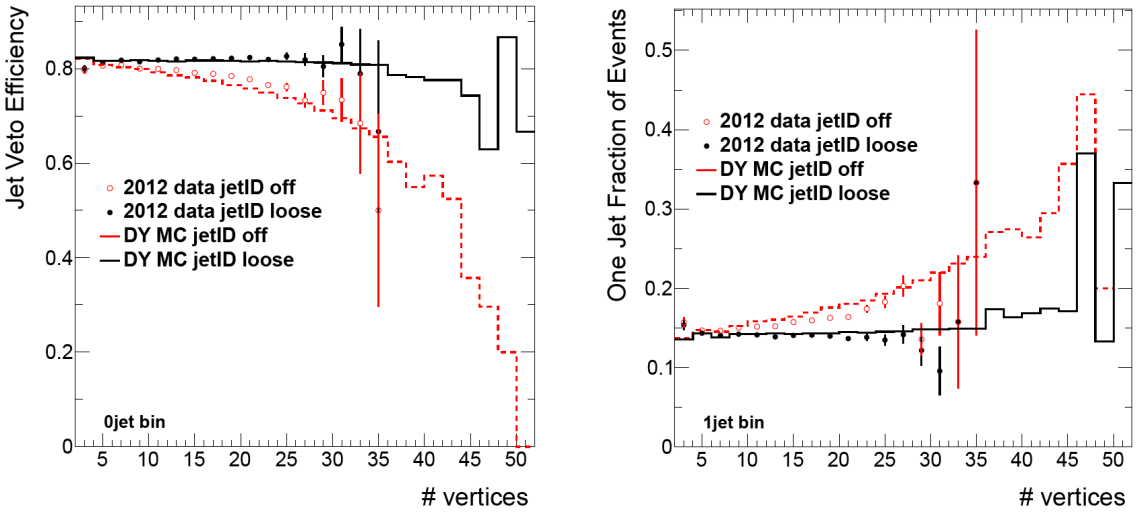

(a) (b)

Figure 4.7.: Comparison of the jet veto efficiency in 0 jet events (a) and fraction of events with 1 jet (b) as a function of the number of vertices with and without MVA jetID applied, using Drell-Yan events.

(or muons) with an invariant mass (m_{ll}) consistent with the Z mass ($|m_{ll} - m_{\mathrm{Z}}| < 15$) and ensuring the two leptons are coming from the same primary vertex. One counts the number of jets in the event, requiring jets to have a minimal p_{T} of 30 GeV and be within $|\eta| < 4.7$. Two categories are looked at, the case with 0 jets and with 1 jet in the event. The jet veto efficiency, in the zero jet case, and the fraction of events with one jet, in the one jet case, can now be studied in function of the number of vertices. In an ideal situation one wants both to be constant versus pile-up. Figure 4.7 shows the comparison of data to Monte Carlo of the Jet Veto efficiency in the zero jet case and the fraction of events with one jet as a function of the number of good primary vertices for jets with and without the jetID being applied. After applying the jetID, both the Jet Veto efficiency and the fraction of events with one jet are stable with the number of vertices and the data is well described by the Monte Carlo. For this reason, the jetID is applied in this thesis.

4.5. Missing transverse energy

The missing transverse energy $E_{\mathrm{T}}^{\mathrm{miss}}$ is a very powerful variable in the present analysis due to the presence of neutrinos in the signal final state. The $E_{\mathrm{T}}^{\mathrm{miss}}$ is defined as the norm of the negative vector sum of the transverse momenta of all reconstructed particles

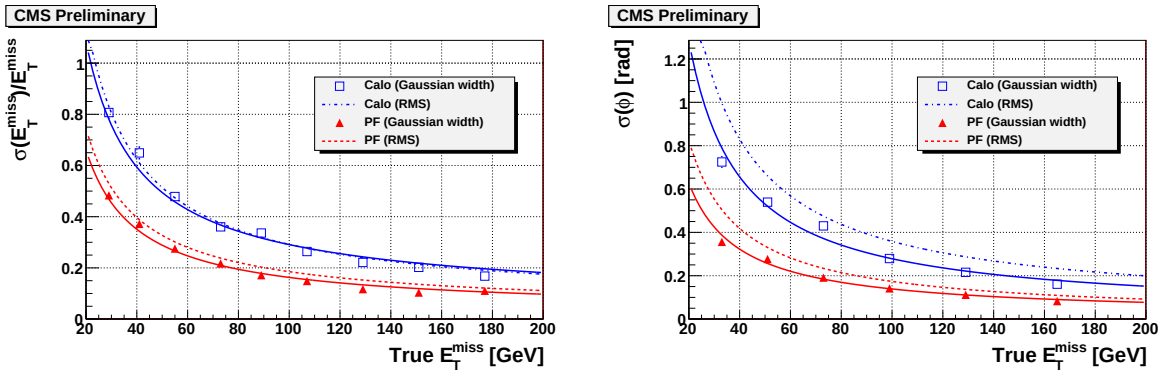

(a) **(b)**

Figure 4.8.: $E_{\mathrm{T}}^{\mathrm{miss}}$ reconstruction performance in a $t\bar{t}$ event sample for particle-flow reconstruction (triangles) and for calorimeter reconstruction (open squares): (a) $\sigma(E_{\mathrm{T}}^{\mathrm{miss}})/E_{\mathrm{T,true}}^{\mathrm{miss}}$ versus the $E_{\mathrm{T,true}}^{\mathrm{miss}}$ and (b) Gaussian fitted ϕ resolution versus the $E_{\mathrm{T,true}}^{\mathrm{miss}}$ of the event [74].

(charged or neutral) in the event. As in the jet section, $E_{\mathrm{T}}^{\mathrm{miss}}$ can be defined in two ways: calorimeter $E_{\mathrm{T}}^{\mathrm{miss}}$ and particle-flow $E_{\mathrm{T}}^{\mathrm{miss}}$. The former is derived from the calorimeter towers and the latter is simply obtained by adding the contribution of all the reconstructed particle-flow particles of the event (see Section 4.3).

The resolution of the $E_{\mathrm{T}}^{\mathrm{miss}}$ can be tested with physical processes that display no-real $E_{\mathrm{T}}^{\mathrm{miss}}$, such as pure QCD samples or Z bosons decaying to visible leptons. Using a $\mathrm{t\bar{t}}$ event sample, Figure 4.8 shows that the PF-$E_{\mathrm{T}}^{\mathrm{miss}}$ has a much better resolution than the calorimeter one.

Similar to the jet reconstruction, problems arise in a high pile-up environment. As pile-up increases, the $E_{\mathrm{T}}^{\mathrm{miss}}$ distribution gets smeared towards higher values, due to the contribution of missing particles from the pile-up events, as shown in Figure 4.9 with $\mathrm{Z} \to \mu\mu$ events. The high pile-up has a severe impact on the $E_{\mathrm{T}}^{\mathrm{miss}}$ resolution when no real $E_{\mathrm{T}}^{\mathrm{miss}}$ is expected. To suppress the dependence of the $E_{\mathrm{T}}^{\mathrm{miss}}$ on the amount of pile-up, an algorithm was developed called trk$E_{\mathrm{T}}^{\mathrm{miss}}$ (track missing transverse energy), constructed from the charged particles originating from the primary vertex. The trk$E_{\mathrm{T}}^{\mathrm{miss}}$ is defined as:

$$\mathrm{trk}E_{\mathrm{T}}^{\mathrm{miss}} = -\sum_{i} \vec{p_{\mathrm{T}}}(i) \tag{4.5}$$

where $\vec{p_{\mathrm{T}}}(i)$ respresents the transverse momentum vectors of the charged PF candidates, with the condition that the tracks matched to the PF candidates have $\Delta z < 0.1$ cm

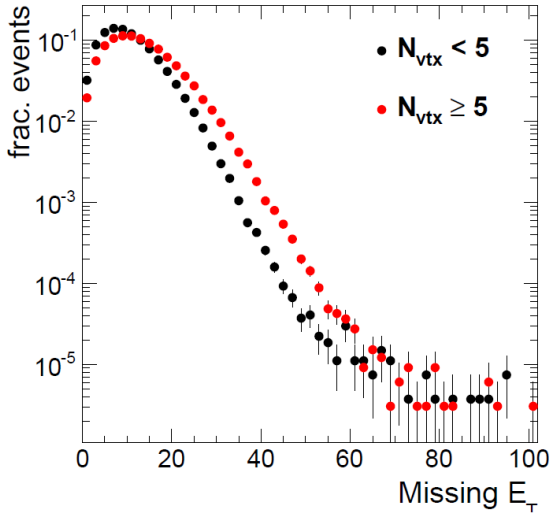

Figure 4.9.: $E_{\mathrm{T}}^{\mathrm{miss}}$ distribution for simulated $Z \to \mu\mu$ events with low (black) and higher (red) pile-up. The number of reconstructed vertices $\mathrm{N_{vtx}}$ is strongly correlated with the number of true pile-up events and is a reasonable measure of the amount of pile-up interactions in the event.

with respsect to the signal primary vertex. In the analysis, a more complicate combination of both types of $E_{\mathrm{T}}^{\mathrm{miss}}$ is used and we will come back to them in the analysis strategy Section 5.4.6.

4.6. Electrons

As mentioned at the end of the PF section, electrons are reconstructed with an alternative algorithm, partially due to historical reasons and partially due to resolution reasons, as explained below. Nevertheless, in the analysis electrons will be required to have a compatible PF reconstructed electron.

Electrons are reconstructed in CMS with the standard *Gaussian Sum Filter (GSF)* algorithm [83]. It combines the tracker and the ECAL information. For each electron reaching the ECAL surface, an electromagnetic shower will arise and most of the electron energy will be collected within a small matrix of crystals around the hit. However, due to the interaction of the electrons with the tracker material, the electrons will lose energy through the radiation of photons by bremsstrahlung before reaching the calorimeter. As the electrons lose energy, the magnetic field will enhance the bending of their trajectories, resulting in a spread of the irradiated photons along the ϕ coordinate. To obtain an accurate measurement of the electron energy, one has to account these bremsstrahlung

photons. This is done by the GSF algorithm, resulting in a better electron resolution than one can obtain with the PF algorithm. This is the reason why we use GSF electrons instead of PF electrons.

To account for these bremsstrahlung photons, the energy deposits in the ECAL are grouped in clusters of ECAL cells and a clustering algorithm is collecting single clusters and merging them into the prototype of an electron candidate called a *supercluster* (SC). Superclusters are typically a matrix of 5×5 ECAL cells and can be considered as a seed when the summed energy deposit is above 4 GeV [83].

Once a supercluster is found, the track-building stage can start. The SC is back-propagated in the magnetic field, both under the $+1$ and -1 electron charge hypothesis, to the nominal vertex, looking for compatible hits in the pixel detector. This requirement ensures a high purity of electron candidates and enhances the reconstruction efficiency. When the track seeds (pairs or triplets of hits) are found in the inner tracker layers, the electron tracks can be built. The track is propagated to the outer layers of the tracker with the help of a dedicated modeling of the electron energy loss and in the end the trajectory is fitted with a *Gaussian Sum Filter (GSF)*. This procedure approximates the electron energy loss probability density function, which is well described by the Bethe-Heitler model [84], with a sum of Gaussian functions in which the different components model different degrees of hardness of the bremsstrahlung in the tracker layer under consideration [83].

If multiple trajectory candidates are found for the same SC, the one with the lowest χ^2 (of the fit) is kept. The charge of the electron is determined by the curvature of the track. The energy measurement of the ECAL is combined with the momentum measurement of the tracker to improve the estimate of the electron momentum at the interaction vertex for low energy particles. The improvement is expected to come both from the opposite behavior with energy of the intrinsic calorimetry and tracking resolutions, and from the fact that momentum (in the tracker) and energy (in the ECAL) are differently affected by the bremsstrahlung radiation. Figure 4.10 shows the fractional energy resolution in function of the electron energy for the ECAL supercluster, the electron track and the combination of the two.

The purity of the electron collection can be improved by requiring certain *identification criteria* depending on the particular analysis and the backgrounds one wants to reject. The identification criteria will be covered in the analysis strategy Section 5.4.3.

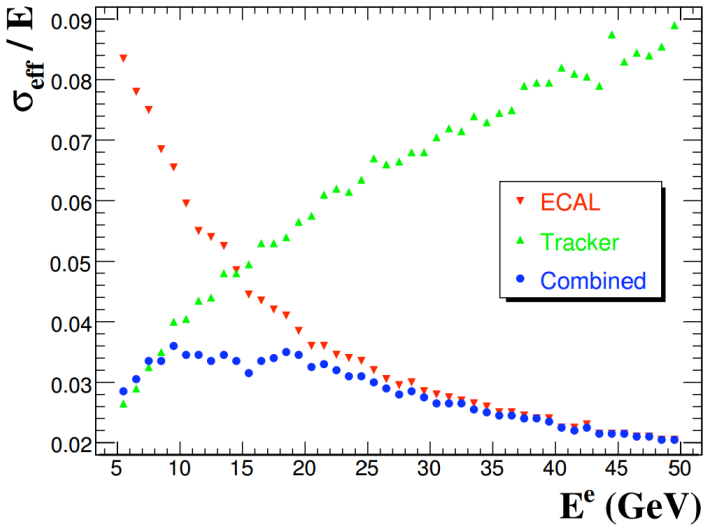

Figure 4.10.: The fractional resolution (effective RMS) as a function of the generated electron energy E^e measured with the ECAL supercluster (downward triangles), the electron track (upward triangles) and the combination of the two (circles) [61].

Isolation

Lastly the concept of *isolation*, an efficient method of rejecting fake leptons (in general), has to be introduced. Jets that fake leptons (i.e. that are accepted as electron or muon candidates) are usually surrounded by a high amount of neutral and charged activity. The requirement of an isolated lepton is equivalent to asking that such activity is small and can sensibly reduce the fake rate.

The performance of isolation is however seriously degraded with pile-up, since particles from pile-up vertices can end up in the close surroundings of a lepton. A neat solution can be found in the use of the particle-flow candidates in the calculation of the isolation. Since the PF algorithm uses the whole CMS detector, one can discard all charged candidates in the surroundings of the lepton that are not attached to the primary vertex that is associated with the lepton. As neutral hadrons and photons cannot directly be associated to the vertex, a threshold on their momenta can be imposed to reduce the probability that they originate from a pile-up vertex. As the identification criteria, the isolation requirement is analysis dependent and it will be covered in the analysis strategy Section 5.4.3.

4.7. Muons

As mentioned at the end of the PF section, muons are reconstructed with an alternative algorithm. This is mainly due to historical reasons. Nevertheless, in the analysis muons will be required to have a compatible PF reconstructed muon.

In the standard CMS muon reconstruction [85] tracks are first reconstructed independently in the tracking system (*tracker track*) and in the muon system (*standalone-muon track*). The reconstruction of the tracker tracks has already been covered in Section 4.1. The reconstruction of the tracks in the muon system starts with the determination of hit positions in the DT, CSC and RPC subsystems. These hits are geometrically matched within each DT and CSC to form *muon track segments*. The segments are collected and matched to each other to generate seeds as a starting point for the actual track fit of all DT, CSC and RPC hits. The resulting reconstructed trajectory is a standalone-muon track.

The two kinds of tracks are combined into a unique object, following two possible approaches:

- *GlobalMuon Reconstruction* (*outside-in*): For each standalone-muon track, one searches for a matching tracker track. A *global-muon track* is fitted combining the hits, using a Kalman-filter technique.
- *TrackerMuon Reconstruction* (*inside-out*): All tracker tracks with $p_{\mathrm{T}} > 0.5$ GeV and total momentum $p > 2.5$ GeV are considered as possible muon candidates and are extrapolated to the muon system, taking into account the magnetic field, the average expected energy losses and multiple scattering in the detector material. If the extrapolated track matches a muon segment (a short track of DT or CSC hits), the tracker track qualifies as a *tracker-muon track*.

Tracker muons are mainly used to recover the efficiency at low p_{T} ($p_{\mathrm{T}} < 5$ GeV), given the weak penetrating power of low momentum muons. Thanks to the high tracker-track efficiency and a very high efficiency of the reconstructing segments in the muon system, about 99 % of the muons produced in proton-proton collisions and having a sufficiently high momentum ($p_{\mathrm{T}} \geq 5$ GeV) are reconstructed either as global or tracker muons.

The misidentification rate for muons is low since they are the only detectable particles able to reach the muon chambers. However, the set of reconstructed muons has to

be cleaned from misidentified (un-decayed) charged hadrons. The analysis dependent identification as the isolation requirements will be covered in Section 5.4.3.

4.8. B-tagging

The reconstruction and identification of decays of the bottom-quark (resulting in jets) are used to discriminate the background processes containing top-quarks that each subsequently decay to a b-quark and W boson. These top induced processes represent a significant fraction of the background for this analysis (see Section 5.2). Since b-hadrons have a longer lifetime than light hadrons, this often results in a displaced vertex. Other characteristics as the high mass of the b-hadrons and their semi-leptonic decay products can be used as discriminating factors.

In CMS, the bottom-quark decay is identified by two criteria: the presence of a soft-muon in the event from the semi-leptonic decay of the b-quark and secondly by bottom-quark jet (b-jet) tagging criteria based on the impact parameter of the constituent tracks [86]. The latter will be explained in more detail in this section. The former soft-muons arise since b-quarks tend to decay leptonically with the lepton decaying perpendicular to the jet axis. Muons rather than electrons are used as they display a higher purity. Soft-muon candidates are defined without isolation requirements and are required to have $p_{\mathrm{T}} > 3$ GeV.

B-tagging algorithms require tracks and jets as input. The identification of the b-jets uses the high granularity of the CMS experiment and relies mainly on hits in the pixel detector as it is the closest detector to the interaction point. Tracks are reconstructed as described in Section 4.1 and selected with the following quality requirements to minimize fake and badly reconstructed tracks [87]:

- total number of tracker hits (pixel + strips) ≥ 8
- number of pixel hits ≥ 2
- transverse impact parameter $d_{xy} < 0.2$ cm
- longitudinal impact parameter $d_z < 17$ cm
- transverse momentum > 1.0 GeV
- χ^2/ndof of the track fit < 5.0

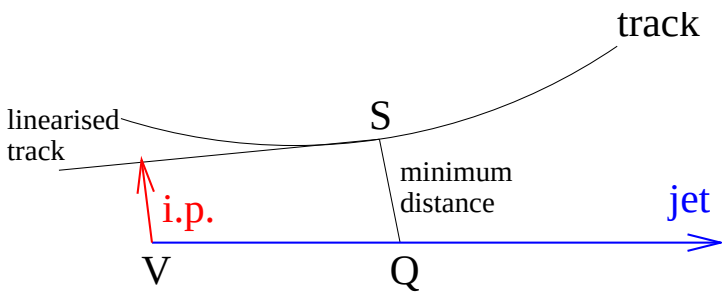

Figure 4.11.: Schematic representation of the impact parameter of a track with respect to the vertex [87].

- distance $\Delta R = \sqrt{\Delta\eta^2 + \Delta\phi^2}$ to the jet axis < 0.5

The *impact parameter* (IP) has to be introduced as the most powerful discriminant for the association of a track to a displaced vertex. It is defined as the distance between the track and the vertex at the point of closest approach either in the transverse plane or in three dimensions. A schematic representation is displayed in Figure 4.11. Since the uncertainty σ_{IP} associated with the IP can be high, one rather uses the significance as a discriminator:

$$\mathrm{sign}_{\mathrm{IP}} = \frac{\mathrm{IP}}{\sigma_{\mathrm{IP}}} \tag{4.6}$$

The tracks IP significance can now be used to create a b-tagging discriminator called the *track counting* algorithm. A jet is identified as a b-jet if there are at least N tracks with $\mathrm{sign}_{\mathrm{IP}} > \mathrm{S}$. A single discriminant is obtained by fixing the value of N and considering the significance of the Nth track (after ordering the tracks in decreasing significance) as discriminating variable. CMS uses two variants of this method:

- TCHE (*Track counting high efficiency*) The number of tracks is fixed to N = 2, resulting in a high b-tagging efficiency at the cost of increasing the mis-tag rate. (The mis-tag rate is defined as the probability that a jet gets tagged as a b-jet, while it does not originate from a b-quark)
- TCHP (*Track counting high purity*) The number of tracks is fixed to N = 3, resulting in a high purity at the cost of lowering the b-tagging efficiency.

Both discriminators are compared in Figure 4.12 using QCD simulated events, with the b-quark distributions indicated with black squares. One can derive that the b-tagging efficiency for THCE is higher than for TCHP, since a higher fraction of b-jets have a high discriminator value for TCHE. Contrary more light jets (red/green) have a higher

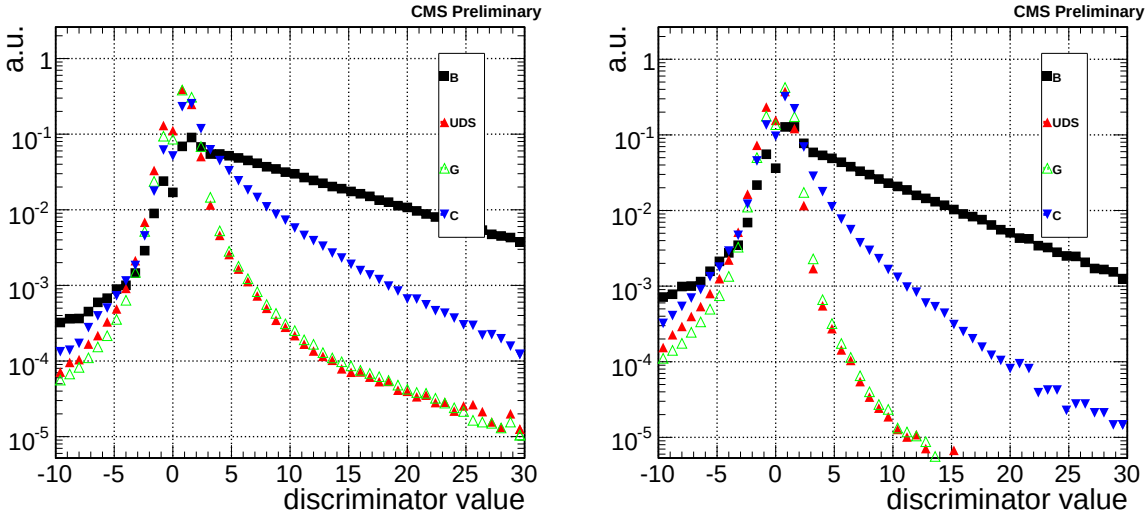

(a) TCHE **(b)** TCHP

Figure 4.12.: The normalized distribution of the discriminator for the TCHE algorithm (a) and for the TCHP algorithm (b) for heavy quarks (B, C), light quarks (U, D, S) and gluons G [87].

discriminator value for TCHE than for TCHP, resulting in a higher mis-tag rate for TCHE. The algorithm choice depends on the relative weight one associates to efficiency versus mis-tag rate and is analysis dependent. More information and other algorithms can be found in [86, 87].

The present analysis uses the TCHE algorithm with a discriminator value greater than 2.1 to assign a given jet as b-tagged. It should be noted that the MVA-based jet identification which is applied for selecting jets, reduces the mistag rate and the dependency on pile-up.

Chapter 5.

The common W^+W^- preselection

The search for the Higgs boson in the $H \to W^+ W^- \to 2\ell\, 2\nu$ final state, where ℓ is an isolated electron or muon, and ν a neutrino of the corresponding flavor, is one of the main searches in a broad Higgs mass spectrum, given the high $H \to W^+ W^-$ branching ratio and the clean signature, as described in Section 1.5.1. It contributes significantly, approximately 1σ of the 5σ, to the discovery of the new boson with a mass close to 125 GeV.

The search discussed in the following chapters is performed over the expected Higgs boson mass range 110-600 GeV, and the data sample corresponds to 4.9 (19.5) fb^{-1} of integrated luminosity collected in 2011 (2012) at a center-of-mass energy of 7 (8) TeV. Given the two different energies, the analysis strategy has changed from 2011 to 2012. In this thesis, the final analysis with the full statistics will be described. References [44, 88, 89] contain details about the analysis at major milestones. Reference [88] covers the analysis with the $\sqrt{s} = 7$ TeV dataset, which I did not contribute to. Reference [44] covers the observation of the new boson, which covers all the Higgs channels with the $\sqrt{s} = 7$ TeV dataset and one quarter of the final $\sqrt{s} = 8$ TeV dataset. In this reference, I contributed to the 0- and 1-jet analysis of the $H \to W^+ W^- \to 2\ell\, 2\nu$ decay channel. Lastly, reference [89] covers the analysis of the leptonic $H \to W^+ W^-$ channel with the full $\sqrt{s} = 7$ TeV and $\sqrt{s} = 8$ TeV dataset. Since I contributed to the 0- and 1-jet final states of the $H \to W^+ W^- \to 2\ell\, 2\nu$ decay channel, this thesis follows the main outline of this paper and contains the same results.

First the signal and the main backgrounds will be covered, followed by the event selection strategy, arriving at the common $W^+ W^-$ preselection level. The main data driven background estimates, the Higgs signal extraction strategy, the systematic uncertainties and the results will be covered in the following chapters.

5.1. Higgs signal

We already discussed the main production mechanisms and decays of the Higgs boson at the LHC in Section 1.5.1. We recall that at the LHC, the possibilities for Higgs production are: gluon-gluon fusion (ggH), vector-boson fusion (qqH or also called VBF), associated production with Z/W and top pair (WH/ZH/$t\bar{t}$H). The ggH mechanism is also predominant at the LHC by a factor of approximately 95 % for low Higgs masses and down to 85 % for a Higgs mass of 600 GeV (see Figure 1.6 in Section 1.5.1).

The Higgs decays predominantly via the $H \to W^+ W^-$ channel when the Higgs mass is close to $m_H \sim 160$ GeV $\sim 2m_W$, since both W bosons are produced on-shell and the WW branching ratio is above 90 %. However if $m_H < 160$ GeV, one of the W bosons is produced off-shell and the decay is gradually kinematically suppressed as m_H becomes smaller. At higher masses, the branching ratio of $H \to W^+ W^-$ lowers due to the increase in the branching ratio of $H \to ZZ$ and $H \to t\bar{t}$ as seen on Figure 1.8. Each W boson can decay into two quarks or into a lepton and a neutrino, leading to three main possibilities for the $H \to W^+ W^-$ final state:

- fully hadronic: ≥ 4 jets in the final state
- semi-hadronic(leptonic): ≥ 2 jets, 1 lepton and missing energy in the final state
- fully leptonic: ≥ 0 jets, 2 leptons in the final state and large missing energy in the final state.

Although the cross section of the fully hadronic and semi-leptonic decays are higher than that of the fully leptonic decay, these searches are very challenging at the LHC due to the high production rate of QCD processes that constitute a background for these decay modes. On the other hand, the fully leptonic search presents a much cleaner final state since the backgrounds are mainly electroweak processes with a much lower cross section. In this work we will only cover the fully leptonic final state.

The expected number of events in 1 fb^{-1} for different Higgs production mechanisms in the $H \to W^+ W^- \to 2\ell\, 2\nu$ decay channel, taking into account the branching ratios of $W^+ W^- \to 2\ell\, 2\nu$, is shown in function of the Higgs mass m_H for both $\sqrt{s} = 7$ TeV and $\sqrt{s} = 8$ TeV in Figure 5.1. It can be seen that the channel is highly exploitable in the range $m_H = 120 - 200$ GeV and it allows to set limits on the Higgs cross section up to High masses.

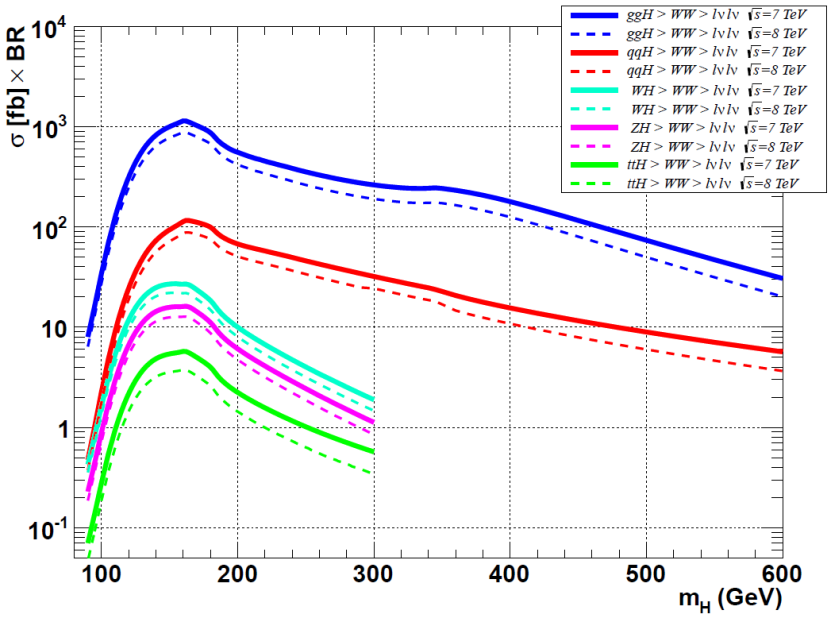

Figure 5.1.: Cross-section values multiplied by the branching ratio for different Higgs production mechanisms in the $\mathrm{H} \to \mathrm{W}^+\,\mathrm{W}^- \to 2\ell\,2\nu$ decay channel for $\sqrt{s} = 7$ TeV (dashed line) and $\sqrt{s} = 8$ TeV of center-of-mass energy (Courtesy of A. Massironi).

When the pair of W bosons decays leptonically, the signature in the detector will be the presence of two leptons with opposite charge and a relatively high transverse momentum (depending on the Higgs mass) and large missing transverse energy due to the neutrinos which can escape detection. The two leptons can be any of the 9 equally-likely possibilities pairing electrons, muons and taus (ee, $\mu\mu$, $\tau\tau$, eμ, eτ, μe, $\mu\tau$, τe, $\tau\mu$).

The τ leptons are unstable and cannot be detected directly. They decay electroweakly to a W boson that in turn decays into hadrons ($\sim$65 %) or stable leptons ($\sim$35 %). The former case leads to a final state different from the *two leptons and* $E_{\mathrm{T}}^{\mathrm{miss}}$ *signature*. The final state of the latter case is seemingly similar to that of a $\mathrm{W}^+\,\mathrm{W}^- \to 2\ell\,2\nu$ decay. However, the stable lepton originating from a τ decay has a lower momentum than that of a lepton orignating directly from a W boson as shown in Figure 5.2 (since the available phase space for such decay is reduced). The analysis will only consider the electron and muon as lepton candidates. As we will have to apply a minimum transverse momentum requirement on the leptons to reduce the W+jets background (see Section 5.2.4), the τ contribution will be strongly reduced. The small remaining τ contribution will be implicitly included in the analysis.

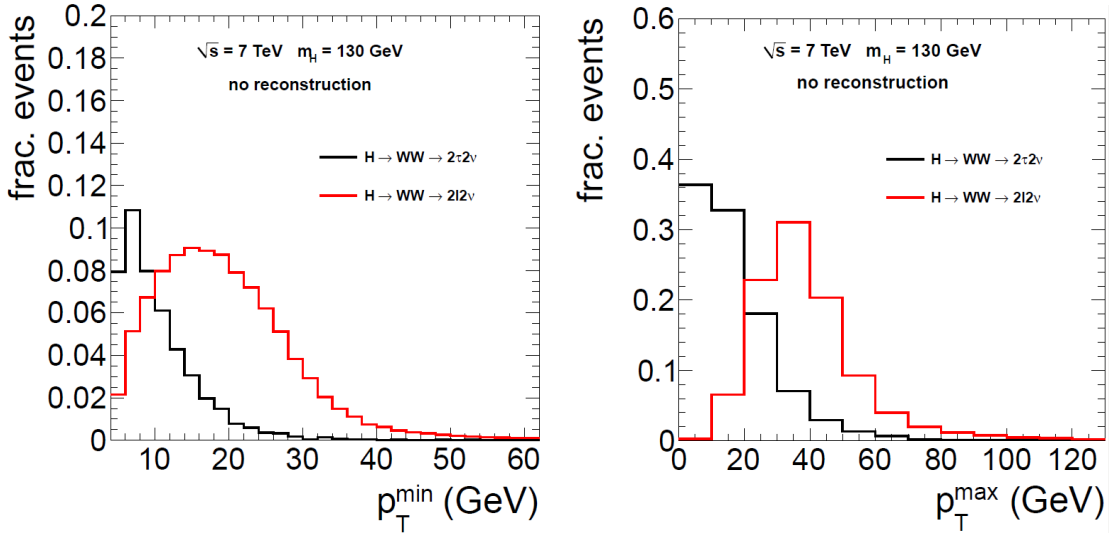

(a) (b)

Figure 5.2.: Transverse momentum distributions of the leptons originating from the $H \to W^+ W^-$ decay comparing the direct decay to stable leptons, e and μ, (red curve), to the τ leptons decaying leptonically (black curve). The less and most energetic lepton are shown in (a) and (b), respectively (Courtesy M. Selvaggi).

Lastly, next to the *two leptons and* E_T^{miss} *signature*, a fraction of the events will also present one or more jets in the final state signature which is related to the different production mechanisms. The analysis is divided into exclusive channels, defined by the number of jets with transverse momentum greater than 30 GeV in the event. The so-called *zero-jet category* analysis (with no jets with $p_T > 30$ GeV) is mostly sensitive to the gluon fusion production mechanism. In the presence of one jet in the event (*one-jet category*), the main production mechanism is still gluon fusion, with the addition of an initial state radiation of a gluon, detected as a jet in the CMS detector. If two jets are reconstructed (*two-jet category*), it is possible to develop an analysis that is sensitive to different Higgs production mechanisms, such as the vector-boson fusion and the associated production. The case with two reconstructed jets will not be covered in the present work, although the results can be found in [89].

5.2. Main backgrounds

All the processes that have the potential to mimic the $H \to W^+ W^- \to 2\ell\, 2\nu$ signature have to be considered as possible sources of background. This means that we need to consider all processes with two isolated leptons and missing energy in the final state,

Table 5.1.: Cross-section values for the main backgrounds, multiplied by the branching ratio. In this figure $\ell = e, \mu, \tau$ (the VVV sample was not used in the $\sqrt{s} = 7$ TeV analysis).

process	$\sqrt{s} = 7$ TeV σ(pb)	$\sqrt{s} = 8$ TeV σ(pb)
$gg/q\bar{q} \to WW \to \ell\nu\ell\nu$	4.94	5.99
WZ	18.2	22.4
ZZ	7.67	9.03
VVV	/	2.55
$W\gamma \to \ell\nu\gamma$	429	554
$W\gamma^* \to \ell\nu 2\ell$	7.15	8.12
$Z\gamma \to 2\ell\gamma$	96.6	132.6
$t\bar{t}$ + jets	163	225
tW	15.7	22.4
$Z/\gamma^{(*)} \to 2\ell$ + jets ($m_{\ell\ell} > 50$ GeV)	3048	3533
$W \to \ell\nu$ + jets	31314	37509

as well as processes with jets reconstructed as leptons by the detector. The main background sources are due to non-resonant diboson production (WW, WZ, ZZ, VVV with V=W/Z, $W\gamma^{(*)}$, $Z\gamma$), Drell-Yan production (DY), top production ($t\bar{t}$ and tW), W + jets production, and QCD multijet processes in which two jets are misidentified as isolated leptons.

Table 5.1 summarizes the cross sections of the different processes, multiplied by the branching ratio, for both $\sqrt{s} = 7$ TeV and $\sqrt{s} = 8$ TeV. To get an idea of the magnitude of the backgrounds with respect to the signal we are looking for, we can combine this table with Figure 5.1. It follows that for the full 2011 and 2012 dataset we expect $\sim$12000 Higgs bosons with m_H =130 GeV decaying into leptons, compared to 9×10^8 W + jets, 8×10^7 Drell-Yan, 5×10^6 $t\bar{t}$ and 1×10^5 W^+W^- events. Searching for such a small signal contribution in such an overwhelming background, requires the careful selection of a phase-space region in which the signal-to-background (S/B) is enhanced.

5.2.1. WW production

The W^+W^- production is certainly not the background with the highest cross section, but it is one of the hardest to deal with. A W^+W^- pair can be produced by a $q\bar{q}$ scattering or by gluon-gluon fusion. The latter gluon-gluon fusion production is highly suppressed as it involves a light quark loop. Figure 5.3 shows a leading order (LO)

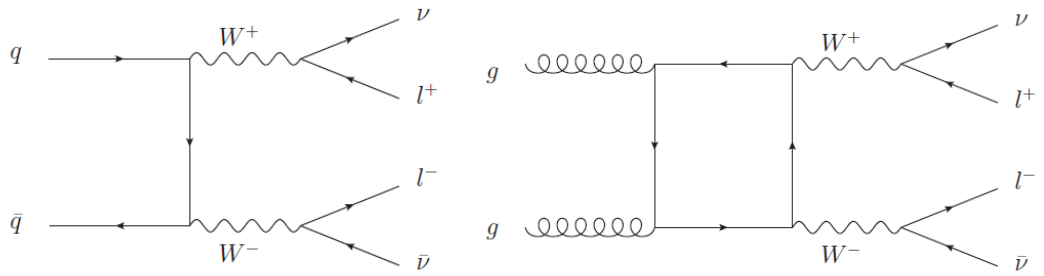

Figure 5.3.: Feynman diagrams of the W^+W^- production: (a) dominant quark production at LO and (b) sub-dominant suppressed gluon fusion due to the light quark loop.

diagram of the former quark production and a diagram of the latter suppressed gluon fusion. The W^+W^- background is an *irreducible* background in the sense that there is nothing else than the exact W pair produced in the process, making it almost identical to the $H \to W^+ W^-$ decay. In Section 7.1.1 we will see how it is still possible to (partially) deal with this background.

5.2.2. Top production

The top production is another major background and is split up into $t\bar{t}$ pair and single top production. The $t\bar{t}$ pairs are produced by $q\bar{q}$ scattering or by gluon-gluon fusion. Each top decays with a branching ratio of 98 % into a W boson and a b-quark. When the W bosons are decaying leptonically, this results into a final state alongside the additional pair of b-jets, well reproducing the signal topology as it consists of two opposite sign leptons, $E_{\mathrm{T}}^{\mathrm{miss}}$ and two b-jets. This is shown in Figure 5.4. Top quarks can also be produced alone, predominantly through the tW channel, as shown in Figure 5.5. The final state consists of two leptons, $E_{\mathrm{T}}^{\mathrm{miss}}$ and one b-jet. In order to reduce the top contamination we will apply a veto on the presence of b-jets.

5.2.3. Drell-Yan production of $Z/\gamma^{(*)}$

The Drell-Yan (DY) $Z/\gamma^{(*)} \to 2\ell$ production has a very high cross section. The $Z/\gamma^{(*)}$ boson decays to two leptons, as shown in Figure 5.6, potentially mimicking the signal. The missing energy comes mainly from the mis-reconstruction of energies in the detector, leading to a fake lack of momentum balancing. To reduce the background, a soft cut on

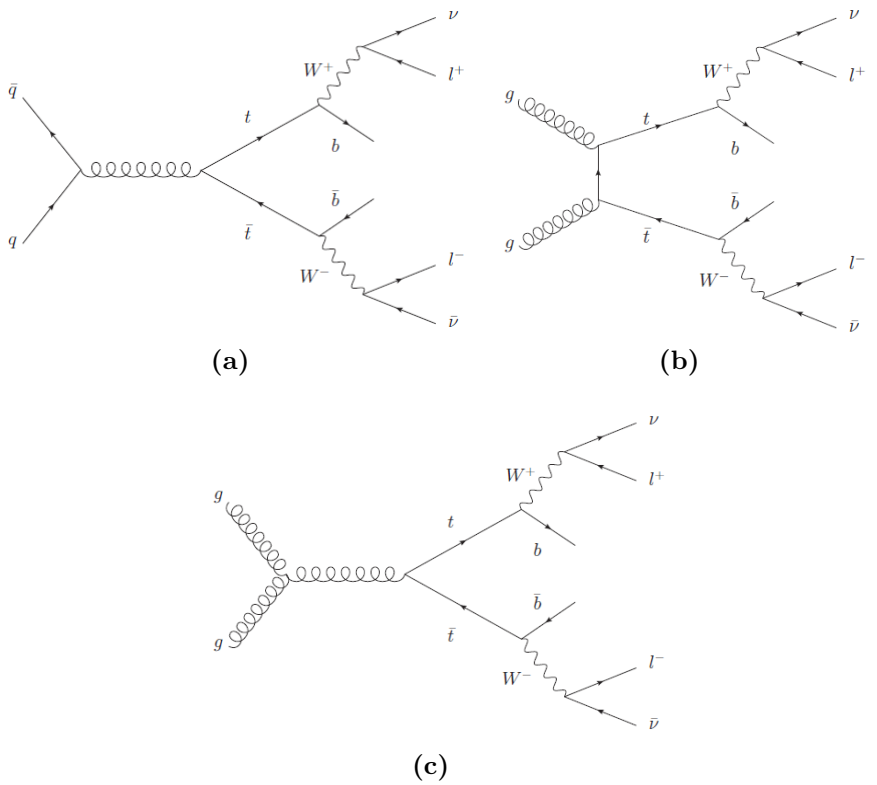

Figure 5.4.: Feynman diagrams of the $t\bar{t}$ production at LO: (a) quark production, (b) gluon fusion and (c) three gluon vertex.

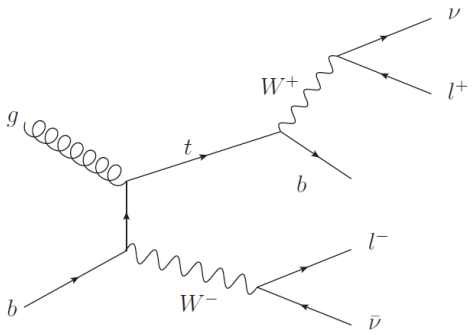

Figure 5.5.: Feynman diagram of the single top production via the tW channel at LO.

the $E_{\mathrm{T}}^{\mathrm{miss}}$ is applied combined with a multivariate technique to identify and suppress DY events. In addition we apply a veto on events with two electrons or two muons with an invariant mass close to m_{Z}. In principle the background affects only the $\mathrm{e^+e^-}$ and $\mu^+\mu^-$ signal final states, although one has to consider that the $\mathrm{Z}/\gamma^{(*)} \to \tau\tau$ can also affect the mixed flavor final states (through leptonic decay of the τ leptons).

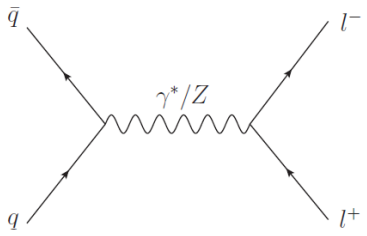

Figure 5.6.: Feynman diagram of the Drell-Yan production at LO.

5.2.4. W + jets production and QCD multijets

The production of a single W boson in association with jets has a huge cross section at the LHC. The W can decay leptonically to one lepton and $E_{\mathrm{T}}^{\mathrm{miss}}$, and a jet can be misreconstructed as a lepton, resulting in a similar signature to the signal one. The so-called *fake-rate*, the probability that a jet can fake a stable lepton, is higher for electrons than for muons and depends on the momentum of the jet (the lower the jet momentum, the higher the fake-rate probability).

The lepton identification has been developed in order to minimize the jet misidentification probability while keeping a good efficiency for the real leptons. Technically this means that we are applying a minimum threshold on the identified lepton momenta and that we apply identification and isolation criteria on the identified leptons. The former goes at the expense of the possibility to study the $\mathrm{H} \rightarrow \mathrm{W}^+ \mathrm{W}^-$ to one or two τ leptons. The latter is caused by the activity of a jet faking a lepton. This activity is usually due to other particles surrounding the lepton in the detector.

The optimized lepton identification also reduces QCD multijet processes, where two jets are reconstructed as leptons. In addition, jets may contain real electrons and muons from leptonic b quark decays, but those leptons are vetoed by the isolation requirements.

5.2.5. Other backgrounds

We still have a few smaller backgrounds left to discuss. First we have the diboson production (WZ, ZZ) and the triboson production VVV (with V=W/Z) that can mimic the signal, although they are not producing exactly two leptons in the final state. They can fake the signal due to possible misidentification of leptons or due to the loss of leptons out of the detector acceptance. These backgrounds can be reduced by requiring exactly two opposite sign leptons in the final state.

As a last group we have the associated production of a vector boson and a photon (Wγ, Wγ^*, Zγ), which becomes a background when the photon converts to a lepton pair. To reject those events, we veto on leptons coming from conversions based on their track information, making these backgrounds small after all the selections are applied.

In this work, data-MC comparison plots will generally, if not mentioned otherwise, show the following backgrounds grouped together and called **VV**: WZ, ZZ, VVV, Wγ, Wγ^* and Zγ.

5.3. Data and simulation samples

5.3.1. Data samples

The datasets used in this analysis correspond to the full 2011 and 2012 data. They are organized in so-called *primary datasets* (PD), which combine various collections of the HLT, and are produced centrally in CMS.

Given the e^+e^-, $\mu^+\mu^-$ and $e^\pm\mu^\mp$ final states in our analysis, we consider the following 5 primary datasets for signal extraction. The *DoubleElectron* PD serves the e^+e^- final state, while the *DoubleMu* PD serves the $\mu^+\mu^-$ final state. The cross-lepton *MuEG* (Muon-ElectronGamma) PD serves the $e^\pm\mu^\mp$ final state. Finally, to recover some efficiency, the *SingleElectron* and *SingleMu* PD are used to recover events that do not fire the double lepton triggers, but do fire the single lepton triggers.

For the analysis we only consider the subset of data which have passed all the data quality tests of the Physics Validation Team of CMS. Taking this into account, the data samples used in this analysis correspond to an integrated luminosity of 4.9 fb^{-1} at a center-of-mass energy of $\sqrt{s} = 7$ TeV collected in 2011 and an integrated luminosity of 19.4 fb^{-1} at $\sqrt{s} = 8$ TeV collected in 2012. The uncertainties on these numbers are 2.2 % in 2011 and 2.6 % in 2012.

5.3.2. Simulation samples

Several Monte Carlo event generators are used to simulate the signal and background processes. The POWHEG generator [90] provides event samples for the $H \to W^+ W^-$ signal. The line shape of the mass spectrum of the Higgs boson signal at the generator

level is corrected to match the results presented in [91–94], where the complex-mass scheme for the Higgs propagator is used. The effects on the cross section due to the interference between the SM Higgs boson signal and the $gg \to WW$ background, as computed in references [95, 96] are included.

The Drell-Yan production of $Z/\gamma^{(*)}$, $W + jets$ and $q\bar{q} \to WW$ processes are generated using the MADGRAPH 5.1 event generator [97], the $gg \to WW$ process using the GG2WW 3.1 generator [98], and the $t\bar{t}$ and the tW processes are generated with POWHEG. The remaining processes are generated with PYTHIA 6.424 [99]. All the generated events were passed to PYTHIA for the showering of partons, whereafter they were simulated and reconstructed in the CMS detector. For all processes, the detector response is simulated using a detailed description of the CMS detector, based on the GEANT4 package [63].

The set of parton distribution functions (PDF) used is CTEQ6L [100] for leading order (LO) generators, while CT10 [101] is used for next-to-leading order (NLO) generators. Cross section calculations at next-to-next-to-leading order (NNLO) are used for the $H \to W^+ W^-$ process [39], while NLO calculations are used for background cross sections and taken from MCFM [102].

5.4. Event selection strategy

As stated in the introduction of this chapter, the $H \to W^+ W^- \to 2\ell\, 2\nu$ decay features a signature with two isolated, opposite charged, high p_T leptons (electrons or muons) and moderate missing transverse momentum E_T^{miss}, due to the two undetected neutrinos. This is the same final state as the non-resonant irreducible $W^+ W^-$ background. In addition, the Higgs cross section is several orders of magnitude lower than the major reducible background processes: $t\bar{t}$, $W + jets$ and Drell-Yan. Lastly, due to the presence of the undetectable neutrinos, we can not search for a signal resonance.

For these reasons, we will start by working our way down to a general event selection, where we maximize the signal-to-background (S/B) ratio as much as possible with the main goal to suppress all the reducible backgrounds. This general selection is common to all Higgs mass hypotheses. Afterwards in a next step, we will extract the Higgs boson signal from the remaining events with two different mass dependent selections: one cut-based and one shape-based. This is described in Chapter 7. Here we will have to

deal with the irreducible W^+W^- background and other residual backgrounds. Lastly, we will cover in Chapter 6 how we can estimate our backgrounds with the help of data, to remove our dependence on the simulated Monte Carlo samples.

First of all, to reduce certain backgrounds more easily, we will divide the search channel up into different categories, where the S/B ratio in each of them can be optimized in view of maximally exploiting our statistics. Splitting the events into categories that differ in signal and background composition imposes additional constraints on the backgrounds and defines regions with high signal purity.

The events are split according to the jet multiplicity in a *0-jet* and *1-jet* category, with 0 and 1 jet above 30 GeV respectively. This makes it significantly easier to handle the top background. Secondly, the signal candidates are split into three final states denoted by e^+e^-, $\mu^+\mu^-$, and $e^\pm\mu^\mp$ and the analysis is developed independently in the $(e^+e^-) + (\mu^+\mu^-)$, called *same-flavor* (SF) final state, and $e^\pm\mu^\mp$, called *different-flavor* (DF) final state. This last separation makes it easier to handle the Drell-Yan background, which is different in both flavor final states (see Section 5.2.3).

The bulk of the signal arises through direct W decays to electrons or muons of opposite charge, where the small contribution proceeding through an intermediate τ lepton is implicitly included.

To summarize:

1. We select events that pass pre-defined lepton triggers
2. We then select those events with two opposite-charged high-p_T isolated leptons (e^+e^-, $\mu^+\mu^-$, and $e^\pm\mu^\mp$) requiring:
   - $p_T > 20$ GeV for the leading lepton (highest p_T);
   - $p_T > 10$ GeV for the trailing lepton (lowest p_T) and the stricter $p_T > 15$ GeV for the e^+e^- and $\mu^+\mu^-$ final states at $\sqrt{s} = 7$ TeV[1];
   - identification and isolation requirements on both leptons.
3. We apply a common W^+W^- preselection, which requires in brief:
   - categorization of events by the number of reconstructed jets with a $p_T > 30$ GeV in a 0-jet and 1-jet category;

[1]The reasoning for the stricter cut is covered in Section 5.4.3.

- exactly two high-p_{T} isolated leptons that are inconsistent with a Z decay;
- anti b-tagging to exclude top decays;
- large transverse missing energy due to the neutrinos.

4. Finally, we perform two Higgs mass dependent event selections, one cut-based and one shape-based, described in the Higgs signal extraction strategy chapter, Chapter 7.

5.4.1. Triggers

Triggering on Higgs boson decays in the dilepton final state gets more difficult with increasing instantaneous luminosity. A low mass Higgs boson decays preferably to low momentum leptons, but the rate of such leptons is too high at the LHC. One is able to keep the rate acceptable by applying most of the lepton requirements, that would be demanded at analysis level, already at the HLT level. This translates in single lepton triggers with very tight identification and isolation requirements and large transverse momentum thresholds. As a consequence, double lepton triggers are the only viable option to maintain sensitivity to a low mass Higgs boson, where the leptons transverse momentum can be kept small. The dilepton triggers have a high efficiency to collect Higgs boson events and they are sufficiently loose to collect control events to estimate fake lepton backgrounds and selection efficiencies with adequate precision. The single lepton triggers are used to recover events where one lepton passes the tight identification and kinematic thresholds, while the second is on the turn-on curve of the dilepton trigger. The list of triggers is summarized in Table 5.2. The sum of the rates of the analysis triggers is about 20 Hz.

The main dielectron triggers require two HLT electron candidates with loose shower shape and calorimeter isolation requirements on both electrons and a match to a Level-1 seed for the leading electron. Since the offline selections requires $E_{\mathrm{T}} > 20$ (10) GeV for the leading (trailing) electron, $E_{\mathrm{T}} > 17$ (8) GeV is required at the HLT level. Controlling the total trigger rate is most challenging in the dielectron channel, due to the large fake electron background rates. Additional requirements must be added to the track-to-cluster matching and track isolation to control the total trigger rate (see Section 5.4.3 for details about the tracker-ECAL matching for electrons). The identification and isolation requirements are described in Table 5.3. Because the electron HLT uses simplified

Table 5.2.: Trigger paths used to select events in data. The number behind *Ele* or *Mu* represents the minimum required p_{T} of the electron or muon respectively. The identification and isolation requirements are described in Table 5.3.

dataset	**trigger paths**
SingleElectron, e	HLT_Ele27_WP80
SingleMu, μ	HLT_IsoMu24_eta2p1
DoubleElectron, ee	HLT_Ele17_CaloIdT_CaloIsoVL_TrkIdVL_TrkIsoVL_ _Ele8_CaloIdT_CaloIsoVL_TrkIdVL_TrkIsoVL
DoubleMu, $\mu\mu$	HLT_Mu17_Mu8 HLT_Mu17_TkMu8
MuEG, eμ	HLT_Mu17_Ele8_CaloIdT_CaloIsoVL_TrkIdVL_TrkIsoVL HLT_Mu8_Ele17_CaloIdT_CaloIsoVL_TrkIdVL_TrkIsoVL

algorithms compared to the offline selections, the variables used online and offline do not always correspond exactly. Nevertheless, the efficiencies of the offline requirements with respect to the online trigger selections are above 99 %. For this reason, no trigger requirements are made on the simulated events. Instead, scale factors that take into account the differences between data and MC are measured as a function of kinematic variables of the leptons (p_{T} and η).

The main dimuon triggers require two HLT muon candidates with transverse momentum larger than 17 and 8 GeV and a match to a Level-1 seed is required for both muons. These are described in Table 5.2.

In the electron-muon channel two complementary triggers are used, requiring both muon and electron HLT candidates, as summarized in Table 5.2.

Additional triggers are used to collect control or calibration events not covered by the main analysis triggers. Since the main dielectron analysis triggers put requirements on both leptons, events collected by them cannot be used to measure efficiencies without introducing biases. For this reason, specialized tag and probe triggers have been designed to maximize the number of $\mathrm{Z}/\gamma^{(*)} \to \ell^+\ell^-$ events for both low and high p_{T} leptons, while keeping the total trigger rate at a reasonable level. The triggers are summarized in Table 5.4 and the tag and probe method is described in more detail in Section 5.4.3 under lepton efficiencies. The trigger efficiency for signal events that pass the full event selection is measured to be about 97 % in the $\mu^+\mu^-$ final state, about 98 % in the $\mathrm{e}^+\mathrm{e}^-$ final state and about 96 % in the $\mathrm{e}^\pm\mu^\mp$ final state for a Higgs boson mass of about 125 GeV. The trigger efficiency increases with the Higgs boson mass. The efficiency is

Table 5.3.: Summary of the requirements applied to electrons in the triggers used for this analysis. The selection requirements are given for electrons in the barrel (endcap). L=Loose, VL=Very loose, T=Tight and VT=Very Tight. The variables $|\Delta\phi|$ and $|\Delta\eta|$ represent the absolute ϕ and η differences between the two electrons.

name	**criterion**
CaloId_L	H/E < 0.15 (0.10)
	$\sigma_{\eta\eta} < 0.014$ (0.035)
CaloId_T	H/E < 0.15 (0.10)
	$\sigma_{\eta\eta} < 0.011$ (0.031)
CaloId_VT	H/E < 0.05 (0.05)
	$\sigma_{\eta\eta} < 0.011$ (0.031)
TrkId_VL	$\|\Delta\eta\| < 0.01$ (0.01)
	$\|\Delta\phi\| < 0.15$ (0.10)
TrkId_T	$\|\Delta\eta\| < 0.008$ (0.008)
	$\|\Delta\phi\| < 0.07$ (0.05)
CaloIso_VL	ECalISO/$E_T < 0.20$ (0.20)
	HCalISO/$E_T < 0.20$ (0.20)
CaloIso_T	ECalISO/$E_T < 0.15$ (0.075)
	HCalISO/$E_T < 0.15$ (0.075)
CaloIso_VT	ECalISO/$E_T < 0.05$ (0.05)
	HCalISO/$E_T < 0.05$ (0.05)
TrkIso_VL	TrkIso/$E_T < 0.20$ (0.20)
TrkIso_T	TrkIso/$E_T < 0.15$ (0.075)
TrkIso_VT	TrkIso/$E_T < 0.05$ (0.05)
WP80	H/E < 0.10 (0.05)
	$\sigma_{\eta\eta} < 0.01$ (0.03)
	$\|\Delta\eta\| < 0.007$ (0.007)
	$\|\Delta\phi\| < 0.06$ (0.03)
	$\|\frac{1}{E} - \frac{1}{p}\| < 0.05$ (0.05)
	ECalISO/$E_T < 0.15$ (0.10)
	HCalISO/$E_T < 0.10$ (0.10)
	TrkIso/$E_T < 0.05$ (0.05)

high since most of the residual inefficiency of the double lepton triggers are recovered by the single lepton triggers.

Finally another set of specialized triggers is used to collect events enriched in fake electrons and muons for the measurement of the jet induced backgrounds. Details about this measurement will be described in detail in Section 6.1.1. The required triggers for the electron and muon fake rate are described in Table 5.5.

Table 5.4.: Trigger paths used in data to study the trigger efficiencies.

lepton flavor	trigger paths
muon efficiency	HLT_IsoMu24_eta2p1
	HLT_IsoMu30_eta2p1
	HLT_Mu40_eta2p1
	HLT_Mu50_eta2p1
electron efficiency	HLT_Ele27_WP80

Table 5.5.: Trigger paths used in data to study the fake rates.

lepton flavor	trigger paths
electron fakes	HLT_Ele8_CaloIdL_CaloIsoVL
	HLT_Ele17_CaloIdL_CaloIsoVL
muon fakes	HLT_Mu8
	HLT_Mu17

5.4.2. Primary vertex

For each triggered event, one has to reconstruct the vertex associated to the hard scattering and remove the ones coming from pile-up events. In this analysis primary vertices are reconstructed with the Deterministic Annealing clustering of tracks as described in Section 4.2. The reconstructed vertices are required to have a z position within 24 cm of the nominal detector center and a radial position within 2 cm of the beamspot region. From the set of primary vertices satisfying these requirements, the vertex with the largest summed squared-p_{T} of the associated tracks is chosen as the event primary vertex. Reconstructed leptons will be required to have small impact parameters with respect to this vertex.

The simulated MC samples are reweighted to represent the distribution of the number of p-p interactions per bunch crossing (pile-up) as measured in the data. As covered in Section 2.3, the average number of pile-up events in the 2011 and 2012 data are approximately 9 and 21, respectively due to the increase of instantaneous luminosity. The correct simulation of multiple interactions per bunch crossing is guaranteed by the good data-MC agreement in the distribution of the number of reconstructed vertices, as shown in Figure 5.7. One can also see that the average number of primary vertices increased from 7 to 15 between 2011 and 2012.

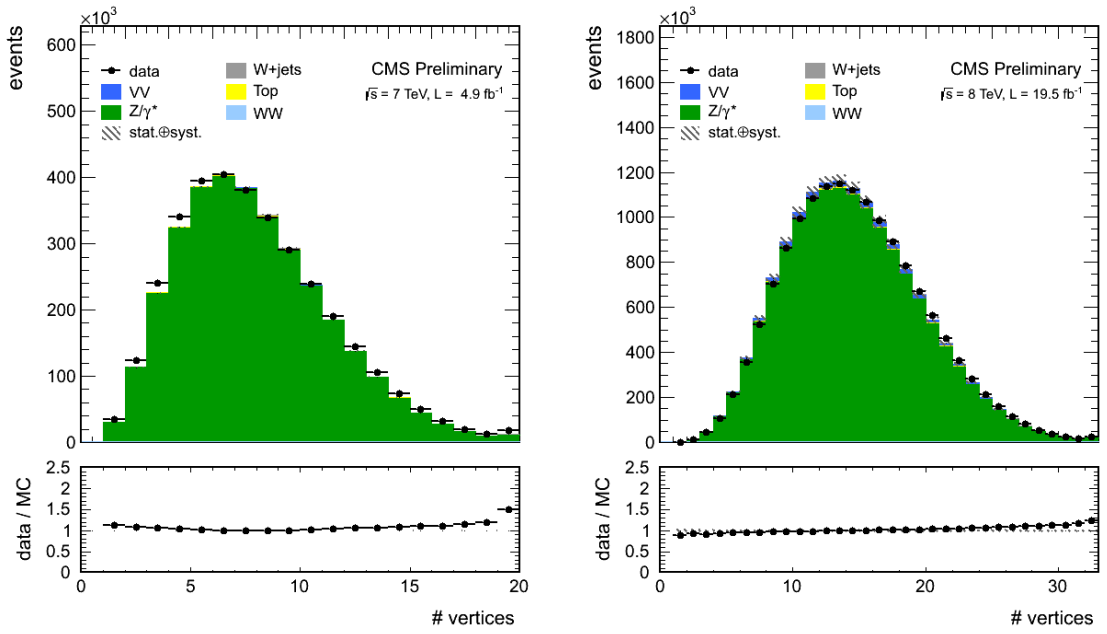

Figure 5.7.: Distribution of the number of vertices after the simulation has been pile-up reweighted for (a) 2011 data period and (b) 2012 data period. The events in this figure are required to have exactly two same-flavor leptons (fulfilling the lepton selection of Section 5.4.3) and have $m_{\ell\ell} > 12$ GeV. A good agreement between data (points with error bars) and MC (stacked histograms) is observed, assuring the correct description of pile-up events.

5.4.3. Lepton selection

Once the primary vertex is defined, one wants to select the leptons that are (most likely) originating from it. To keep most of the signal events and to reject the background events (mainly W+jets), the leptons are required to satisfy a number of identification and isolation criteria and a minimum transverse momentum. The end of the section will also cover the signal efficiencies of the muon and electron selection.

Muon selection

Most good quality muons are reconstructed as both *GlobalMuon* and *TrackerMuon* at the same time (see Section 4.7). The muon momentum resolution is dominated by the inner tracker system up to about 200 GeV in transverse momentum. Muons are required to be reconstructed as *GlobalMuon* with $\chi^2/\text{ndof} < 10$ on the global fit, must have at least one muon hit included in the final track fit, and at least two matches to

muon segments in different muon stations; or as *TrackerMuon* provided, it satisfies the *TrackerMuonLastStationTight* selection requiring at least two muon segments matched at 3σ in local X and Y coordinates, with one being in the outermost muon station. This last requirement allows the recovery of events in which the two muons are close by in the spectrometer, for which the *GlobalMuon* reconstruction is known to be inefficient [85].

In addition, mainly to reject muons from jets and to make sure that the muons do not originate from pile-up vertices, the following requirements to select good prompt isolated muons are:

- minimum transverse momentum of 10 GeV
- more than 5 tracker layers hit
- at least one pixel hit
- transverse impact parameter $|d_{xy}| < 0.02$ (0.01) cm for muons with p_{T} greater (smaller) than 20 GeV, calculated with respect to the primary vertex
- longitudinal impact parameter $|d_z| < 0.1$ cm, calculated with respect to the primary vertex
- absolute pseudorapidity $|\eta|$ must be smaller than 2.4
- relative p_{T} resolution better than 10 %
- identified as a particle-flow muon

Furthermore to distinguish between muons from W-boson decays and those from QCD background processes, which are usually in or near jets, muons are required to be isolated. The isolation algorithm is built on the energy deposits of PF candidates (photons, charged hadrons and neutral hadrons) measured in five concentric rings around the muon direction of size 0.1 in the $\eta \times \phi$ plane. These values are combined with a MVA which exploits the differences in the differential energy deposition between prompt muons and muons from hadron decays inside a jet, to discriminate between signal and background. The values are also corrected for the average density of energy from pile-up particles using ρ and A_{eff} similar to the L1 jet correction in Section 4.4. A muon is considered isolated when the MVA isolation value is bigger than a given threshold optimized separately for different p_{T} ranges ($p_{\mathrm{T}} \lesseqgtr 20$ GeV) and barrel (endcap) region.

For the $\sqrt{s} = 7$ TeV analysis, a linear cut on the PF candidate-based isolation variable is used instead of an MVA-based variable as this selection is sufficient in the lower PU

environment. $\mathrm{Iso_{PF}}$ is defined as the scalar sum of the p_T of the PF candidates satisfying the following requirements:

- $\Delta\mathrm{R} < 0.3$ between the PF candidate and the muon in the $\eta \times \phi$ plane
- distance difference along the z coordinate measured at the primary vertex, $|d_z(\text{PF candidate}) - d_z(\text{muon})| < 0.1$ cm, if the PF candidate is charged
- $p_\mathrm{T} > 1.0$ GeV, if the PF candidate is classified as a neutral hadron or a photon

Muons in the barrel with p_T greater (smaller) than 20 GeV are required to have $\frac{\mathrm{Iso_{PF}}}{p_\mathrm{T}} < 0.13$ (0.06). Muons in the endcap with p_T greater (smaller) than 20 GeV are required to have $\frac{\mathrm{Iso_{PF}}}{p_\mathrm{T}} < 0.09$ (0.05).

Electron selection

The minimum transverse momentum of the electrons is required to be 10 GeV with $|\eta| < 2.5$. Since this is a pretty loose requirement (in order to increase the signal efficiency), strict requirements on the identification variables are needed to reduce the jet induced background. For this reason a multivariate variable, that exploits a large set of inputs, is trained against jets and non-isolated electrons, that would pass electron selections if not properly rejected. The variables used in the electron identification MVA are:

- kinematics: p_T, η
- shower shape
- track fit quality: χ^2/ndof
- number of tracker layers
- cluster-track matching (geometry): $\Delta\phi_{SC-Tk}$, $\Delta\eta_{SC-Tk}$
- cluster-track matching (energy-momentum): E/p
- fraction of energy carried away by bremsstrahlung: $f_\mathrm{brem} = (p_{in} - p_{out})/p_{in}$, with p_{in} (p_{out}) the momentum reconstructed with the first (last) layers of the tracker
- ratio of hadronic energy to EM energy: $\mathrm{E_{HCAL}/E_{ECAL}}$
- impact parameter: transverse and 3D impact parameters with respect to the primary vertex

- ECAL PreShower contribution to the supercluster: E_{PS}/E_{SC}

Next the isolation requirements are imposed by computing the particle-flow isolation, defined as the scalar sum of the p_T of the particle-flow candidates, after excluding the electron and muon candidates, satisfying the following requirements:

- $\Delta R < 0.4$ between the PF candidate and the electron in the $\eta \times \phi$ plane
- for gamma PF candidates, they require to be outside the footprint veto region of $\Delta R < 0.08$ to the electron
- for charged hadron PF candidates, they require to be outside the footprint veto region of $\Delta R < 0.015$ to the electron
- for charged hadron PF candidates, they require to be associated with the primary vertex
- neutral components are corrected by subtracting pile-up contributions which is calculated by $\rho \times A_{eff}$, with ρ (kt6PFJets) the event-by-event energy density and A_{eff} the effective area (similar to the L1 jet correction in Section 4.4)

With these conditions, the isolation variable can be written down as

$$\frac{\text{Iso}_{\text{PF}}}{p_T} = (\text{Iso}_{\text{charged hadron}} + \text{Iso}_{\text{gamma}} + \text{Iso}_{\text{neutral hadron}} - \rho \times A_{eff}) \frac{1}{p_T} \qquad (5.1)$$

where $\text{Iso}_{\text{charged hadron}}$, $\text{Iso}_{\text{gamma}}$ and $\text{Iso}_{\text{neutral hadron}}$ are the scalar sum of the p_T of the charged hadron, gamma and neutral hadron PF candidates, respectively, in the isolation cone of 0.4 around the electron. The value $\frac{\text{Iso}_{\text{PF}}}{p_T}$ is required to be below 0.15.

In order to veto fake electrons originating from a conversion of a photon into an e^+e^- pair in the tracker material, the number of missed inner tracker layers of the electron track is required to be exactly zero. In addition, any event is rejected in which the selected electron is close in space to a track and the electron-track pair is compatible with a photon conversion. Detailed selection requirements based on the distance of the two tracks in the longitudinal and transverse plane can be found in [103]. The contribution from the $W\gamma$ background, when the photon is misidentified as an electron, is reduced by about 90 % in the dielectron final state by these γ conversion rejection requirements.

Finally to reduce the number of fake electrons from non-prompt sources, the transverse and longitudinal impact parameters with respect to the primary vertex are required to be less than 0.02 and 0.1 cm respectively.

Lepton efficiencies

Both the online (trigger) and offline (analysis) lepton selection efficiency is calculated with the Tag&Probe technique on $Z/\gamma^{(*)} \to \ell^+\ell^-$ events. The technique uses a lepton pair coming from the heavy Z resonance, where one of the leptons is very well identified (tag) and the other one is tested (probe). The efficiency is measured counting the number of events where the probe passes the whole selection. This measurement involves a fit of the $m_{\ell\ell}$ distribution accounting for non-resonant contributions, that is substracted. The measurement is performed in bins of η and p_T of the probe lepton to guarantee a good description of the geometrical acceptance of the detector.

Both trigger and lepton selection efficiencies are measured from the data and a scale factor is applied to the MC in order to correct for small effects not taken into account by the simulation of the interaction with the detector.

The trigger efficiency numbers were already listed in the trigger section, Section 5.4.1. The efficiency scale factors for the muon and electron can be found in Table 5.6 and Table 5.7, respectively. The muon efficiency is close to 1 and the electron efficiency is lower in certain η regions for low p_T electrons. The lower efficiency originates from the last part of the data taking. It was also reported in other CMS analyses and has been investigated. It is not coming from an increase in pile-up and it is of no concern to this analysis. It gets corrected with the data/simulation scale factors.

Table 5.6.: Muon efficiency data/simulation scale factors. Errors are statistical only.

p_T [GeV]	$\lvert\eta\rvert < 0.9$	$0.9 < \lvert\eta\rvert < 1.2$	$1.2 < \lvert\eta\rvert < 2.5$
$10 < p_T < 15$	0.99 ± 0.01	0.97 ± 0.03	1.01 ± 0.01
$15 < p_T < 20$	0.96 ± 0.01	0.95 ± 0.01	1.00 ± 0.00
$20 < p_T < 25$	0.98 ± 0.00	0.98 ± 0.00	1.02 ± 0.00
$25 < p_T < 30$	1.00 ± 0.00	0.99 ± 0.00	1.02 ± 0.00
$30 < p_T < 50$	0.99 ± 0.00	0.99 ± 0.00	1.00 ± 0.00
$50 < p_T < 150$	0.99 ± 0.00	0.99 ± 0.00	1.01 ± 0.00

Table 5.7.: Electron efficiency data/simulation scale factors. Errors are statistical only.

p_{T} [GeV]	$\lvert\eta\rvert < 0.8$	$0.8 < \lvert\eta\rvert < 1.4442$	$1.4442 < \lvert\eta\rvert < 1.556$	$1.556 < \lvert\eta\rvert < 2.0$	$2.0 < \lvert\eta\rvert < 2.5$
$10 < p_{\mathrm{T}} < 15$	0.66 ± 0.02	0.73 ± 0.03	0.81 ± 0.09	0.61 ± 0.04	0.64 ± 0.03
$15 < p_{\mathrm{T}} < 20$	0.90 ± 0.01	0.94 ± 0.01	0.86 ± 0.07	0.83 ± 0.02	0.76 ± 0.02
$20 < p_{\mathrm{T}} < 30$	0.94 ± 0.00	0.95 ± 0.00	0.92 ± 0.01	0.92 ± 0.01	0.97 ± 0.01
$30 < p_{\mathrm{T}} < 40$	0.96 ± 0.00	0.94 ± 0.15	0.96 ± 0.01	0.93 ± 0.00	0.98 ± 0.01
$40 < p_{\mathrm{T}} < 50$	0.98 ± 0.00	0.97 ± 0.09	0.95 ± 0.00	0.96 ± 0.00	0.98 ± 0.00
$50 < p_{\mathrm{T}} < 200$	0.97 ± 0.00	0.97 ± 0.01	0.99 ± 0.01	0.96 ± 0.17	0.97 ± 0.00

Lepton pair

All the muons and electrons of a given event that pass the related selections are candidates to form a *lepton pair*. A lepton pair needs to satisfy the following two conditions:

- the two leptons have opposite charge,
- one lepton, called the *leading* lepton, must have $p_{\mathrm{T}} > 20$ GeV and the other one, called the *trailing* lepton, must have $p_{\mathrm{T}} > 10$ GeV. At $\sqrt{s} = 7$ TeV, the trailing lepton p_{T} threshold is raised to 15 GeV for the $\mathrm{e}^+\mathrm{e}^-$ and $\mu^+\mu^-$ final states. This is due to the fact that the $E_{\mathrm{T}}^{\mathrm{miss}}$ selection (see Section 5.4.6) is different between 2011 and 2012, since a more advanced technique to deal with the higher pile-up conditions for $\sqrt{s} = 8$ TeV has been introduced, which can handle lower p_{T} leptons.

The simulated signal events are reweighted by the scale factors described in Table 5.6 and Table 5.7. All the criteria applied up to this point is referred to as the *Lepton Selection*.

5.4.4. Extra-lepton rejection

To reduce the background from diboson processes, we veto events containing an additional lepton meeting the previously described lepton selection requirements. This removes ~ 60 % of the WZ component but only ~ 10 % of the ZZ component, which is dominated by $\mathrm{ZZ} \to 2\ell 2\nu$ decays after the full event selection and surviving the Z veto. The efficiency for $\mathrm{W}^+\mathrm{W}^- \to 2\ell\, 2\nu$ events is ~ 99.9 %.

5.4.5. Z veto and suppression of low mass resonances

To reduce the Drell-Yan background in the same-flavor (e^+e^- and $\mu^+\mu^-$) final states, events with a dilepton invariant mass, $m_{\ell\ell} = \sqrt{(p_{\ell_1} + p_{\ell_2})^2}$, within 15 GeV of the Z are vetoed. The lepton invariant mass for both flavors is shown in Figure 5.8. Events with a dilepton invariant mass below 12 GeV are also rejected to suppress contributions from low mass resonances, such as J/ψ (3 GeV), $Y(1S)$ (9.5 GeV), $Y(2S)$ (10.0 GeV), $Y(3S)$ (10.4 GeV), as shown in Figure 5.9. For the $\sqrt{s} = 7$ TeV analysis we require an extra condition of $m_{\ell\ell} > 20$ GeV for the same-flavor final states (e^+e^- and $\mu^+\mu^-$). This is again a condition that got relaxed for the $\sqrt{s} = 8$ TeV analysis due to the use of a more advanced $E_{\mathrm{T}}^{\mathrm{miss}}$ selection (including a DY MVA) to deal with the higher pile-up (see Section 5.4.6).

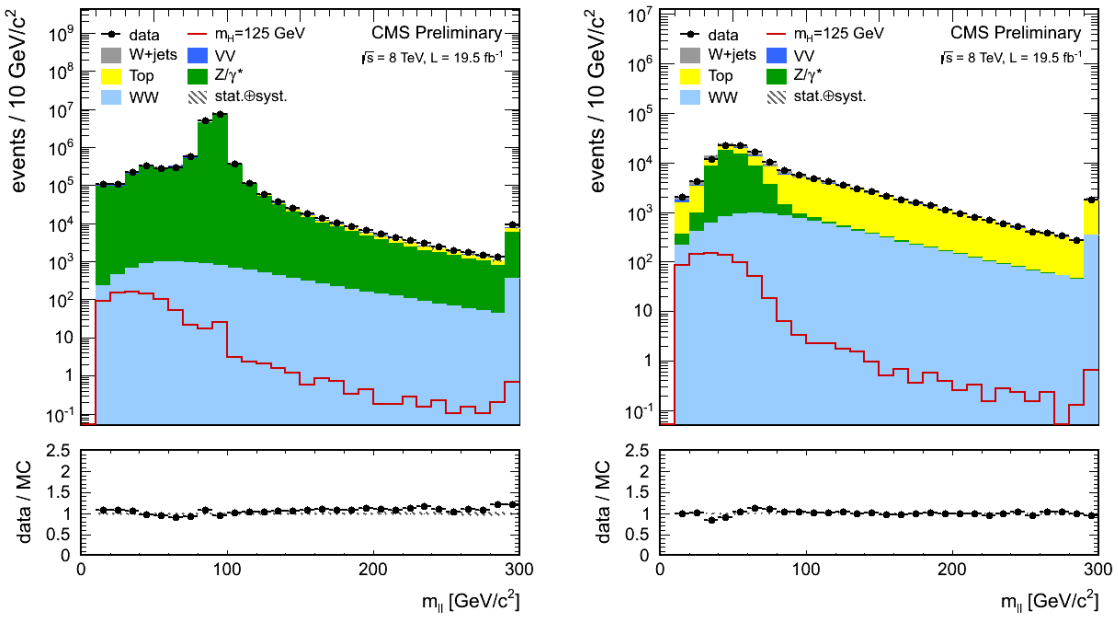

Figure 5.8.: Distribution of the invariant dilepton mass at $\sqrt{s} = 8$ TeV at the lepton selection level with the extra lepton veto and the $m_{\ell\ell} > 12$ GeV applied, for data (points with error bars), for the main backgrounds (stacked histograms) and for a Higgs boson signal with $m_{\mathrm{H}} = 125$ GeV (superimposed) at $\sqrt{s} = 8$ TeV for (a) the same-flavor channel (e^+e^- and $\mu^+\mu^-$) and (b) the different-flavor channel ($e^{\pm}\mu^{\mp}$).

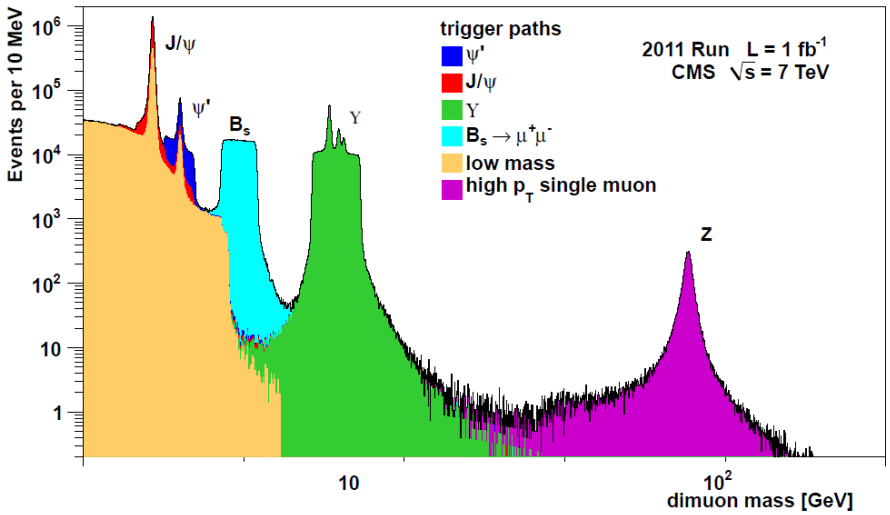

Figure 5.9.: Distribution of the dimuon mass for early $\sqrt{s} = 7$ TeV data. Low mass resonances can be removed by requiring a minimal invariant dilepton mass [104].

5.4.6. MET

Since a typical $H \to W^+W^- \to 2\ell\,2\nu$ event is accompanied by large missing energy due to the neutrinos, the missing transverse energy can be used to reject background events where there is no natural source of missing energy, as in Drell-Yan and QCD events. However there are also some backgrounds, such as $Z/\gamma^{(*)} \to \tau^+\tau^-$ that do have large E_T^{miss}, but whose kinematics are different than our Higgs signal. In the $Z/\gamma^{(*)} \to \tau^+\tau^-$ process there is a large difference in the masses of τ and Z. Due to this fact, the taus are produced with a large boost and their decay products, including neutrinos, are aligned with the leptons as outlined in Figure 5.10.

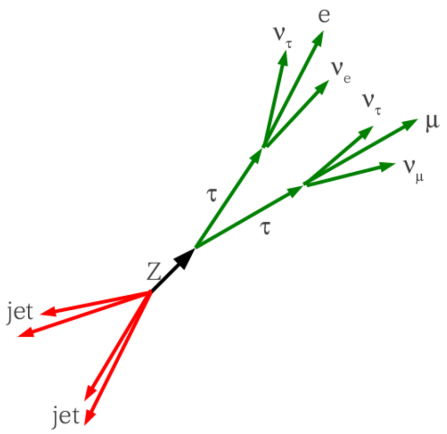

Figure 5.10.: Sketch of a $Z \to \tau^+\tau^-$ decay (Courtesy of A. Massironi).

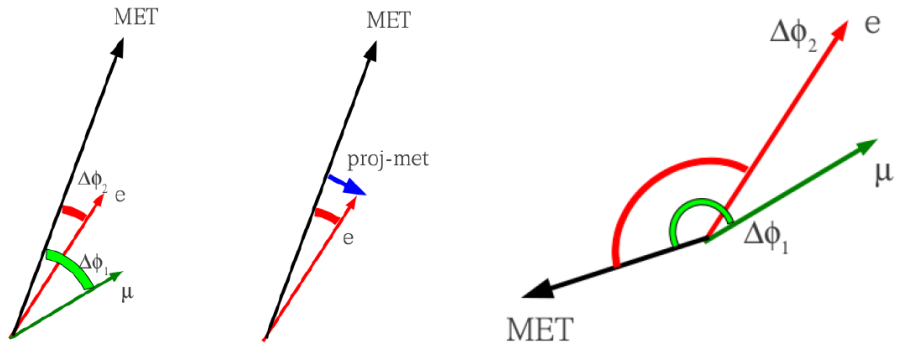

(a) procedure for background **(b)** procedure for signal

Figure 5.11.: $E_{\mathrm{T}}^{\mathrm{miss}}$ projection procedure: (a) shows the procedure for a background event (such as $\mathrm{Z} \to \tau^+\tau^-$). First the minimum between the two $\vec{E}_{\mathrm{T}}^{\mathrm{miss}}$-lepton angles is found (here the electron) and the $\vec{E}_{\mathrm{T}}^{\mathrm{miss}}$ is projected towards the nearest lepton in the transverse plane. This reduces the $E_{\mathrm{T}}^{\mathrm{miss}}$ for $\mathrm{Z} \to \tau\tau$ events, as pictured in Figure 5.10; (b) shows the procedure for a signal event, where the $\vec{E}_{\mathrm{T}}^{\mathrm{miss}}$ and the leptons are expected to be in opposite directions. Since $\Delta\phi_{min} \geq \frac{\pi}{2}$, the projection leaves the $E_{\mathrm{T}}^{\mathrm{miss}}$ untouched (Courtesy of A. Massironi).

Therefore a transverse component of missing energy with respect to the leptons direction is a better measure of missing energy in the event, not originating from τ decays. In order to reject such background events with a small opening angle between the $\vec{E}_{\mathrm{T}}^{\mathrm{miss}}$ and one of the leptons, the *projected* $E_{\mathrm{T}}^{\mathrm{miss}}$ is used in the event selection. It is defined as:

$$\text{proj. } E_{\mathrm{T}}^{\mathrm{miss}} = \begin{cases} E_{\mathrm{T}}^{\mathrm{miss}} & \text{if } \Delta\phi_{min} \geq \frac{\pi}{2} \\ E_{\mathrm{T}}^{\mathrm{miss}} \sin(\Delta\phi_{min}) & \text{if } \Delta\phi_{min} < \frac{\pi}{2} \end{cases} \tag{5.2}$$

$$\text{with } \Delta\phi_{min} = \min(\Delta\phi(\ell_1, \vec{E}_{\mathrm{T}}^{\mathrm{miss}}), \Delta\phi(\ell_2, \vec{E}_{\mathrm{T}}^{\mathrm{miss}})) \tag{5.3}$$

where $\Delta\phi(\ell_i, \vec{E}_{\mathrm{T}}^{\mathrm{miss}})$ is the angle between $\vec{E}_{\mathrm{T}}^{\mathrm{miss}}$ and lepton i in the transverse plane as shown in Figure 5.11.

Furthermore in presence of high pile-up, as mentioned in Section 4.5, the tail of the $E_{\mathrm{T}}^{\mathrm{miss}}$ distribution in $\mathrm{Z}/\gamma^{(*)} \to \ell^+\ell^-$ events increases significantly (with $\ell = \mathrm{e}/\mu$). We recap that the *tracker* $E_{\mathrm{T}}^{\mathrm{miss}}$ can be used to improve the signal over background performance of $E_{\mathrm{T}}^{\mathrm{miss}}$ selections in the presence of pile-up, since it is reconstructed using only the charged particles originating from the primary vertex, and is thus pile-up

independent. We can now refine the definition of the trk$E_{\mathrm{T}}^{\mathrm{miss}}$ in the context of the analysis:

$$\mathrm{trk}\vec{E}_{\mathrm{T}}^{\mathrm{miss}} = -\vec{p_{\mathrm{T}}}(\ell_1) - \vec{p_{\mathrm{T}}}(\ell_2) - \sum_i \vec{p_{\mathrm{T}}}(i) \tag{5.4}$$

where $\vec{p_{\mathrm{T}}}(\ell_1)$ and $\vec{p_{\mathrm{T}}}(\ell_2)$ are the transverse momentum vectors of the two leptons passing the lepton selections as described in Section 5.4.3, and $\sum_i \vec{p_{\mathrm{T}}}(i)$ the transverse momentum vectors of the charged PF candidates satisfying the following two conditions:

- the track matched to the PF candidate has $\Delta z < 0.1$ cm with respect to the signal primary vertex.
- the track has $\Delta R > 0.1$ with respect to both leptons, to avoid the double-counting of the leptons.

The physical difference between the trk$E_{\mathrm{T}}^{\mathrm{miss}}$ and the PF$E_{\mathrm{T}}^{\mathrm{miss}}$ is that the former is only build out of the charged PF candidates compatible with the primary vertex, while the latter is calculated using all the PF candidates, including the neutral hadrons, which cannot be attributed to a certain vertex. Compared to the projected Particle Flow $E_{\mathrm{T}}^{\mathrm{miss}}$ (proj.PF$E_{\mathrm{T}}^{\mathrm{miss}}$), the projected track $E_{\mathrm{T}}^{\mathrm{miss}}$ (proj.trk$E_{\mathrm{T}}^{\mathrm{miss}}$) has a larger tail in $\mathrm{Z}/\gamma^{(*)} \to \ell^+\ell^-$ events. However these two $E_{\mathrm{T}}^{\mathrm{miss}}$ variables are weakly-correlated in backgrounds with no genuine $E_{\mathrm{T}}^{\mathrm{miss}}$, and strongly correlated for the signal processes with genuine $E_{\mathrm{T}}^{\mathrm{miss}}$, as shown in Figure 5.12. On top of that, for the signal processes they both peak at high values. Therefore the signal-to-background ratio is improved by selecting events based on the minimum of these two projected $E_{\mathrm{T}}^{\mathrm{miss}}$ variables, called the *min-proj.*$E_{\mathrm{T}}^{\mathrm{miss}}$:

$$\mathrm{min-proj.}\ E_{\mathrm{T}}^{\mathrm{miss}} = \mathrm{min}(\mathrm{proj.trk}\ E_{\mathrm{T}}^{\mathrm{miss}}, \mathrm{proj.PF}\ E_{\mathrm{T}}^{\mathrm{miss}}) \tag{5.5}$$

As a soft preselection we require events to have PF$E_{\mathrm{T}}^{\mathrm{miss}} > 20$ GeV. On top of that, the soft baseline requirement of min-proj.$E_{\mathrm{T}}^{\mathrm{miss}} > 20$ GeV is applied on all final states and jet bins. For same-flavor final states, we enforce tighter selection requirements to deal with the same-flavor DY background. The are discussed in the following *DY MVA* subsection.

In Figure 5.13 one can find a comparison of the performance of three different choices of $E_{\mathrm{T}}^{\mathrm{miss}}$ variables: PF$E_{\mathrm{T}}^{\mathrm{miss}}$, min-proj$E_{\mathrm{T}}^{\mathrm{miss}}$ and min-proj$E_{\mathrm{T}}^{\mathrm{miss}} - \mathrm{N_{vtx}}/2$ (the latter is one of the stricter requirements that will be discussed in following subsection). In the figure, the efficiency of the $E_{\mathrm{T}}^{\mathrm{miss}}$ variables is compared for a Higgs signal of 120 GeV and 2012

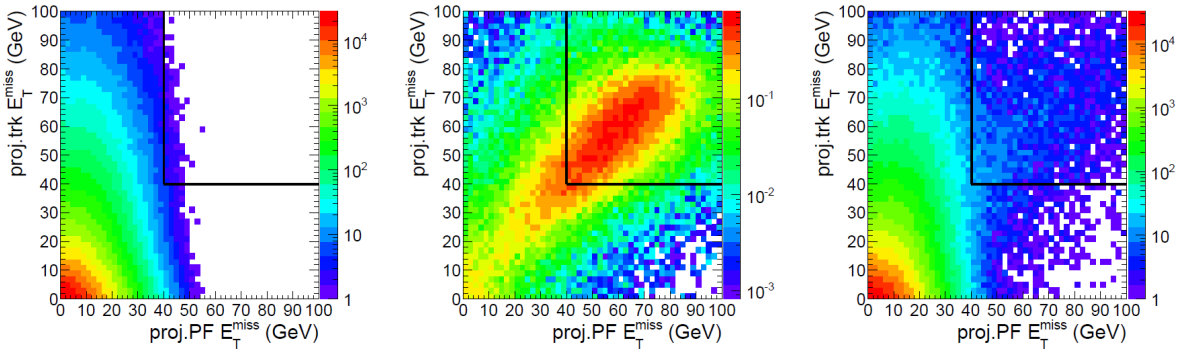

Figure 5.12.: Distributions of proj.PF$E_{\mathrm{T}}^{\mathrm{miss}}$ versus proj.trk$E_{\mathrm{T}}^{\mathrm{miss}}$ in (a) simulated Drell-Yan, (b) simulated signal ($m_{\mathrm{H}} = 160$ GeV), and (c) data. The figures were obtained by only applying the lepton selections.

data selected in the Z-peak with different-flavor $\mathrm{e}^{\pm}\mu^{\mp}$ subtracted ("DY data"). The comparison is performed after the following cuts have been applied:

- $m_{\ell\ell} > 20$ GeV
- no extra leptons
- anti b-tagging (see Section 5.4.8)
- PF$E_{\mathrm{T}}^{\mathrm{miss}} > 20$ GeV
- min-proj.$E_{\mathrm{T}}^{\mathrm{miss}} > 20$ GeV

The chosen working points (a star on the ROC curve[2] of the figure) to show the efficiency-dependence with the number of primary vertices are the following: PF$E_{\mathrm{T}}^{\mathrm{miss}} > 45$ GeV, min-proj.$E_{\mathrm{T}}^{\mathrm{miss}} > 45$ GeV and min-proj.$E_{\mathrm{T}}^{\mathrm{miss}} - \mathrm{N_{vtx}}/2 > 37$ GeV. First of all, it is clear from the ROC curve in subfigure 5.13(a) that the PF$E_{\mathrm{T}}^{\mathrm{miss}}$ is performing the worst in removing as much as possible DY while keeping the signal efficiency as high as possible. Next in subfigure (b) one can see that the PF$E_{\mathrm{T}}^{\mathrm{miss}}$ is less performant with the removal of DY data when the pile-up increases. The other two $E_{\mathrm{T}}^{\mathrm{miss}}$ variables are clearly able to deliver us a better signal efficiency at the cost of the same contamination.

[2]A Receiver Operating Characteristic (ROC) is a graphical plot which illustrates the performance of a binary classifier system as its discrimination threshold is varied. Each point on the ROC curve represents a pair corresponding to a particular decision threshold. The area under the ROC curve is a measure of how well a parameter can distinghuish between signal and background.

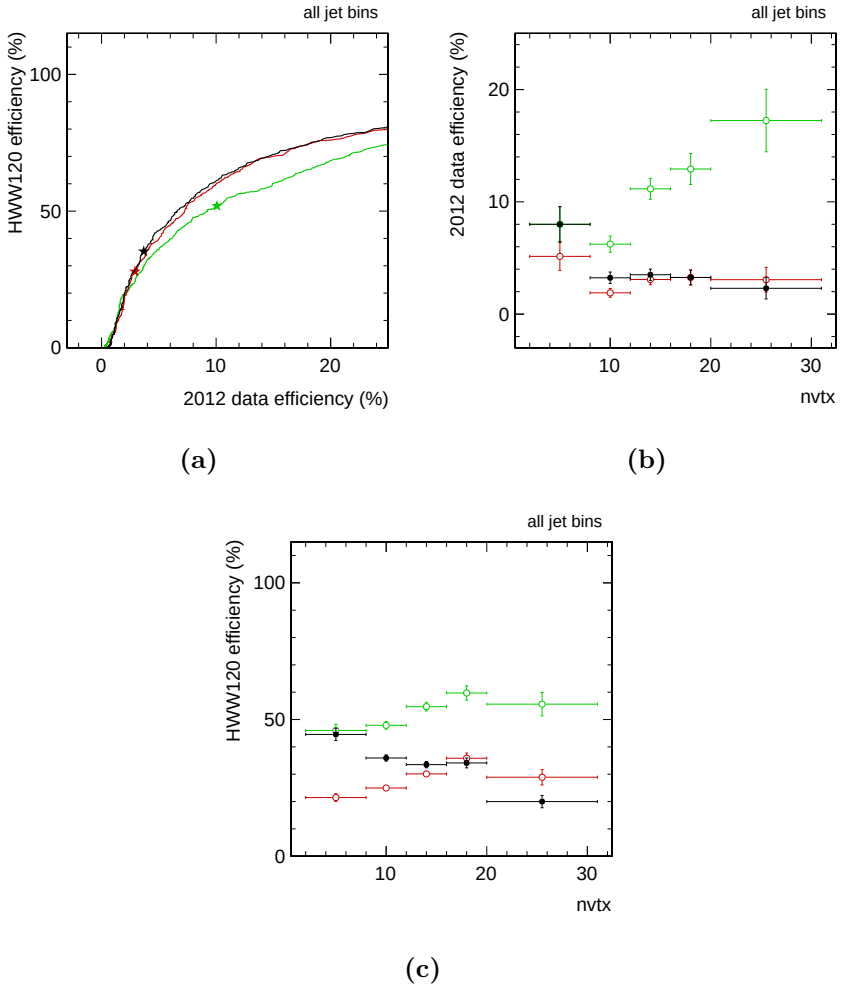

Figure 5.13.: Performance comparison for the PF$E_{\mathrm{T}}^{\mathrm{miss}}$ (green), min-proj.$E_{\mathrm{T}}^{\mathrm{miss}}$ (red) and min-proj.$E_{\mathrm{T}}^{\mathrm{miss}} - \mathrm{N}_{\mathrm{vtx}}/2$ (black): (a) ROC curves between 2012 data (in the Z-peak and with different flavor subtracted) versus a Higgs signal of 120 GeV, (b) the data efficiencies against the number of primary vertices for the working points given in the text (and starred in the ROC curve), and (c) the same efficiencies but for the Higgs signal.

DY MVA

To further deplete the Drell-Yan background in the $\mathrm{e}^+\mathrm{e}^-$ and $\mu^+\mu^-$ final states, with no deterioration of the signal yield, a multivariate technique has been derived. This multivariate technique, called *DY MVA*, exploits the difference between the Higgs signal and the Drell-Yan background better. A complete description can be found in [105]. The list of variables used in the training is the following:

- missing energy variables

  - proj.PF$E_{\mathrm{T}}^{\mathrm{miss}}$
  - proj.trk$E_{\mathrm{T}}^{\mathrm{miss}}$
  - PF$E_{\mathrm{T}}^{\mathrm{miss}}/\sum E_{\mathrm{T}}^{\mathrm{miss}}$
- kinematic variables:
  - dilepton p_{T}
  - *transverse mass* $m_{\mathrm{T}}^{\ell\ell-\mathrm{E}_{\mathrm{T}}^{\mathrm{miss}}}$ or short m_{T}, the invariant mass of the whole final state system in the transverse plane defined as:

$$m_{\mathrm{T}} = (p_{\mathrm{T}}^{\ell\ell} + E_{\mathrm{T}}^{\mathrm{miss}})^2 - (\vec{p_{\mathrm{T}}^{\ell\ell}} + \vec{E_{\mathrm{T}}^{\mathrm{miss}}})^2 \quad (5.6)$$

$$= \sqrt{2p_{\mathrm{T}}^{\ell\ell}E_{\mathrm{T}}^{\mathrm{miss}}\left(1-\cos\Delta\phi_{\ell\ell-E_{\mathrm{T}}^{\mathrm{miss}}}\right)} \quad (5.7)$$

  - leading jet p_{T}
  - recoil, which is the magnitude of the vector sum of PF$E_{\mathrm{T}}^{\mathrm{miss}}$ and the dilepton system in the transverse plane
- azimuthal angle differences (with j standing for jet):
  - angle between the dilepton system and the jet, $\Delta\phi(\ell\ell, j)$
  - angle between the dilepton system and the $E_{\mathrm{T}}^{\mathrm{miss}}$, $\Delta\phi(\ell\ell, E_{\mathrm{T}}^{\mathrm{miss}})$
  - angle between the jet and the $E_{\mathrm{T}}^{\mathrm{miss}}$, $\Delta\phi(j, E_{\mathrm{T}}^{\mathrm{miss}})$
- other variables:
  - number of primary vertices

For the same-flavor final states, we only retain events where the output of the MVA satisfies:

- 0-jet bin: $\mathrm{MVA}^{\mathrm{DY}} > 0.88$
- 1-jet bin: $\mathrm{MVA}^{\mathrm{DY}} > 0.84$

Figure 5.14 shows the DY MVA output for the Higgs signal of $m_{\mathrm{H}} = 125$ GeV and the DY MC at the lepton selection level. In this figure both MC samples are normalized to each other and it clearly shows the separation power of the MVA.

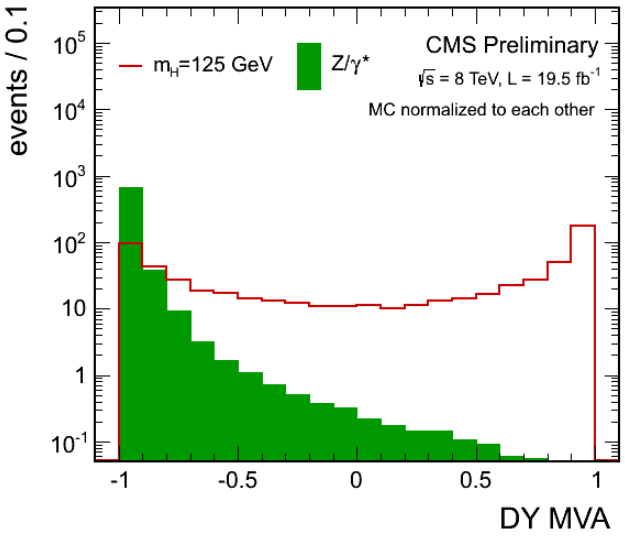

Figure 5.14.: Distributions of the DY MVA output for a Higgs signal of $m_{\mathrm{H}} = 125$ GeV and the DY MC at the lepton selection level for the same-flavor lepton channel. The MC samples are normalized to each other.

The DY MVA was only recently developed and is only used for the 2012 dataset. For the 2011 dataset we use the following two requirements on the same-flavor final states:

- a stronger requirement on the min-proj.$E_{\mathrm{T}}^{\mathrm{miss}}$: min-proj.$E_{\mathrm{T}}^{\mathrm{miss}} > (37 + \mathrm{N_{vtx}}/2)$ GeV, with $\mathrm{N_{vtx}}$ the number of vertices in the event.
- $\Delta\phi(\ell\ell, \mathrm{jet} < 165)$ degrees for jets with $p_{\mathrm{T}} > 15$ GeV, to reject events where the momenta of the dilepton system and the jet are back-to-back in the transverse plane

As a comparison, the use of the DY MVA increases the signal with ~ 60 % at the same level of DY contamination for the 2011 dataset after all the selections [105]. The combination of the Z veto and the just described selections, reduce the Drell-Yan background by three orders of magnitude, while rejecting less than 50 % of the signal.

5.4.7. Jet Counting

Jets are reconstructed using particle flow and the anti-k_{T} clustering algorithm with R = 0.5, as described in Section 4.4. As discussed in that section, all the jet corrections are applied, including the L1 Fast Jets corrections, and the jets must satisfy the jetID requirement to handle the high pile-up conditions. To exclude electrons and muons from

the sample, jets are required to be separated from each of the two selected leptons in ΔR by at least $\Delta R^{\text{jet-lepton}} > 0.3$.

This analysis uses high p_{T} jets to define the analysis jet bin categories (0-jet and 1-jet category) and low p_{T} jets to do the top events veto (see Section 5.4.8):

- *counted jet*: a reconstructed jet with $p_{\mathrm{T}} > 30$ GeV within $|\eta| < 4.7$
- *low-p_{T} jet*: a reconstructed jet with $10 < p_{\mathrm{T}} < 30$ GeV within $|\eta| < 4.7$

All the events will be split up in two categories, which will be analyzed separately, based on the number of counted jets in the event. In this analysis we only treat the 0-jet and 1-jet categories.

5.4.8. Top tagging

The top background poses a significant challenge since its production cross section is significantly higher than the W^+W^- cross section. To suppress the top-quark background, a *top tagging* technique based on soft-muon and b-jet tagging is applied, as already described in detail in Section 4.8.

The first method vetoes events containing soft muons which likely come from semileptonic b-decays coming from top-quark decays. The detailed requirements still have to be given:

- $p_{\mathrm{T}} > 3$ GeV
- reconstructed as a TrackerMuon
- meet the TrackerMuonLastStationTight muon identification requirement
- hit more than 5 tracker layers
- transverse impact parameter $|d_{xy}| < 0.2$ cm, calculated with respect to the primary vertex
- longitudinal impact parameter $|d_z| < 0.2$ cm, calculated with respect to the primary vertex
- non-isolated ($\mathrm{Iso}_{\mathrm{Total}}/p_{\mathrm{T}} > 0.1$) if $p_{\mathrm{T}} > 20$ GeV

The second method uses the track counting high efficiency (TCHE) b-tagging method which looks for tracks with a large impact parameter within jets. All the events that contain low-p_{T} jets, as defined in Section 5.4.7, are vetoed when they have a TCHE discriminator value greater than 2.1. The condition is also applied in the case of the zero-counted-jet category, as it can still contain some low-p_{T} tagged jets.

To summarize, in the zero-jet bin we require that no low-p_{T} jets are b-tagged and that no soft muons are found. In the 1-jet bin we require that the hard jet, the counted jet, is not b-tagged (also called *anti b-tagged*) and we again require no extra soft muons in the event.

Vetoing on b-tagged jets combined with the soft muon veto retains about 95 % of the light-quark jets, while rejecting about 67 % of the b-jets. The performance of b-jet identification for light-quark jets is verified in $\mathrm{Z}/\gamma^{(*)} \to \ell\ell$ candidate events, and is found to be consistent between data and simulation within 1 %. By using the expected tagging efficiency for the two methods, it is possible to estimate the residual top background after the vetoes have been applied. This is described in detail in Section 6.1.3.

5.4.9. Minimum dilepton transverse momentum

In order to reduce the W + jets background, a minimal dilepton transverse momentum cut of ${p_{\mathrm{T}}}^{\ell\ell} > 30$ (45) GeV is required for the following shape-based and (cut-based) mass-dependent analysis, that will be described in the Higgs signal extraction strategy chapter 7.

5.4.10. Summary of the common $\mathrm{W^+W^-}$ selection

The previously described set of selections, is defined as the W^+W^- *selection level*. At this selection level, the remaining data sample is dominated by non-resonant $\mathrm{W^+W^-}$ events. The main signal efficiency loss is due to the lepton selection and the stringent $E_{\mathrm{T}}^{\mathrm{miss}}$ requirements. At this point in the analysis, a sanity check of the main variables distribution is performed. Next to that, the $\mathrm{W^+W^-}$ selection level combined with the 0-jet analysis category are used to measure the $\mathrm{W^+W^-}$ cross section in CMS [106, 107]. The next step in the analysis is to apply Higgs mass dependent selections to extract the Higgs signal. However, in order to see the excess of Higgs signal events, a precise knowledge of the background contamination is needed. For this reason, the next chapter

will cover the description of the data-driven background determination procedure together with the sanity check at the W^+W^- selection level, whereafter the Higgs signal extraction selection will be covered.

The whole W^+W^- selection level can be summarized for both the $\sqrt{s} = 7$ TeV and $\sqrt{s} = 8$ TeV analysis as followings:

1. Lepton preselection:
   - at least two opposite-sign leptons are reconstructed in the event passing all identification and isolation requirements
   - $|\eta| < 2.5$ for electrons and $|\eta| < 2.4$ for muons
   - $p_T > 20$ GeV for the leading lepton. For the trailing lepton, the transverse momentum is required to be larger than 15 GeV for e^+e^- and $\mu^+\mu^-$ at $\sqrt{s} = 7$ TeV, and larger than 10 GeV otherwise.
2. Extra lepton veto: the event is required to have two and only two opposite-sign leptons passing the lepton selection.
3. E_T^{miss} preselection: PF$E_T^{miss} > 20$ GeV
4. Low mass resonances rejection: $m_{\ell\ell} > 12$ GeV and $m_{\ell\ell} > 20$ GeV for e^+e^- and $\mu^+\mu^-$ at $\sqrt{s} = 7$ TeV
5. Z-peak veto: $|m_{\ell\ell} - m_Z| > 15$ GeV for e^+e^- and $\mu^+\mu^-$ events
6. Soft projected E_T^{miss} selection: $\min(\text{proj.}E_T^{miss}) > 20$ GeV. For the $\sqrt{s} = 7$ TeV analysis, it is required to be larger than $(37 + N_{vtx}/2)$ GeV for e^+e^- and $\mu^+\mu^-$ events, with N_{vtx} the number of vertices in the event
7. Soft muon veto: the event is required to not have soft muons likely to come from b-jets
8. Anti b-tagging: the event is required not to have any jets passing the b-tagging selection
9. Kinematical cut: the event is required to have $p_T^{\ell\ell} > 30$ (45) GeV for the shape (cut-based) signal extraction analysis
10. Azimuthal separation between dilepton and jet at $\sqrt{s} = 7$ TeV: $\Delta\phi(\ell\ell, \text{jet} < 165)$ degrees for jets with $p_T > 15$ GeV

11. Hard $E_{\mathrm{T}}^{\mathrm{miss}}$ selection at $\sqrt{s} = 8$ TeV: a multivariate shape-base approach to reject the remaining Z events is applied for $\mathrm{e}^{+}\mathrm{e}^{-}$ and $\mu^{+}\mu^{-}$ events:

    - 0-jet category: $\mathrm{MVA}^{\mathrm{DY}} > 0.88$
    - 1-jet category: $\mathrm{MVA}^{\mathrm{DY}} > 0.84$

Chapter 6.

Background estimation and data to MC comparison

This chapter covers the methods used to estimate each background, whereafter the data can be compared to the MC at the W^+W^- selection level as an important cross-check to make sure that all the objects and backgrounds used in the analysis are well-understood.

6.1. Background estimation

A combination of data-driven methods and detailed Monte Carlo simulation studies are used to estimate the background contributions in the signal region. The following backgrounds are estimated with real collision data: $W + \text{jets}$ and $Z/\gamma^{(*)} \to \tau^+\tau^-$. Both the shape of the kinematic distributions and the normalization of the background are taken from data. The top, W^+W^-, $Z/\gamma^{(*)} \to \ell^+\ell^-$ ($\ell = e, \mu$) and $W\gamma^{(*)}$ background processes are evaluated with a combination of simulated and data control samples. In these cases only the background normalization is obtained from data. The remaining backgrounds are taken from simulation.

It is important to note that the background composition and yields depend on the final state and on the Higgs boson mass hypothesis under study. In the 0-jet final state, the non-resonant W^+W^- background dominates, while the $W + \text{jets}$ background contribution becomes sizable in the low Higgs mass hypotheses. In the 1-jet final state, the largest background contribution comes from top decays, while the non-resonant W^+W^- background contribution is the second largest. For this reason, the data-driven estimates are performed separately in each jet category. Furthermore, the data-driven

estimates need to be recalculated for each combination of selections where we want to use them (W^+W^- selection level, each mass-dependent cut-based Higgs selection level and each shape-based Higgs selection level).

The choice to use data-driven estimates instead of using the Monte Carlo simulation is motivated by several reasons. When applying the full Higgs selection and using simulation, it is required to know the efficiency of every selection requirement from simulation, such as the top-tagging efficiency and the $E_{\mathrm{T}}^{\mathrm{miss}}$ resolution. Problems already arise for example for the b-tagging efficiency, where the details of b-jet fragmentation cannot be reliably simulated at low energy. Another example is the $E_{\mathrm{T}}^{\mathrm{miss}}$ distribution with the presence of pile-up interactions. Moreover the systematic uncertainty on some of the efficiencies simply cannot be estimated by simulation. For these reasons, we make use of data-driven methods.

The data-driven background estimations can be grouped in three main approaches: *AB*, *ABCD* and fake-rate methods. The *AB* method defines two regions:

- *A*: the signal region, defined by the nominal selections applied in the analysis;
- *B*: a background dominated region (that is signal free), where the most important selections used to remove the specific background are reversed.

By measuring the number of background events in region B, N^B, in data and extracting the ratio for a given background between the contamination in region A and B, $R^{A/B} = N^A/N^B$, from MC, one can derive the number of background events in region A, N^A, as:

$$N^A = R^{A/B}_{\mathrm{MC}} N^B_{\mathrm{data}} = \frac{N^A_{\mathrm{MC}}}{N^B_{\mathrm{MC}}} N^B_{\mathrm{data}} \tag{6.1}$$

The main hypothesis of this method is that the ratio $R^{A/B}$ is well modeled in the MC. Additionally the region N^B_{data} must be dominated by the selected background under investigation.

The second method, *ABCD*, removes the Monte Carlo dependence that is still present in the *AB* method. Therefore the method makes use of four regions:

- *A*: the signal region defined by the nominal selections applied;
- *B*: a background dominated region (that is signal free), where the most important selections used to remove the specific background are reverted;

- C: a background dominated region (that is signal free), with the same selections of region A except for one cut;
- D: a background dominated region (that is signal free), with the same selections of region B except for one cut, the same one as for region C.

Under the hypothesis of the independence between the selection that defines the regions AB with respect to CD, which has to be tested on a MC sample, the number of background events in region A can be estimated as:

$$N^A = \frac{N^C_{\text{data}}}{N^D_{\text{data}}} N^B_{\text{data}} \tag{6.2}$$

The hypothesis of this method is that the ratio N^C/N^D is the same as N^A/N^B. The main issue is the estimation of the degree of belief of this assumption and the measurement of the systematics related to it. In addition, the region B, C and D must be dominated by the selected background under investigation. Other background components have to be subtracted and the error due to their subtraction has to be propagated to the final estimation of N^A.

The third method, the fake-rate method, is a data-driven procedure for the modeling of backgrounds arising from particle misidentification. The rate at which these misidentifications happen cannot be properly simulated by Monte Carlo. As an example, a jet could be misidentified as a lepton. In this case, one typically defines a set of loosely selected lepton-like objects, referred to as the *fakeable objects* or *denominator objects*. The efficiency for these denominator objects to pass the full lepton selection criteria is measured and is referred to as the *fake rate*:

$$\text{fake rate} = \frac{\#\text{of fully reconstructed leptons}}{\#\text{of fakeable objects}} \tag{6.3}$$

The fake rate is typically parameterized as a function of the p_{T} and η of the denominator objects in order to capture any dependence on geometric and kinematic quantities. These fake rates are then used as weights to extrapolate the background yield from a sample of denominator objects to the sample of leptons satisfying the full selection.

In the following, the background estimations for all backgrounds will be described. The methods used for the data-driven estimations are:

- jet-induced backgrounds: W + jets and QCD: fake-rate method

- $Z/\gamma^{(*)} \to \ell^+\ell^-$: AB method with a cross check with the $ABCD$ method
- $Z/\gamma^{(*)} \to \tau^+\tau^-$: embeded method explained in Section 6.1.5
- top background: $ABCD$ method
- W^+W^- background: AB method

6.1.1. Jet-induced backgrounds: W + jets and QCD

As discussed before, the non-prompt lepton background originates from leptonic decays of heavy quarks (hadrons) misidentified as leptons and also from photon conversions in W + jets and QCD multi-jet production. This background is suppressed by the identification and isolation requirements on electrons and muons (as described in Section 5.4.3). The remaining contribution from the non-prompt lepton background is estimated directly from data. Since the background was not specifically addressed in this thesis, a short summary of the method will be given with a reference to our latest $H \to W^+ W^-$ paper [89]. A more detailed version of the procedure can be found in Reference [108].

A control sample is defined by one lepton that passes the standard lepton selection criteria and another lepton candidate that fails the criteria, but passes a looser selection, resulting in a sample of *pass-fail* lepton pairs. The efficiency, ϵ_{pass}, for a jet that satisfies the loose lepton requirements to pass the standard selection is determined using an independent sample, dominated by events with non-prompt leptons from QCD multijet processes. This efficiency, parameterized as a function of p_{T} and η of the lepton, is then used to weigh the events in the pass-fail sample by $\epsilon_{\text{pass}}/(1-\epsilon_{\text{pass}})$, to obtain the estimated contribution from the non-prompt lepton background in the signal region.

The systematic uncertainties from the determination of ϵ_{pass} dominate the overall uncertainty of this method. The systematic uncertainty has two sources: the dependence of ϵ_{pass} on the sample composition, and the method. The first source is due to the difference in the p_{T} spectrum of the jets in the measurement sample, dominated by QCD multijet events, compared to the p_{T} spectrum in the pass-fail sample, dominated by W + jets events. Since the efficiency ϵ_{pass} is measured in bins of p_{T}, an object with a fixed p_{T} will be weighted with a different efficiency if the jet producing this object has a larger or smaller p_{T}. The uncertainty is estimated by modifying the jet p_{T} threshold in the QCD multijet sample, which modifies the jet sample composition and has an uncertainty of about 30 %. The uncertainty on the method is obtained from a closure

test, where ϵ_{pass} is derived from simulated QCD multijet events and applied to simulated samples to predict the number of background events, leading to an absolute uncertainty of about 21 %. The total uncertainty in ϵ_{pass}, including the statistical precision of the control sample, is of the order of 36 %.

Lastly a further closure test on the fake lepton background estimate is performed using data events with two same-charge leptons. This control sample is highly enriched in the W + jets background and can serve as an additional cross-check of the systematic uncertainties estimated above from Monte Carlo simulation. The comparison of various distributions at the $\mathrm{W^+W^-}$ selection level (with $p_{\mathrm{T}}^{\ell\ell} > 45$ GeV) in the 0- and 1-jet categories for same-charge leptons, reweighted to the data-driven estimates, are shown in Figure 6.1 and 6.2. In these plots, all statistic and normalization systematic errors on the backgrounds are applied, including the systematic uncertainty due to the luminosity (see Section 7.3). A good data-MC agreement is found, which demonstrates that the extrapolation systematics estimated from the Monte Carlo simulation is applicable to data.

6.1.2. Drell-Yan background: $\mathrm{Z}/\gamma^{(*)} \to \ell^+\ell^-$

As stated before in the $E_{\mathrm{T}}^{\mathrm{miss}}$ selection section, Section 5.4.6, it is very complicated to simulate mis-measured $E_{\mathrm{T}}^{\mathrm{miss}}$ at high pile-up. Figure 6.3 shows the min-proj.$E_{\mathrm{T}}^{\mathrm{miss}}$ and the DY MVA output variable at the lepton selection level with the extra-lepton veto applied for the same-flavor final states. A discrepancy between the data and the simulation is observed. This stresses the importance of the determination of the DY background with a data-driven technique in order to reduce the dependency on the simulation.

The contribution of the Drell-Yan background $\mathrm{Z}/\gamma^{(*)} \to \{\mathrm{ee}, \mu\mu\}$ to the same-flavor $\ell^+\ell^-$ final states is estimated with a method based on measurements in data. The expected contributions from $\mathrm{Z}/\gamma^{(*)} \to \ell\ell$ events outside the Z mass region in data (*out* region) can be estimated by counting the number of events in the Z mass region in data (*in* region), subtracting from it the non-Z contributions, and scaling it by a ratio $R_{\text{out/in}}$ defined as the fraction of events outside and inside the Z mass region in the simulation. The Z mass region is defined as $|m_{\ell\ell} - \mathrm{m_Z}| < 7.5$ GeV. Such a tight window is chosen to reduce the non-Z background contributions inside the Z mass region. These contributions can be split in two categories:

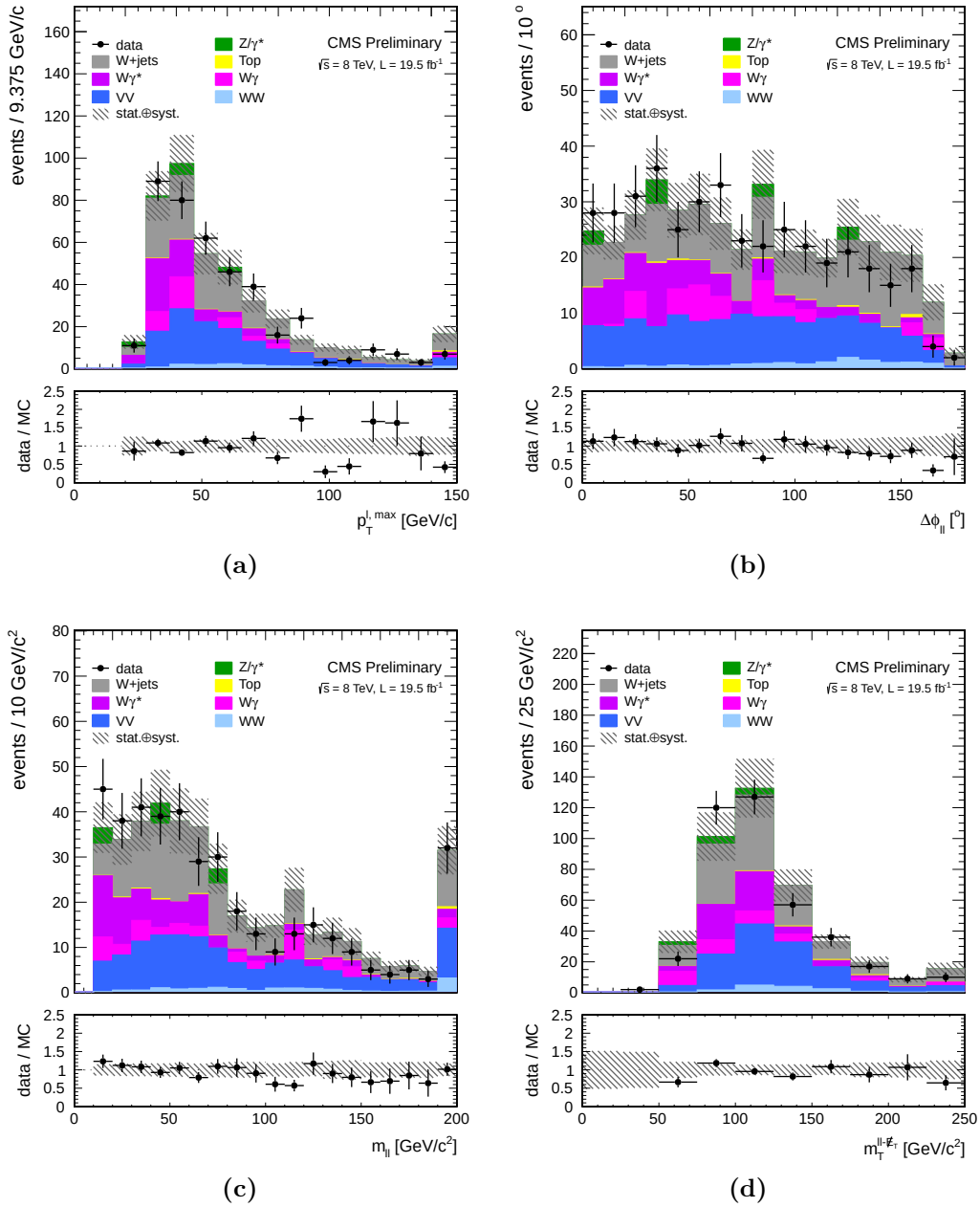

Figure 6.1.: Distributions at the W^+W^- selection level with $p_T^{\ell\ell} > 45$ GeV for same-charge dilepton events in the **0-jet** category for data (points with error bars) and for the main backgrounds (stacked histograms) at $\sqrt{s} = 8$ TeV: (a) leading lepton p_T (b) dilepton $\Delta\phi$, (c) dilepton invariant mass $m_{\ell\ell}$ and (d) transverse mass m_T of the dilepton-E_T^{miss} system. The WZ, ZZ, VVV and Zγ backgrounds are grouped together and labeled as VV. The last bin contains the overflow.

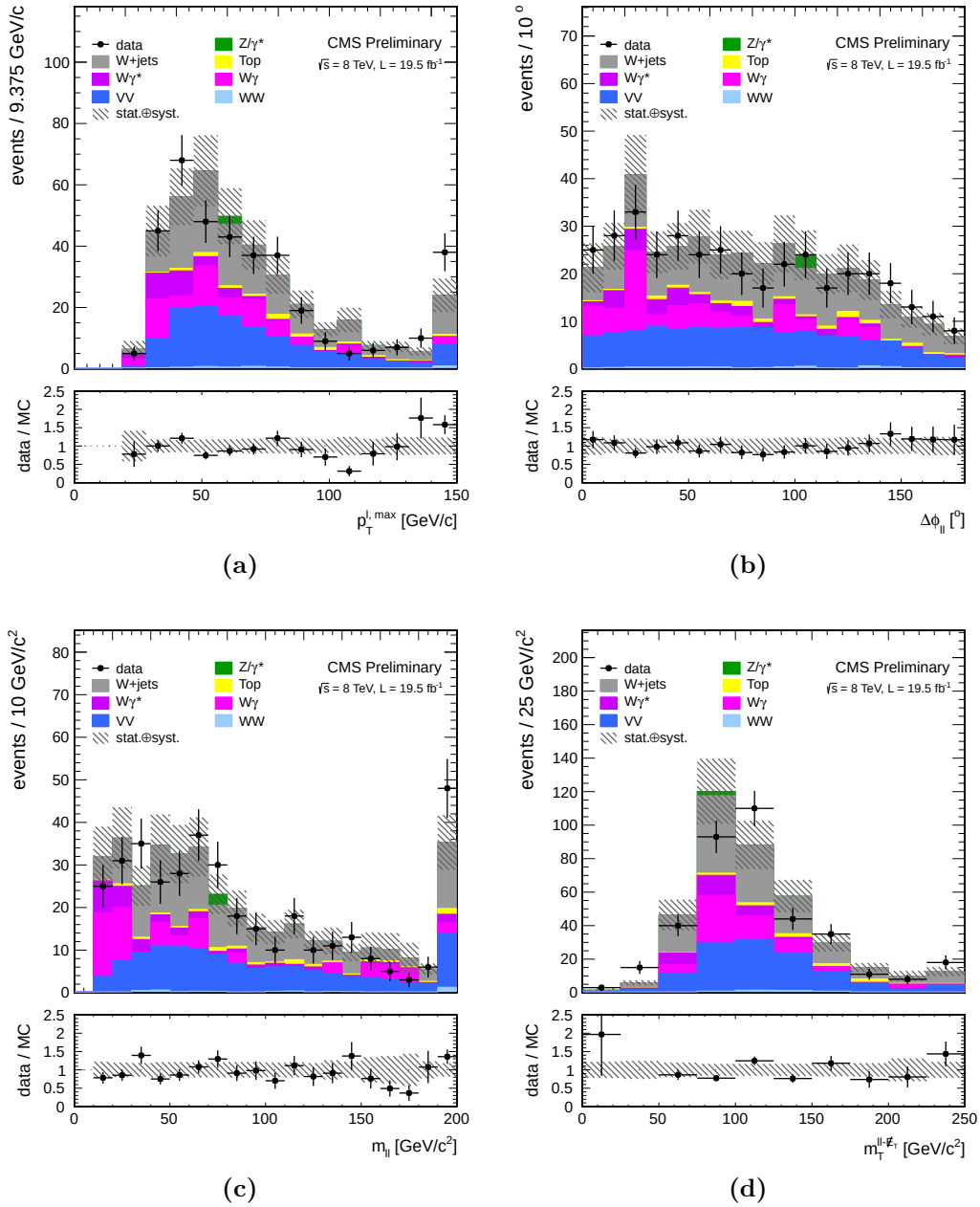

Figure 6.2.: Distributions at the W^+W^- selection level with $p_T^{\ell\ell} > 45$ GeV for same-charge dilepton events in the **1-jet** category for data (points with error bars) and for the main backgrounds (stacked histograms) at $\sqrt{s} = 8$ TeV: (a) leading lepton p_T (b) dilepton $\Delta\phi$, (c) dilepton invariant mass $m_{\ell\ell}$ and (d) transverse mass m_T of the dilepton-E_T^{miss} system. The WZ, ZZ, VVV and Zγ backgrounds are grouped together and labeled as VV. The last bin contains the overflow.

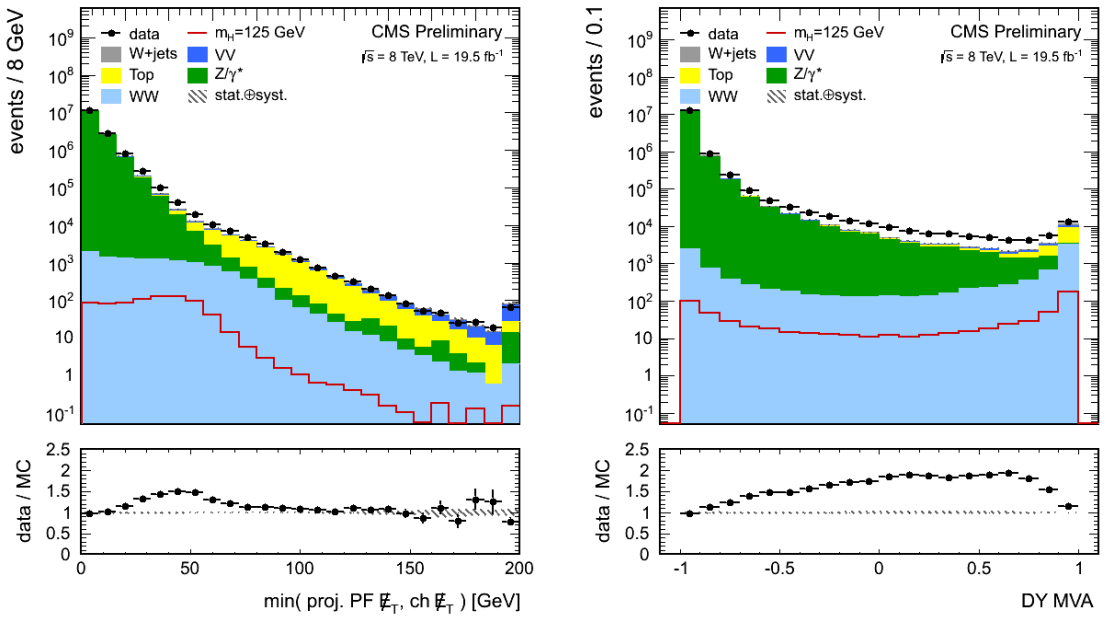

(a) (b)

Figure 6.3.: Distributions of (a) the min.proj$E_{\mathrm{T}}^{\mathrm{miss}}$ and (b) the DY MVA output at the lepton selection level with the extra-lepton veto applied for the same-flavor channel ($\mathrm{e^+e^-}$ and $\mu^+\mu^-$), for data (points with error bars), for the main backgrounds (stacked histograms) and for a Higgs boson signal with $m_{\mathrm{H}} = 125$ GeV (superimposed) at $\sqrt{s} = 8$ TeV.

- The backgrounds such as top, $\mathrm{W^+W^-}$ and $\mathrm{W}+\mathrm{jets}$ that equally decay into the four flavor final states (ee, eμ, μe and $\mu\mu$). Their contribution to the Z mass region in data can be estimated from the number of events in the $\mathrm{e^{\pm}\mu^{\mp}}$ final state ($N_{\mathrm{e}\mu}^{\mathrm{in}}$), applying a correction factor that accounts for the differences in the detection efficiency between electrons and muons (k_{ee} and $k_{\mu\mu}$):

$$N_{\ell\ell}^{\mathrm{background}} = \frac{1}{2} k_{\ell\ell} N_{\mathrm{e}\mu} \tag{6.4}$$

where $\ell\ell$ stands for ee or $\mu\mu$ with $k_{\mathrm{ee}} = \sqrt{\frac{N_{\mathrm{in}}^{\mathrm{ee},loose}}{N_{\mathrm{in}}^{\mu\mu,loose}}}$ for $\mathrm{Z}/\gamma^{(*)} \to \mathrm{ee}$ and $k_{\mu\mu} = \sqrt{\frac{N_{\mathrm{in}}^{\mu\mu,loose}}{N_{\mathrm{in}}^{\mathrm{ee},loose}}}$ for $\mathrm{Z}/\gamma^{(*)} \to \mu\mu$. The factor $\frac{1}{2}$ comes from the relative branching fraction between the $\ell\ell$ and eμ final states.[1] In the $k_{\ell\ell}$ calculation, the selection on the $E_{\mathrm{T}}^{\mathrm{miss}}$ is loosened to increase the available number of events under the Z peak. The

[1] This approach is allowed since $N_{\mathrm{ee}/\mu\mu} >> N_{\mathrm{e}\mu}$ in the in-peak region around the Z mass.

value of k_{ee} ($k_{\mu\mu}$) is about 0.8 (1.2), with a very loose dependence both on the center-of-mass energy and jet category.

- The backgrounds such as the diboson background WZ and ZZ (together denoted as VV), that decay mostly into a same-flavor final state via a Z boson resonance. As these backgrounds are characterized by the presence of real $E_{\mathrm{T}}^{\mathrm{miss}}$ for which the detector simulation is reliable, we take their contamination from simulation.

Figure 6.4 shows the dilepton invariant mass at the $\mathrm{W^+W^-}$ selection level without the Z veto applied for the same-flavor events in the 0-jet category at $\sqrt{s} = 8$ TeV. The Z peak is clearly visible, acknowledging the choice of the tight $|m_{\ell\ell} - \mathrm{m_Z}| < 7.5$ GeV control region. The contribution of the ZW and ZZ backgrounds are also clearly visible.

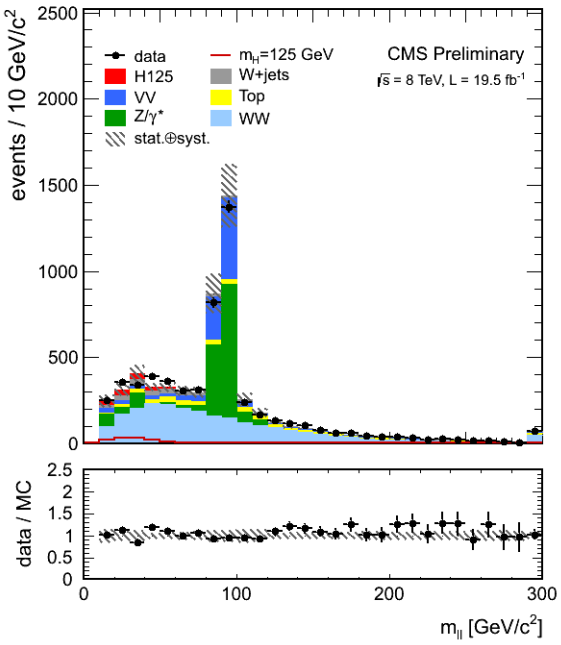

Figure 6.4.: The invariant dilepton mass $m_{\ell\ell}$ at $\mathrm{W^+W^-}$ selection level without the Z veto cut applied for the 0-jet category, for data (points with error bars), for the main backgrounds (stacked histograms) and for a Higgs boson signal with $m_{\mathrm{H}} = 125$ GeV (superimposed and stacked histogram) at $\sqrt{s} = 8$ TeV. A clear peak of Z events accompanied with VV events is visible around the Z mass..

Using all the above mentioned information, the number of Drell-Yan events in the signal region can be derived as:

$$N^{\text{out}}_{\text{Z}\to\text{ee}} = R_{\text{out/in}}\left(N^{\text{in}}_{\text{ee}} - \frac{1}{2}k_{\text{ee}}N^{\text{in}}_{\text{e}\mu} - N^{\text{in}}_{\text{ee}}(VV)\right) \quad (6.5)$$

$$N^{\text{out}}_{\text{Z}\to\mu\mu} = R_{\text{out/in}}\left(N^{\text{in}}_{\mu\mu} - \frac{1}{2}k_{\mu\mu}N^{\text{in}}_{\text{e}\mu} - N^{\text{in}}_{\mu\mu}(VV)\right) \quad (6.6)$$

with $R_{\text{out/in}} = N^{\text{MC}}_{\text{out}}/N^{\text{MC}}_{\text{in}}$ estimated with simulation. As no statistically significant difference is observed between the ee and $\mu\mu$ final states, both estimations are combined in one estimation.

The value of $R_{\text{out/in}}$ is estimated applying a relaxed selection with respect to the nominal one. This is done to increase statistics and is justified by a relative constant behavior of $R_{\text{out/in}}$ when relaxing the $E^{\text{miss}}_{\text{T}}$ selection as will be shown later in this section. Three relaxed selections, listed in Table 6.1, are used. The nominal value of $R_{\text{out/in}}$ is estimated using the values in the bin 2 column. When a lack of statistics is detected, the estimate is done with the relaxed selection of the bin 1 column. A systematic is associated to the $R_{\text{out/in}}$ estimate corresponding to the difference between the value obtained with the used selection and the bin $N-1$ column. This leads to a systematic uncertainty of about 40 % on the estimation of the DY yield. Lastly it should be noted that for the cut-based Higgs signal extraction selection, the m_{T} cut (see Section 7.2.1) is not applied to gain statistics.

Table 6.1.: Top: bins in min-proj.$E^{\text{miss}}_{\text{T}}$ used for the $R_{\text{out/in}}$ estimate in the $\sqrt{s} = 7$ TeV analysis. Bottom: bins in MVA^{DY} used for the $R_{\text{out/in}}$ estimate in the $\sqrt{s} = 8$ TeV analysis. The first three bin columns represent ranges for the control region. See the text for more explanation. The nominal analysis cuts are of course the ones in the signal region column.

jet bin	bin 0	bin 1	bin 2	signal region
7 TeV: min-proj.$E^{\text{miss}}_{\text{T}}$	–	–	$[30, (37 + N_{vtx}/2)]$	$> (37 + N_{vtx}/2)$
8 TeV, 0 (1)-jet: MVA^{DY}	$[-0.9, -0.85]$	$[-0.86, -0.6]$	$[-0.6, 0.88\ (0.84)]$	$> 0.88\ (0.84)$

The $R_{\text{out/in}}$ value is also cross-checked in data. Here we subtract the number of expected VV events in simulation and the number of different-flavor events in the same region in data (the remaining backgrounds are symmetric in opposite and same-flavor final states). A good statistical agreement is found. As an example, the $R_{\text{out/in}}$ values as a function of the DY MVA output variable in the 0-jet and 1-jet categories for the $m_{\text{H}} = 125$ GeV cut-based analysis at $\sqrt{s} = 8$ TeV are shown in Figure 6.5. The Drell-Yan

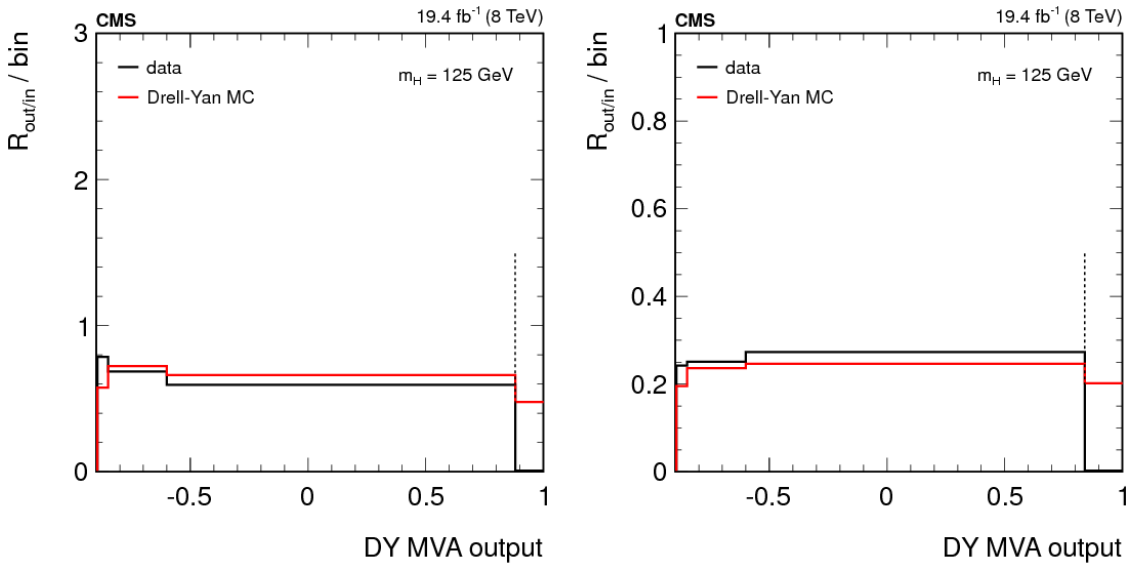

Figure 6.5.: The $R_{\text{out/in}}$ values as a function of the multivariate Drell-Yan output variable in (a) the 0-jet and (b) the 1-jet categories for the $m_{\text{H}} = 125$ GeV counting analysis at $\sqrt{s} = 8$ TeV. High output values are signal-like events, while low output values are more likely to be Drell-Yan events. The vertical dashed line indicates the minimum threshold on the discriminant value used to select events for the analysis, which is 0.88 (0.84) for the 0-jet (1-jet) category. The dependence of the $R_{\text{out/in}}$ ratio on the Drell-Yan discriminant value and the agreement between the data and the simulation are studied in the regions below this threshold.

estimation method relies on the assumption that the dependence of the ratio $R_{\text{out/in}}$ on the $E_{\text{T}}^{\text{miss}}$ requirement is relatively flat, what can be seen in the figure.

The estimated DY contributions at the W^+W^- selection level with $p_{\text{T}}^{\ell\ell} > 45$ GeV, together with the quantities involved in the measurement, are listed in Table 6.2 and 6.3. In Table 6.4 and 6.5 we summarize the $R_{\text{out/in}}^{\text{MC}}$ estimations for a few Higgs masses, together with the yields estimated on data in the case of the cut-based selection that will be described in Section 7.2.1.

Table 6.2.: Estimation of the Drell-Yan background at the W^+W^- selection level with $p_{\text{T}}^{\ell\ell} > 45$ GeV at $\sqrt{s} = 7$ TeV.

jet bin	$R_{\text{out/in}}^{\text{MC}}$	$N_{\ell\ell}^{\text{control,data}}$	$N_{DY}^{\text{signal,data}}$	$N_{DY}^{\text{signal,MC}}$
0	0.13 ± 0.04 ± 0.08	271	9.4 ± 5.9	3.7 ± 1.0
1	0.17 ± 0.02 ± 0.08	337	42.8 ± 8.1	16.0 ± 2.0

Table 6.3.: Estimation of the Drell-Yan background at the W^+W^- selection level with $p_T^{\ell\ell} > 45$ GeV at $\sqrt{s} = 8$ TeV.

jet bin	$R_{\text{out/in}}^{\text{MC}}$	$N_{\ell\ell}^{\text{control,data}}$	$N_{DY}^{\text{signal,data}}$	$N_{DY}^{\text{signal,MC}}$
0	0.28 ± 0.01 ± 0.08	1696	223.6 ± 32.8	32.7 ± 8.7
1	0.24 ± 0.01 ± 0.08	740	84.4 ± 7.4	22.8 ± 7.1

Table 6.4.: Estimation of the Drell-Yan background at the Higgs selection level, for various Higgs masses at $\sqrt{s} = 7$ TeV. The first uncertainty on $R_{\text{out/in}}^{\text{MC}}$ represents the statistical uncertainty in the simulation. The second value is the systematic uncertainty due to the MET dependency.

0-jet bin				
m_H [GeV]	n_{in}^{data}	R_{MC}	n_{DY}^{data}	n_{DY}^{MC}
110	50	0.05 ± 0.03 ± 0.10	1.75 ± 3.64	0.58 ± 0.42
125	42	0.15 ± 0.08 ± 0.19	3.09 ± 3.79	1.21 ± 0.61
160	10	0.86 ± 0.28 ± 0.06	2.74 ± 1.70	0.62 ± 0.45
200	46	0.12 ± 0.09 ± 0.07	1.05 ± 1.11	0.38 ± 0.38
300	50	0.17 ± 0.11 ± 0.12	-0.22 ± 0.84	0.46 ± 0.32
1-jet bin				
m_H [GeV]	n_{in}^{data}	R_{MC}	n_{DY}^{data}	n_{DY}^{MC}
110	55	0.06 ± 0.01 ± 0.02	3.10 ± 1.06	1.30 ± 0.58
125	59	0.08 ± 0.02 ± 0.04	4.43 ± 2.47	2.64 ± 0.80
160	30	0.24 ± 0.03 ± 0.06	5.89 ± 1.77	1.37 ± 0.56
200	114	0.15 ± 0.03 ± 0.03	13.54 ± 3.96	2.14 ± 0.77
300	107	0.12 ± 0.03 ± 0.04	9.73 ± 4.03	2.28 ± 0.66

Table 6.5.: Estimation of the Drell-Yan background at the Higgs selection level, for various Higgs masses at $\sqrt{s} = 8$ TeV. The first uncertainty on $R^{\mathrm{MC}}_{\mathrm{out/in}}$ represents the statistical uncertainty in the simulation. The second value is the systematic uncertainty due to the DY MVA dependency.

0-jet bin				
m_H [GeV]	n^{data}_{in}	R_{MC}	n^{data}_{DY}	n^{MC}_{DY}
110	198	0.32 ± 0.02 ± 0.09	47.01 ± 14.38	9.06 ± 5.23
125	223	0.65 ± 0.04 ± 0.09	103.64 ± 18.29	16.54 ± 6.26
160	54	0.74 ± 0.11 ± 0.29	15.18 ± 4.05	4.73 ± 3.38
200	281	0.21 ± 0.02 ± 0.01	20.82 ± 4.30	2.78 ± 2.28
300	347	0.08 ± 0.01 ± 0.03	8.01 ± 5.45	7.05 ± 4.06
1-jet bin				
m_H [GeV]	n^{data}_{in}	R_{MC}	n^{data}_{DY}	n^{MC}_{DY}
110	55	0.17 ± 0.01 ± 0.01	4.45 ± 0.63	2.22 ± 2.20
125	87	0.25 ± 0.01 ± 0.01	12.93 ± 1.26	4.54 ± 3.21
160	37	0.38 ± 0.03 ± 0.06	7.35 ± 1.45	2.33 ± 2.33
200	202	0.16 ± 0.01 ± 0.02	17.31 ± 2.24	0 ± 0
300	206	0.10 ± 0.01 ± 0.01	7.98 ± 1.38	5.20 ± 3.68

6.1.3. Top background

The contribution of the top background is suppressed in the analysis through the use of the top-tagging veto, which combines a b-tagging discriminator with the requirement that no soft muons are present in the final state (see Section 5.4.8). If the top-tagging efficiency is known, it is possible to extrapolate the top contamination from a control region, defined as the inversion of one of the top rejection cuts. Since top tagging and top vetoing are the inverse of each other, this translates in the following formula:

$$N_{\text{top-veto}}^{\text{sig reg}} = \frac{1 - \epsilon_{\text{top-tag}}}{\epsilon_{\text{top-tag}}} \cdot N_{\text{top-tag}}^{\text{ctrl reg}} \tag{6.7}$$

where $N_{\text{top-veto}}^{\text{sig reg}}$ is the number of top events that pass the top-tagging veto, $N_{\text{top-tag}}^{\text{ctrl reg}}$ is the number of top events that are in the inverted control region (so they are top tagged) and $\epsilon_{\text{top-tag}}$ is the top-tagging efficiency as measured in another control region in data dominated by top events. Both in the evaluation of $N_{\text{top-tag}}^{\text{ctrl reg}}$ and $\epsilon_{\text{top-tag}}$, the non-top backgrounds are properly subtracted using data-driven or MC estimates depending on the process. The systematic uncertainty on the top background estimation is due to the uncertainty in non-top backgrounds and due to the statistical error in the efficiency measurement. The associated systematic uncertainties are below 5 %, but due to the still dominating statistical error of the top estimation, the overal uncertainty is of the order of 20 %. The actual implementation of the estimation method depends on the jet category and is detailed below.

The top background is estimated at the $\mathrm{W^+W^-}$ selection level where a common scale factor for the Monte Carlo $\mathrm{t\bar{t}}$ and tW is computed. Once properly normalized, those samples can be used through the rest of the signal extraction analysis i.e. assuming that the MC is predicting the kinematics correctly. The latter will be validated with control figures later in this section.

0-jet category

Most of the top background, composed of $\mathrm{t\bar{t}}$ and tW processes, is rejected in the 0-jet category by the jet veto requirement. The $\mathrm{t\bar{t}}$ events are characterized by two b-jets below 30 GeV, while the tW events have one single low-p_{T} b-jet, except for a fraction x containing two jets from b-quarks and effectively indistinguishable from $\mathrm{t\bar{t}}$. The procedure described in the following steps accounts for this feature properly:

- First, the top-tagging efficiency for one *top-taggable* leg ($\epsilon_{1leg}^{\text{data}}$), a jet in a two-jet event, is computed. A top enriched region in data is defined requiring exactly one b-tagged counted jet ($p_{\text{T}} > 30$ GeV). Hereafter called the denominator. This sample is almost a clean $\text{t}\bar{\text{t}}$ sample with a 97 % purity as estimated from simulation. Events in this sample but with an additional low-p_{T} b-tagged jet ($10 < p_{\text{T}} < 30$ GeV) or one soft muon define the numerator. The ratio of the yields in the numerator and the denumerator provides the top-tagging efficiency $\epsilon_{1leg}^{\text{data}}$. This efficiency is computed for $\text{t}\bar{\text{t}}$ only by subtracting the 3 % of non-top-quark backgrounds and tW from the measured data in the control region (so for both the numerator and the denominator). The tW yield is estimated from simulation, which is normalized accordingly, using the predictions previously evaluated from the 1-jet category.

- The efficiency for a tW event to be top-tagged is simply $\epsilon_{1leg}^{\text{data}}$. For a $\text{t}\bar{\text{t}}$ event however, it is the probability that one of the top quarks or both are tagged, that is one minus the probability that neither of them is tagged, $\epsilon_{1or2leg}^{\text{data}} = 1 - (1 - \epsilon_{1leg}^{\text{data}})^2$.

- Now, the overall top-tagging efficiency, $\epsilon_{\text{top-tag}}$, is defined to account for the fraction x of tW events that look similar as $\text{t}\bar{\text{t}}$ events, that is with two top-taggable legs:

$$\begin{aligned} \epsilon_{\text{top-tag}} &= f_{\text{t}\bar{\text{t}}}^{\text{MC}} \epsilon_{1or2leg}^{\text{data}} + f_{\text{tW}}^{\text{MC}} \left(x \epsilon_{1or2leg}^{\text{data}} + (1-x)\, \epsilon_{1leg}^{\text{data}} \right) \\ &= \left(f_{\text{t}\bar{\text{t}}}^{\text{MC}} + x(1 - f_{\text{t}\bar{\text{t}}}^{\text{MC}}) \right) \left(1 - (1 - \epsilon_{1leg}^{\text{data}})^2 \right) + \left(1 - f_{\text{t}\bar{\text{t}}}^{\text{MC}} \right) (1-x)\, \epsilon_{1leg}^{\text{data}} \end{aligned} \tag{6.8}$$

  where $f_{\text{t}\bar{\text{t}}}^{\text{MC}}$ and $f_{\text{tW}}^{\text{MC}}$ are the $\text{t}\bar{\text{t}}$ and tW event fractions with respect to the total $\text{t}\bar{\text{t}}$ + tW, respectively, and x is the fraction of tW events containing two b-jets. Using the NLO $\text{t}\bar{\text{t}}$ and tW Monte Carlo samples, we estimate $f_{\text{t}\bar{\text{t}}} = 66$ % in the 0-jet category at the $\text{W}^+\,\text{W}^-$ selection level, without applying the top-quark veto requirements. This number is however subject to a large uncertainty, mainly due to the fact that the cross-section ratio of $\text{t}\bar{\text{t}}$ and tW is only known with an uncertainty of 17 % at the LHC [109]. In addition, the MC simulation does not take into account the interference due to the overlap of some NLO tW diagrams with LO $\text{t}\bar{\text{t}}$ diagrams.

- Finally we can use (6.7). A dedicated inverted control region is defined as the events with zero counted jets which fail either the soft-muon or the b-tagging veto. The data yields in this region are corrected for the other backgrounds contaminations and are then used together with the just derived top-tagging efficiency to predict

the top background at the $\mathrm{W^+W^-}$ selection level:

$$N_{\text{top-veto}}^{\text{WW reg}} = \frac{1-\epsilon_{\text{top-tag}}}{\epsilon_{\text{top-tag}}} \cdot \left(N_{\text{ctrl reg}}^{\text{all}} - N_{\text{ctrl reg}}^{\text{other bkg}} \right) \tag{6.9}$$

The details of the 0-jet top estimate calculation are summarized in Tables 6.6 and 6.7 for $p_{\mathrm{T}}^{\ell\ell} > 45$ GeV and Tables 6.8 and 6.9 for $p_{\mathrm{T}}^{\ell\ell} > 30$ GeV. The kinematics of the top background in the 0-jet category analysis is studied in a control sample enriched by $\mathrm{t\bar{t}}$ and tW by requiring zero counted jets with a low-p_{T} b-tagged jet ($15 < p_{\mathrm{T}}^{\ell\ell} < 30$ GeV). Comparison of data and total MC prediction for a selected set of basic kinematic variables and jet-related variables in the top control region for $p_{\mathrm{T}}^{\ell\ell} > 30$ GeV are shown in Figures 6.6 and 6.7 at $\sqrt{s} = 8$ TeV. Good data-MC agreement can be found.

1-jet category

In the 1-jet category the top background is the main background at the $\mathrm{W^+W^-}$ selection. The extrapolation method is similar to the 0-jet category.

To measure the top veto efficiency a control sample of events with two counted jets ($p_{\mathrm{T}} > 30$ GeV) is used. From simulation we know that the top-tagging efficiency for the highest p_{T} jet is approximately the same in the 1-jet and 2-jet categories. So we take events with two counted jets, requiring that the lower p_{T} jet is b-tagged and that there are no other soft b-tagged jets, and measure the efficiency for the higher p_{T} jet to pass the b-tagging requirement. These requirements significantly increase the purity of $\mathrm{t\bar{t}}$ events.

The inverted control region needed for (6.7) and for which the efficiency of the highest p_{T} jet is used to propagate back into the signal region is then defined as the events with one and only one counted jet that is b-tagged with no soft b-tagged jets. The signal and the control region then differ only by the requirement that the leading jet is b-tagged. The closure test, performed by comparing the estimate using this procedure in simulated events, gives the same result to within 2 %.

The scale factor is actually derived in a region that is slightly different from the signal region, but then it is consistently applied to the yield from simulated samples in the signal region. The difference is due to the soft-muon selection. In the signal region, events with soft muons are always rejected. Instead, in the 1-jet top-quark background estimation, soft muons are allowed inside the leading jet. So the soft muons are also

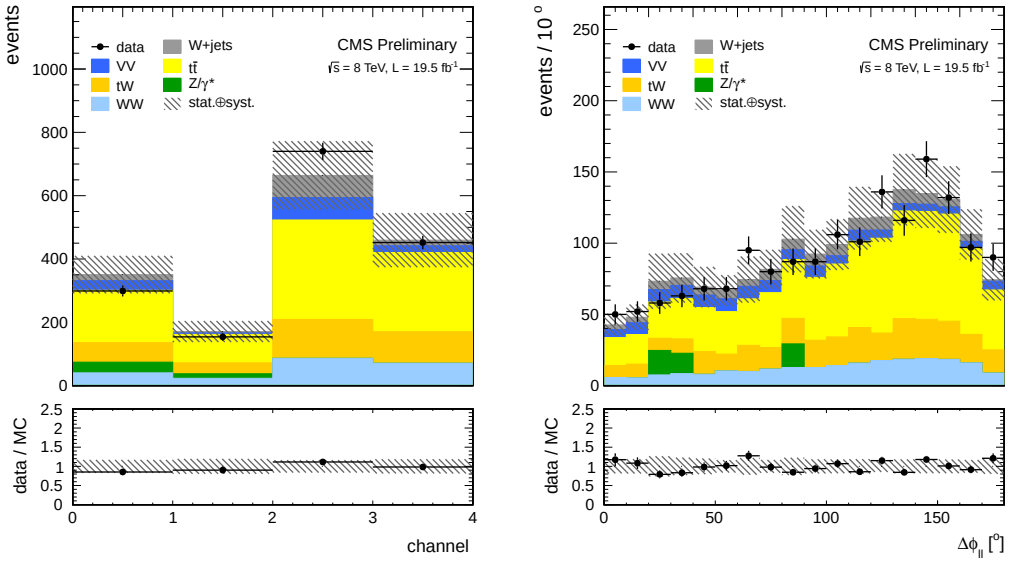

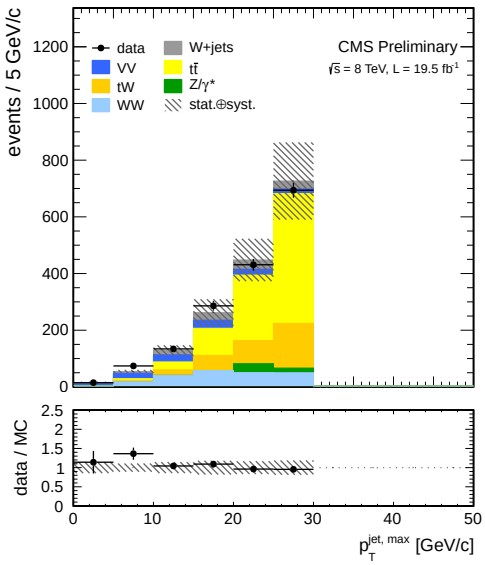

Figure 6.6.: Various distributions in the top control region with zero counted jets and one soft b-tagged jet with $15 < p_{\mathrm{T}}^{\ell\ell} < 30$ GeV, for data (points with error bars) and for the main backgrounds (stacked histograms) at $\sqrt{s} = 8$ TeV where DY, W+jets, WW and top contributions are corrected by data-driven estimates and other samples are taken from the MC prediction: (a) $\mu\mu$/ee/eμ/μe channel composition, (b) azimuthal separation and (c) leading jet p_{T}.

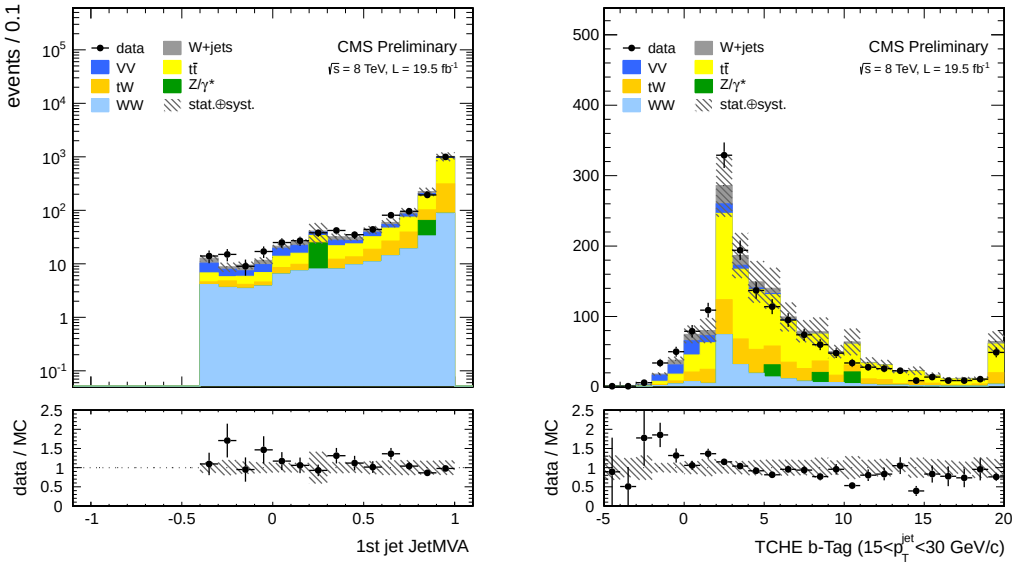

(a) (b)

Figure 6.7.: Various distributions in the top control region with zero counted jets and one soft b-tagged jet with $15 < p_{\mathrm{T}}^{\ell\ell} < 30$ GeV, for data (points with error bars) and for the main backgrounds (stacked histograms) at $\sqrt{s} = 8$ TeV where DY, W+jets, WW and top contributions are corrected by data-driven estimates and other samples are taken from the MC prediction: (a) jet ID discriminant and (b) the highest TCHE b-tag discriminant of all jets between 15 GeV and 30 GeV.

allowed in the top-veto region, in the top-tag region and in the efficiency measurement. The reason comes from the correlation between the soft muons and the b-tagging. When a soft muon is present in a jet, its b-tagging efficiency is slightly higher. To avoid this correlation, the top-quark background is estimated without any requirement on soft muons close to the jet.

The details of the 1-jet top estimate calculation are summarized in the 1-jet category column of Tables 6.6 and 6.7 for $p_{\mathrm{T}}^{\ell\ell} > 45$ GeV and Tables 6.8 and 6.9 for $p_{\mathrm{T}}^{\ell\ell} > 30$ GeV.

The kinematics of the top background which is one of the dominant contributions in the 1-jet category analysis is studied in a control sample enriched by $\mathrm{t\bar{t}}$ and tW by requiring one counted b-tagged jet. Comparison of data and total MC prediction for a selected set of basic kinematic variables and jet-related variables in the top control region for $p_{\mathrm{T}}^{\ell\ell} > 30$ GeV at $\sqrt{s} = 8$ TeV are shown in Figures 6.8 and 6.9. Good data-MC agreement can be found.

Table 6.6.: Estimation of top backgrounds in the 0- and 1-jet categories at $\sqrt{s} = 7$ TeV for $p_{\mathrm{T}}^{\ell\ell} > 45$ GeV.

	0-jet bin	1-jet bin
denominator (bkg. sub.)	1009	3482
numerator (bkg. sub.)	349	2400
ϵ_{1leg}	0.35 ± 0.01	-
$\epsilon_{1or2leg}$	0.57 ± 0.01	-
$f_{\mathrm{t\bar{t}}}$ (%)	66 ± 26	-
$\epsilon_{\mathrm{top-tag}}$ (%)	0.52 ± 0.04	0.68 ± 0.01
$N^{\mathrm{all}}_{\mathrm{ctrl\ reg}}$	193	912
$N^{\mathrm{other\ bkg}}_{\mathrm{ctrl\ reg}}$	38.8 ± 1.3	52.9 ± 2.6
data-driven top background estimate	139.9 ± 24.8	387.3 ± 14.6
estimated top events in simulation	108.6 ± 1.2	355.5 ± 2.0
data/MC	1.29 ± 0.23	1.09 ± 0.04

Table 6.7.: Estimation of top backgrounds in the 0- and 1-jet categories at $\sqrt{s} = 8$ TeV for $p_{\mathrm{T}}^{\ell\ell} > 45$ GeV.

	0-jet bin	1-jet bin
denominator (bkg. sub.)	5252	13864
numerator (bkg. sub.)	1679	9039
ϵ_{1leg}	0.32 ± 0.01	-
$\epsilon_{1or2leg}$	0.54 ± 0.01	-
$f_{\mathrm{t\bar{t}}}$ (%)	66 ± 26	-
$\epsilon_{\mathrm{top-tag}}$ (%)	0.49 ± 0.04	0.65 ± 0.01
$N^{\mathrm{all}}_{\mathrm{ctrl\ reg}}$	1020	4908
$N^{\mathrm{other\ bkg}}_{\mathrm{ctrl\ reg}}$	330.2 ± 40.1	373.5 ± 25.1
data-driven top background estimate	717.6 ± 124.9	2420.5 ± 44.4
estimated top events in simulation	743.8 ± 6.9	2224.6 ± 11.0
data/MC	0.96 ± 0.17	1.09 ± 0.02

Table 6.8.: Estimation of top backgrounds in the 0- and 1-jet categories at $\sqrt{s} = 7$ TeV for $p_{\mathrm{T}}^{\ell\ell} > 30$ GeV.

	0-jet bin	1-jet bin
denominator (bkg. sub.)	1168	3482
numerator (bkg. sub.)	403	2400
ϵ_{1leg}	0.34 ± 0.01	-
$\epsilon_{1or2leg}$	0.57 ± 0.01	-
$f_{\mathrm{t\bar{t}}}$ (%)	66 ± 26	-
$\epsilon_{\mathrm{top-tag}}$ (%)	0.52 ± 0.04	0.69 ± 0.01
$N^{\mathrm{all}}_{\mathrm{ctrl\ reg}}$	245	1052
$N^{\mathrm{other\ bkg}}_{\mathrm{ctrl\ reg}}$	62.2 ± 1.5	65.6 ± 2.6
data-driven top background estimate	167.3 ± 29.7	444.7 ± 16.7
estimated top events in simulation	128.1 ± 1.3	411.8 ± 2.1
data/MC	1.31 ± 0.23	1.08 ± 0.04

Table 6.9.: Estimation of top backgrounds in the 0- and 1-jet categories at $\sqrt{s} = 8$ TeV for $p_{\mathrm{T}}^{\ell\ell} > 30$ GeV.

	0-jet bin	1-jet bin
denominator (bkg. sub.)	6198	13864
numerator (bkg. sub.)	1960	9039
ϵ_{1leg}	0.32 ± 0.01	-
$\epsilon_{1or2leg}$	0.53 ± 0.01	-
$f_{\mathrm{t\bar{t}}}$ (%)	66 ± 26	-
$\epsilon_{\mathrm{top-tag}}$ (%)	0.49 ± 0.04	0.65 ± 0.01
$N^{\mathrm{all}}_{\mathrm{ctrl\ reg}}$	1313	5783
$N^{\mathrm{other\ bkg}}_{\mathrm{ctrl\ reg}}$	511.4 ± 47.6	483.6 ± 29.2
data-driven top background estimate	847.9 ± 147.9	2828.8 ± 51.8
estimated top events in simulation	862.9 ± 7.4	2615.4 ± 11.9
data/MC	0.98 ± 0.17	1.08 ± 0.02

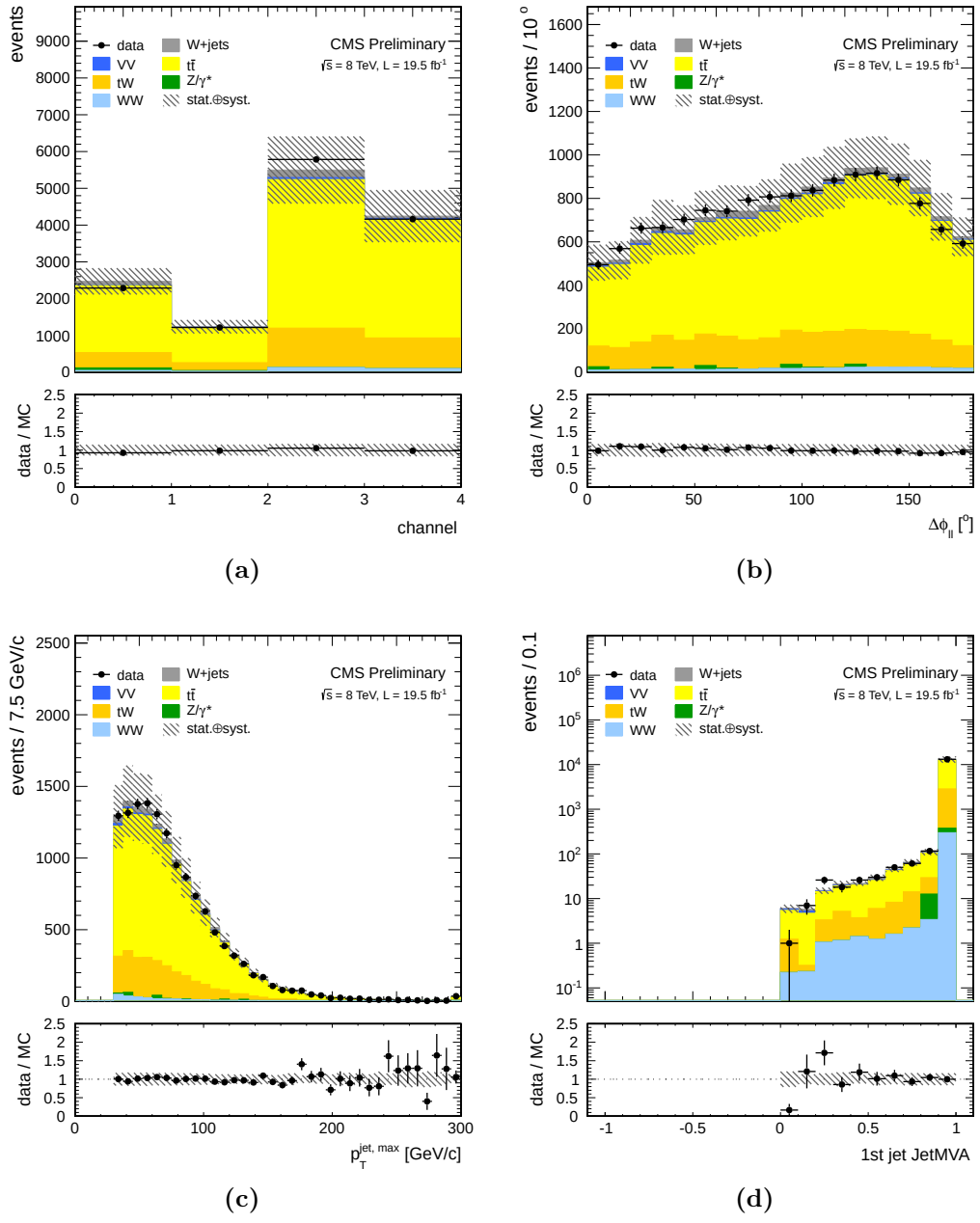

Figure 6.8.: Various distributions in the top control region with one b-tagged jet with $p_{\mathrm{T}}^{\ell\ell} > 30$ GeV, for data (points with error bars) and for the main backgrounds (stacked histograms) at $\sqrt{s} = 8$ TeV where DY, W+jets, WW and top contributions are corrected by data-driven estimates and other samples are taken from the MC prediction: (a) $\mu\mu$/ee/eμ/μe channel composition, (b) azimuthal separation, (c) leading jet p_{T} and (d) jet ID discriminant.

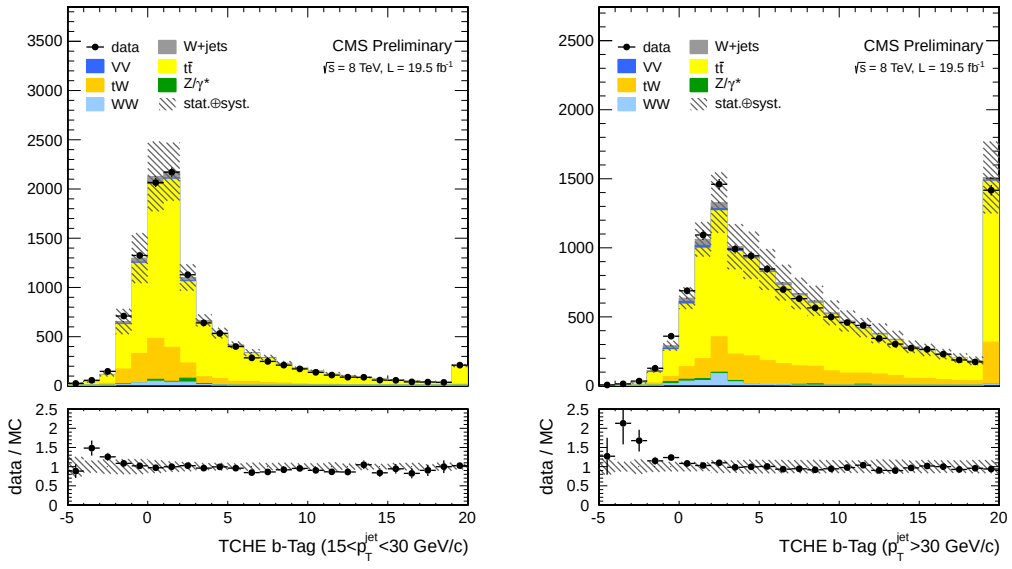

(a) (b)

Figure 6.9.: Various distributions in the top control region with one b-tagged jet with $p_{\mathrm{T}}^{\ell\ell} > 30$ GeV, for data (points with error bars) and for the main backgrounds (stacked histograms) at $\sqrt{s} = 8$ TeV where DY, W+jets, WW and top contributions are corrected by data-driven estimates and other samples are taken from the MC prediction: (a) the highest TCHE b-tag discriminant of all jets between 15 GeV and 30 GeV, and (b) the highest TCHE b-tag discriminant of all jets above 30 GeV in the event.

6.1.4. $\mathrm{W^+W^-}$ background

Different methods to estimate the $\mathrm{W^+W^-}$ background are used in the cut- and shape-based signal extraction analysis. The latter shape-based analysis for the eμ final states uses a floating nomalization for the $\mathrm{W^+W^-}$ background. This is possible since the template fit is able to constrain the normalization of the $\mathrm{W^+W^-}$ background using a large signal free sideband at high m_{T} and $m_{\ell\ell}$ that is dominated by the $\mathrm{W^+W^-}$ background. The former cut-based analysis uses a data-driven estimation for the normalization of the $\mathrm{W^+W^-}$ background, as described in the rest of this section.

The non-resonant $\mathrm{W^+W^-}$ production is dominated by the $\mathrm{q\bar{q} \to WW}$ component, which can be estimated from data as covered below. The smaller $\mathrm{gg \to WW}$ component (contributes for only 3 %) is taken from Monte Carlo, where a 50 % uncertainty to its normalization is assigned, which is mainly coming from the theoretical uncertainties related to the parton distribution functions and to the QCD renormalization and factorization scales. The breakdown of the $\mathrm{W^+W^-}$ background in these two contributions

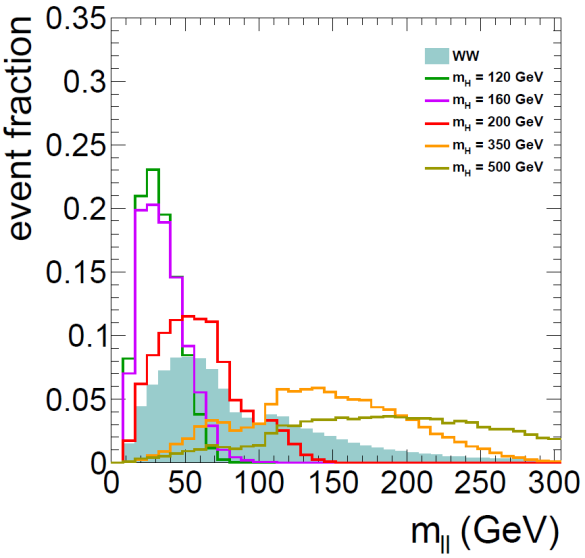

Figure 6.10.: The dilepton invariant mass distributions for the W^+W^- background and the Higgs signal for different Higgs masses in simulation at the W^+W^- selection level at $\sqrt{s} = 7$ TeV. The distributions are normalized to unity (events at $m_{\ell\ell} \sim m_Z$ belong to the different-flavor final state where no Z veto is applied) [110].

has an historical origin, as it makes it possible to vary the systematical error related to the parton density functions independently for each of the two components. We will see however that it is still possible to derive one scale factor for both components.

Although the W^+W^- selection level provides by construction a control region for the W^+W^- background, an additional selection is required to move to a signal free region. The non-resonant W^+W^- contribution in the signal region can be estimated from data using the dilepton invariant mass distribution. Figure 6.10 shows the dilepton invariant mass distributions for the W^+W^- background and the $H \to W^+ W^-$ signal for different values of the Higgs mass. For Higgs masses above 200 GeV there is a significant overlap in the dilepton invariant mass distribution with the W^+W^- background. In this case it is difficult to define an efficient control region and therefore the contribution of the background is taken from simulation. However for searches for low mass Higgs bosons with $m_H < 200$ GeV, a control region can be defined as the events with $m_{\ell\ell} > 100$ GeV. This region is appropriate for both 0- and 1-jet categories since the kinematics of the dilepton system do not depend on the jet structure of the event. Similarly, the measurement from the $m_{\ell\ell}$ sidebands is not sensitive to the kinematics difference between the $q\bar{q} \to WW$ and $gg \to WW$, we estimate the scale factor with respect to the Monte Carlo expectation of the sum of the two contributions.

The W^+W^- contribution estimated in the control region, $N_{WW}^{\text{ctrl reg}}$, is then extrapolated into the signal region, $N_{WW}^{\text{sig reg}}$, using the equation:

$$N_{WW}^{\text{sig reg}} = \epsilon_{WW} \cdot N_{WW}^{\text{ctrl reg}} \quad (6.10)$$

$$= \epsilon_{WW} \cdot \left(N_{\text{all}}^{\text{ctrl reg}} - N_{\text{other}}^{\text{ctrl reg}} \right) \quad (6.11)$$

with $N_{\text{all}}^{\text{ctrl reg}}$ the total number of events in the control region, $N_{\text{other}}^{\text{ctrl reg}}$ the number of non-W^+W^- events in the control region and ϵ_{WW} the control-to-signal region ratio defined as the number of W^+W^- events with $m_{\ell\ell} < 100$ GeV to the number of W^+W^- events with $m_{\ell\ell} > 100$ GeV estimated from simulation.

The procedure to obtain the W^+W^- contribution in the signal region is as follows:

- We measure the total number of events in the control region from the data $N_{\text{all}}^{\text{ctrl reg}}$;
- We then subtract the contamination from all the other (non-W^+W^-) backgrounds, such as top and $W+\text{jets}$, which are estimated using data-driven methods or simulation depending on the process as covered in this chapter;
- The resulting yield is subsequently extrapolated to the signal region using the control-to-signal region ratio ϵ_{WW} estimated from the dilepton invariant mass spectrum in simulation.

Since the measurement of the W^+W^- yield with a luminosity of 4.9 fb^{-1} and 19.5 fb^{-1} is not totally statistically dominated, we also account for the systematic on ϵ_{WW} due to the uncertainty on the shape of the $m_{\ell\ell}$ distribution for W^+W^- events. As an estimation of the uncertainty we use the difference in ϵ_{WW} between the nominal MC sample (MADGRAPH) and a sample at NLO (MC@NLO). The difference is 10 % and is propagated through the W^+W^- estimation.

By applying the above recipe to events that are required to pass the W^+W^- selection, we derive the estimation of the W^+W^- background at the mass-independent W^+W^- selection level. The estimates can be found in Table 6.10 for $\sqrt{s} = 7$ TeV and in Table 6.11 for $\sqrt{s} = 8$ TeV. The data/simulation scale factor is close to 1, showing that the background is consistent with simulation. The small upward fluctuation of the scale factor is caused by the same effect found in the W^+W^- cross-section measurement in both ATLAS and CMS [106, 107]. Figures of the resulting $m_{\ell\ell}$ distribution at the W^+W^- selection level with the data-driven scale factor applied, are covered at the end of this

Table 6.10.: Estimation of the W^+W^- background at the mass-independent W^+W^- selection level at $\sqrt{s} = 7$ TeV.

0-jet bin, $p_T^{\ell\ell} > 45$ GeV					
$m_{\ell\ell}$ region	data	all bkg	N_{WW}^{data}	N_{WW}^{MC}	data/MC
control	485	116.1 ± 13.8	368.9 ± 26.0	323.7 ± 2.4	1.1 ± 0.1
all	1363	-	1045.4 ± 97.1	917.4 ± 4.0	-
1-jet bin, $p_T^{\ell\ell} > 45$ GeV					
$m_{\ell\ell}$ region	data	all bkg	N_{WW}^{data}	N_{WW}^{MC}	data/MC
control	359	189.1 ± 8.5	169.9 ± 20.8	146.2 ± 1.6	1.2 ± 0.1
all	430	-	429.5 ± 100.8	369.6 ± 2.5	-
0-jet bin, $p_T^{\ell\ell} > 30$ GeV					
$m_{\ell\ell}$ region	data	all bkg	N_{WW}^{data}	N_{WW}^{MC}	data/MC
control	660	155.4 ± 17.6	504.6 ± 31.1	434.0 ± 2.8	1.2 ± 0.1
all	1957	-	1455.3 ± 125.7	1251.6 ± 4.7	-
1-jet bin, $p_T^{\ell\ell} > 30$ GeV					
$m_{\ell\ell}$ region	data	all bkg	N_{WW}^{data}	N_{WW}^{MC}	data/MC
control	406	215.0 ± 9.5	191.0 ± 22.3	170.9 ± 1.7	1.1 ± 0.1
all	497	-	496.6 ± 115.1	444.5 ± 2.8	-

chapter, in Section 6.2, specifically covering the data-MC comparison at the W^+W^- selection level.

The W^+W^- background contribution also needs to be estimated for the cut-based mass-dependent signal extraction selection that will be discussed in Section 7.2.1. For each Higgs mass hypothesis, the events used in this recipe are required to pass the full mass-dependent cut-based selection except for the requirements on m_T and $\Delta\phi_{\ell\ell}$. The yields in the signal region are multiplied by the m_T and $\Delta\phi_{\ell\ell}$ cut efficiency, obtained from simulation, to retrieve the W^+W^- contribution in the signal region after the full selection.

6.1.5. Drell-Yan to $\tau\,\tau$ background

The low E_T^{miss} threshold applied in the different-flavor final state allows for a significant contribution of events from $Z/\gamma^{(*)} \to \tau^+\tau^-$, that is in fact estimated from data. This is accomplished by using $Z/\gamma^{(*)} \to \mu^+\mu^-$ events where in each event each muon is replaced with a τ with the same kinematics as the muon. For each τ the decay $\tau \to \ell\nu_\tau\bar{\nu}$ is

Table 6.11.: Estimation of the W^+W^- background at the mass-independent W^+W^- selection level at $\sqrt{s} = 8$ TeV.

0-jet bin, $p_T^{\ell\ell} > 45$ GeV					
$m_{\ell\ell}$ region	data	all bkg	N_{WW}^{data}	N_{WW}^{MC}	data/MC
control	2399	620.2 ± 73.6	1778.8 ± 88.4	1641.3 ± 9.6	1.08 ± 0.05
all	6902	-	4775.2 ± 373.5	4406.1 ± 15.5	-
1-jet bin, $p_T^{\ell\ell} > 45$ GeV					
$m_{\ell\ell}$ region	data	all bkg	N_{WW}^{data}	N_{WW}^{MC}	data/MC
control	1719	1110.0 ± 38.4	609.0 ± 56.5	688.8 ± 6.2	0.88 ± 0.08
all	1522	-	1522.3 ± 336.0	1721.5 ± 9.7	-
0-jet bin, $p_T^{\ell\ell} > 30$ GeV					
$m_{\ell\ell}$ region	data	all bkg	N_{WW}^{data}	N_{WW}^{MC}	data/MC
control	3119	844.6 ± 91.9	2274.4 ± 107.5	2170.7 ± 11.1	1.05 ± 0.05
all	9677	-	6254.4 ± 479.2	5969.1 ± 18.1	-
1-jet bin, $p_T^{\ell\ell} > 30$ GeV					
$m_{\ell\ell}$ region	data	all bkg	N_{WW}^{data}	N_{WW}^{MC}	data/MC
control	2014	1287.1 ± 43.2	726.9 ± 62.3	806.5 ± 6.7	0.90 ± 0.08
all	1875	-	1875.0 ± 408.4	2080.1 ± 10.7	-

simulated [111]. This procedure is called *embedding*. After replacing the muons from $Z/\gamma^{(*)} \to \mu^+\mu^-$ decays with the simulated τ decays, the set of pseudo $Z/\gamma^{(*)} \to \tau^+\tau^-$ events undergoes the reconstruction step. Good agreement in kinematic distributions for this sample and a Monte Carlo based $Z/\gamma^{(*)} \to \tau^+\tau^-$ sample is found. Using this technique, the resulting $Z/\gamma^{(*)} \to \tau^+\tau^-$ sample used in this analysis is completely data driven, thus providing a more accurate description of the experimental conditions with respect to the full simulation. The global normalization of the pseudo $Z/\gamma^{(*)} \to \tau^+\tau^-$ events is checked in the low m_T spectrum where a rather pure $Z/\gamma^{(*)} \to \tau^+\tau^-$ sample is expected. The uncertainty in the estimation of this background process is about 10 %.

6.1.6. Other backgrounds

The remaining processes are partly estimated from Monte Carlo simulation, after the application of the proper data corrections for lepton, trigger and jet veto efficiencies. The processes are: WZ, ZZ, VVV, $W\gamma^{(*)}$ and $Z\gamma$.

The $W\gamma$ and $W\gamma^*$ background processes are also evaluated with a combination of simulated and data samples. This is done outside the scope of this thesis, so only a summary with a reference will be given. The MADGRAPH generator is used to estimate

the $W\gamma^*$ background contribution from asymmetric virtual photon decays [112], in which one lepton escapes detection. The $W\gamma^*$ cross section is measured from data to obtain the normalization scale of the simulated sample. A high-purity control sample of $W\gamma^*$ events with three reconstructed leptons is defined and compared to the simulation, as described in the $H \to W^+ W^-$ paper [89] in appendix A. As a result of the analysis in this control sample, a factor of 1.5 ± 0.5 with respect to the predicted LO cross section is found, that will be used as scale factor. Finally, the shapes of the discriminant variables used in the signal extraction for the $W\gamma$ process are obtained from data, as explained in appendix B of the same paper [89].

6.2. Data to MC comparison at the W^+W^- selection level

Now that we have covered the background estimation methods for all the backgrounds, it is possible to perform a sanity check at the W^+W^- selection level. Table 6.12 lists the background estimates and the data yields for the mass-independent W^+W^- selection level for the 0- and 1-jet categories. The WZ, ZZ and VVV backgrounds are grouped together and labeled as VV. The errors in the table are the statistical errors only.

The most natural variables defining the final state of the analysis are the lepton transverse momenta of the leading and the trailing lepton ($p_{\mathrm{T}}^{\mathrm{l,max}}$ and $p_{\mathrm{T}}^{\mathrm{l,min}}$), and the missing transverse energy that is an indirect measure of the neutrino energies. For reasons already stated in Section 5.4.6, the minimum projected missing transverse energy (min-proj.$E_{\mathrm{T}}^{\mathrm{miss}}$) is more appropriate to disentangle the signal from particular backgrounds rather than using $E_{\mathrm{T}}^{\mathrm{miss}}$. Next to these three, the distributions of the invariant mass of the two leptons ($m_{\ell\ell}$), the dilepton opening angle in the transverse plane ($\Delta\phi_{\ell\ell}$), and the invariant mass of the whole final state system in the transverse plane, $m_{\mathrm{T}}^{\ell\ell-\mathrm{E}_{\mathrm{T}}^{\mathrm{miss}}}$, or in short the transverse mass, m_{T}, will be shown. The latter was defined in (5.6) in Section 5.4.6.

Figures 6.11 to 6.18 contain the distributions of the previously described six variables at the W^+W^- selection level for $p_{\mathrm{T}}^{\ell\ell} > 30$ (45) GeV in the 0- and 1- jet categories for the different (same) flavor final states. In all the figures the background distributions have been reweighted to the expected values obtained with 4.9 (19.5) fb^{-1} of data at $\sqrt{s} = 7$ (8) TeV. The uncertainty band includes the statistical and normalization

Table 6.12.: Observed number of events and background estimates after applying the W^+W^- selection requirements for an integrated luminosity of 4.9 fb^{-1} at $\sqrt{s} = 7$ TeV and of 19.5 fb^{-1} at $\sqrt{s} = 8$ TeV. The WZ, ZZ and VVV backgrounds are grouped together and labeled as VV. For the same-flavor (SF) final states, the $p_{\mathrm{T}}^{\ell\ell} > 45$ GeV selection is applied while the $p_{\mathrm{T}}^{\ell\ell} > 30$ GeV selection is applied for the different-flavor (DF) final states.

$\sqrt{s} = 7$ TeV				
	data	tot bkg.	WW	$t\bar{t}$+tW
0-jet SF	530	495 ± 33	395 ± 30	51 ± 9
0-jet DF	1349	1348 ± 108	997 ± 76	111 ± 20
1-jet SF	327	322 ± 26	139 ± 11	116 ± 21
1-jet DF	733	746 ± 63	344 ± 26	276 ± 50
	W+jets	VV	$Z/\gamma^{(*)}$	$V+\gamma^{(*)}$
0-jet SF	20 ± 7	17.9 ± 0.4	9 ± 3	2.4 ± 0.5
0-jet DF	203 ± 74	15.1 ± 0.2	6 ± 2	16 ± 4
1-jet SF	13 ± 5	8.9 ± 0.2	43 ± 10	2.4 ± 0.5
1-jet DF	78 ± 29	15.8 ± 0.2	27 ± 5	4.7 ± 3
$\sqrt{s} = 8$ TeV				
	data	tot bkg.	WW	$t\bar{t}$+tW
0-jet SF	2767	2573 ± 170	1807 ± 138	264 ± 48
0-jet DF	6322	6120 ± 462	4216 ± 321	548 ± 99
1-jet SF	1511	1420 ± 141	481 ± 37	715 ± 129
1-jet DF	3929	3928 ± 368	1289 ± 98	1715 ± 309
	W+jets	VV	$Z/\gamma^{(*)}$	$V+\gamma^{(*)}$
0-jet SF	128 ± 47	113 ± 1	224 ± 74	37 ± 6
0-jet DF	878 ± 316	112 ± 1	80 ± 14	286 ± 19
1-jet SF	72 ± 27	53 ± 1	85 ± 33	15 ± 5
1-jet DF	460 ± 166	107 ± 1	291 ± 53	70 ± 10

systematic uncertainty of all backgrounds processes. The systematic uncertainty due to the luminosity is also included (see Section 7.3). A good data-MC agreement is found. For a SM Higgs boson with $m_{\mathrm{H}} = 125$ GeV, an excess of events with respect to the backgrounds is expected at low $m_{\ell\ell}$.

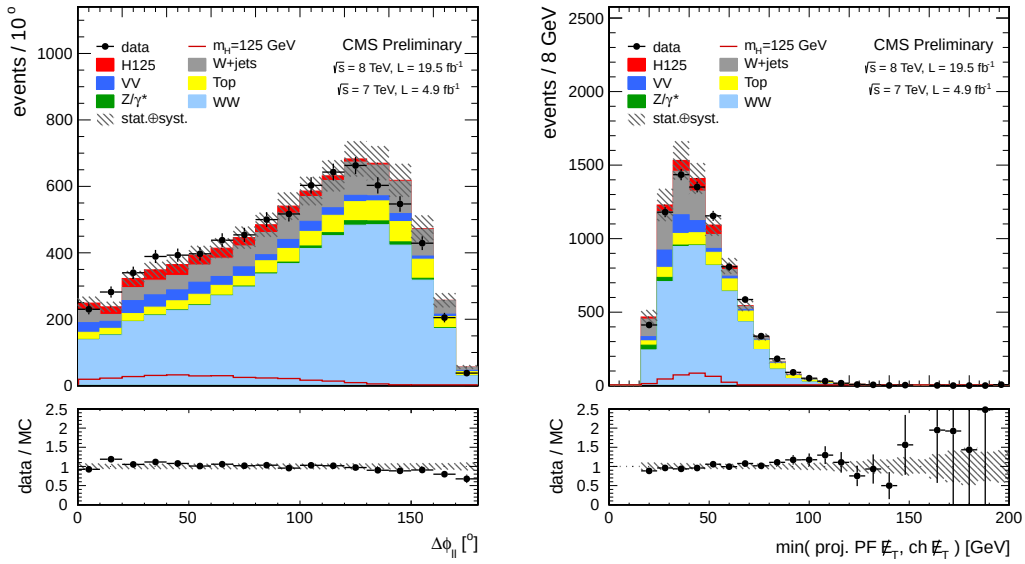

Figure 6.11.: Distributions at the W^+W^- selection level in the **0-jet** category for the **different-flavor** final state, for data (points with error bars), for the main backgrounds (stacked histograms) and for a Higgs boson signal with $m_H = 125$ GeV (superimposed and stacked histogram): (a) dilepton $\Delta\phi$, (b) minimum projected E_T^{miss} and (c) dilepton invariant mass $m_{\ell\ell}$.

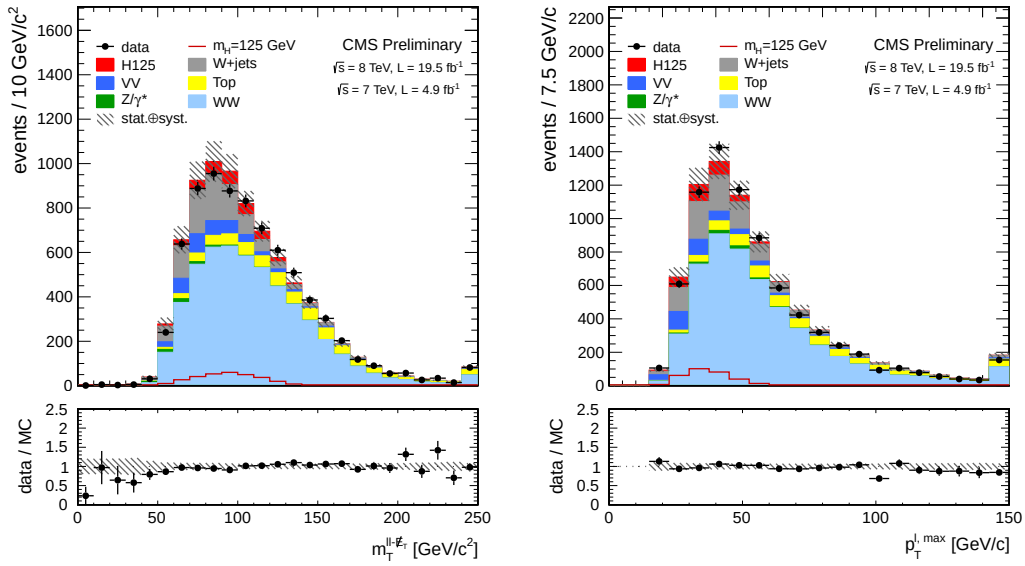

(a) (b)

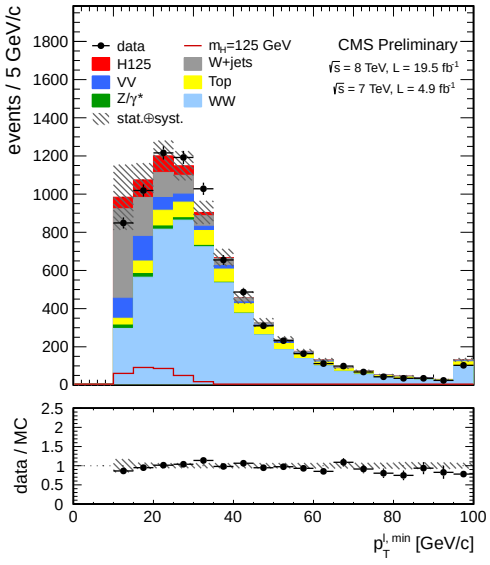

(c)

Figure 6.12.: Distributions at the W^+W^- selection level in the **0-jet** category for the **different-flavor** final state, for data (points with error bars), for the main backgrounds (stacked histograms) and for a Higgs boson signal with $m_H = 125$ GeV (superimposed and stacked histogram): (a) transverse mass m_T of the dilepton-E_T^{miss} system, (b) leading lepton p_T and (c) trailing lepton p_T.

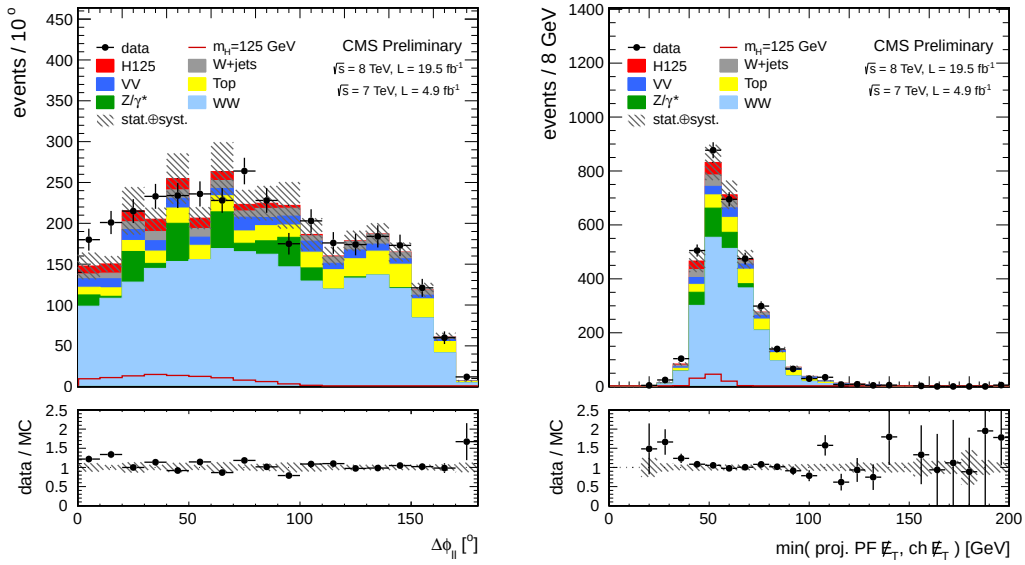

(a) (b)

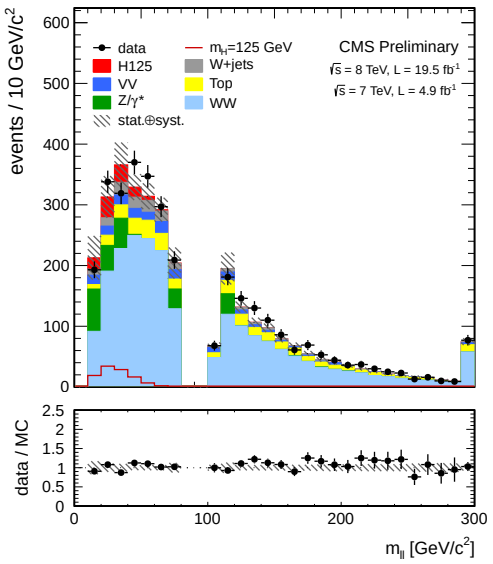

(c)

Figure 6.13.: Distributions at the W^+W^- selection level in the **0-jet** category for the **same-flavor** final state, for data (points with error bars), for the main backgrounds (stacked histograms) and for a Higgs boson signal with $m_H = 125$ GeV (superimposed and stacked histogram): (a) dilepton $\Delta\phi$, (b) minimum projected E_T^{miss} and (c) dilepton invariant mass $m_{\ell\ell}$.

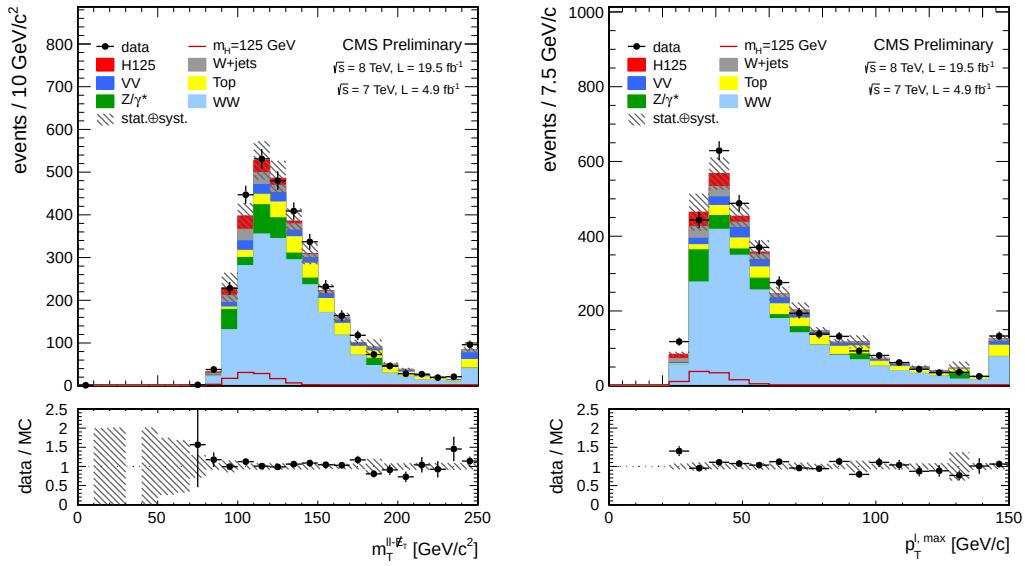

(a) (b)

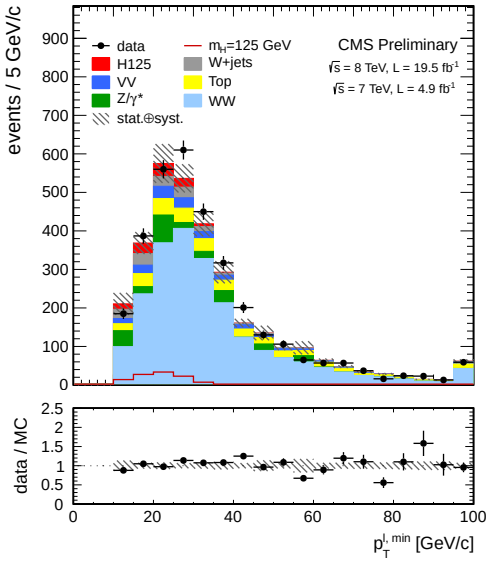

(c)

Figure 6.14.: Distributions at the W^+W^- selection level in the **0-jet** category for the **same-flavor** final state, for data (points with error bars), for the main backgrounds (stacked histograms) and for a Higgs boson signal with $m_H = 125$ GeV (superimposed and stacked histogram): (a) transverse mass m_T of the dilepton-E_T^{miss} system, (b) leading lepton p_T and (c) trailing lepton p_T.

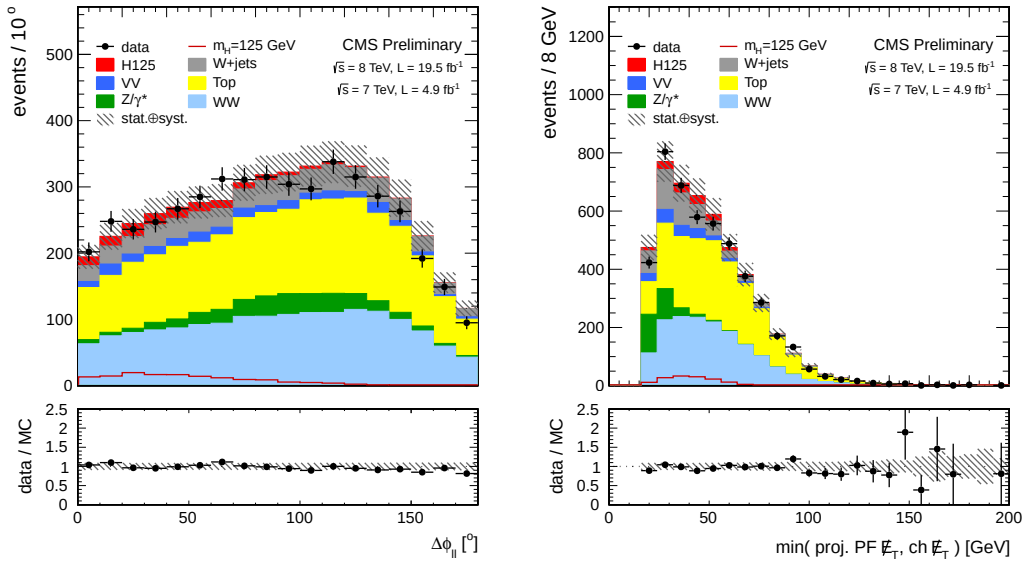

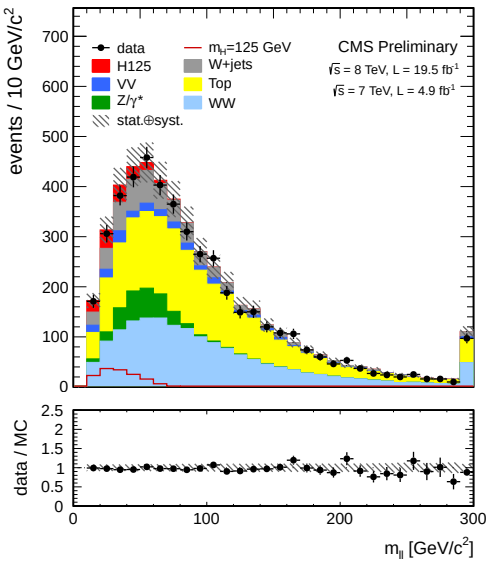

Figure 6.15.: Distributions at the W^+W^- selection level in the **1-jet** category for the **different-flavor** final state, for data (points with error bars), for the main backgrounds (stacked histograms) and for a Higgs boson signal with $m_H = 125$ GeV (superimposed and stacked histogram): (a) dilepton $\Delta\phi$, (b) minimum projected E_T^{miss} and (c) dilepton invariant mass $m_{\ell\ell}$.

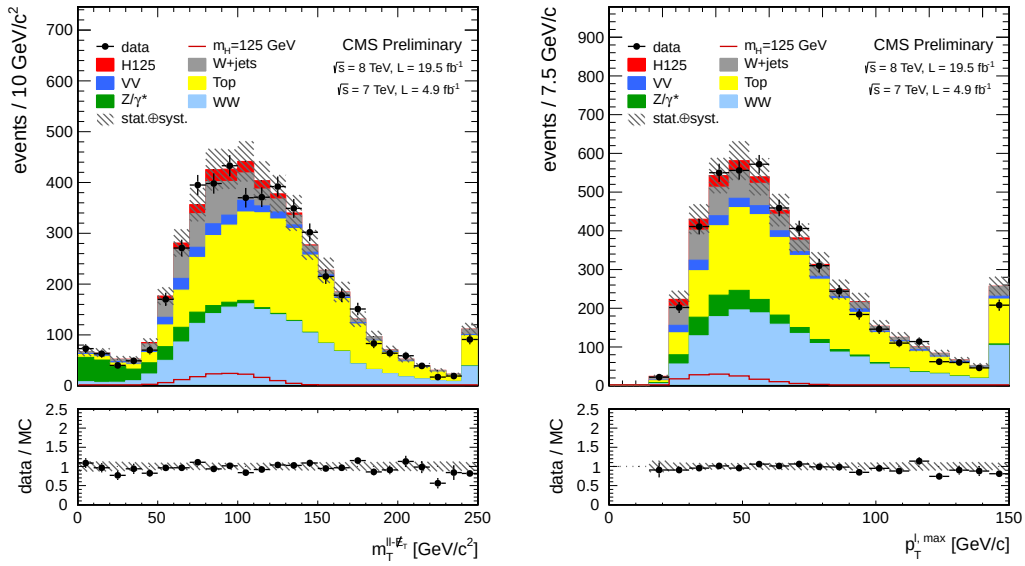

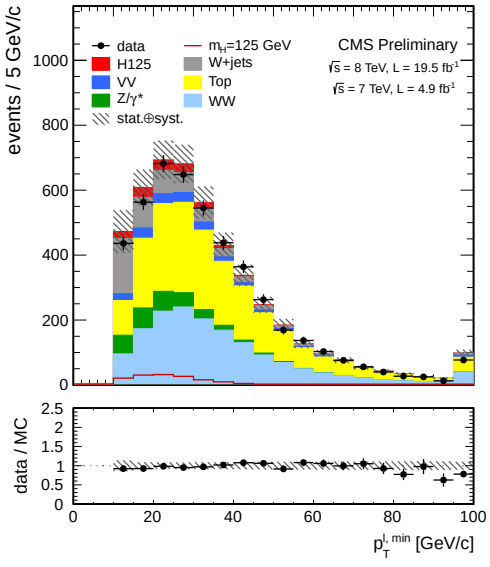

Figure 6.16.: Distributions at the $\mathrm{W^+W^-}$ selection level in the **1-jet** category for the **different-flavor** final state, for data (points with error bars), for the main backgrounds (stacked histograms) and for a Higgs boson signal with $m_{\mathrm{H}} = 125$ GeV (superimposed and stacked histogram): (a) transverse mass m_{T} of the dilepton-$E_{\mathrm{T}}^{\mathrm{miss}}$ system, (b) leading lepton p_{T} and (c) trailing lepton p_{T}.

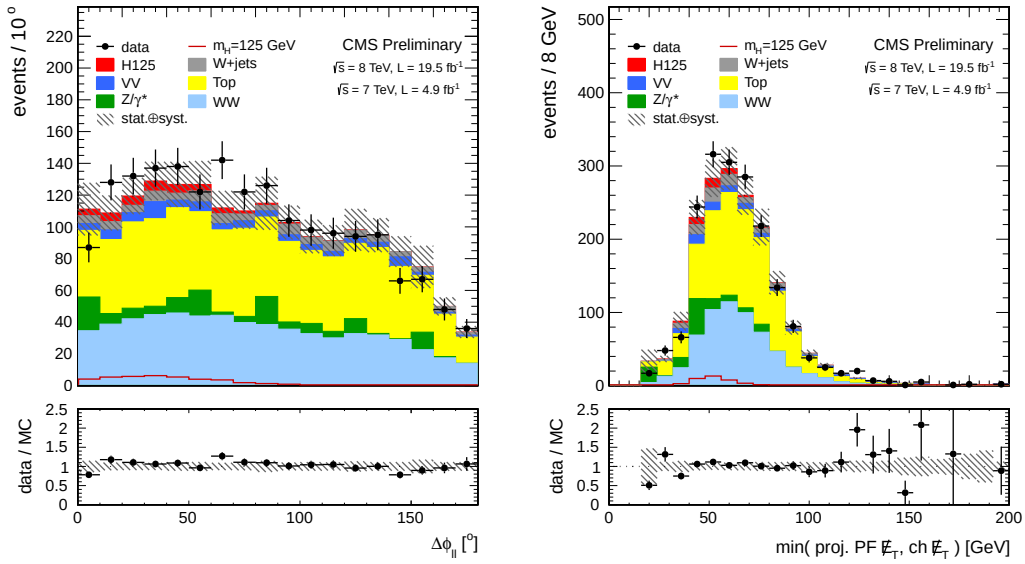

(a) (b)

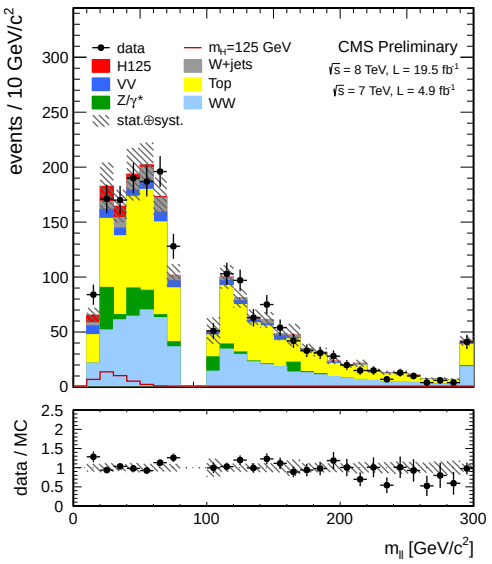

(c)

Figure 6.17.: Distributions at the W^+W^- selection level in the **1-jet** category for the **same-flavor** final state, for data (points with error bars), for the main backgrounds (stacked histograms) and for a Higgs boson signal with $m_H = 125$ GeV (superimposed and stacked histogram): (a) dilepton $\Delta\phi$, (b) minimum projected E_T^{miss} and (c) dilepton invariant mass $m_{\ell\ell}$.

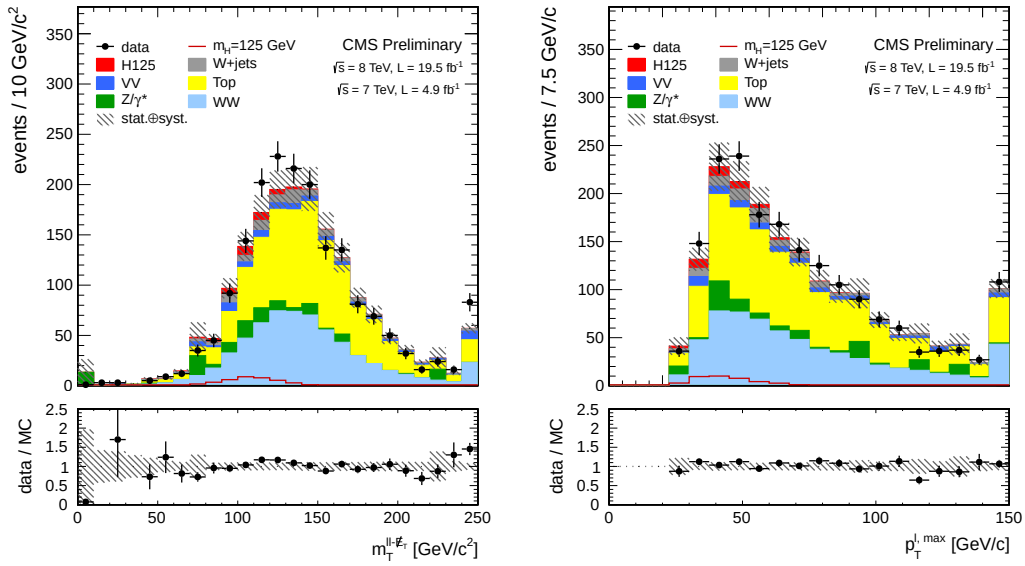

(a) (b)

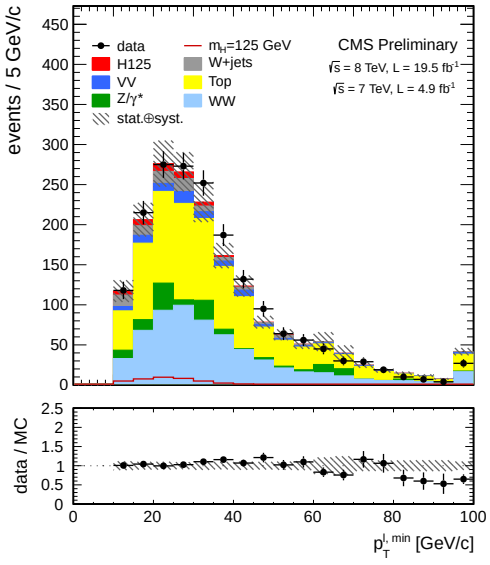

(c)

Figure 6.18.: Distributions at the W^+W^- selection level in the **1-jet** category for the **same-flavor** final state, for data (points with error bars), for the main backgrounds (stacked histograms) and for a Higgs boson signal with $m_H = 125$ GeV (superimposed and stacked histogram): (a) transverse mass m_T of the dilepton-E_T^{miss} system, (b) leading lepton p_T and (c) trailing lepton p_T.

Chapter 7.

Higgs signal extraction strategy and systematics

This chapter will first cover a few properties of the Higgs signal that differ from the W^+W^- background, which can be used to identify variables that are able to differentiate the signal from the W^+W^- background. Next, the most sensible variables to extract the Higgs signal will be discussed. In order to enhance the sensitivity to the Higgs boson signal, two different analysis approaches are performed. The first one is a *cut-based counting analysis* applied to all the flavor final states where further requirements on a few observables are applied. Because the kinematics of signal events change as a function of the Higgs mass, separate optimizations are performed for different m_{H} hypotheses. The second approach is a *shape-based two-dimensional analysis* only applied to the different-flavor eμ final states making use of a binned 2D template fit using two sensitive variables to the presence of the signal. This second analysis is more sensitive than the first one (as shown in Chapter 8) and is used as the default analysis for the eμ final state. The counting analysis is used as the default analysis for the ee/$\mu\mu$ final states. Lastly the systematics that enter the analysis will be covered in Section 7.3.

7.1. Higgs properties with respect to the W^+W^- background

First of all, as mentioned in the sanity check at the W^+W^- selection level, there is a clear difference in the shape of the $\Delta\phi_{\ell\ell}$ distribution between the signal and the W^+W^- background (see for example Figure 6.11(a)). The shape difference originates from the

spin nature of the Standard Model Higgs boson and will be covered in the first subsection. Afterwards, the variables that are able to differentiate the Higgs signal from the other backgrounds, in particular the W^+W^- background, are discussed.

7.1.1. Spin correlation of the W^+W^- system

This section covers the origin of the spin correlations and how it can be used as an effective discriminant between the $H \to W^+ W^-$ signal and the W^+W^- background. The discussion is a summary of [113].

First we will consider the signal case. The SM Higgs boson is a scalar spin-0 particle, while the W boson is a vectorial spin-1 particle. In the Higgs rest frame, the two W bosons are emitted back-to-back. In this process the spin vector has to be conserved due to the angular momentum conservation. This implies that the z-component of the spin needs to be conserved as well (the z-axis defined along the direction of the propagation of the W bosons). Since the Higgs boson is a spin-0 particle it follows that $S_z(W^+W^-) = 0$ and since the W boson is a spin-1 particle that $S_z(W^\pm) = \{0, \pm 1\}$. The polarization states with respect to the z-axis are called transverse, W_T, when $S_z(W) = \pm 1$ and longitudinal, W_L, when $S_z(W) = 0$. Therefore, the spins of the W bosons produced in the $H \to W^+ W^-$ decay have to be anticorrelated and thus only the following two decays are allowed:

$$H \to W_T^+ W_T^- \quad \text{and} \tag{7.1}$$

$$H \to W_L^+ W_L^-. \tag{7.2}$$

The mixed decay $H \to W_T^\pm W_L^\mp$ is forbidden. The W polarizations are not directly observable, instead the final state charged leptons are observed. The decay rate of the $W_T^+ \to \ell^+ \nu$ is proportional to $(1 + \cos\theta)^2$, where θ is the angle between the lepton direction and the W_T^+ spin. Therefore the right-handed lepton is emitted in most of the cases in the same direction as the W_T^+ spin. Similarly, the left-handed lepton is mostly emitted in the opposite direction with respect to the W_T^- spin since its decay follows a $(1 - \cos\theta)^2$ distribution. Since the two W bosons are anticorrelated, the leptons are mainly emitted in the same direction. Similar considerations apply to the case of the longitudinal polarized W bosons and can be found in [113]. A sketch of a most likely scenario where the leptons are emitted in the same direction is shown in Figure 7.1.

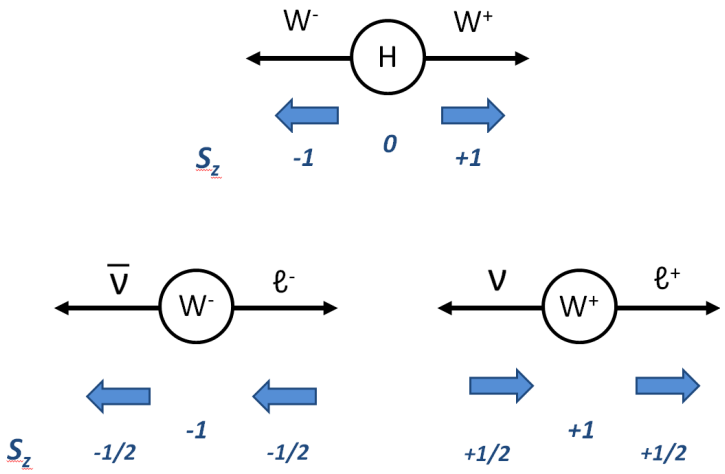

Figure 7.1.: Scheme of the spin correlations for $H \to W^+ W^-$. The two leptons are mainly emitted in the same direction with the consequence that a $\Delta\phi_{\ell\ell}$ selection can discriminate $H \to W^+ W^-$ from the $W^+ W^-$ background.

Now in the case of the $W^+ W^-$ background, the initial state is unpolarized, meaning that all the following combinations are allowed:

$$W_T^+ W_T^-, \quad W_L^+ W_L^- \quad \text{and} \quad W_T^\pm W_L^\mp . \tag{7.3}$$

The first two are equivalent to the signal case. On the contrary, the combination $W_T^\pm W_L^\mp$ corresponds to a spin-1 configuration (z-projected) in which the two W bosons have an uncorrelated spin. Therefore the W bosons do not impose any correlation between the leptons momenta and thus allow for a wider opening angle between the leptons. It has been shown in [113] that the magnitude of $W_T^\pm W_L^\mp$ production is approximately half of the total $W^+ W^-$ production for $m_{WW} \approx 160$ GeV.

This difference in spin correlation implies that a small opening angle between the two leptons $\Delta\phi_{\ell\ell}$ is a good discriminating variable to separate the $W^+ W^-$ signal from the $W^+ W^-$ background. Figure 7.2 shows the opening angle distribution of the visible leptons for the signal and background at generator level, without any preselection or detector effects included. It is clear that the signal peaks at small angles and that the background peaks at high values of angle in the transverse plane. The resulting effect at the $W^+ W^-$ selection level can be seen in the $\Delta\phi_{\ell\ell}$ distributions of Figures 6.11, 6.13, 6.15 and 6.17. This will be further utilized in the analysis to partially remove the $W^+ W^-$ background.

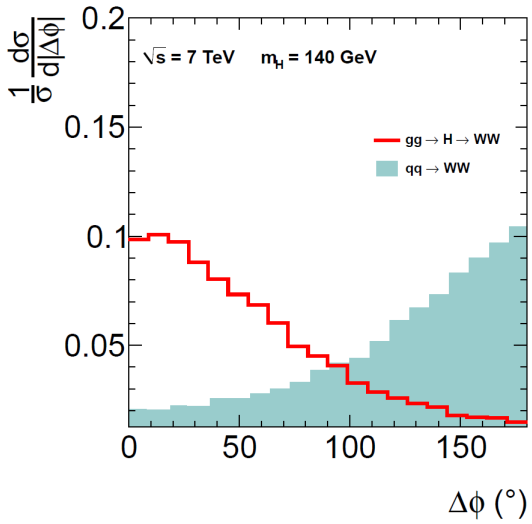

Figure 7.2.: Opening angle between the two leptons in the case of the W^+W^- signal (open histogram) and the W^+W^- background (filled histogram) at generator level without any preselections or detector effects applied [110].

In addition to the spin correlation, there is also a difference in the boost of the W^+W^- system between the background and the signal events. A boost for the W^+W^- background is coming from an average momentum imbalance in the W^+W^- production, originating from the asymmetry between the q and $\bar{q}$ PDFs of the $q\bar{q} \to W^+W^-$ process (see [113]). This boost gets bigger as the energy of the collisions increases. In contrary for the $gg \to H$ process, the Higgs signal, regardless of collision energy and its mass, will be produced in average at rest, which is consistent with the fact that the same PDF describes the gluon in each of the two protons. A more detailed explanation of the origin of the boost effect can be found in [113]. As a result, the W^+W^- background events populate higher rapidity values, while the signal events lie in more central regions. Due to this extra boost, the decay leptons for the background will be folded towards the beam axis, while the signal leptons will be central. The boost of the W bosons only dilutes the angular correlation and thus the discrimination power of the $\Delta\phi_{\ell\ell}$ variable to separate the $H \to W^+ W^-$ signal from the W^+W^- background for high Higgs masses.

7.1.2. Sensitive variables to extract the Higgs signal

As previously deduced, the $\Delta\phi_{\ell\ell}$ variable is a sensible variable to separate the $H \to W^+ W^-$ signal from the W^+W^- background, although the separation power decreases for high Higgs masses.

Two other very sensitive variables exist. Although it is not possible to reconstruct the Higgs mass peak itself, since it is impossible to measure the neutrinos, we can still use variables that come close to the full reconstructed Higgs mass variable. What we can measure is the transverse mass of the Higgs boson which is of course the same variable as the previously defined transverse mass of the dilepton-$E_{\mathrm{T}}^{\mathrm{miss}}$ system $m_{\mathrm{T}}^{\ell\ell-\mathrm{E}_{\mathrm{T}}^{\mathrm{miss}}}$ or m_{T}. In this variable the Higgs signal exhibits a broad peak structure. When the Higgs boson becomes heavier, the decay products are more and more Lorentz boosted and the peak structure will move to higher m_{T} values, making it possible to separate it from the $\mathrm{W}^+\mathrm{W}^-$ background that has a much broader distribution as can be seen in Figure 6.12 (a).

Next to the m_{T} variable, another very natural variable is the invariant mass of the two leptons $m_{\ell\ell}$, which is very sensitive to the Higgs mass. Higher Higgs masses give rise to a broader peak structure that will move to higher $m_{\ell\ell}$ values. A comparison between signals with different Higgs masses and the $\mathrm{W}^+\mathrm{W}^-$ background was already shown in Figure 6.10. This will again make it possible to separate the Higgs signal with a certain mass from the broad $\mathrm{W}^+\mathrm{W}^-$ background.

Finally to a smaller impact, the transverse momentum p_{T} of the two charged leptons can be used, as they are also affected by the Lorentz boost in a similar way as the m_{T} variable. Higher Higgs masses will be accompanied by higher minimum transverse lepton momenta.

Control distributions for all above mentioned variables at the $\mathrm{W}^+\mathrm{W}^-$ selection level have been shown in Section 6.2. Combinations of these variables will be used in the cut- and shape-based analysis to extract the Higgs signal.

7.2. Cut- and shape-based analysis strategy

7.2.1. Cut-based counting analysis

A simple counting experiment is performed as a basic cross-check for all jet and flavor categories, and as default approach for the same-flavor ee/$\mu\mu$ final states. A tighter selection is applied to increase the signal-to-background ratio using kinematic variables that characterize the Higgs boson final state. The common $\mathrm{W}^+\mathrm{W}^-$ selection with a dilepton p_{T} of $p_{\mathrm{T}}^{\ell\ell} > 45$ GeV is used, combined with a series of selections based on the

lepton momenta ($p_{\mathrm{T}}^{\mathrm{l,max}}$ and $p_{\mathrm{T}}^{\mathrm{l,min}}$), the dilepton invariant mass ($m_{\ell\ell}$), the azimuthal separation between the two leptons ($\Delta\phi_{\ell\ell}$) and the transverse mass of the whole final state system m_{T}. The threshold values are optimized for each Higgs boson mass hypothesis to maximize $\frac{s}{\sqrt{s+b}}$ and they are the same in both the 0- and 1-jet categories. Table 7.1 summarizes the selection requirements used in the counting analysis. A few comments about the selection should be made:

- Increasing Higgs masses require higher and higher thresholds on the $p_{\mathrm{T}}^{\mathrm{l,max}}$, $p_{\mathrm{T}}^{\mathrm{l,min}}$ and m_{T} variables. This is obvious due to the fact that when the Higgs boson becomes heavier, the decay products are more and more Lorentz boosted with respect to the $\mathrm{W^+W^-}$ background. However due to the very low cross section at high masses ($m_{\mathrm{H}} \geq 200$ GeV) the lower bound on the m_{T} cut is kept constant, not rejecting most of the signal.

- The cut on the $m_{\ell\ell}$ variable is always lower than the value of the Higgs mass itself, which is logically since events also consist of neutrinos, expressed as $E_{\mathrm{T}}^{\mathrm{miss}}$, where a minimum amount of $E_{\mathrm{T}}^{\mathrm{miss}}$ is needed in order to pass the common $\mathrm{W^+W^-}$ preselection.

- Due to the large Lorentz boost of the W bosons at high Higgs masses, the leptons are folded along their direction and the angle $\Delta\phi_{\ell\ell}$ between the leptons opens up, decreasing the discriminating power of this variable against the $\mathrm{W^+W^-}$ background. This is reflected in the changed cut values for different masses.

- Finally, note that the missing energy is not used as an additional discriminating variable, as it is very much correlated with the m_{T} variable.

The kinematic distributions after the full mass-dependent cut-based selection for the different-flavor final states split in the 0- and 1-jet categories, are shown in Figures 7.3 to 7.8 for a Higgs mass of 125 GeV, 160 GeV and 250 GeV. The cut on the plotted variable is each time omitted. The simulation is scaled to the data-driven estimates. The uncertainty band includes the statistical and normalization systematic uncertainty of all backgrounds processes. The systematic uncertainty due to the luminosity is also included (see Section 5.3.1). The Higgs boson signal is also stacked on top of the histograms in the plots for a mass of 125 GeV, since this signal was found in multiple Higgs decay channels as covered in the discovery paper [44]. From these plots one can already conclude that a Higgs of 160 GeV or 250 GeV is clearly not present in the data, while a Higgs of 125 GeV

Table 7.1.: Final event selection requirements for the cut-based analysis in the 0- and 1-jet categories.

m_{H} [GeV]	${p_{\mathrm{T}}}^{\mathrm{leading}}$ [GeV]	${p_{\mathrm{T}}}^{\mathrm{trailing}}$ [GeV]	$m_{\ell\ell}$ [GeV]	$\Delta\phi_{\ell\ell}$ [°]	m_{T} [GeV]
110	> 20	> 10	< 40	< 115	[80 - 110]
115	> 20	> 10	< 40	< 115	[80 - 110]
120	> 20	> 10	< 40	< 115	[80 - 120]
125	> 23	> 10	< 43	< 100	[80 - 123]
130	> 25	> 10	< 45	< 90	[80 - 125]
135	> 25	> 10	< 45	< 90	[80 - 128]
140	> 25	> 15	< 45	< 90	[80 - 130]
145	> 25	> 15	< 45	< 90	[80 - 130]
150	> 27	> 25	< 50	< 90	[80 - 150]
155	> 27	> 25	< 50	< 90	[80 - 150]
160	> 30	> 25	< 50	< 60	[90 - 160]
170	> 34	> 25	< 50	< 60	[110 - 170]
180	> 36	> 25	< 60	< 70	[120 - 180]
190	> 38	> 25	< 80	< 90	[120 - 190]
200	> 40	> 25	< 90	< 100	[120 - 200]
250	> 55	> 25	< 150	< 140	[120 - 250]
300	> 70	> 25	< 200	< 175	[120 - 300]
350	> 80	> 25	< 250	< 175	[120 - 350]
400	> 90	> 25	< 300	< 175	[120 - 400]
450	> 110	> 25	< 350	< 175	[120 - 450]
500	> 120	> 25	< 400	< 175	[120 - 500]
550	> 130	> 25	< 450	< 175	[120 - 550]
600	> 140	> 25	< 500	< 175	[120 - 600]

is able to describe the data. The final predicted and observed yields, and the correct way to derive limits and signal strenghts will be covered in the results chapter, Chapter 8.

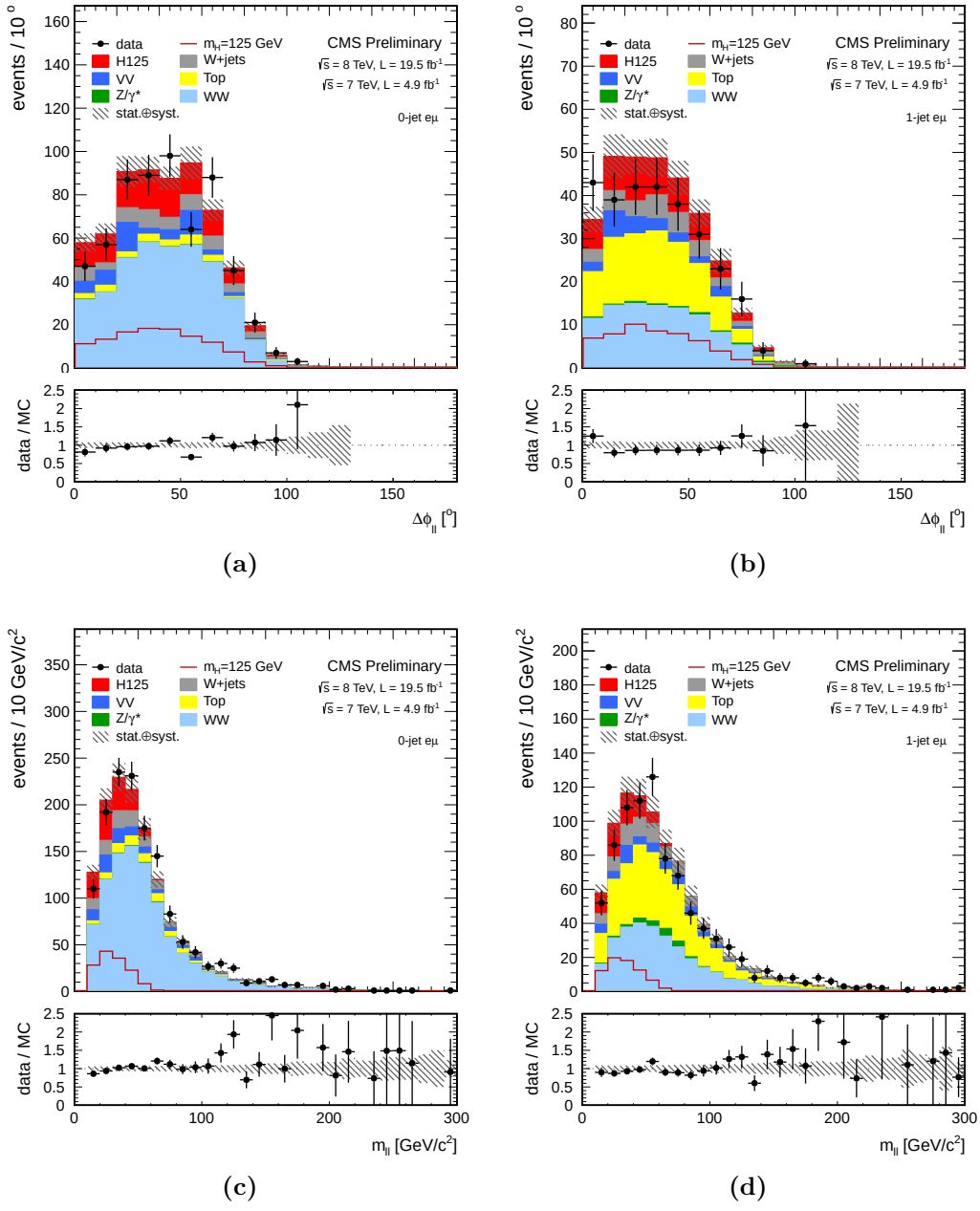

Figure 7.3.: Dilepton $\Delta\phi$ and dilepton invariant mass $m_{\ell\ell}$ distributions at the $\boldsymbol{m_H = 125}$ **GeV cut-based selection** level in the 0-jet (left) and 1-jet (right) categories in the different-flavor final states, for data (points with error bars), for the main backgrounds (stacked histograms) and for a Higgs boson signal with $m_H = 125$ GeV (superimposed and stacked histogram). The cut on each plotted variable is omitted.

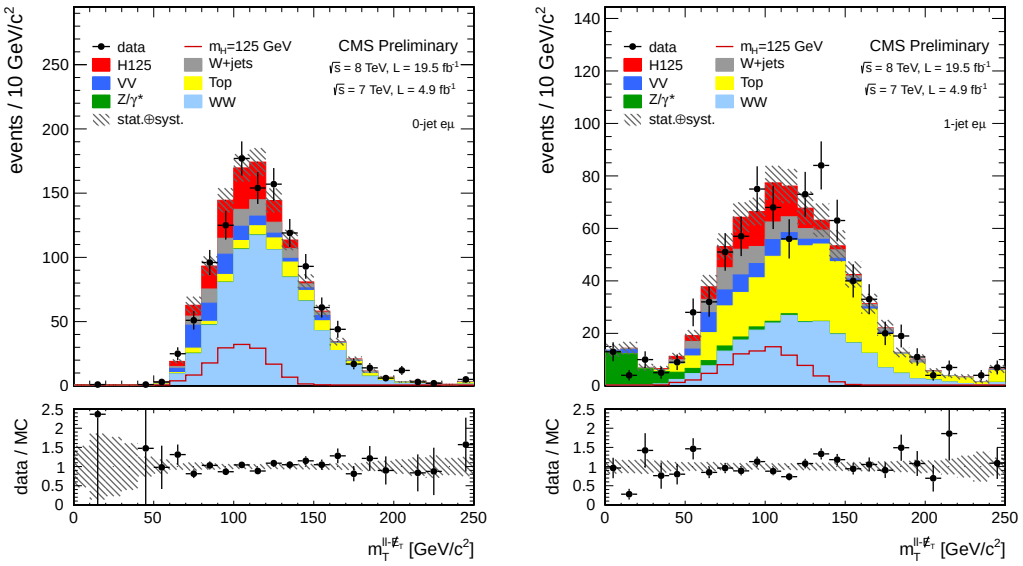

(a) (b)

Figure 7.4.: Transverse mass m_{T} distributions at the $\boldsymbol{m_{\mathrm{H}} = 125}$ **GeV cut-based selection** level in the 0-jet (left) and 1-jet (right) categories in the different-flavor final states, for data (points with error bars), for the main backgrounds (stacked histograms) and for a Higgs boson signal with $m_{\mathrm{H}} = 125$ GeV (superimposed and stacked histogram). The cut on each plotted variable is omitted.

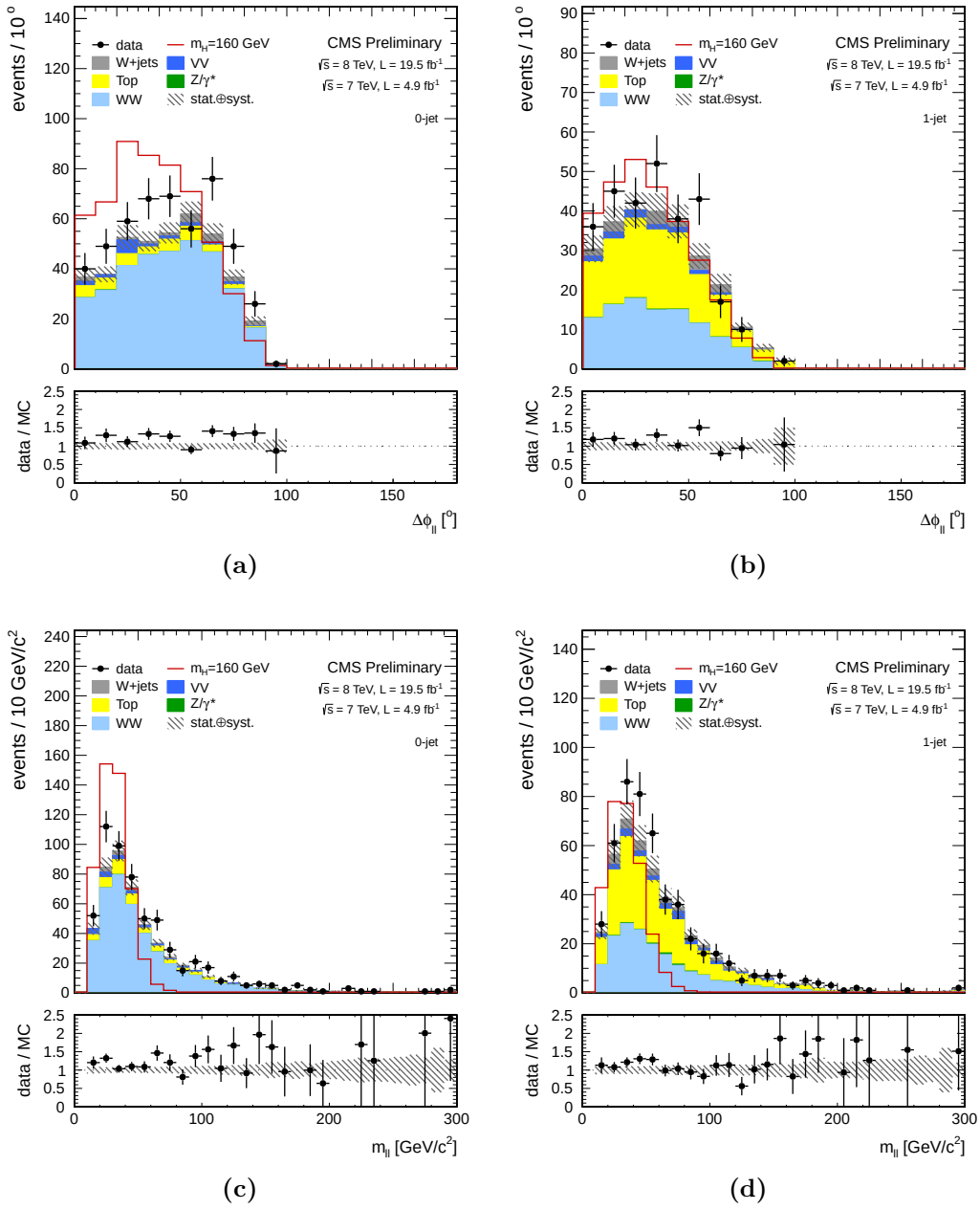

Figure 7.5.: Dilepton $\Delta\phi$ and dilepton invariant mass $m_{\ell\ell}$ distributions at the **$m_H = 160$ GeV cut-based selection** level in the 0-jet (left) and 1-jet (right) categories in the different-flavor final states, for data (points with error bars), for the main backgrounds (stacked histograms) and for a Higgs boson signal with $m_H = 160$ GeV (superimposed). The cut on each plotted variable is omitted.

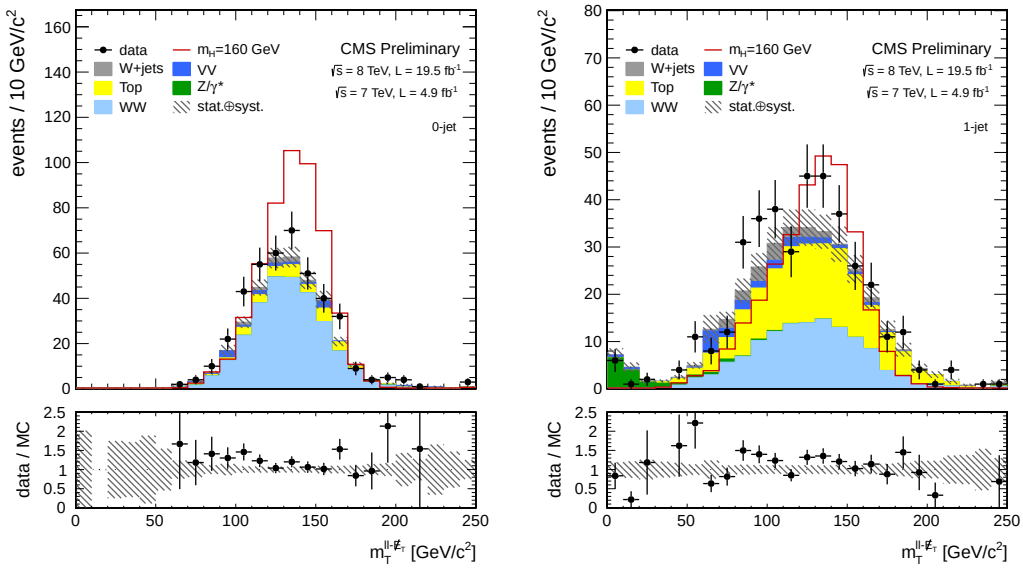

Figure 7.6.: Transverse mass m_{T} distributions at the $\boldsymbol{m_{\mathrm{H}} = 160}$ **GeV cut-based selection** level in the 0-jet (left) and 1-jet (right) categories in the different-flavor final states, for data (points with error bars), for the main backgrounds (stacked histograms) and for a Higgs boson signal with $m_{\mathrm{H}} = 160$ GeV (superimposed). The cut on each plotted variable is omitted.

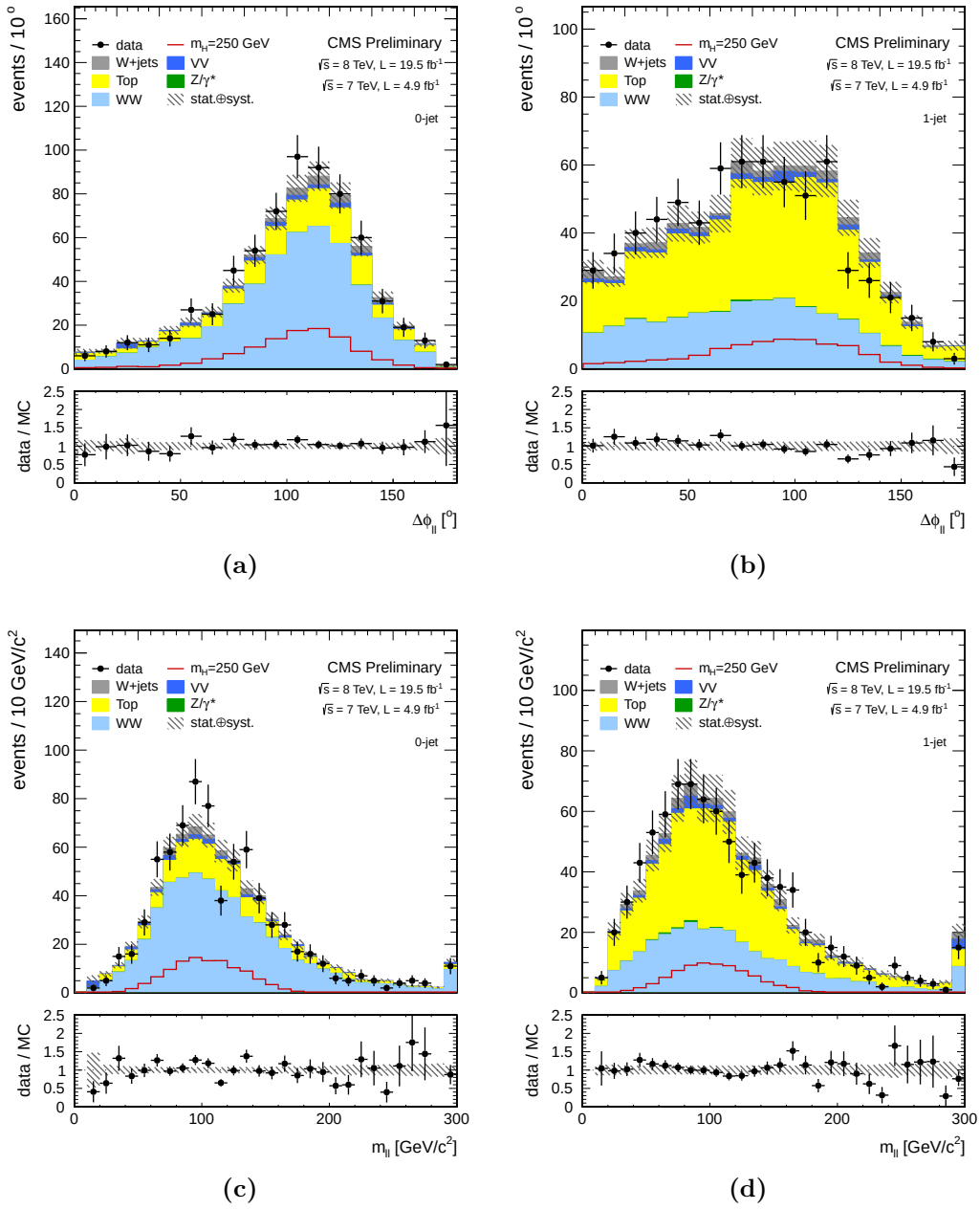

Figure 7.7.: Dilepton $\Delta\phi$ and dilepton invariant mass $m_{\ell\ell}$ distributions at the **$m_H = 250$ GeV cut-based selection** level in the 0-jet (left) and 1-jet (right) categories in the different-flavor final states, for data (points with error bars), for the main backgrounds (stacked histograms) and for a Higgs boson signal with $m_H = 250$ GeV (superimposed). The cut on each plotted variable is omitted.

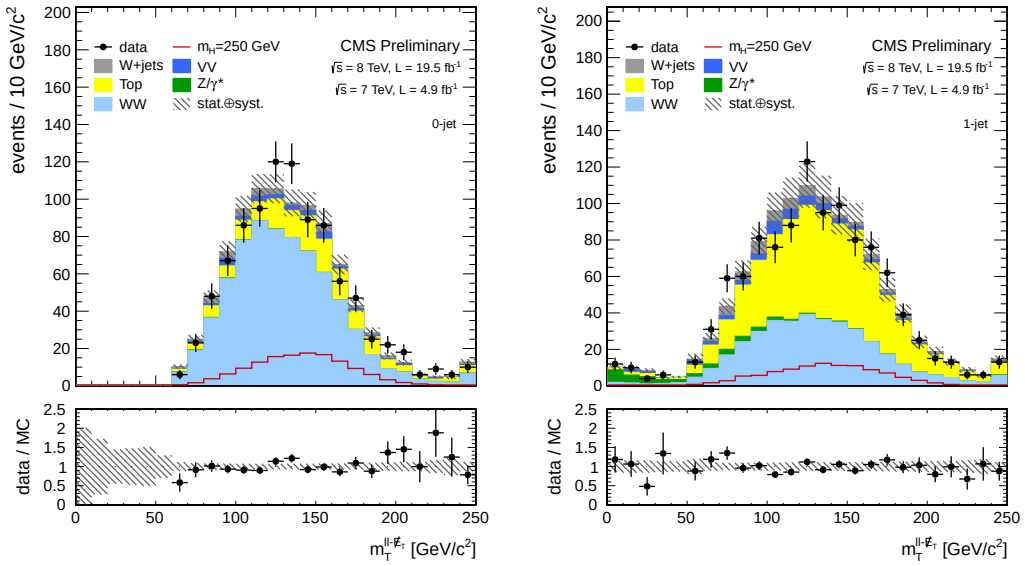

Figure 7.8.: Transverse mass m_{T} distributions at the $\boldsymbol{m_{\mathrm{H}} = 250}$ **GeV cut-based selection** level in the 0-jet (left) and 1-jet (right) categories in the different-flavor final states, for data (points with error bars), for the main backgrounds (stacked histograms) and for a Higgs boson signal with $m_{\mathrm{H}} = 250$ GeV (superimposed). The cut on each plotted variable is omitted.

7.2.2. Shape-based binned template fit in the different-flavor final states

The most simple approach of a template fit to extract the Higgs signal from the data would be an one-dimensional template fit. Nevertheless the analysis has been conducted with a two-dimensional approach using the kinematic variables $m_{\ell\ell}$ and m_{T} as the combination of these two variables results in the most effective discrimination of the signal against some of the backgrounds in both the 0-jet and 1-jet categories. The use of two-dimensional spectral information enhances the sensitivity as some of the backgrounds are better discriminated from the signal than in the one-dimensional case. The analysis has been cross-checked with an one-dimensional template fit applied in $m_{\ell\ell}$ (and in m_{T}) [108]. The expected significance for the full 8 TeV shape-based analysis is 3.34σ with the one-dimensional fit in $m_{\ell\ell}$, while it increases to 4.62σ with the two-dimensional fit[1].

A two-dimensional binned fit using ($m_{\ell\ell}$,m_{T}) template histograms that are obtained from the signal and the background models at the level of the $\mathrm{W^+W^-}$ selection is, in this analysis, used to extract the Higgs boson signal from data. The method is not applied in the same-flavor final state since the modeling of the DY template is too challenging. The data-driven estimate of the normalization of the DY background has already a huge systematic uncertainty of 40 % and it is even harder to estimate the shape of the DY distribution since we have to deal with the mis-measured $E_{\mathrm{T}}^{\mathrm{miss}}$.

In addition to the $\mathrm{W^+W^-}$ selection with the looser $p_{\mathrm{T}}^{\ell\ell} > 30$ GeV (to give the fit more room compared to $p_{\mathrm{T}}^{\ell\ell} > 45$ GeV for the cut-based analysis), a set of requirements are applied before the fit is performed.
For m_{H} hypotheses smaller or equal than 250 GeV:

- $60 < m_{\mathrm{T}} < 280$ GeV
- $12 < m_{\ell\ell} < 200$ GeV

For m_{H} hypotheses greater than 250 GeV:

- $80 < m_{\mathrm{T}} < 380$ GeV, overflow included in the last bin up to $m_{\mathrm{T}} = 600$ GeV
- $12 < m_{\ell\ell} < 450$ GeV, overflow included in the last bin up to $m_{\ell\ell} = 600$ GeV
- $p_{\mathrm{T}}^{\mathrm{l,max}} > 50$ GeV

[1]The definition of the significance is covered in Chapter 8

The selection logic is as follows:

- The transverse mass of the whole system m_{T} is always smaller (or maximally equal) to the Higgs mass m_{H} itself. For this reason the $\frac{s}{\sqrt{s+b}}$ improves by requiring an upper bound of 280 GeV for the low mass selection.
- A similar deduction can be made for the invariant mass of the leptons $m_{\ell\ell}$. Since we require a minimum amount of $E_{\mathrm{T}}^{\mathrm{miss}}$ to be present in the event, the upper bound on $m_{\ell\ell}$ for the low Higgs mass selection is already cut at 200 GeV. This can also be seen in the cut-based analysis.
- The $p_{\mathrm{T}}^{\mathrm{l,max}}$ cut for the high Higgs mass selection increases the $\frac{s}{\sqrt{s+b}}$ as it can be seen in the cut-based selection table, where $p_{\mathrm{T}}^{\mathrm{l,max}} > 55$ GeV for a mass of 250 GeV is required with a rising threshold for higher Higgs masses due to the Lorentz boost of the decay products.
- The signal free high m_{T}, high $m_{\ell\ell}$ region is used in the fit to constrain the $\mathrm{W^+W^-}$ background. Its normalization is left floating in the shape-based analysis as opposed to the data-driven estimate used in the cut-based analysis.

The low Higgs mass templates have 9 bins in $m_{\ell\ell}$ and 14 bins in m_{T}. The bin widths vary within the given range, and are optimized to achieve good separation between the Higgs boson signal and the backgrounds, while retaining adequate template statistics for all processes in the bins. For the high mass templates, there are 8 bins in $m_{\ell\ell}$ and 10 bins in m_{T}. Examples of 2D distributions are shown in Figure 7.9 to illustrate the binning, and a full library of the input distributions for signal and various backgrounds as well as data used for the two-dimensional fits can be found in Appendix A.

All the template bins enter a binned likelihood fit of the data to the signal and background hypotheses in this two-dimensional shape analysis. The fit to the data is able to constrain the main background processes from the distribution of the two-dimensional histograms. The results will be covered in the results chapter, Chapter 8, after we have covered all the systematics entering the fit in Section 7.3.

7.3. Systematics

Since it is impossible to reconstruct an invariant mass peak including all Higgs decay products, the analysis is to a large extent a counting experiment. Therefore it is important to understand the signal efficiency and the background predictions.

The following experimental systematic uncertainties are taken into account:

- **Luminosity:** Based on the CMS online luminosity monitoring the uncertainty is 2.2 % for $\sqrt{s} = 7$ TeV and 2.6 % for $\sqrt{s} = 8$ TeV.

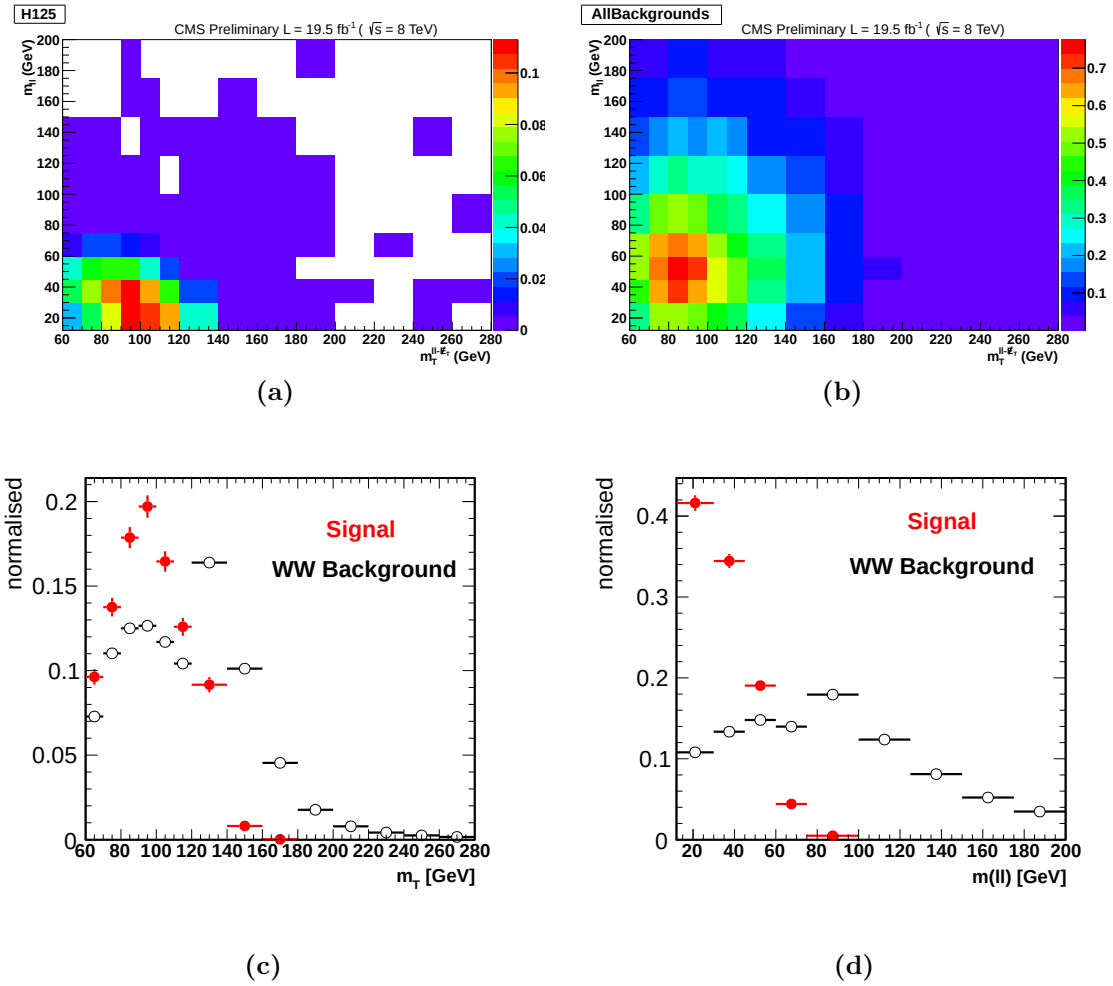

Figure 7.9.: Two-dimensional templates for (a) $m_{\mathrm{H}} = 125$ GeV signal, (b) all backgrounds summed together and (c-d) the projection of the $m_{\mathrm{H}} = 125$ GeV signal and the $\mathrm{W^+W^-}$ background against each axes for $e\mu$ events in the 0-jet category at $\sqrt{s} = 8$ TeV. Each bin in the 2D figures is divided by its bin width.

- **Trigger efficiency:** The data-driven trigger efficiency measurement has its own error. The uncertainty on the trigger efficiency is propagated through the whole analysis workflow and the error on the electron and muon trigger efficiency is at the order of 2 %.

- **Lepton reconstruction and identification efficiency:** The efficiencies are measured in data using the tag and probe method that is shortly described in Section 5.4.3. The reconstruction efficiency uncertainty is at the order of 2 % per lepton leg.

- **Muon momentum and electron energy scale:** Due to several detector effects, the energy scale of the electrons and the momentum scale of the muons have relatively large uncertainties. For electrons, a scale uncertainty of 2 % for the barrel and 4 % for the endcaps, respectively, is assigned. For muons, a momentum scale uncertainty of 1 % independent on the pseudorapidity is assigned. The effect of the lepton scale uncertainty is estimated by scaling the lepton momentum up and down by the associated uncertainty. The contribution to the uncertainty on the lepton efficiency is about 1 %. In addition all correlated observables as e.g. the invariant and tranverse mass, the di-lepton p_{T} and the missing transverse momentum, are recalculated.

- $\boldsymbol{E_{\mathrm{T}}^{\mathrm{miss}}}$ **modeling:** A data-driven method is used to estimate the $\mathrm{Z}/\gamma^{(*)} \to \ell\ell$ background, which is affected by the $E_{\mathrm{T}}^{\mathrm{miss}}$ resolution. Events with neutrinos giving real $E_{\mathrm{T}}^{\mathrm{miss}}$ in the final state also have a small uncertainty. This uncertainty on the event selection efficiency is assessed by applying a Gaussian smearing of 10 % on the x- and y-components of the $E_{\mathrm{T}}^{\mathrm{miss}}$. The 10 % smearing is derived from the comparison of the observation and the MC prediction of the x- and y-components of the $E_{\mathrm{T}}^{\mathrm{miss}}$ for $\mathrm{Z} \to \mathrm{e}^{+}\mathrm{e}^{-}$ and $\mathrm{Z} \to \mu^{+}\mu^{-}$ events. The resulting uncertainty on the event selection efficiency of around 2 % is found.

- **Jet energy scale (JES):** The jet energy scale affects both the jet multiplicity and the jet kinematics. Since we split our analysis in different jet categories it is important that the jet multiplicity is well reproduced. The error is estimated by applying variations of the offical jet uncertainties on the jet energy scale (which depends on the η and the p_{T} of the jet) and computing the variation of the selection efficiency. It is less than 1 %.

- **Pile-up:** The simulated Monte Carlo events have been reweighted according to the data instantaneous luminosity. This re-weighting procedure only slightly affects the

results of the analysis, the event yields changing by less than $\sim 1\,\%$. Due to the conservative approach and the small effect, no systematic uncertainty is attributed to this effect.

- **Background estimation:** All the details of the data-driven estimations were already discussed in Section 6.1, so only a small summary will be given here. It is also important to note that all the above mentioned normalization uncertainties do not apply if a background is estimated with a data-driven technique.
  - W^+W^- *background:* The uncertainty to this background is 10 % for the integrated luminosity of 19.5 fb^{-1}. There is an additional uncertainty of 50 % on the $gg \to WW$ component taken from MC, originating from theoretical uncertainties related to the parton distribution functions and to the QCD renormalization and scales.
  - *Jet-induced backgrounds, W + jets and QCD:* The uncertainty associated to this background has even contributions from statistical and systematic errors. The total systematic uncertainty is, depending on the channel, about 36 %.
  - *Top background:* This background is estimated using b-tagged events and the b-tagging efficiency, which is measured in control regions in data. The associated systematic uncertainties are below 5 % but due to the still dominating statistical error, the overal uncertainty is of the order of 20 %.
  - *Drell-Yan background:* The estimation of this background is affected by the extrapolation from a region with a relaxed $E_{\mathrm{T}}^{\mathrm{miss}}$ cut to the signal region. The uncertainty is conservatively quantified by propagating the variation in the ratio $R_{\mathrm{out/in}}$ between the signal region and a region with a looser $E_{\mathrm{T}}^{\mathrm{miss}}$ cut, leading to an estimate of about 40 %. This effect is small on the final result, due to the reduced Drell-Yan yield expected at the end of the selection ($\sim 1\,\%$).
  - *Other background:* The sub-dominant backgrounds are estimated from simulation with appropriate systematic uncertainties on their cross section. For the WZ and ZZ events the uncertainty is 3 %. These uncertainties must be augmented by the luminosity normalization uncertainty.

The following theoretical systematic uncertainties have been considered:

- **Higgs boson prodcution cross section:** The uncertainties on the inclusive cross section for the Higgs samples have been taken from the LHC Higgs Cross Section

working group report [39]. The uncertainty on the $gg \to \mathrm{H}$ production is about 15 % and it is one of the dominant effects.

- **PDF uncertainties:** The PDF uncertainties are estimated according to the recipe provided by the LHC Higgs Cross Section working group [39]. Different sets of Parton Density Functions (PDFs) have been tested which change the acceptance of the measurement. The effect on the selection efficiency is 2 %.
- **QCD scale uncertainties:** The QCD scale uncertainties are estimated according to the recipe provided by the LHC Higgs Cross Section working group [39]. The normalization and factorization scales in the production of the MC events are varied. The effect on the selection efficiency is between 10 % and 30 % depending on the MC sample.
- **UEPS:** The uncertainty on the underlying event (UE) and parton shower (PS) models is estimated by comparing the signal efficiencies with different parton showers and different tunes of the underlying event generator. The effect is of the order of 8 %.

Since the analysis is divided in different jet categories, we must be sure that the jet multiplicity is well reproduced by the simulation. The jet counting categorization error can be derived by combining the JES uncertainty with the theoretical PDF, QCD scale and UEPS uncertainties. However one has to take into account the missing higher order terms in the production cross section for a certain number of jets [114]. The uncertainty to these missing terms is evaluated through the effect of a variation of the renormalization and factorization scales on the predicted jet bin fractions, estimated using the MC@NLO calculator [115]. This leads to an overall uncertainty on the signal efficiency of about 7 % and 10 % for the 0-jet and 1-jet categories, respectively.

The limited statistics of some MC samples are then considered as an additional uncertainty:

- **Monte Carlo statistics:** The size of the simulated event samples is taken into account. This contributes an uncertainty of about 1 % to the signal efficiency and around 20 % for most backgrounds.

All systematic uncertainties taken into account in this analysis are summarized in Table 7.2, although they should be taken as guidelines, the actual values depend on the Higgs mass hypothesis. The total uncertainty depends on the Higgs mass and the jet

category considered, is typically 15 % on the background estimation and about 20 % on the signal efficiency. The uncertainties are treated as log-normal distributions.

Table 7.2.: Summary of systematic uncertainties relative to the yields (in %) from various signal and background processes. Precise values depend on the final state, jet category and data taking period. The values listed in the table apply to the 0-jet and 1-jet categories. The horizontal bar (−) indicates that the corresponding uncertainty is not applicable. The jet categorization uncertainty originates from the uncertainties in the renormalization and factorization scales that change the fraction of events in each jet category. The systematic uncertainty from the same source is considered fully correlated across all relevant processes listed.

Source	$H \to WW$	$q\bar{q} \to WW$	$g\bar{g} \to WW$	WZ/ZZ	$t\bar{t} + tW$	$Z/\gamma^{(*)} \to \ell\ell$	W+jets	$V/\gamma^{(*)}$
Luminosity	2.2-2.6	–	–	2.2-2.6	–	–	–	2.2-2.6
Lepton efficiency	3.5	3.5	3.5	3.5	–	–	–	3.5
Lepton momentum scale	2.0	2.0	2.0	2.0	–	–	–	2.0
$E_{\mathrm{T}}^{\mathrm{miss}}$ resolution	2.0	2.0	2.0	2.0	–	–	–	1.0
Jet counting categorization	7-20	–	5.5	5.5	–	–	–	5.5
Signal cross section	5-15	–	–	–	–	–	–	–
$q\bar{q} \to WW$ normalization	–	10	–	–	–	–	–	–
$g\bar{g} \to WW$ normalization	–	–	30	–	–	–	–	–
WZ/ZZ cross section	–	–	–	4.0	–	–	–	–
$t\bar{t} + tW$ normalization	–	–	–	–	20	–	–	–
$Z/\gamma^{(*)} \to \ell\ell$ normalization	–	–	–	–	–	40	–	–
W + jets normalization	–	–	–	–	–	–	36	–
MC statistics	1.0	1.0	1.0	4.0	5.0	20	20	20

7.3.1. Systematic uncertainties in the shape-based analysis

There are three different ways to account for systematic uncertainties for a given source:

- *Normalization uncertainty:* - accounts only for the overall normalization assuming that the shape is perfectly known
- *Statistical shape uncertainties:* - account for limited number of events available for the shape extraction
- *Shape variation uncertainties:* - account for uncertainty on the shape itself

Normalization uncertainties are the most straightforward to treat. They are identical to those used in the cut-based analysis. To simplify the analysis in some cases, such as background contributions with large normalization uncertainties, it can be used as the only source of systematic uncertainty ignoring the shape variation. Statistical uncertainties on shape extraction are often negligible. Only if the sample that is used for the shape extraction has a small number of events this effect may become sizable. Lastly, shape variation uncertainties are implemented using three shapes: nominal, *up*-alternative and *down*-alternative.

Experimental uncertainties

The effects from the experimental uncertainties, discussed above, are studied by applying a scaling and/or smearing of certain variables of the physics objects, followed by a subsequent recalculation of all the correlated variables. This is done for Monte Carlo simulation, to account for possible systematic mismeasurements of the data. In the case of scale uncertainties, as the jet energy scale and the lepton momentum scales, the objects transverse momenta are scaled by some factor, and all correlated variables are recalculated. For example the missing transverse momentum, where prior the scaling, the jets are added to the missing transverse momentum and after scaling, re-subtracted. This results in a change of the magnitude as well as in a change of the direction of the missing momentum.

Theoretical uncertainties

The above covered theoretical uncertainties are all treated as normalization uncertainties. Next, we have to discuss the shapes of the main backgrounds of the analysis. Due to the fact that the $\mathrm{W^+W^-}$ shape is entirely taken from Monte Carlo simulation, the analysis is strongly relying on theoretical models and can thus be strongly affected by their uncertainties. Especially higher order QCD radiation effects have an influence on the generated $\mathrm{W^+W^-}$ shape. For this reason, separate $\mathrm{q\bar{q}} \to \mathrm{W^+W^-}$ samples are produced with varied renormalization and factorization scales using the MC@NLO generator to address the shape uncertainty in the theoretical model. The kinematic differences with respect to an alternate event generator are used as an additional uncertainty for $\mathrm{q\bar{q}} \to \mathrm{W^+W^-}$ (MADGRAPH versus MC@NLO) and top-quark production (MADGRAGPH versus POWHEG). The normalization and the shape uncertainty in the $\mathrm{W}+$ jets background

is included by varying the efficiency for misidentified leptons to pass the tight lepton selection and by comparing to the results of a closure test using simulated samples.

Statistical uncertainties

To account for statistical uncertainties, for each distribution going into the shape analysis, the $+1\sigma$ and -1σ shapes were obtained by adding/subtracting the statistical error in each bin and renormalizing it to the nominal distribution. In addition to this procedure a constant normalization uncertainty due to the finite statistics of the sample, used to extract the shape, is assigned.

Chapter 8.

Results of the SM Higgs boson search

Now that all the ingredients of the analysis have been discussed, a small introduction to the statistical procedure to extract the signal will be given, whereafter the results of the Higgs search in the leptonic $H \to W^+ W^-$ channel will be discussed.

8.1. Introduction to the statistical procedure

The statistical methodology used to both interpret subsets of data selected for the $H \to W^+ W^-$ analysis as well as to combine the results from the independent categories, has been developed by the ATLAS and CMS collaborations in the context of the LHC Higgs Combination Group. A general description of the methodology can be found in refs. [116, 117].

Several quantities are defined to compare the observation in data with the expectation: *upper limits* on the production cross section of the $H \to W^+ W^-$ process with and without the presence of the observed new boson; a *significance*, or a *p-value*, characterizing the probability of background fluctuations to reproduce an observed excess; and *signal strengths* (σ/σ_{SM}) that quantify the compatibility of the sizes of the observed excess with the SM signal expectation. The modified frequentist method, CL_s [118, 119], is used to define the exclusion limits. A description of the statistical formula defining these quantities is found in refs. [44, 116].

The number of events in each category and in each bin of the discriminant distributions used to extract the signal is modeled as a Poisson random variable, whose mean value is the sum of the contributions from the processes under consideration. Systematic uncertainties are represented by individual nuisance parameters with log-normal distributions. An

exception is applied to the $q\bar{q} \to W^+W^-$ normalization in the 0- and 1-jet shape-based analyses, described in Section 7.2.2, which is an unconstrained parameter in the fit. The uncertainties affect the overall normalization of the signal and backgrounds as well as the shape of the predictions across the distribution of the observables. Correlation between systematic uncertainties in different categories and final states are taken into account.

8.2. Cut-based results

The data yields and the expected yields for the SM Higgs boson signal and various backgrounds in each of the jet categories and lepton-flavor final states are listed in Table 8.1 and 8.2 for $\sqrt{s} = 7$ TeV and $\sqrt{s} = 8$ TeV, respectively. The data-driven corrections are applied and the reported errors reflect the main normalization systematic uncertainties discussed in Section 7.3. For a SM Higgs boson with $m_H = 125$ GeV around 260 signal events are expected in total for both datasets together. An excess of data with respect to the total background prediction is observed in most final states for the low Higgs mass selections.

The 95% observed and median expected CL upper limits on the production cross section of the $H \to W^+ W^-$ process relative to the SM prediction, both for the same- and different-flavor final state, are shown for the 0- and 1-jet category at $\sqrt{s} = 8$ TeV in Figure 8.1 and Figure 8.2, respectively. While the observed limit is obtained with the observed number of events in data, the expected limit is obtained by setting the number of observed events equal to the total background expectation without any signal. This means that for a given value R, cross sections $\sigma \geq R \cdot \sigma_{SM}$ would be excluded at the 95 % confidence level if the observation would match the background expectation. Next, the green and yellow bands represent the 1σ and 2σ probability intervals around the expected limit. These are obtained by simply varying the number of observed events (in this case equal to the total number of background events) by 1 or 2 standard deviations, respectively, with respect to the nominal background expectation. When the observed upper limit stays above the horizontal red line at 95 % CL limit on $\sigma/\sigma_{SM} = 1$, a Higgs boson produced at the rate predicted by the Standard Model cannot be excluded. Conversely when the observed upper limit drops below the horizontal red line for a certain mass range, one excludes a SM Higgs boson along this mass range at the confidence level of 95 %.

Table 8.1.: Background contributions and yields for 4.9 fb^{-1} of integrated luminosity of $\sqrt{s} = 7$ **TeV** data after the full **cut-based** selection. The data-driven corrections are applied and the reported errors reflect the main systematic uncertainties.

cut-based 0-jet ($\sqrt{s} = 7$ TeV)									
	$Z/\gamma^{(*)}$	$t\bar{t}$ +tW	W+jets	VV	$V\gamma^{(*)}$	WW	all bkg.	m_H120 GeV	data
ee/$\mu\mu$	2.2 ± 4.5	1.4 ± 0.5	3.7 ± 1.3	1.3 ± 0.1	1.2 ± 0.4	37.3 ± 3.7	47.2 ± 6.0	4.9 ± 1.0	49
eμ	0.1 ± 0.1	3.8 ± 1.3	11.1 ± 4.0	1.0 ± 0.1	4.3 ± 0.9	63.7 ± 5.8	84.1 ± 7.3	11.6 ± 2.5	87
total	2.3 ± 4.5	5.2 ± 1.4	14.9 ± 4.2	2.3 ± 0.1	5.5 ± 1.0	101.0 ± 6.9	131.2 ± 9.4	16.5 ± 2.7	136
	$Z/\gamma^{(*)}$	$t\bar{t}$ +tW	W+jets	VV	$V\gamma^{(*)}$	WW	all bkg.	m_H125 GeV	data
ee/$\mu\mu$	3.1 ± 4.2	1.9 ± 0.7	3.8 ± 1.4	1.5 ± 0.1	1.6 ± 0.5	49.1 ± 4.8	61.1 ± 6.6	10.4 ± 2.2	66
eμ	0.1 ± 0.1	4.9 ± 1.7	12.3 ± 4.4	1.2 ± 0.1	4.7 ± 1.0	77.6 ± 7.1	100.8 ± 8.6	20.9 ± 4.3	106
total	3.3 ± 4.2	6.8 ± 1.8	16.1 ± 4.6	2.7 ± 0.2	6.3 ± 1.2	126.7 ± 8.6	161.9 ± 10.8	31.3 ± 4.8	172
	$Z/\gamma^{(*)}$	$t\bar{t}$ +tW	W+jets	VV	$V\gamma^{(*)}$	WW	all bkg.	m_H130 GeV	data
ee/$\mu\mu$	3.4 ± 3.9	2.5 ± 0.9	4.6 ± 1.7	1.8 ± 0.2	1.6 ± 0.5	57.2 ± 5.6	71.1 ± 7.1	16.5 ± 3.5	80
eμ	0.2 ± 0.1	5.8 ± 2.0	13.2 ± 4.7	1.2 ± 0.1	4.7 ± 1.0	86.5 ± 7.9	111.7 ± 9.5	31.3 ± 6.6	113
total	3.6 ± 3.9	8.4 ± 2.2	17.8 ± 5.0	3.0 ± 0.2	6.3 ± 1.2	143.8 ± 9.7	182.8 ± 11.8	47.8 ± 7.4	193
	$Z/\gamma^{(*)}$	$t\bar{t}$ +tW	W+jets	VV	$V\gamma^{(*)}$	WW	all bkg.	m_H160 GeV	data
ee/$\mu\mu$	2.7 ± 1.9	4.1 ± 1.4	0.3 ± 0.1	1.1 ± 0.1	0.6 ± 0.2	39.1 ± 3.8	47.9 ± 4.5	58.1 ± 13.5	51
eμ	0.0 ± 0.0	4.3 ± 1.5	2.7 ± 1.0	0.5 ± 0.0	0.4 ± 0.1	46.1 ± 4.2	54.0 ± 4.6	72.4 ± 16.8	60
total	2.7 ± 1.9	8.4 ± 2.0	3.0 ± 1.0	1.5 ± 0.1	1.1 ± 0.3	85.2 ± 5.7	101.9 ± 6.4	130.5 ± 21.5	111
	$Z/\gamma^{(*)}$	$t\bar{t}$ +tW	W+jets	VV	$V\gamma^{(*)}$	WW	all bkg.	m_H200 GeV	data
ee/$\mu\mu$	1.0 ± 1.1	7.7 ± 2.6	1.0 ± 0.4	2.4 ± 0.2	0.7 ± 0.3	58.6 ± 5.7	71.5 ± 6.4	23.9 ± 6.6	71
eμ	0.0 ± 0.0	10.7 ± 3.6	2.4 ± 0.8	0.8 ± 0.1	0.4 ± 0.2	74.2 ± 6.8	88.5 ± 7.7	27.8 ± 7.7	88
total	1.0 ± 1.1	18.4 ± 4.5	3.3 ± 0.9	3.2 ± 0.2	1.1 ± 0.3	132.8 ± 8.8	159.9 ± 10.0	51.7 ± 10.2	159
	$Z/\gamma^{(*)}$	$t\bar{t}$ +tW	W+jets	VV	$V\gamma^{(*)}$	WW	all bkg.	m_H400 GeV	data
ee/$\mu\mu$	2.1 ± 4.2	12.0 ± 4.1	2.3 ± 0.8	3.2 ± 0.3	0.1 ± 0.1	31.9 ± 3.1	51.6 ± 6.7	8.7 ± 2.5	48
eμ	0.0 ± 0.0	18.4 ± 6.2	3.2 ± 1.2	0.7 ± 0.1	1.6 ± 0.7	41.6 ± 3.8	65.5 ± 7.4	10.7 ± 3.1	61
total	2.1 ± 4.2	30.4 ± 7.4	5.5 ± 1.4	3.9 ± 0.3	1.8 ± 0.7	73.4 ± 4.9	117.1 ± 10.0	19.4 ± 3.9	109
	$Z/\gamma^{(*)}$	$t\bar{t}$ +tW	W+jets	VV	$V\gamma^{(*)}$	WW	all bkg.	m_H600 GeV	data
ee/$\mu\mu$	0.6 ± 1.2	3.3 ± 1.1	1.1 ± 0.4	1.0 ± 0.1	0.1 ± 0.1	7.1 ± 0.8	13.3 ± 1.9	1.4 ± 0.2	15
eμ	0.1 ± 0.1	6.1 ± 2.1	0.9 ± 0.3	0.2 ± 0.0	0.2 ± 0.1	12.3 ± 1.2	19.7 ± 2.4	2.0 ± 0.3	18
total	0.7 ± 1.2	9.4 ± 2.4	2.0 ± 0.5	1.3 ± 0.1	0.3 ± 0.1	19.4 ± 1.5	33.0 ± 3.1	3.5 ± 0.4	33
cut-based 1-jet ($\sqrt{s} = 7$ TeV)									
	$Z/\gamma^{(*)}$	$t\bar{t}$ +tW	W+jets	VV	$V\gamma^{(*)}$	WW	all bkg.	m_H120 GeV	data
ee/$\mu\mu$	5.4 ± 1.9	4.9 ± 1.1	0.2 ± 0.1	0.7 ± 0.1	0.5 ± 0.2	8.9 ± 1.5	20.6 ± 2.7	1.7 ± 0.6	26
eμ	0.3 ± 0.2	11.3 ± 2.4	5.2 ± 1.9	1.2 ± 0.1	1.4 ± 0.4	18.6 ± 2.9	38.0 ± 4.2	5.0 ± 1.7	46
total	5.7 ± 1.9	16.3 ± 2.6	5.4 ± 1.9	1.9 ± 0.1	1.8 ± 0.5	27.5 ± 3.3	58.6 ± 5.0	6.7 ± 1.8	72
	$Z/\gamma^{(*)}$	$t\bar{t}$ +tW	W+jets	VV	$V\gamma^{(*)}$	WW	all bkg.	m_H125 GeV	data
ee/$\mu\mu$	4.4 ± 2.5	6.4 ± 1.4	0.3 ± 0.1	0.9 ± 0.1	0.7 ± 0.3	11.7 ± 1.9	24.3 ± 3.5	3.5 ± 1.1	36
eμ	0.4 ± 0.2	14.5 ± 3.0	5.2 ± 1.9	1.4 ± 0.1	1.4 ± 0.4	22.7 ± 3.6	45.6 ± 5.1	8.9 ± 2.8	54
total	4.8 ± 2.5	20.9 ± 3.3	5.6 ± 1.9	2.3 ± 0.1	2.1 ± 0.5	34.4 ± 4.1	70.0 ± 6.2	12.4 ± 3.0	90
	$Z/\gamma^{(*)}$	$t\bar{t}$ +tW	W+jets	VV	$V\gamma^{(*)}$	WW	all bkg.	m_H130 GeV	data
ee/$\mu\mu$	4.2 ± 2.5	7.4 ± 1.6	1.1 ± 0.4	1.0 ± 0.1	0.7 ± 0.3	13.7 ± 2.3	28.1 ± 3.8	5.7 ± 1.8	40
eμ	0.4 ± 0.2	16.7 ± 3.5	5.4 ± 1.9	1.6 ± 0.1	1.6 ± 0.5	25.6 ± 4.0	51.3 ± 5.7	12.4 ± 3.9	65
total	4.5 ± 2.5	24.2 ± 3.9	6.5 ± 2.0	2.6 ± 0.2	2.3 ± 0.6	39.3 ± 4.6	79.4 ± 6.9	18.1 ± 4.3	105
	$Z/\gamma^{(*)}$	$t\bar{t}$ +tW	W+jets	VV	$V\gamma^{(*)}$	WW	all bkg.	m_H160 GeV	data
ee/$\mu\mu$	5.9 ± 2.1	11.2 ± 2.4	1.0 ± 0.3	0.8 ± 0.1	0.5 ± 0.3	14.6 ± 2.4	34.0 ± 4.0	26.3 ± 9.5	52
eμ	0.1 ± 0.1	15.8 ± 3.3	2.2 ± 0.8	0.8 ± 0.1	0.2 ± 0.1	20.1 ± 3.1	39.2 ± 4.6	36.3 ± 13.1	34
total	6.0 ± 2.1	27.0 ± 4.1	3.1 ± 0.9	1.6 ± 0.1	0.8 ± 0.3	34.7 ± 3.9	73.2 ± 6.1	62.7 ± 16.2	86
	$Z/\gamma^{(*)}$	$t\bar{t}$ +tW	W+jets	VV	$V\gamma^{(*)}$	WW	all bkg.	m_H200 GeV	data
ee/$\mu\mu$	13.5 ± 4.2	22.9 ± 5.0	2.3 ± 0.8	1.4 ± 0.1	0.5 ± 0.2	25.3 ± 4.1	66.0 ± 7.7	11.1 ± 3.9	61
eμ	0.2 ± 0.1	33.7 ± 7.0	2.9 ± 1.1	0.9 ± 0.1	0.0 ± 0.0	36.0 ± 5.5	73.8 ± 9.0	15.8 ± 5.5	50
total	13.7 ± 4.2	56.7 ± 8.6	5.3 ± 1.3	2.3 ± 0.1	0.5 ± 0.2	61.3 ± 6.9	139.8 ± 11.8	26.9 ± 6.7	111
	$Z/\gamma^{(*)}$	$t\bar{t}$ +tW	W+jets	VV	$V\gamma^{(*)}$	WW	all bkg.	m_H400 GeV	data
ee/$\mu\mu$	5.5 ± 2.0	22.5 ± 4.9	1.4 ± 0.5	1.8 ± 0.2	0.8 ± 0.3	20.1 ± 3.3	52.0 ± 6.2	5.7 ± 2.3	66
eμ	0.1 ± 0.1	35.9 ± 7.5	4.8 ± 1.7	0.8 ± 0.1	0.4 ± 0.2	35.3 ± 5.5	77.4 ± 9.5	8.0 ± 3.2	62
total	5.5 ± 2.0	58.4 ± 8.9	6.3 ± 1.8	2.6 ± 0.2	1.2 ± 0.4	55.4 ± 6.5	129.4 ± 11.4	13.8 ± 4.0	128
	$Z/\gamma^{(*)}$	$t\bar{t}$ +tW	W+jets	VV	$V\gamma^{(*)}$	WW	all bkg.	m_H600 GeV	data
ee/$\mu\mu$	0.3 ± 0.6	5.2 ± 1.2	1.1 ± 0.4	0.6 ± 0.1	0.3 ± 0.2	6.6 ± 1.1	14.2 ± 1.8	1.4 ± 0.4	16
eμ	0.0 ± 0.0	9.8 ± 2.1	2.4 ± 0.9	0.3 ± 0.0	0.2 ± 0.2	12.3 ± 2.0	24.9 ± 3.0	2.1 ± 0.7	21
total	0.3 ± 0.6	15.0 ± 2.4	3.5 ± 1.0	0.9 ± 0.1	0.5 ± 0.3	18.9 ± 2.3	39.2 ± 3.5	3.4 ± 0.8	37

Table 8.2.: Background contributions and yields for 19.5 fb^{-1} of integrated luminosity of $\sqrt{s} = 8$ **TeV** data after the full **cut-based** selection. The data-driven corrections are applied and the reported errors reflect the main systematic uncertainties.

cut-based 0-jet ($\sqrt{s} = 8$ TeV)									
	$Z/\gamma^{(*)}$	$t\bar{t}$ +tW	W+jets	VV	$V\gamma^{(*)}$	WW	all bkg.	m_H120 GeV	data
ee/$\mu\mu$	87.3 ± 22.4	7.9 ± 1.4	22.0 ± 7.9	9.6 ± 0.8	8.6 ± 2.3	160.7 ± 14.5	296.1 ± 27.9	33.8 ± 7.2	348
eμ	1.2 ± 0.4	17.4 ± 2.7	43.5 ± 15.6	6.8 ± 0.6	36.8 ± 9.1	249.1 ± 20.5	354.7 ± 27.5	56.9 ± 12.0	406
total	88.5 ± 22.4	25.2 ± 3.0	65.5 ± 17.5	16.4 ± 1.0	45.4 ± 9.4	409.8 ± 25.1	650.8 ± 39.2	90.7 ± 14.0	754
	$Z/\gamma^{(*)}$	$t\bar{t}$ +tW	W+jets	VV	$V\gamma^{(*)}$	WW	all bkg.	m_H125 GeV	data
ee/$\mu\mu$	105.8 ± 17.0	10.2 ± 1.8	27.2 ± 9.8	12.0 ± 1.0	9.8 ± 2.6	209.4 ± 18.7	374.3 ± 27.3	58.2 ± 12.2	431
eμ	1.3 ± 0.4	21.6 ± 3.3	53.7 ± 19.3	8.4 ± 0.7	40.2 ± 9.7	311.2 ± 25.5	436.4 ± 33.6	93.4 ± 19.5	497
total	107.1 ± 17.0	31.8 ± 3.8	80.9 ± 21.7	20.4 ± 1.3	49.9 ± 10.0	520.7 ± 31.7	810.8 ± 43.3	151.6 ± 23.0	928
	$Z/\gamma^{(*)}$	$t\bar{t}$ +tW	W+jets	VV	$V\gamma^{(*)}$	WW	all bkg.	m_H130 GeV	data
ee/$\mu\mu$	114.1 ± 16.5	12.8 ± 2.2	28.7 ± 10.3	13.2 ± 1.1	11.1 ± 2.9	242.2 ± 21.5	422.1 ± 29.3	90.9 ± 19.2	466
eμ	1.4 ± 0.5	24.6 ± 3.8	55.6 ± 20.0	9.4 ± 0.8	42.9 ± 10.4	348.5 ± 28.5	482.4 ± 36.6	140.7 ± 29.6	559
total	115.5 ± 16.5	37.4 ± 4.4	84.4 ± 22.5	22.5 ± 1.4	54.0 ± 10.7	590.7 ± 35.8	904.5 ± 46.9	231.6 ± 35.3	1025
	$Z/\gamma^{(*)}$	$t\bar{t}$ +tW	W+jets	VV	$V\gamma^{(*)}$	WW	all bkg.	m_H160 GeV	data
ee/$\mu\mu$	15.1 ± 7.2	13.6 ± 2.8	6.3 ± 2.3	8.1 ± 0.7	2.2 ± 0.7	169.9 ± 15.2	215.2 ± 17.2	332.4 ± 77.2	263
eμ	0.3 ± 0.1	24.7 ± 4.7	6.2 ± 2.2	4.5 ± 0.4	6.4 ± 2.8	201.1 ± 16.7	243.2 ± 17.8	384.6 ± 89.1	281
total	15.3 ± 7.2	38.2 ± 5.5	12.6 ± 3.2	12.6 ± 0.8	8.6 ± 2.9	371.0 ± 22.6	458.4 ± 24.7	716.9 ± 117.8	544
	$Z/\gamma^{(*)}$	$t\bar{t}$ +tW	W+jets	VV	$V\gamma^{(*)}$	WW	all bkg.	m_H200 GeV	data
ee/$\mu\mu$	20.6 ± 4.1	44.5 ± 7.8	7.4 ± 2.7	16.5 ± 1.4	3.7 ± 1.3	269.1 ± 23.9	361.8 ± 25.7	122.6 ± 33.8	396
eμ	0.6 ± 0.3	58.0 ± 9.5	8.1 ± 2.9	7.0 ± 0.6	4.1 ± 1.5	327.8 ± 27.1	405.6 ± 28.9	153.4 ± 42.4	468
total	21.2 ± 4.1	102.5 ± 12.2	15.6 ± 4.0	23.5 ± 1.5	7.9 ± 2.0	596.8 ± 36.1	767.4 ± 38.6	276.1 ± 54.2	864
	$Z/\gamma^{(*)}$	$t\bar{t}$ +tW	W+jets	VV	$V\gamma^{(*)}$	WW	all bkg.	m_H400 GeV	data
ee/$\mu\mu$	1.3 ± 3.2	57.9 ± 10.1	11.1 ± 4.0	17.7 ± 1.5	1.2 ± 0.5	187.9 ± 16.7	277.2 ± 20.2	56.2 ± 16.1	290
eμ	0.5 ± 0.2	72.2 ± 11.8	13.5 ± 4.9	5.2 ± 0.5	5.3 ± 1.9	214.8 ± 17.7	311.5 ± 21.9	64.8 ± 18.5	303
total	1.8 ± 3.2	130.1 ± 15.5	24.7 ± 6.3	22.8 ± 1.6	6.5 ± 2.0	402.7 ± 24.3	588.6 ± 29.8	120.9 ± 24.5	593
	$Z/\gamma^{(*)}$	$t\bar{t}$ +tW	W+jets	VV	$V\gamma^{(*)}$	WW	all bkg.	m_H600 GeV	data
ee/$\mu\mu$	1.9 ± 3.8	16.4 ± 4.0	4.7 ± 1.7	5.9 ± 0.5	0.4 ± 0.2	61.9 ± 5.7	91.4 ± 8.2	9.0 ± 1.3	97
eμ	0.2 ± 0.1	22.6 ± 5.4	5.2 ± 1.9	1.4 ± 0.2	3.9 ± 1.5	68.2 ± 5.9	101.6 ± 8.3	10.5 ± 1.5	94
total	2.1 ± 3.8	39.1 ± 6.7	9.9 ± 2.5	7.3 ± 0.6	4.4 ± 1.5	130.2 ± 8.2	193.0 ± 11.6	19.6 ± 2.0	191
cut-based 1-jet ($\sqrt{s} = 8$ TeV)									
	$Z/\gamma^{(*)}$	$t\bar{t}$ +tW	W+jets	VV	$V\gamma^{(*)}$	WW	all bkg.	m_H120 GeV	data
ee/$\mu\mu$	11.9 ± 1.5	34.6 ± 3.0	6.1 ± 2.2	4.1 ± 0.4	2.5 ± 1.0	30.6 ± 4.9	89.8 ± 6.4	10.6 ± 3.4	114
eμ	2.8 ± 0.9	69.2 ± 4.0	27.1 ± 9.8	7.1 ± 0.6	11.0 ± 2.8	62.4 ± 9.4	179.6 ± 14.4	26.0 ± 8.2	179
total	14.7 ± 1.8	103.9 ± 5.0	33.2 ± 10.0	11.3 ± 0.8	13.4 ± 3.0	93.0 ± 10.6	269.4 ± 15.8	36.6 ± 8.9	293
	$Z/\gamma^{(*)}$	$t\bar{t}$ +tW	W+jets	VV	$V\gamma^{(*)}$	WW	all bkg.	m_H125 GeV	data
ee/$\mu\mu$	12.9 ± 1.9	44.8 ± 3.8	6.6 ± 2.4	4.9 ± 0.5	2.5 ± 1.0	39.8 ± 6.4	111.5 ± 8.1	19.5 ± 6.1	146
eμ	3.5 ± 1.1	86.5 ± 4.9	31.7 ± 11.4	8.6 ± 0.8	11.1 ± 2.8	77.5 ± 11.6	219.0 ± 17.3	45.4 ± 14.5	224
total	16.5 ± 2.2	131.3 ± 6.2	38.4 ± 11.7	13.5 ± 0.9	13.6 ± 3.0	117.3 ± 13.2	330.5 ± 19.1	64.9 ± 15.7	370
	$Z/\gamma^{(*)}$	$t\bar{t}$ +tW	W+jets	VV	$V\gamma^{(*)}$	WW	all bkg.	m_H130 GeV	data
ee/$\mu\mu$	12.6 ± 2.2	50.8 ± 4.3	8.3 ± 3.0	5.5 ± 0.5	2.2 ± 0.9	44.9 ± 7.2	124.4 ± 9.2	29.2 ± 8.5	173
eμ	3.7 ± 1.2	98.2 ± 5.5	33.2 ± 12.0	9.4 ± 0.8	11.5 ± 2.9	87.0 ± 12.9	242.9 ± 18.7	63.8 ± 18.9	256
total	16.3 ± 2.5	149.0 ± 7.0	41.6 ± 12.3	14.9 ± 1.0	13.7 ± 3.0	131.9 ± 14.8	367.3 ± 20.9	93.0 ± 20.7	429
	$Z/\gamma^{(*)}$	$t\bar{t}$ +tW	W+jets	VV	$V\gamma^{(*)}$	WW	all bkg.	m_H160 GeV	data
ee/$\mu\mu$	7.6 ± 2.0	55.6 ± 4.8	5.3 ± 1.9	4.2 ± 0.4	0.5 ± 0.3	45.6 ± 7.1	118.8 ± 9.0	123.6 ± 43.0	136
eμ	0.7 ± 0.3	95.0 ± 5.8	11.0 ± 4.0	6.0 ± 0.5	1.1 ± 0.4	71.4 ± 10.5	185.2 ± 12.7	214.6 ± 74.1	222
total	8.3 ± 2.1	150.6 ± 7.5	16.3 ± 4.4	10.2 ± 0.7	1.6 ± 0.5	116.9 ± 12.7	304.0 ± 15.5	338.2 ± 85.7	358
	$Z/\gamma^{(*)}$	$t\bar{t}$ +tW	W+jets	VV	$V\gamma^{(*)}$	WW	all bkg.	m_H200 GeV	data
ee/$\mu\mu$	17.8 ± 2.8	133.0 ± 10.7	8.3 ± 3.0	7.9 ± 0.7	0.0 ± 0.0	85.2 ± 13.2	252.1 ± 17.4	56.5 ± 19.3	265
eμ	1.9 ± 0.7	206.5 ± 11.4	17.5 ± 6.3	7.0 ± 0.6	3.0 ± 1.5	129.3 ± 18.9	365.3 ± 23.0	93.2 ± 31.5	418
total	19.8 ± 2.8	339.4 ± 15.6	25.8 ± 7.0	14.9 ± 0.9	3.0 ± 1.5	214.5 ± 23.0	617.4 ± 28.9	149.7 ± 36.9	683
	$Z/\gamma^{(*)}$	$t\bar{t}$ +tW	W+jets	VV	$V\gamma^{(*)}$	WW	all bkg.	m_H400 GeV	data
ee/$\mu\mu$	4.2 ± 1.3	119.5 ± 9.8	7.5 ± 2.7	8.5 ± 0.8	1.7 ± 1.1	73.3 ± 11.6	214.8 ± 15.6	33.8 ± 13.5	221
eμ	2.9 ± 1.0	204.4 ± 11.8	23.7 ± 8.5	7.1 ± 0.6	0.4 ± 0.2	133.2 ± 19.9	371.6 ± 24.7	48.0 ± 19.1	361
total	7.1 ± 1.6	323.9 ± 15.4	31.2 ± 8.9	15.6 ± 1.0	2.1 ± 1.1	206.6 ± 23.0	586.4 ± 29.2	81.8 ± 23.4	582
	$Z/\gamma^{(*)}$	$t\bar{t}$ +tW	W+jets	VV	$V\gamma^{(*)}$	WW	all bkg.	m_H600 GeV	data
ee/$\mu\mu$	0.4 ± 0.8	27.6 ± 2.9	2.4 ± 0.9	2.6 ± 0.3	0.0 ± 0.0	26.1 ± 4.2	59.2 ± 5.2	6.8 ± 2.1	63
eμ	1.2 ± 0.5	58.9 ± 4.9	11.4 ± 4.1	2.5 ± 0.3	0.0 ± 0.0	50.2 ± 7.6	124.2 ± 9.9	10.8 ± 3.3	113
total	1.6 ± 0.9	86.5 ± 5.7	13.7 ± 4.2	5.1 ± 0.4	0.0 ± 0.0	76.3 ± 8.7	183.4 ± 11.2	17.6 ± 3.9	176

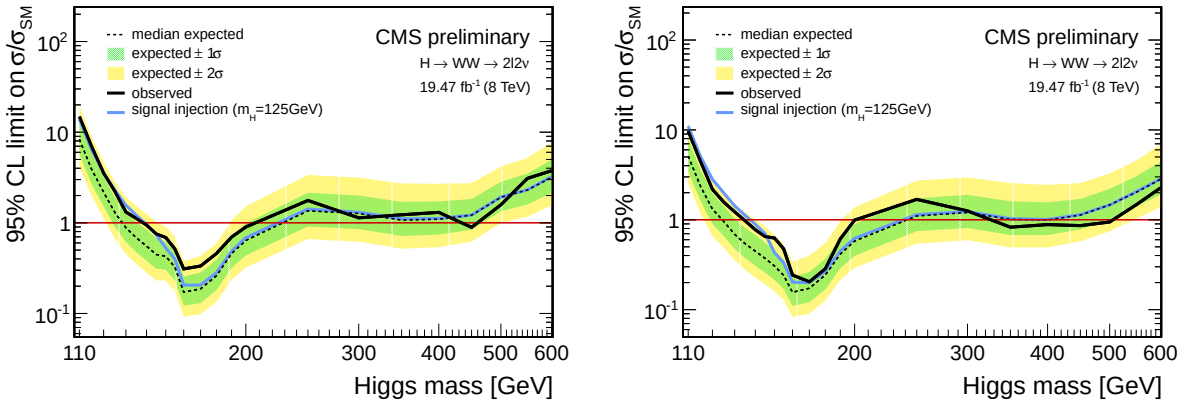

Figure 8.1.: Expected and observed 95 % CL upper limits on the cross section times branching fraction, $\sigma_{\mathrm{H}} \times \mathrm{BR}(\mathrm{H} \to \mathrm{W}^+\,\mathrm{W}^-)$, relative to the SM Higgs expectation for the **cut-based** analysis for the separate lepton-flavor final states in the **0-jet** category for 19.5 fb^{-1} of $\boldsymbol{\sqrt{s} = 8}$ **TeV** data: (a) the same-flavor final state and (b) the different-flavor final state. The expected limit in the presence of the Higgs with $m_{\mathrm{H}} = 125$ GeV is also shown.

An excess of events is observed for low Higgs boson mass hypotheses in all categories except for the 1-jet different-flavor category at $\sqrt{s} = 8$ TeV, which makes the observed limits weaker than expected. A signal injection of a Higgs boson with $m_{\mathrm{H}} = 125$ GeV is also shown[1] as it was found in multiple Higgs decay channels as covered in the discovery paper [44]. The expected limits in these plots show that the same-flavor final state is less sensitive than the different-flavor final state, mainly due to the fact that there is no $\mathrm{Z}/\gamma^{(*)} \to \ell^+\ell^-$ (with $\ell = \mathrm{e}, \mu$) background in the latter.

Both the lepton-flavor final states and both jet categories can be combined resulting in Figure 8.3 for $\sqrt{s} = 7$ TeV and $\sqrt{s} = 8$ TeV. One can still observe the excess of events for the low Higgs boson mass hypotheses, in both the $\sqrt{s} = 7$ TeV as the $\sqrt{s} = 8$ TeV data. The excess extends over a large mass range, due to the poor mass resolution of the $\mathrm{H} \to \mathrm{W}^+\,\mathrm{W}^-$ channel. More detailed conclusions will be drawn after the combination of both data sets in the combined results section, Section 8.4.

[1] One should keep in mind that the signal injection is not just a line, as its expected 1σ band is not shown in the figures.

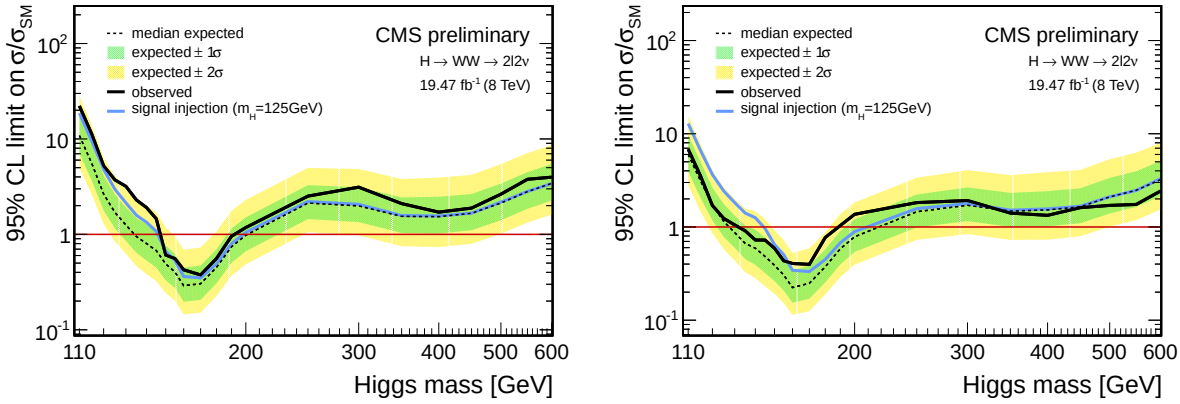

Figure 8.2.: Expected and observed 95 % CL upper limits on the cross section times branching fraction, $\sigma_{\mathrm{H}} \times \mathrm{BR}(\mathrm{H} \to \mathrm{W}^+\,\mathrm{W}^-)$, relative to the SM Higgs expectation for the **cut-based** analysis for the separate lepton-flavor final states in the **1-jet** category for 19.5 fb^{-1} of $\sqrt{s} = 8$ **TeV** data: (a) the same-flavor final state and (b) the different-flavor final state. The expected limit in the presence of the Higgs with $m_{\mathrm{H}} = 125$ GeV is also shown.

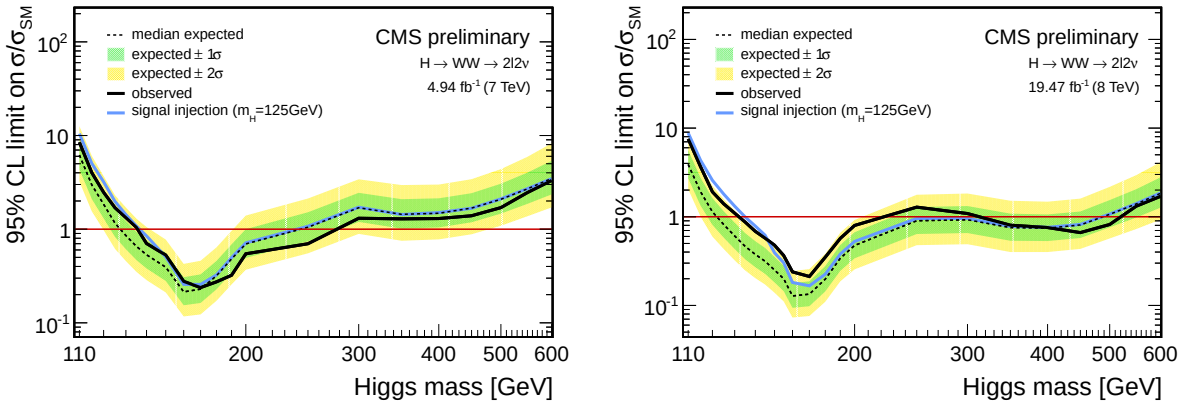

Figure 8.3.: Expected and observed 95 % CL upper limits on the cross section times branching fraction, $\sigma_{\mathrm{H}} \times \mathrm{BR}(\mathrm{H} \to \mathrm{W}^+\,\mathrm{W}^-)$, relative to the SM Higgs expectation for the **cut-based** analysis for all the lepton-flavor final states in the 0- and 1-jet categories combined for (a) 4.9 fb^{-1} of $\sqrt{s} = 7$ TeV data and (b) 19.5 fb^{-1} of $\sqrt{s} = 8$ TeV data. The expected limit in the presence of the Higgs with $m_{\mathrm{H}} = 125$ GeV is also shown.

8.3. Shape-based results

The data yields and the expected yields for the SM Higgs boson signal and various backgrounds in each of the jet categories for the different-flavor final states before the fit takes place are listed in Table 8.4a and Table 8.4b for $\sqrt{s} = 7$ TeV and $\sqrt{s} = 8$ TeV, respectively. The data-driven corrections are applied and the reported errors reflect the main normalization systematic uncertainties discussed in Section 7.3. The looser selection used for the shape-based analysis recovers a large fraction of the signal events, 430 expected different-flavor signal events for $m_{\mathrm{H}} = 125$ GeV, and also accommodates background-dominated regions allowing the fit to impose constraints on the background contributions. No conclusions can be made from these tables alone, since the fit has to be applied.

The expected and observed 95 % CL upper limits on the production cross section of the $\mathrm{H} \to \mathrm{W}^+ \mathrm{W}^-$ process relative to the SM prediction are shown for the 0- and 1-jet category for the different-flavor final state at $\sqrt{s} = 8$ TeV in Figure 8.4. Comparing these two figures to the cut-based result for the different-flavor final state, comparing to Figure 8.1b and Figure 8.2b, respectively, one can see the improvement in the expected limit for the shape-based analysis. Another feature is that the 1-jet different-flavor final state now does show a small excess at $\sqrt{s} = 8$ TeV, while none was visible in the cut-based analysis.

The full shape-based analysis result consists of the combination of the analyses of the shape-based different-flavor final state with the cut-based same-flavor final state and is shown in Figure 8.5 for $\sqrt{s} = 7$ TeV and $\sqrt{s} = 8$ TeV. Comparing these to Figure 8.3, one can see a significant improvement in the expected limit. Again, more detailed conclusions on the result will be drawn after the combination of the two datasets in Section 8.4.

After the template fit to the $(m_{\mathrm{T}}, m_{\ell\ell})$ distribution, the observed signal events as a function of m_{T} and $m_{\ell\ell}$ are shown for the 0- and 1-jet category, for $\sqrt{s} = 7$ TeV and $\sqrt{s} = 8$ TeV combined in Figure 8.6 and Figure 8.7, respectively. In this figure, each process is normalized to the fit result and weighted using the other variable. This means that for the m_{T} distribution, the $m_{\ell\ell}$ distribution is used to compute the ratio of the fitted signal (S) to the sum of signal and background (S+B) in each bin of the $m_{\ell\ell}$ distribution integrating over the m_{T} variable. Since the m_{T} and $m_{\ell\ell}$ variables are essentially uncorrelated, the procedure allows to show unbiased background-subtracted

Table 8.3.: Background contributions and yields for (a) 4.9 fb^{-1} of integrated luminosity of $\sqrt{s} = 7$ **TeV** data and (b) 19.5 fb^{-1} of integrated luminosity of $\sqrt{s} = 8$ **TeV** data after the selection used for the **shape-based** analysis for the different-flavor final states only. The data-driven corrections are applied and the errors reported reflect main systematic uncertainties. Two mass points from the low/high mass selection are shown.

2D shapebased 0-jet ($\sqrt{s} = 7$ TeV)									
	$Z/\gamma^{(*)}$	$t\bar{t}$ +tW	W+jets	VV	$V\gamma^{(*)}$	WW	all bkg.	m_H125 GeV	data
eμ	6.7 ± 2.1	108.4 ± 28.9	179.5 ± 64.6	13.6 ± 0.9	63.6 ± 15.9	908.4 ± 79.1	1280.1 ± 107.4	53.1 ± 10.6	1229
	$Z/\gamma^{(*)}$	$t\bar{t}$ +tW	W+jets	VV	$V\gamma^{(*)}$	WW	all bkg.	m_H400 GeV	data
eμ	1.3 ± 0.5	46.5 ± 16.6	34.5 ± 12.4	6.0 ± 0.4	7.5 ± 2.2	415.9 ± 36.2	511.8 ± 41.8	22.4 ± 6.3	487
2D shape-based 1-jet ($\sqrt{s} = 7$ TeV)									
	$Z/\gamma^{(*)}$	$t\bar{t}$ +tW	W+jets	VV	$V\gamma^{(*)}$	WW	all bkg.	m_H125 GeV	data
eμ	12.0 ± 3.7	251.4 ± 39.6	68.5 ± 24.7	13.5 ± 0.9	11.4 ± 2.6	293.1 ± 45.1	649.9 ± 65.0	22.4 ± 6.9	618
	$Z/\gamma^{(*)}$	$t\bar{t}$ +tW	W+jets	VV	$V\gamma^{(*)}$	WW	all bkg.	m_H400 GeV	data
eμ	4.4 ± 1.4	166.7 ± 31.5	31.5 ± 11.3	7.3 ± 0.5	2.3 ± 0.8	193.1 ± 29.7	405.3 ± 44.8	17.1 ± 6.9	391

(a) 4.9 fb^{-1} of integrated luminosity of $\sqrt{s} = 7$ **TeV** data

2D shape-based 0-jet ($\sqrt{s} = 8$ TeV)									
	$Z/\gamma^{(*)}$	$t\bar{t}$ +tW	W+jets	VV	$V\gamma^{(*)}$	WW	all bkg.	m_H125 GeV	data
$e\mu$	49.7 ± 15.3	499.0 ± 67.9	776.0 ± 279.4	99.8 ± 7.4	282.6 ± 62.3	3751.0 ± 301.6	5458.1 ± 421.6	244.7 ± 49.2	5696
	$Z/\gamma^{(*)}$	$t\bar{t}$ +tW	W+jets	VV	$V\gamma^{(*)}$	WW	all bkg.	m_H400 GeV	data
$e\mu$	12.0 ± 3.7	357.2 ± 49.6	206.2 ± 74.2	43.7 ± 3.3	35.3 ± 7.8	1826.5 ± 146.8	2481.0 ± 172.1	132.4 ± 37.5	2496
2D shape-based 1-jet ($\sqrt{s} = 8$ TeV)									
	$Z/\gamma^{(*)}$	$t\bar{t}$ +tW	W+jets	VV	$V\gamma^{(*)}$	WW	all bkg.	m_H125 GeV	data
$e\mu$	95.4 ± 29.3	1500.1 ± 73.3	372.1 ± 134.0	88.8 ± 6.6	53.6 ± 11.8	1085.4 ± 160.4	3195.3 ± 223.8	111.7 ± 33.9	3255
	$Z/\gamma^{(*)}$	$t\bar{t}$ +tW	W+jets	VV	$V\gamma^{(*)}$	WW	all bkg.	m_H400 GeV	data
$e\mu$	33.7 ± 10.4	1123.9 ± 56.0	172.5 ± 62.1	51.9 ± 3.9	21.3 ± 5.2	743.0 ± 109.9	2146.3 ± 138.7	102.7 ± 40.8	2141

(b) 19.5 fb^{-1} of integrated luminosity of $\sqrt{s} = 8$ **TeV** data

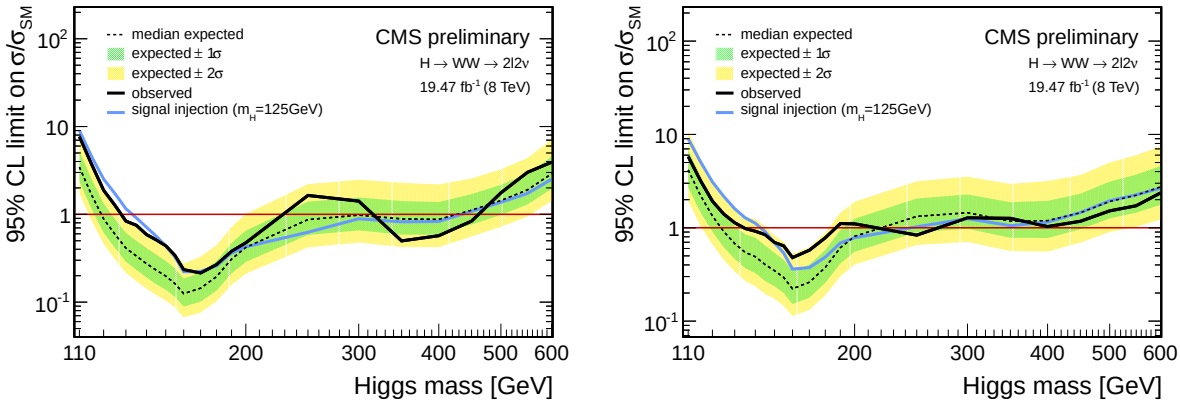

Figure 8.4.: Expected and observed 95 % CL upper limits on the cross section times branching fraction, $\sigma_{\mathrm{H}} \times \mathrm{BR}(\mathrm{H} \to \mathrm{W}^+\,\mathrm{W}^-)$, relative to the SM Higgs expectation for the **shape-based** analysis for the **different-flavor** final states for 19.5 fb^{-1} of $\sqrt{s} = 8$ **TeV** data: (a) 0-jet category and (b) 1-jet category. The expected limit in the presence of the Higgs with $m_{\mathrm{H}} = 125$ GeV is also shown.

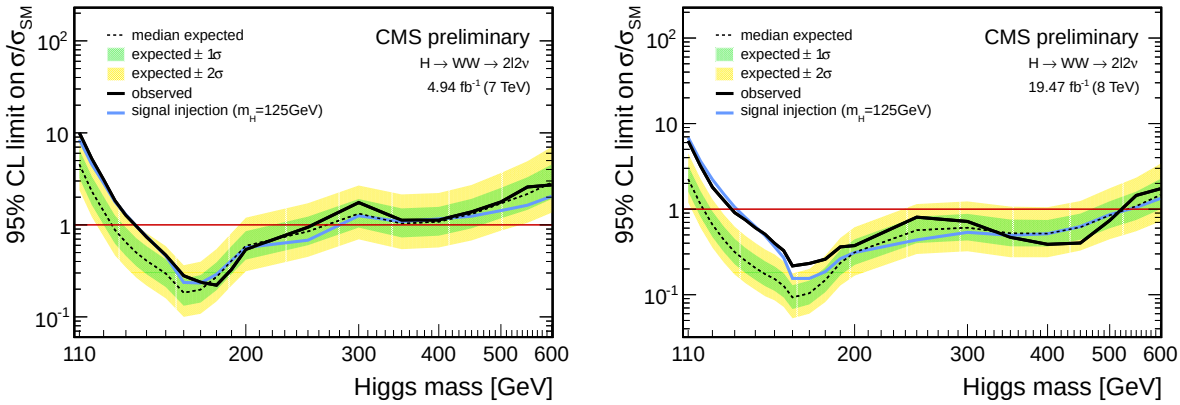

Figure 8.5.: Expected and observed 95 % CL upper limits on the cross section times branching fraction, $\sigma_{\mathrm{H}} \times \mathrm{BR}(\mathrm{H} \to \mathrm{W}^+\,\mathrm{W}^-)$, relative to the SM Higgs expectation for the **shape-based** analysis for (a) 4.9 fb^{-1} of $\sqrt{s} = 7$ TeV data and (b) 19.5 fb^{-1} of $\sqrt{s} = 8$ TeV data. The analysis in the different-flavor final state in the 0- and 1-jet categories is combined with the cut-based analysis in the same-flavor final state. The expected limit in the presence of the Higgs with $m_{\mathrm{H}} = 125$ GeV is also shown.

data distributions. The observed distributions show good agreement with the expected SM Higgs boson distributions.

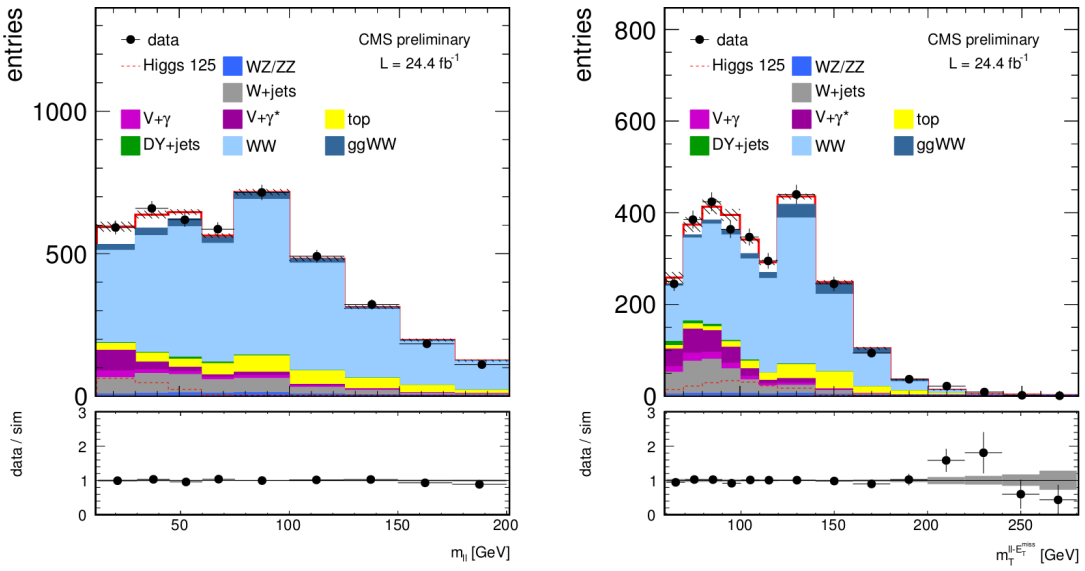

(a) $m_{\ell\ell}$ projection (b) m_T projection

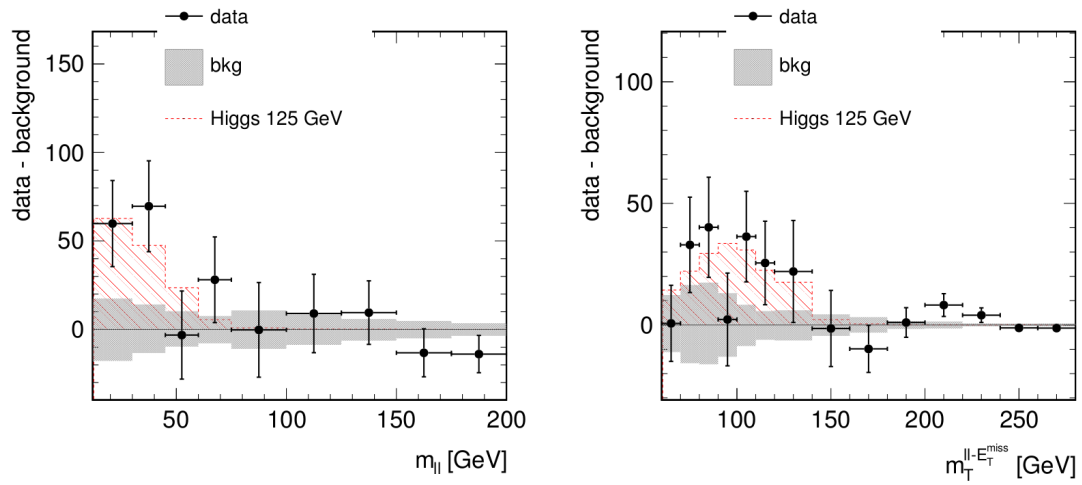

(c) $m_{\ell\ell}$ projection, bkg subtracted data (d) m_T projection, bkg subtracted data

Figure 8.6.: The m_T and $m_{\ell\ell}$ distributions in the eμ final state for the **0-jet category** for observed data superimposed on signal + background events and separately for the signal events alone (a,b) and background-subtracted data with best-fit signal component (c,d). The signal and background processes are normalized to the result of the template fit to the $(m_{\ell\ell}, m_T)$ distribution and weighted according to the observed S/(S + B) ratio in each bin of the $m_{\ell\ell}$ (m_T) distribution integrating over the m_T ($m_{\ell\ell}$) variable. In order to better visualize a peak structure, an extended m_T range including $m_T = 0 - 60$ GeV is shown, with the normalization of signal and background events extrapolated from the fit result.

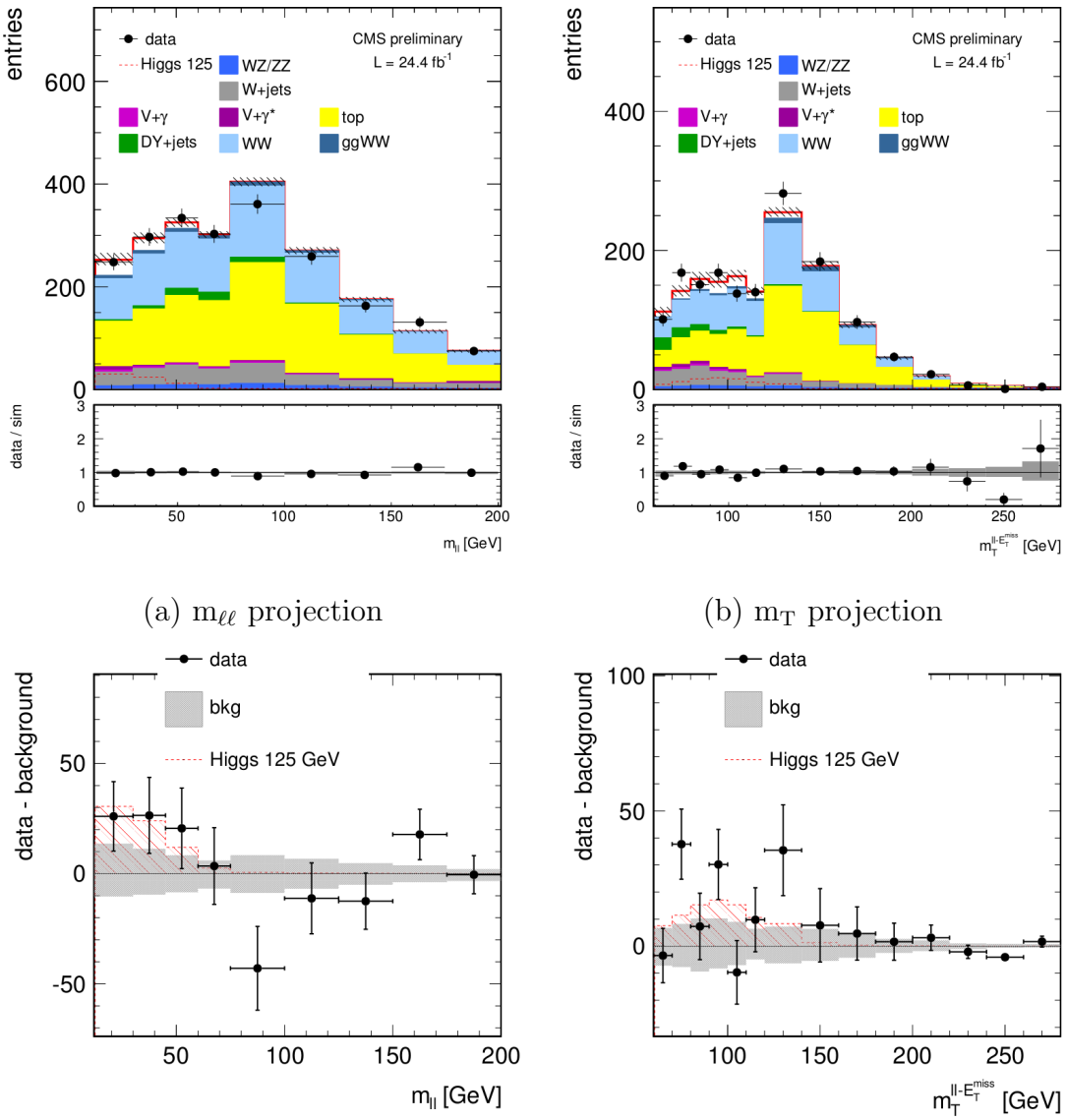

(a) $m_{\ell\ell}$ projection

(b) m_T projection

(c) $m_{\ell\ell}$ projection, bkg subtracted data

(d) m_T projection, bkg subtracted data

Figure 8.7.: The m_T and $m_{\ell\ell}$ distributions in the eμ final state for the **1-jet category** for observed data superimposed on signal + background events and separately for the signal events alone (a,b) and background-subtracted data with best-fit signal component (c,d). The signal and background processes are normalized to the result of the template fit to the $(m_{\ell\ell}, m_T)$ distribution and weighted according to the observed S/(S + B) ratio in each bin of the $m_{\ell\ell}$ (m_T) distribution integrating over the m_T ($m_{\ell\ell}$) variable. To better visualize a peak structure, an extended m_T range including $m_T = 0 - 60$ GeV is shown, with the normalization of signal and background events extrapolated from the fit result.

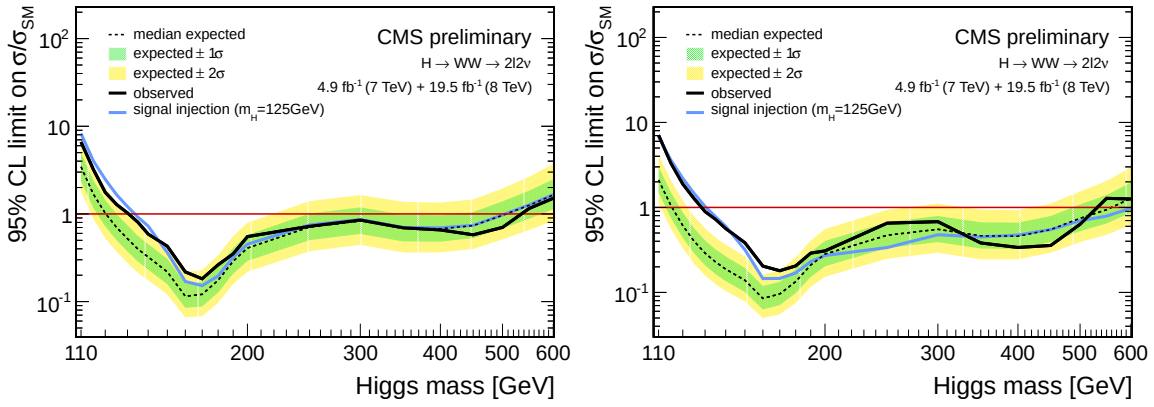

Figure 8.8.: Expected and observed 95 % CL upper limits on the cross section times branching fraction, $\sigma_{\mathrm{H}} \times \mathrm{BR}(\mathrm{H} \to \mathrm{W}^+\,\mathrm{W}^-)$, relative to the SM Higgs expectation for **the full combined $\sqrt{s} = 7$ TeV + $\sqrt{s} = 8$ TeV analysis**: (a) cut-based and (b) shape-based. The expected limit in the presence of the Higgs with $m_{\mathrm{H}} = 125$ GeV is also shown.

8.4. Combined results

The final results of the cut-based and shape-based analysis for the combined $\sqrt{s} = 7$ TeV and $\sqrt{s} = 8$ TeV dataset are shown in Figure 8.8. The expected and observed upper limits, together with the significances for the background-only hypothesis to account for the excess in units of standard deviations (sd) are tabulated in Table 8.4 and Table 8.5. Similar tables for the separate datasets can be found in Appendix B. From the expected upper limit, one can deduce that the shape-based analysis is able to constrain the upper limits further than the cut-based analysis.

The combination of the results from the $\sqrt{s} = 7$ TeV and the $\sqrt{s} = 8$ TeV data, using the shape analysis, excludes a Higgs boson in the mass range $128 - 530$ GeV at 95 % CL. The expected exclusion range for the background-only hypothesis is $115 - 560$ GeV. An excess of events is observed for hypothetical low Higgs boson masses, which makes the observed limits weaker than the expected ones. Due to the poor mass resolution of the $\mathrm{H} \to \mathrm{W}^+\,\mathrm{W}^-$ channel the excess extends over a large mass range. To confirm that there is no other significant excess, the 95 % CL upper limits for the shape-based analysis using the full dataset is shown in Figure 8.9 for which a Higgs with $m_{\mathrm{H}} = 125$ GeV has been added to the background processes. No excess is observed and additional Higgs bosons with SM-like properties are excluded in the mass range $117 - 538$ GeV at 95 %

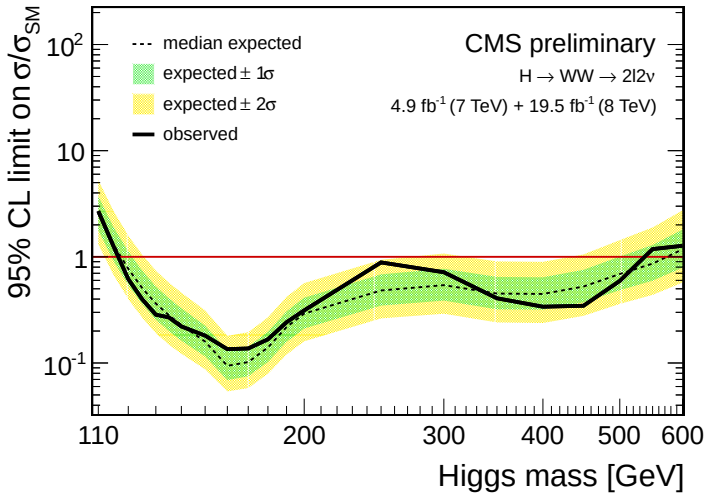

Figure 8.9.: Expected and observed 95 % CL upper limits on the cross section times branching fraction, $\sigma_{\mathrm{H}} \times \mathrm{BR}(\mathrm{H} \to \mathrm{W}^+\,\mathrm{W}^-)$, relative to the SM Higgs expectation for the **full combined** $\sqrt{s} = 7$ TeV + $\sqrt{s} = 8$ TeV **shape-based** analysis, where a Higgs with $\boldsymbol{m_{\mathrm{H}} = 125}$ **GeV** has been **added to the background processes**.

confidence level, when assuming that a SM Higgs with $m_{\mathrm{H}} = 125$ GeV is present in the data.

The expected and observed significances shown in the different tables in this section and Appendix B are summarized together with the signal strength, the best fit value of $\sigma/\sigma_{\mathrm{SM}}$, for a SM Higgs with a mass of 125 GeV in Table 8.6. The significance of the excess with respect to the background-only hypothesis at this mass are 2.3 and 3.5 standard deviations for the $\sqrt{s} = 7$ TeV and $\sqrt{s} = 8$ TeV shape-based analysis, respectively, and 4.3 standard deviations for the combined dataset. The observed $\sigma/\sigma_{\mathrm{SM}}$ value for $m_{\mathrm{H}} = 125$ GeV using the shape-based analysis is $0.85^{+0.24}_{-0.21}$ (stat.+ syst.), making it compatible with the Standard Model Higgs boson. Lastly, Figure 8.10 shows the compatibility of the signal strength of all the different channels for both the $\sqrt{s} = 7$ TeV and $\sqrt{s} = 8$ TeV data for the shape-based analysis for different Higgs masses. A good compatibility is found.

On the fourth of July 2012, the CMS collaboration annouced the observation of a new boson [44, 120]. The search result consited of the combination of five decay modes: $\gamma\gamma$, ZZ, $\mathrm{W}^+\,\mathrm{W}^-$, $\tau^+\tau^-$ and $\mathrm{b\bar{b}}$, with an integrated luminosity of 4.9 fb^{-1} at $\sqrt{s} = 7$ TeV and 5.3 fb^{-1} at $\sqrt{s} = 8$ TeV. The $\mathrm{H} \to \mathrm{W}^+\,\mathrm{W}^- \to 2\ell\,2\nu$ decay mode discussed

Table 8.4.: Expected and observed **cut-based** upper limits on the $H \to W^+ W^-$ production cross section relative to the SM prediction, and the expected and observed significances for the background-only hypothesis to account for the excess in units of standard deviations, for all the lepton-flavor final states and 0- and 1-jet categories combined using **4.9 fb^{-1} of $\sqrt{s} = 7$ TeV and 19.5 fb^{-1} of $\sqrt{s} = 8$ TeV data**.

Higgs mass [GeV]	Observed limits	Median limits	68% Range	95% Range	Observed significance	Expected significance
110	6.62	3.45	[2.39, 4.98]	[1.80, 6.90]	2.03	0.65
115	3.21	1.68	[1.17, 2.42]	[0.88, 3.36]	2.04	1.30
120	1.76	1.02	[0.72, 1.45]	[0.53, 2.00]	1.79	2.09
125	1.28	0.70	[0.50, 0.99]	[0.37, 1.35]	1.98	2.97
130	1.03	0.52	[0.37, 0.74]	[0.28, 1.01]	2.19	3.91
135	0.80	0.40	[0.29, 0.56]	[0.21, 0.76]	2.37	5.03
140	0.59	0.32	[0.23, 0.45]	[0.17, 0.62]	2.02	6.01
150	0.43	0.22	[0.16, 0.31]	[0.12, 0.42]	2.56	7.98
160	0.22	0.11	[0.08, 0.16]	[0.07, 0.22]	2.30	11.24
170	0.18	0.12	[0.09, 0.17]	[0.07, 0.23]	1.47	10.33
180	0.26	0.18	[0.13, 0.25]	[0.10, 0.34]	0.00	8.12
190	0.35	0.29	[0.21, 0.41]	[0.16, 0.56]	0.63	5.90
200	0.55	0.41	[0.29, 0.58]	[0.22, 0.79]	1.04	4.61
250	0.72	0.71	[0.50, 1.01]	[0.38, 1.40]	0.14	2.83
300	0.85	0.83	[0.59, 1.19]	[0.44, 1.64]	0.00	2.40
350	0.69	0.69	[0.49, 0.98]	[0.36, 1.37]	0.00	2.89
400	0.66	0.68	[0.48, 0.97]	[0.36, 1.35]	0.00	2.85
450	0.58	0.74	[0.53, 1.05]	[0.40, 1.46]	0.00	2.54
500	0.70	0.96	[0.68, 1.39]	[0.51, 1.95]	0.00	1.99
550	1.15	1.25	[0.88, 1.84]	[0.65, 2.65]	0.00	1.65
600	1.51	1.65	[1.13, 2.48]	[0.83, 3.70]	0.00	1.33

Table 8.5.: Expected and observed **shape-based** upper limits on the $H \to W^+ W^-$ production cross section relative to the SM prediction, and the significances for the background-only hypothesis to account for the excess in units of standard deviations, for all the lepton-flavor final states and 0- and 1-jet categories combined using **4.9 fb^{-1} of $\sqrt{s}$ = 7 TeV and 19.5 fb^{-1} of $\sqrt{s}$ = 8 TeV data** (same-flavor final states are cut-based).

Higgs mass [GeV]	Observed limits	Median limits	68% Range	95% Range	Observed significance	Expected significance
110	7.09	2.10	[1.49, 3.00]	[1.11, 4.15]	4.02	1.02
115	3.31	1.05	[0.75, 1.50]	[0.56, 2.08]	4.50	1.98
120	1.88	0.61	[0.44, 0.87]	[0.33, 1.21]	4.28	3.37
125	1.27	0.40	[0.29, 0.57]	[0.22, 0.78]	4.32	5.13
130	0.89	0.29	[0.21, 0.41]	[0.16, 0.57]	4.32	7.07
135	0.73	0.23	[0.16, 0.32]	[0.12, 0.44]	4.56	8.95
140	0.56	0.19	[0.14, 0.27]	[0.10, 0.36]	4.42	10.72
150	0.38	0.14	[0.10, 0.19]	[0.08, 0.27]	3.67	13.75
160	0.20	0.09	[0.06, 0.12]	[0.05, 0.16]	3.29	19.25
170	0.18	0.10	[0.07, 0.13]	[0.06, 0.18]	2.19	16.45
180	0.20	0.13	[0.10, 0.19]	[0.08, 0.26]	1.34	11.76
190	0.29	0.21	[0.15, 0.30]	[0.12, 0.41]	0.00	8.46
200	0.31	0.28	[0.20, 0.40]	[0.15, 0.56]	0.00	6.77
250	0.65	0.47	[0.33, 0.67]	[0.25, 0.94]	1.20	4.31
300	0.68	0.55	[0.39, 0.79]	[0.29, 1.11]	0.53	3.69
350	0.38	0.46	[0.33, 0.67]	[0.25, 0.94]	0.00	4.48
400	0.34	0.46	[0.33, 0.66]	[0.24, 0.93]	0.00	4.43
450	0.36	0.55	[0.39, 0.79]	[0.29, 1.11]	0.00	0.00
500	0.63	0.74	[0.52, 1.09]	[0.39, 1.54]	0.00	0.00
550	1.28	0.94	[0.65, 1.40]	[0.48, 2.05]	0.77	0.00
600	1.26	1.28	[0.86, 1.96]	[0.62, 2.96]	0.04	0.00

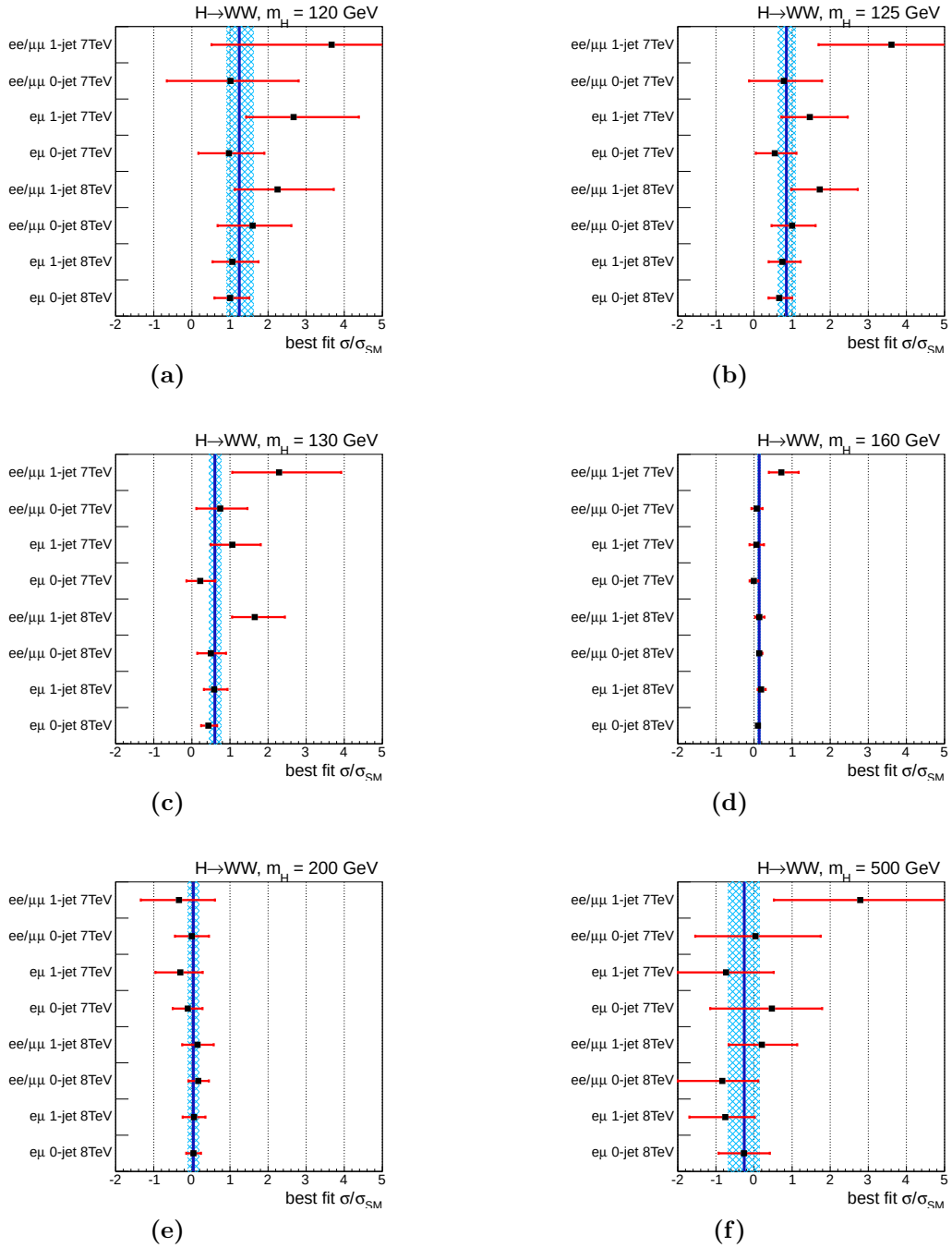

Figure 8.10.: Compatibility of the different channels for the $\sqrt{s} = 7$ TeV and $\sqrt{s} = 8$ TeV data for the shape-based analysis for the following Higgs boson mass hypotheses: (a) 120, (b) 125, (c) 130, (d) 160, (e) 200 and (f) 500 GeV. All the mass hypotheses are tested using the standard set of SM backgrounds.

Table 8.6.: Expected and observed significance and the signal strength $\sigma/\sigma_{\mathrm{SM}}$ for a SM Higgs with a mass of 125 GeV. The results are reported for the cut-based approach and for the shape-based approach.

	expected/observed significance		
analysis	$\sqrt{s} = 7$ TeV	$\sqrt{s} = 8$ TeV	$\sqrt{s} = 7$ TeV + $\sqrt{s} = 8$ TeV
cut	1.8/1.0	2.4/2.3	3.0/2.0
shape	2.6/1.8	4.6/3.5	5.1/4.3
	signal strength $\sigma/\sigma_{\mathrm{SM}}$ (68% C.L.)		
analysis	$\sqrt{s} = 7$ TeV	$\sqrt{s} = 8$ TeV	$\sqrt{s} = 7$ TeV + $\sqrt{s} = 8$ TeV
cut	0.60 -0.60 +0.63	0.71 -0.40 +0.40	0.68 -0.35 +0.35
shape	1.00 -0.44 +0.48	0.82 -0.23 +0.26	0.85 -0.21 +0.24

in this work was part of this combination. An excess of events above the expected background, with a significance of 5.0 σ, at a mass near 125 GeV, was found. A few months later, the search result was updated using the final full 2011 and 2012 datasets [121]. The mass of the new boson has been measured from the $\gamma\gamma$ and $\mathrm{ZZ} \to 4\ell$ channels to be 125.7 ± 0.3 (stat.) ± 0.3 (syst.) GeV. The event yields obtained by the different analyses targeting specific decay modes and production mechanisms are consistent with those expected for the SM Higgs boson. The best-fit signal strength $\sigma/\sigma_{\mathrm{SM}}$ for all channels combined is 0.80 ± 0.14 at the measured mass.

Chapter 9.

Study of the spin-parity properties

The determination of the quantum numbers, such as spin (J) and parity (P), of the Higgs-like boson discovered at approximately 125 GeV by ATLAS and CMS is crucial. A spin-parity hypothesis can be written as J^P. Phenomenological studies of the scattering amplitudes of Higgs [17–19] or exotic boson decays to the WW final state have been performed, and are described in References [122, 123]. It is demonstrated in Reference [123] that the WW channel has a good sensitivity to distinguish between a 0^+ boson like the Standard Model Higgs boson and a spin-2 resonance, which couples to the dibosons through minimal couplings, referred to as 2^+_{min}. The reference also shows some sensitivity to distinguish between a 0^+ boson and the pseudoscalar 0^- boson.

The W^+W^- final state cannot be fully reconstructed if both W bosons decay leptonically, because the two neutrinos are not detected. However, kinematic observables such as the opening angle between the two reconstructed leptons in the transverse plane, the dilepton invariant mass and the transverse mass can be used to distinguish between the SM Higgs boson hypothesis and other exotic resonances with different spin or parity. The low-mass shape-based selection, as discussed in the search analysis in Section 7.2.2 will be used as a baseline for this study.

This chapter of the thesis will cover the performed spin-parity analysis to separate the SM Higgs 0^+ boson from a spin-2 resonance with minimal couplings 2^+_{min} and a SM Higgs-like pseudoscalar 0^- particle [123]. First the needed MC samples will be covered followed by the validation of the samples. Next the analysis strategy is discussed followed by the results. The results of the analysis can also be found in our publication [89].

Table 9.1.: List of the additional Monte Carlo samples. Each sample is generated for both $\sqrt{s} = 7$ TeV and $\sqrt{s} = 8$ TeV. The Standard Model MC samples can be found in Table 5.1.

hypothesis	decay mode
0^+	$gg \to H \to WW \to (\ell\nu)(\ell\nu),\ \ell = e, \mu$
	$gg \to H \to WW \to (\ell\nu)(\tau\nu),\ \ell = e, \mu$
	$gg \to H \to WW \to (\tau\nu)(\tau\nu)$
0^-	$gg \to X \to WW \to (\ell\nu)(\ell\nu), \ell = e,\ \mu$
	$gg \to X \to WW \to (\ell\nu)(\tau\nu), \ell = e,\ \mu$
	$gg \to X \to WW \to (\tau\nu)(\tau\nu)$
2^+_{min}	$gg \to \text{Graviton} \to WW \to (\ell\nu)(\ell\nu),\ \ell = e, \mu$
	$gg \to \text{Graviton} \to WW \to (\ell\nu)(\tau\nu),\ \ell = e, \mu$
	$gg \to \text{Graviton} \to WW \to (\tau\nu)(\tau\nu)$
	$q\bar{q} \to \text{Graviton} \to WW \to (\ell\nu)(\ell\nu),\ \ell = e, \mu$
	$q\bar{q} \to \text{Graviton} \to WW \to (\ell\nu)(\tau\nu),\ \ell = e, \mu$
	$q\bar{q} \to \text{Graviton} \to WW \to (\tau\nu)(\tau\nu)$

9.1. Data samples

The data and Standard Model MC samples used in this analysis are the same as in the SM Higgs search analysis, see Section 5.3. The additional signal samples for the $gg \to X \to W^+ W^- \to 2\ell 2\nu$ reaction with $m_X = 125$ GeV, are simulated using the JHUGen Monte Carlo [124]. In particular, the SM Higgs boson (0^+), the pseudoscalar (0^-) and the spin-2 resonance with minimal couplings (2^+_{min}) hypotheses have been generated, corresponding to the samples listed in Table 9.1. For the latter, also the $q\bar{q} \to X \to W^+ W^-$ production was generated. The fraction of $q\bar{q} \to X$ in the 2^+_{min} hypothesis will be denoted as $f_{q\bar{q}}$ (%). JHUGen is a LO Monte Carlo and is interfaced to PYTHIA for showering, hadronization and the Multiple Parton Interactions. A 0^+ JHUGen sample was generated to be able to validate the JHUGen Monte Carlo event samples, which will be discussed in the following section. In this chapter, the mass of the generated signal samples is $m_X = 125$ GeV, even if it is not specified in the text.

9.2. JHUGen validation

To validate the JHUGen simulation, the main kinematic distributions of the SM Higgs hypothesis are compared between the 0^+ JHUGen sample and the SM Higgs POWHEG

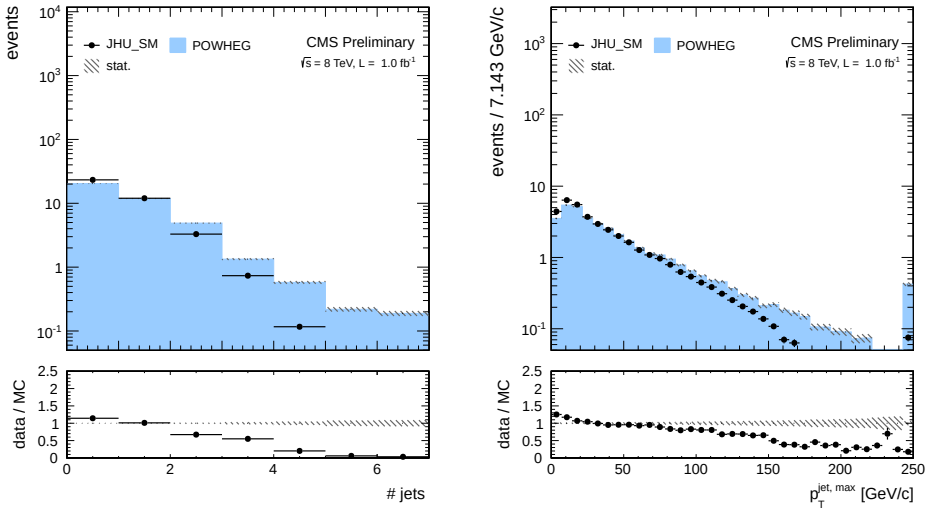

(a) (b)

Figure 9.1.: Distributions of (a) the number of jets and (b) the leading jet p_T of the SM Higgs hypothesis at the reconstruction level comparing JHUGen 0^+ (points with error bars) to POWHEG (histogram). The JHUGen shape is normalized to the POWHEG one.

sample used in the nominal Higgs search at the reconstruction level (just after the trigger selection). It should be noted that the POWHEG sample is a NLO sample, while JHUGen is a LO sample, so it is important to keep an eye open for any LO to NLO effects.

Figure 9.1 shows the distributions of the number of jets and the leading jet p_T of the SM Higgs hypothesis comparing JHUGen 0^+ to the POWHEG at the reconstruction level. Only statistical errors are shown, as will be the case in all the figures of this section. The missing NLO part of the JHUGen sample is clearly visible when there is more than one jet. However, this analysis will restrict itself, as in the SM search analysis, to the 0- and 1-jet category. Figures 9.2 and 9.3 compare some key kinematic distributions of the JHUGen 0^+ sample to the POWHEG sample for respectively the 0- and 1-jet categories at the reconstruction level. A good agreement within 10 % in the bulk of the distributions is found, which is as expected considering the use of NLO matrix element calculations in the generation of the POWHEG sample. Following this agreement, the JHUGen samples are considered validated.

Figure 9.4 shows the separating power between the POWHEG SM Higgs hypothesis and the JHUGen 2^+_{min} hypothesis with $f_{\text{q}\bar{\text{q}}} = 0$ % that can be exploited with the low-mass shape-based selection level, as defined in Section 7.2.2. The top three plots show the

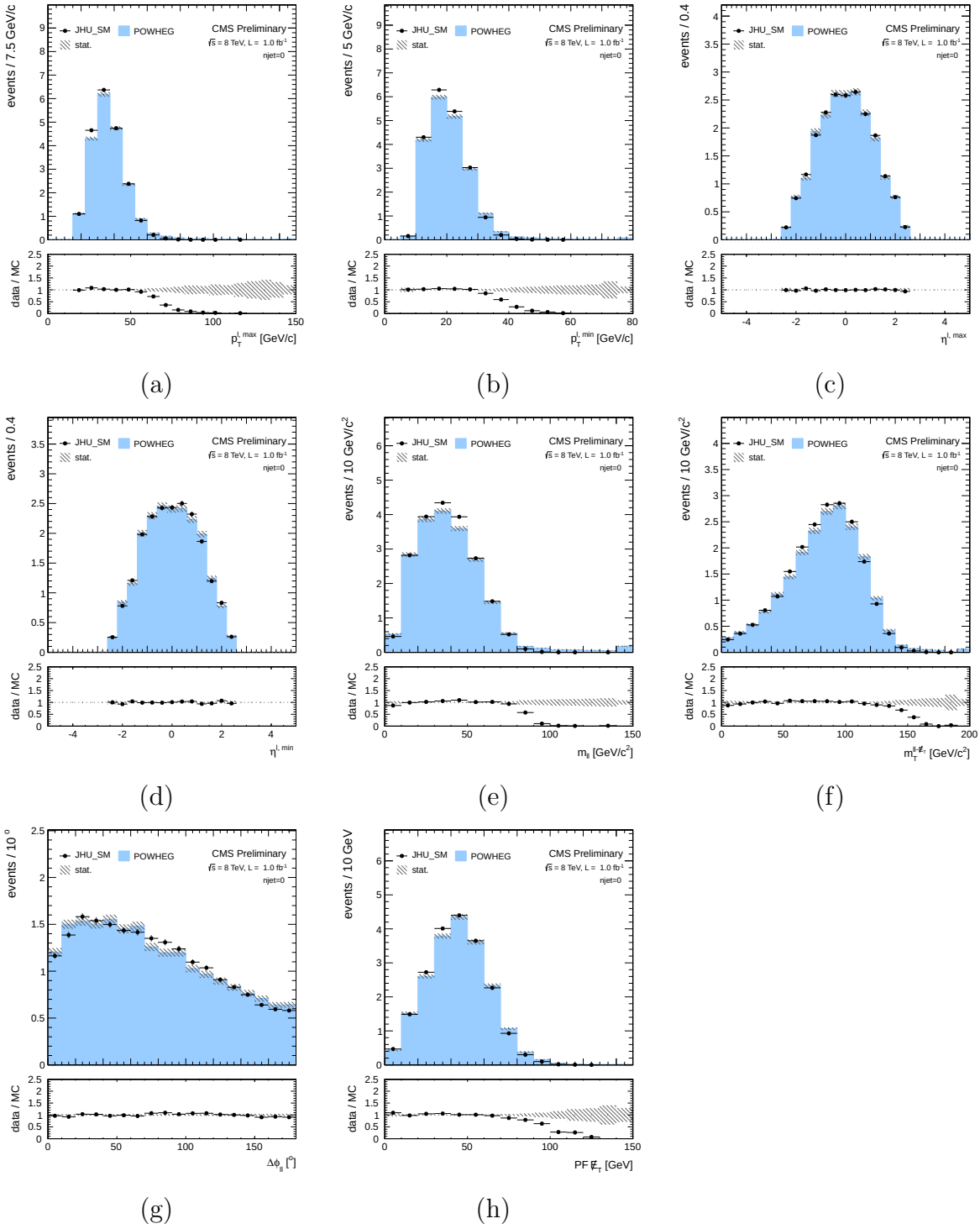

Figure 9.2.: Some key distributions of the SM Higgs hypothesis for the 0-jet category at the reconstruction level comparing JHUGen 0^+ (points with error bars) to POWHEG (histogram) with the JHUGen shape normalized to the POWHEG one: (a) leading lepton p_{T}, (b) trailing lepton p_{T}, (c) leading lepton η, (d) trailing lepton η, (e) dilepton invariant mass $m_{\ell\ell}$, (f) transverse mass m_{T} of the dilepton-$E_{\mathrm{T}}^{\mathrm{miss}}$ system, (g) dilepton $\Delta\phi_{\ell\ell}$ and (h) PF $E_{\mathrm{T}}^{\mathrm{miss}}$.

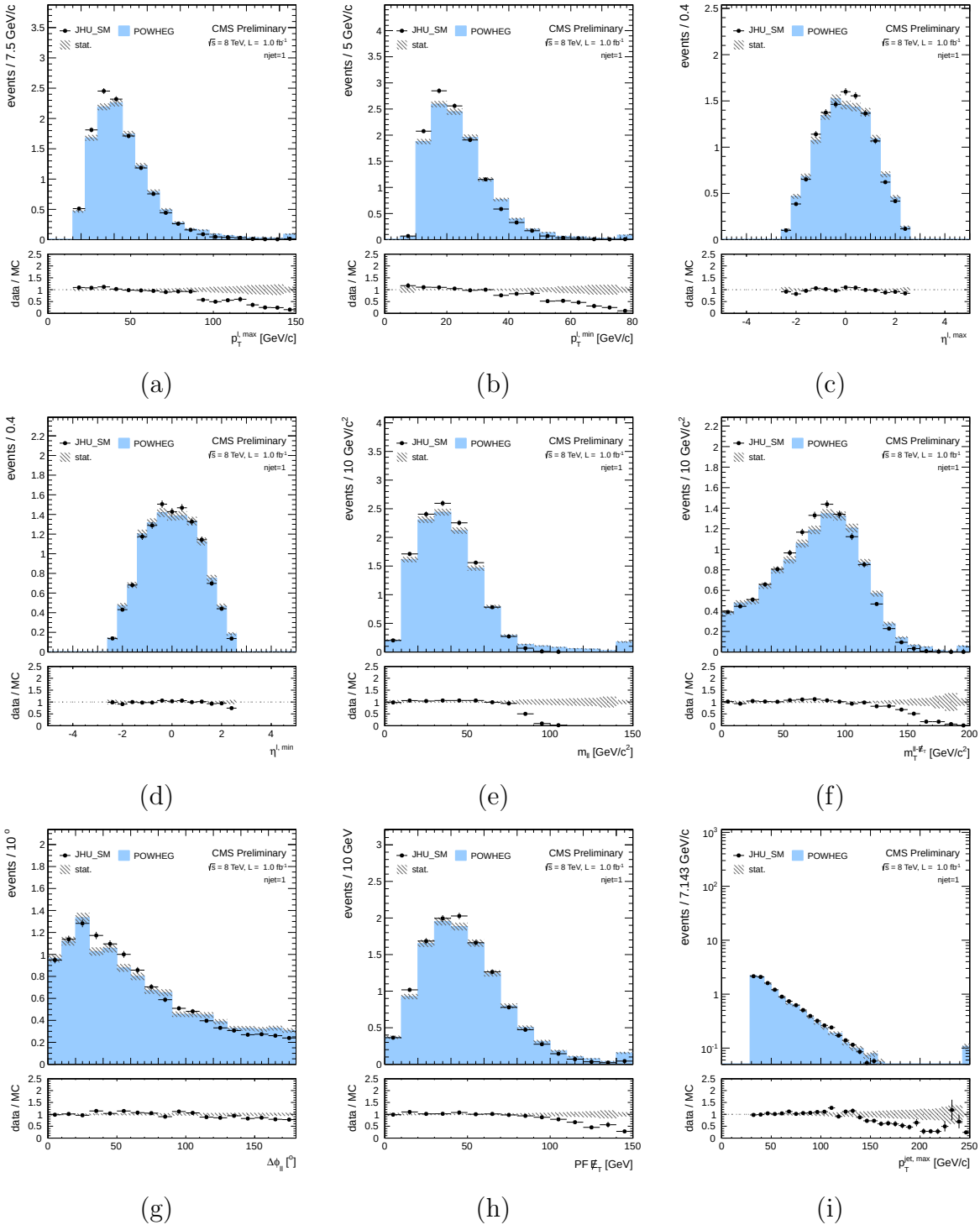

Figure 9.3.: Some key distributions of the SM Higgs hypothesis for the 1-jet category at the reconstruction level comparing JHUGen 0^+ (points with error bars) to POWHEG (histogram) with the JHUGen shape normalized to the POWHEG one: (a) leading lepton p_{T}, (b) trailing lepton p_{T}, (c) leading lepton η, (d) trailing lepton η, (e) dilepton invariant mass $m_{\ell\ell}$, (f) transverse mass m_{T} of the dilepton-$E_{\mathrm{T}}^{\mathrm{miss}}$ system, (g) dilepton $\Delta\phi_{\ell\ell}$, (h) PF $E_{\mathrm{T}}^{\mathrm{miss}}$ and (i) leading jet p_{T}.

separation power for the 0-jet category and the bottom three for the 1-jet category. These distributions show clear shape differences between the two signal samples, making it possible to derive an analysis to separate both signal hypotheses. In contrast to the previous comparison, Figure 9.5 shows the separating power between the POWHEG SM Higgs hypothesis and the JHUGen 0^- hypothesis, again for both the 0- and 1- jet category. Here the shape difference is unfortunately much less present, which will make the separation analysis between 0^+ and 0^- less powerful in the WW decay channel as we will see in the results section, Section 9.4.

9.3. Spin-parity analysis strategy

To distinguish between the Standard Model Higgs boson and one of the J^P hypotheses, a signal-plus-background model is built for each hypothesis, based on two-dimensional templates in $(m_{\mathrm{T}}, m_{\ell\ell})$, using the same bin widths and data selection as for the low-mass shape-based analysis, as described in Section 7.2.2. This has the indirect consequence that only the different-flavor final states are considered.

For the SM Higgs case, the signal templates derived from POHWEG include the gluon fusion, VBF and associated production modes. The 2^+_{min} signal templates obtained from JHUGen include the gluon fusion and $\mathrm{q\overline{q}}$ production modes, where the results will be shown as a function of the fraction of the $\mathrm{q\overline{q}} \to \mathrm{X}$ component, $f_{\mathrm{q\overline{q}}}$. The yields of the $\mathrm{gg} \to \mathrm{X}$ and $\mathrm{q\overline{q}} \to \mathrm{X}$ processes are nominally taken from the simulated samples assuming the SM Higgs boson cross section. The 0^- signal templates are also obtained from JHUGen and only include the gluon fusion production mode, where the yield of the $\mathrm{gg} \to \mathrm{X}$ process is nominally taken from the simulated sample assuming the SM Higgs boson cross section. The background templates are the same as in the SM Higgs boson search analysis.

The 2D $(m_{\mathrm{T}}, m_{\ell\ell})$ distributions for the 0-jet and 1-jet categories for the SM Higgs 0^+ and 2^+_{min} hypotheses (for $f_{\mathrm{q\overline{q}}} = 0$ % and $f_{\mathrm{q\overline{q}}} = 100$ %) are shown in Figure 9.6 for the $\sqrt{s} = 8$ TeV analysis. The distribution of the two variables and the correlation between them clearly separates the two spin hypotheses, which are related to the different $\ell\nu$ masses and $\ell\ell$ azimuthal angle distributions [123].

For each hypothesis a binned maximum likelihood (L) fit is performed, to simultaneously extract the signal strength and background contributions. This likelihood fit

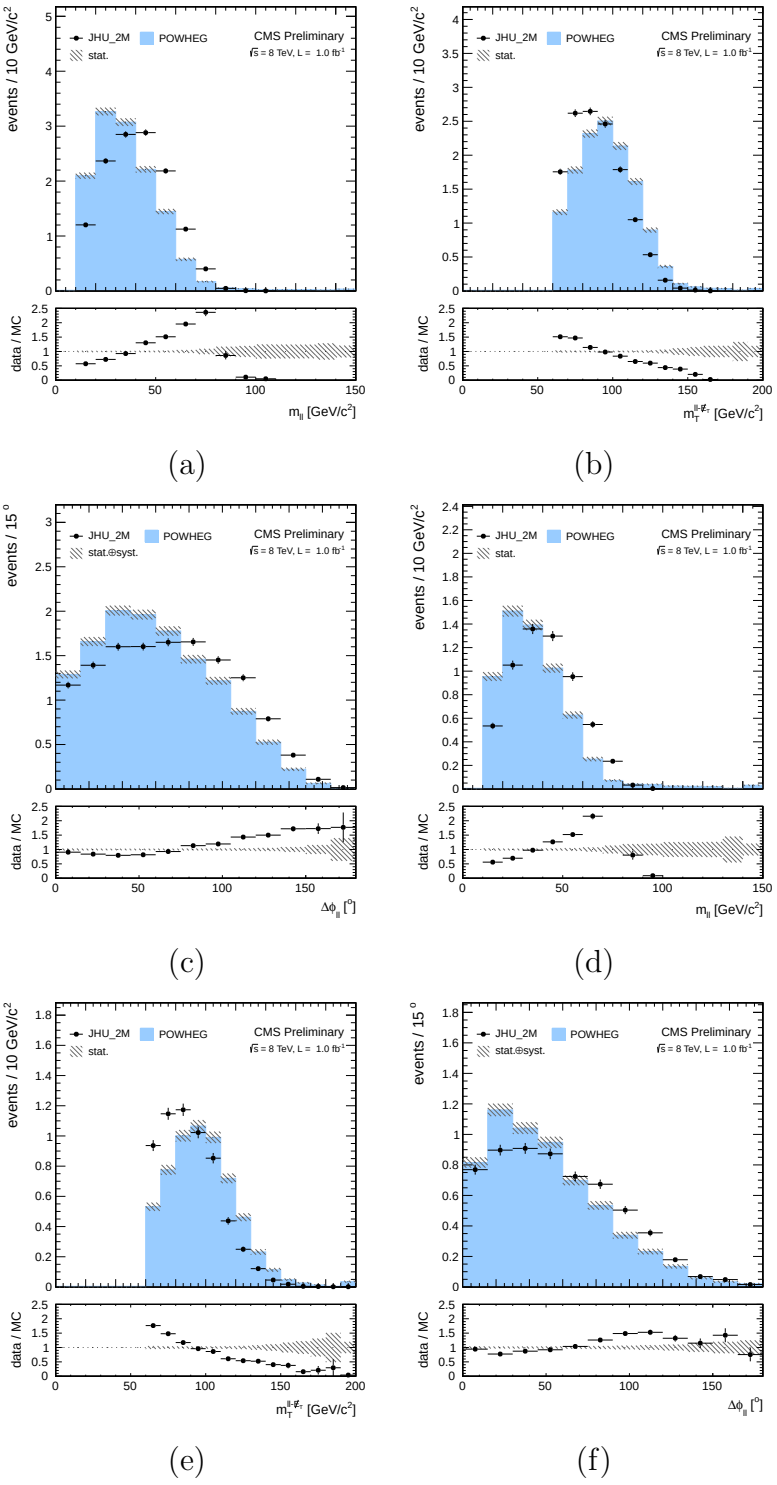

Figure 9.4.: Distributions comparing the JHUGen 2^+_{min} sample with $f_{\text{q}\overline{\text{q}}} = 0$ % (points with error bars) to the POWHEG SM Higgs sample (blue histogram) at the final low-mass shape-based selection level for the 0-jet category: (a) $m_{\ell\ell}$, (b) m_{T} and (c) $\Delta\phi_{\ell\ell}$, and the 1-jet category: (d) $m_{\ell\ell}$, (e) m_{T} and (f) $\Delta\phi_{\ell\ell}$. The JHUGen shape is normalized to the POWHEG one.

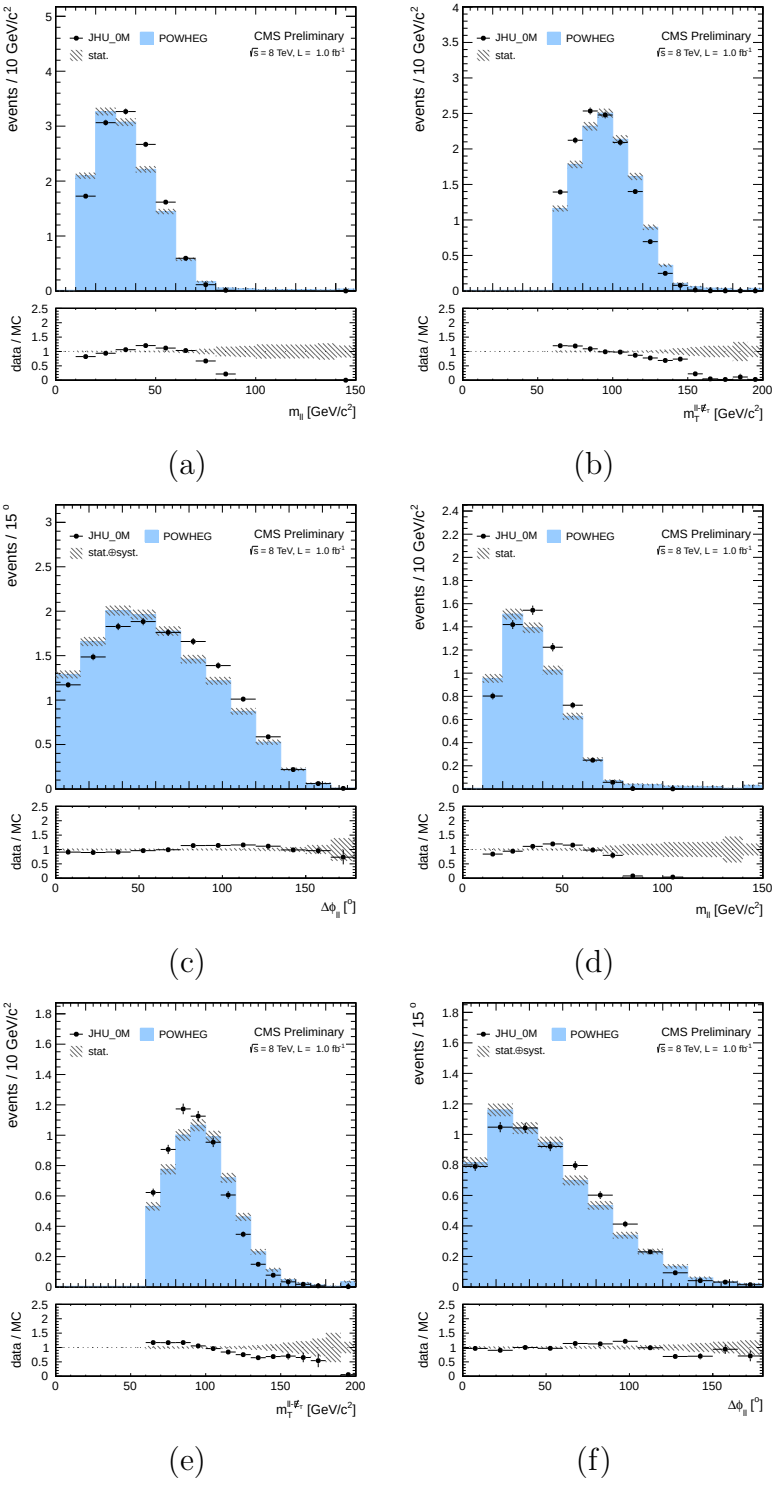

Figure 9.5.: Distributions comparing the JHUGen 0^- sample (points with error bars) to the POWHEG SM Higgs sample (blue histogram) at the final low-mass shape-based selection level for the 0-jet category: (a) $m_{\ell\ell}$, (b) m_{T} and (c) $\Delta\phi_{\ell\ell}$, and the 1-jet category: (d) $m_{\ell\ell}$, (e) m_{T} and (f) $\Delta\phi_{\ell\ell}$. The JHUGen shape is normalized to the POWHEG one.

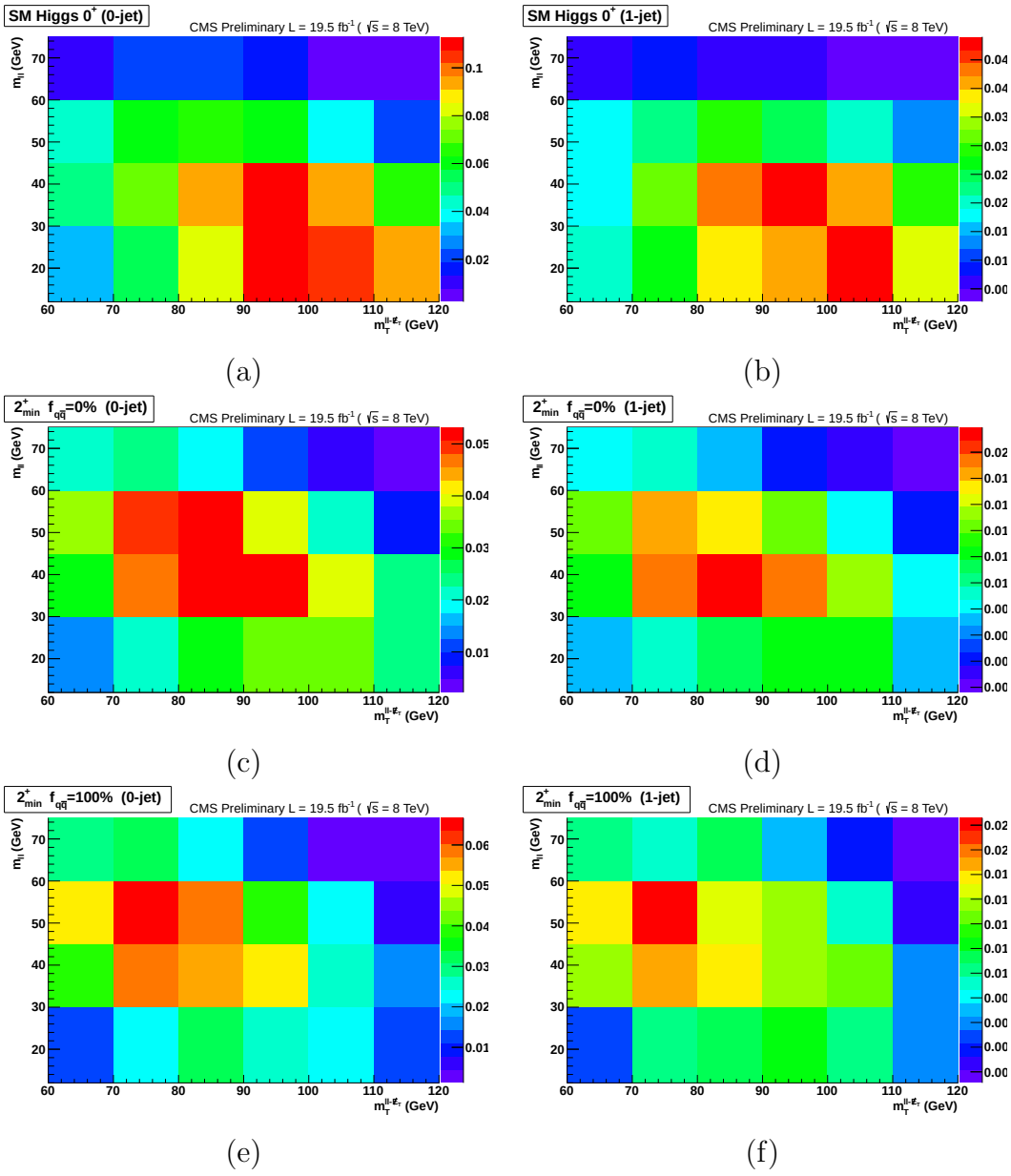

Figure 9.6.: Two-dimensional $(m_{\mathrm{T}}, m_{\ell\ell})$ distributions for the 0-jet (left) and 1-jet (right) categories for the $m_{\mathrm{H}} = 125$ GeV SM Higgs boson signal hypothesis (a,b) and the JHUGen 2^+_{min} hypothesis for $f_{\mathrm{q\bar{q}}} = 0\,\%$ (c,d) and $f_{\mathrm{q\bar{q}}} = 100\,\%$ (e,f) at $\sqrt{s} = 8$ TeV. The plots are a close-up view of the signal-like region for low Higgs masses. All the plots are normalized to a unit integral and the z-axis is scaled to the maximum of each given plot.

model is the same as in the SM Higgs boson search. For a given dataset, the maximum likelihood fits for both models are performed, allowing the signal rates of each signal type to float independently. The systematic uncertainties are the same as the ones from the search analysis covered in Section 7.3. The same theoretical uncertainties are applied to the 2^+_{min} and the 0^- hypotheses as those that are applied to the SM Higgs signal in the search analysis. The test statistic, $q = -2\ln(L_{J^P}/L_{0^+})$, where L_{0^+} and L_{J^P} are the best-fit likelihood values for the SM Higgs boson and the alternative hypothesis is then used to quantify the consistency of the two models with data. The expected separation between the two hypotheses, defined as the median of q expected under the J^P hypothesis, is quoted in two scenarios. In one case, events are generated with the a-priori SM expectation for the signal yields ($\sigma/\sigma_{\text{SM}} \equiv 1$) and in the other case, the signal strength is determined from the fits to data ($\sigma/\sigma_{\text{SM}} \equiv 0.76$ for spin 0 and $\sigma/\sigma_{\text{SM}} \equiv 0.83$ for spin 2)[1].

9.4. Spin-parity results

The distributions of the test statistic $q = -2\ln(L_{J^P}/L_{0^+})$ for the 0^+ and 2^+_{min} hypotheses at $m_{\text{H}} = 125$ GeV for the two scenarios described in the previous section and assuming $f_{\text{q}\bar{\text{q}}} = 0$ % or $f_{\text{q}\bar{\text{q}}} = 100$ % are shown in Figure 9.7. Assuming $\sigma/\sigma_{\text{SM}} = 1$ for both hypotheses, the median test statistic for the 0^+ and 2^+_{min} hypotheses as well as its observed value, as a function of $f_{\text{q}\bar{\text{q}}}$ of the 2^+_{min} particle is shown in Figure 9.8a. The same results using the $\sigma/\sigma_{\text{SM}}$ value determined from the fit to data are shown in Figure 9.8b. In all cases the data favor the SM hypothesis with respect to the 2^+_{min} hypothesis. The alternative hypothesis 2^+_{min} is excluded at a 83.7 % (99.8 %) CL_s or higher for $f_{\text{q}\bar{\text{q}}} = 0$ % (100 %) when the $\sigma/\sigma_{\text{SM}}$ value determined from the fit to data is used.

The same procedure as described above is applied to perform a test of hypotheses between a 0^+ boson, like the SM Higgs boson, and a pseudoscalar 0^- boson. The average separation between the two hypotheses is about one standard deviation, as shown in Figure 9.9. The alternative hypothesis 0^- is disfavored with a CL_s value of 34.7 % when the $\sigma/\sigma_{\text{SM}}$ value determined from the fit to data is used. A summary of the list of models used in the analysis of the spin and parity hypotheses, J^P, is shown in Table 9.2 together with the expected and observed separation.

[1] The value published in Reference [89] is used here and not the one retrieved from the search analysis of this work for spin 0. The spin analysis is build on the published results. However as a matter of course, they fall within each others errors.

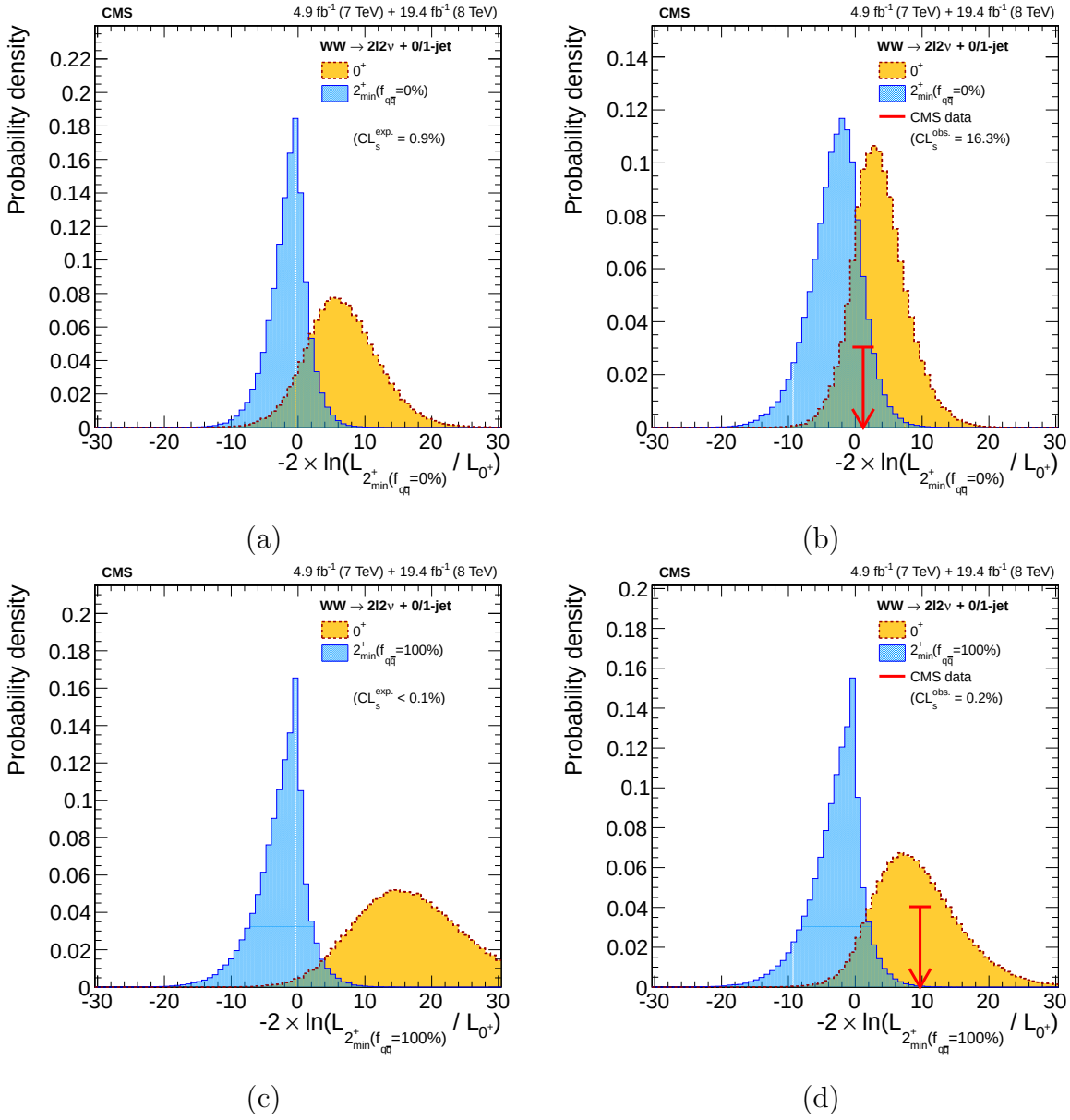

Figure 9.7.: Distributions of $-2\ln(L_{2^+_{\mathrm{min}}}/L_{0^+})$, combining the 0-jet and 1-jet categories in the different-flavor final state, for the 0^+ and 2^+_{min} hypotheses at $m_{\mathrm{H}} = 125$ GeV. The distributions are produced assuming $\sigma/\sigma_{\mathrm{SM}} = 1$ (a,c) and using the signal strength determined from the fit to data (b,d). The distributions are shown for the case of $f_{\mathrm{q\bar{q}}} = 0\,\%$ (a,b) and $f_{\mathrm{q\bar{q}}} = 100\,\%$ (c,d). The observed value is indicated by the red arrow.

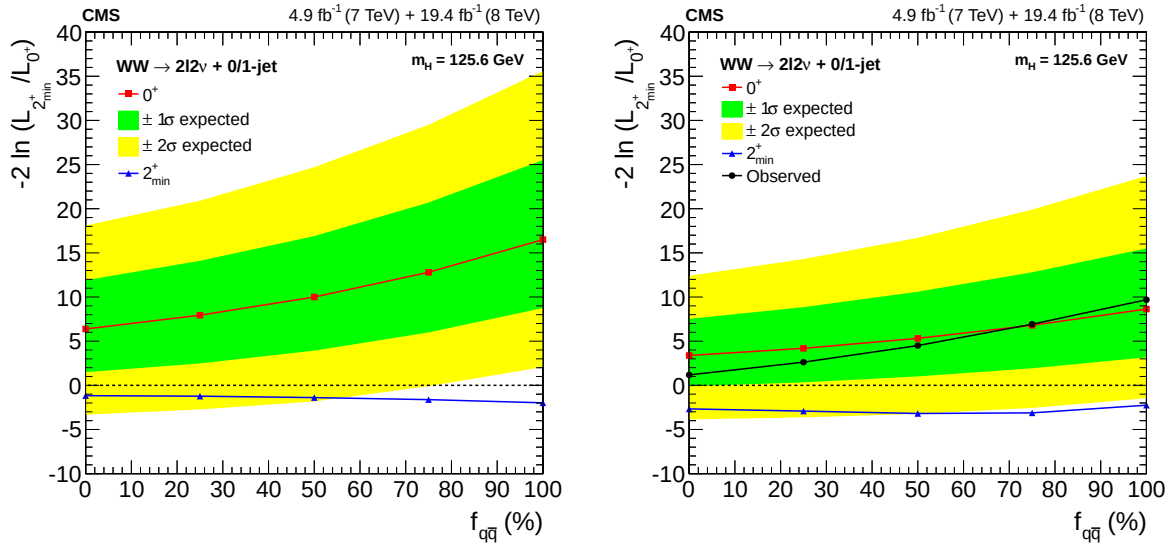

(a) (b)

Figure 9.8.: Median test statistic for the 0^+ and 2^+_{min} hypotheses, as a function of $f_{\text{q}\bar{\text{q}}}$ of the 2^+_{min} particle, assuming $\sigma/\sigma_{\text{SM}} = 1$ (a) and using the $\sigma/\sigma_{\text{SM}}$ value determined from the fit to data (b). The observed values are also reported in the second case.

Table 9.2.: A summary of the models used in the analysis of the spin and parity hypotheses. The expected separation is quoted for two scenarios, where the value of $\sigma/\sigma_{\text{SM}}$ for each hypothesis is determined from the fit to data and where events are generated with $\sigma/\sigma_{\text{SM}} = 1$. The observed separation quotes consistency of the observation with the 0^+ model or J^P model and corresponds to the scenario where $\sigma/\sigma_{\text{SM}}$ is determined from the fit to data. The last column quotes the CL_s value that defines the minimum confidence level (1-CL_s) at which the J^P model is excluded.

J^P model	J^P production	Expected ($\sigma/\sigma_{\text{SM}} = 1$)	obs. 0^+	obs. J^P	CL_s
2^+_{min}	$f_{\text{q}\bar{\text{q}}} = 0$ %	1.8 σ (2.6 σ)	+0.6 σ	+1.2 σ	16.3 %
2^+_{min}	$f_{\text{q}\bar{\text{q}}} = 50$ %	2.3 σ (3.2 σ)	+0.2 σ	+2.1 σ	3.3 %
2^+_{min}	$f_{\text{q}\bar{\text{q}}} = 100$ %	2.9 σ (3.9 σ)	-0.2 σ	+3.1 σ	0.2 %
0^-	any	0.8 σ (1.1 σ)	-0.5 σ	+1.2 σ	34.7 %

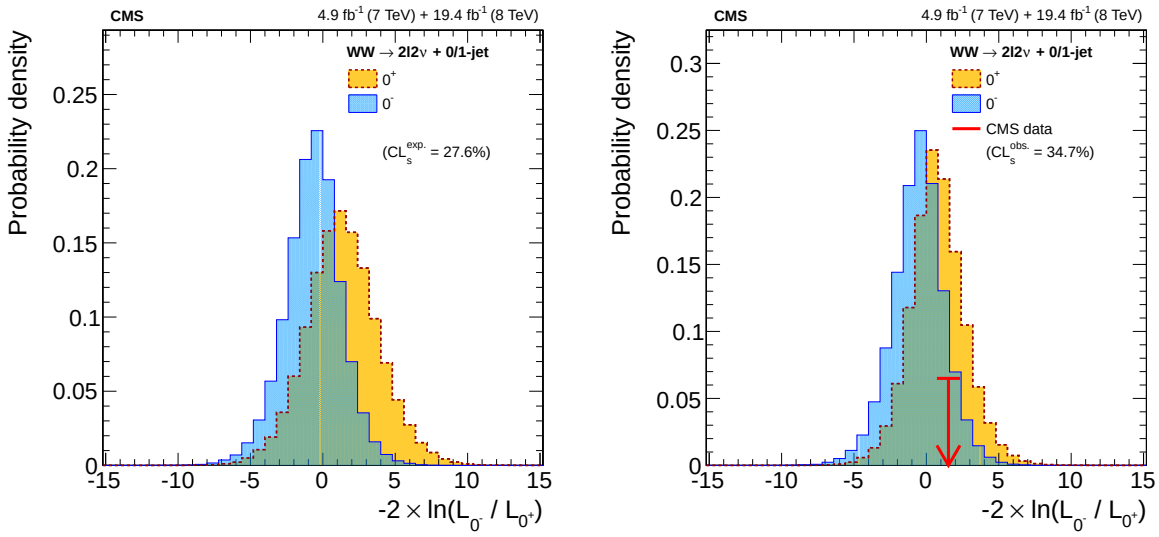

(a) (b)

Figure 9.9.: Distributions of $-2\ln(L_{0^-}/L_{0^+})$, combining the 0-jet and 1-jet categories in the different-flavor final state, for the 0^+ and 0^- hypotheses at $m_{\mathrm{H}} = 125$ GeV. The distributions are produced assuming $\sigma/\sigma_{\mathrm{SM}} = 1$ (a) and using the signal strength determined from the fit to data (b). The observed value is indicated by the red arrow.

Chapter 10.

Summary and Outlook

This thesis covered the measurement of the Brout-Englert-Higgs boson, decaying to two W bosons in the fully leptonic final state at the LHC. The event samples used in the analysis correspond to an integrated luminosity of 4.9 fb^{-1} and 19.5 fb^{-1} collected by the CMS detector in proton-proton collisions at $\sqrt{s} = 7$ TeV (2011) and $\sqrt{s} = 8$ TeV (2012), respectively. The analysis has been performed in the Higgs boson mass range of 110-600 GeV. The signature of the analysis consists of two high p_{T} isolated leptons and large missing energy due to the neutrinos that cannot be detected. To maximize the significance the events are classified in four different categories. The events are first split depending on the number of high p_{T} jets in the final state: 0-jet and 1-jet. Secondly the events are split into same flavor events (ee and $\mu\mu$) and different flavor events (eμ). Next, a number of selection requirements are performed to suppress the contamination of different types of background events that mimic the signal signature. To carefully estimate the contribution of each of these backgrounds, data-driven methods are performed. Finally two approaches are performed to extract the Higgs boson signal from the data: a counting experiment and a more sensitive 2D template fit. Next to the search analysis, a spin-parity property study (spin J, parity P) is performed to distinguish between a $J^P = 0^+$ boson like the SM Higgs boson and a $J^P = 2^+$ boson with minimal coupling or a pseudoscalar $J^P = 0^-$ boson.

The described analysis is the result of years of optimization and extensive studies to adapt to the changing conditions and scenarios in the Large Hadron Collider. Using the 2011 dataset the analysis narrowed down the Higgs mass window by excluding as much mass regions as possible within the mass region under study. At the end of 2011, first hints of the presence of the SM Higgs boson where found at low mass. During my PhD, the $\sqrt{s} = 8$ TeV dataset was collected and the main focus was on the optimization of

the sensitivity of the channel for the low mass region. My work covered many of the key aspects of the analysis. I contributed in the accommodation of selection changes to cope with the changing data taking conditions, I assisted in the validation of the new data and I was responsible for the data driven estimations of the W^+W^-, top and Drell-Yan backgrounds. Furthermore, I greatly contributed to the development of the spin-parity property study.

Using the full luminosity collected in 2011 and 2012, an excess of events is observed above background, consistent with the expectations from the SM Higgs boson with a mass of around 125 GeV. The probability to observe an excess equal to or larger than the one seen for a SM Higgs boson mass of 125 GeV, under the background-only hypothesis, corresponds to a significance of 4.3 standard deviations, while 5.1 standard deviations are expected assuming the SM prediction. The corresponding observed $\sigma/\sigma_{\mathrm{SM}}$ value is $0.85^{+0.24}_{-0.21}$. No other significant deviations are observed, and therefore upper limits on the Higgs boson production relative to the Standard Model Higgs expectation are derived. The Standard Model Higgs boson is excluded in the mass range of 128-530 GeV at 95 % confidence level. The spin-parity $J^P = 0^+$ hypothesis is favored against a narrow resonance with $J^P = 2^+$ with minimal couplings or $J^P = 0^-$ that decays to a W-boson pair. This result provides strong evidence for a Higgs-like boson decaying to a W-boson pair.

The results of this analysis were combined with the results of the other W^+W^- Higgs decaying subchannels and are published in Reference [89]. Furthermore, the results of the W^+W^- decay channel were combined within the CMS collaboration with those of the other main search channels, making it possible to claim the observation of a Higgs-like boson with a mass of approximately 125 GeV on the fourth of July 2012, as described in our observation paper [44]. The ATLAS collaboration came to the same findings as described in [45]. The double confirmation on the observation of a Higgs-like boson led in 2013 to the awarding of the Nobel Prize to François Englert and Peter Higgs, for the theoretical discovery of a mechanism that contributes to our understanding of the origin of mass of subatomic particles. A theoretical discovery which was recently confirmed through the discovery of the predicted fundamental particle, by the ATLAS and CMS experiments at CERN's Large Hadron Collider.

Looking forward, the future of the fully leptonic Higgs to W^+W^- decay mode is very bright. Collecting more data and repeating the search study at higher center-of-mass energies are key in the search for any deviation between the found scalar and the SM Higgs boson. First of all the coupling strengths have to be measured more precisely to

look for deviations from the SM precision measurements. Secondly the width of the Higgs boson, a parameter that determines the particle's lifetime, can be determined using the high invariant mass tail as done in the Higgs to two Z bosons analysis [125]. Next, more spin-parity models can be tested and the (differential) cross-section of the Higgs production should be measured. Lastly, one can also directly search for new physics. The high mass search region can be extended, allowing the search for new physics using the SM Higgs boson as a background. This would make it possible to accommodate the search for Higgs models consisting of multiple Higgs bosons, for example: a scalar with a pseudoscalar or a two Higgs doublet model resulting in five Higgs bosons. We have only just touched the tip of the iceberg, the future awaits us!

Appendices

Appendix A.

2D ($m_{\ell\ell}$,m_{T}) distributions for data, backgrounds and signal

Two dimensional kinematic distributions in the $m_{\ell\ell}$ versus m_{T} plane are shown for the observed data, expected backgrounds and signal for the case of the low Higgs mass analysis ($m_{\mathrm{H}} \leq 250$ GeV) at $\sqrt{s} = 8$ TeV. The distributions correspond to the average expectation used as inputs to the kinematic fits. In all the following 2D figures, each bin is divided by its bin width.

The 2D input distributions in the 0-jet eμ channel are shown in Figures A.1, A.2 and A.3. The ones in the 1-jet eμ channel are shown in Figures A.4, A.5 and A.6. Additionally, the signal at eight different Higgs masses is shown in Figures A.7 and A.8 for the 0- and 1-jet category, respectively. Keep in mind that depending on the Higgs mass, the low or high Higgs mass shape analysis is used. It is clearly visible that, for increasing Higgs masses, the signal distribution gets broader and moves to higher m_{T} and $m_{\ell\ell}$ values.

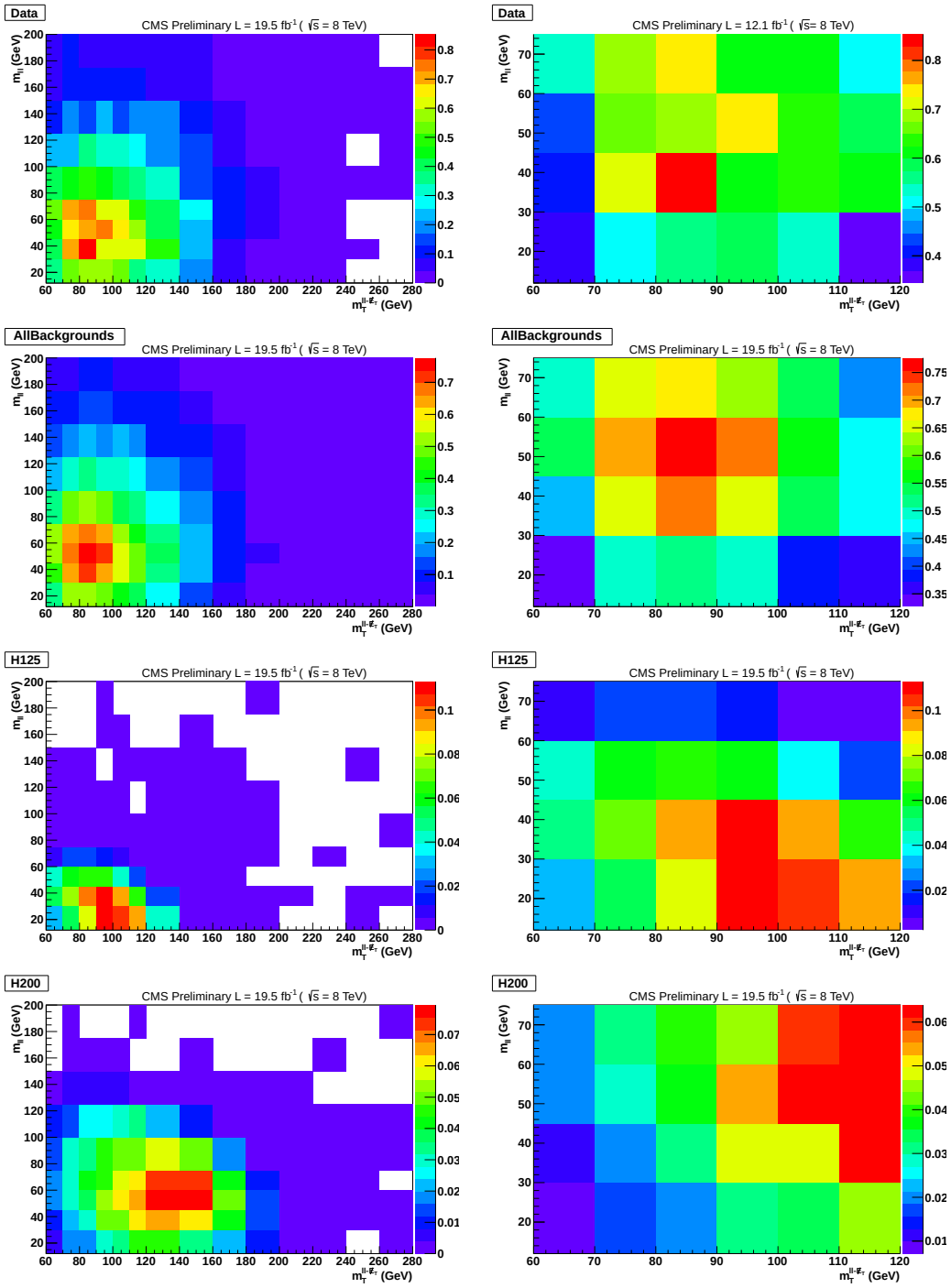

Figure A.1.: 2D ($m_{\ell\ell}$,m_{T}) distributions used as inputs for the shape analysis for **data**, **sum of backgrounds** and **signal** at m_H = 125 GeV and m_H = 200 GeV in the **0-jet eμ** channel. The selection and the binning correspond to those used for the low mass analysis up to m_H = 250 GeV. The plots on the right side are a close-up view of the signal-like region (for low Higgs masses). All the plots are normalized to a unit integral and the z-axis is scaled to the maximum of each given plot.

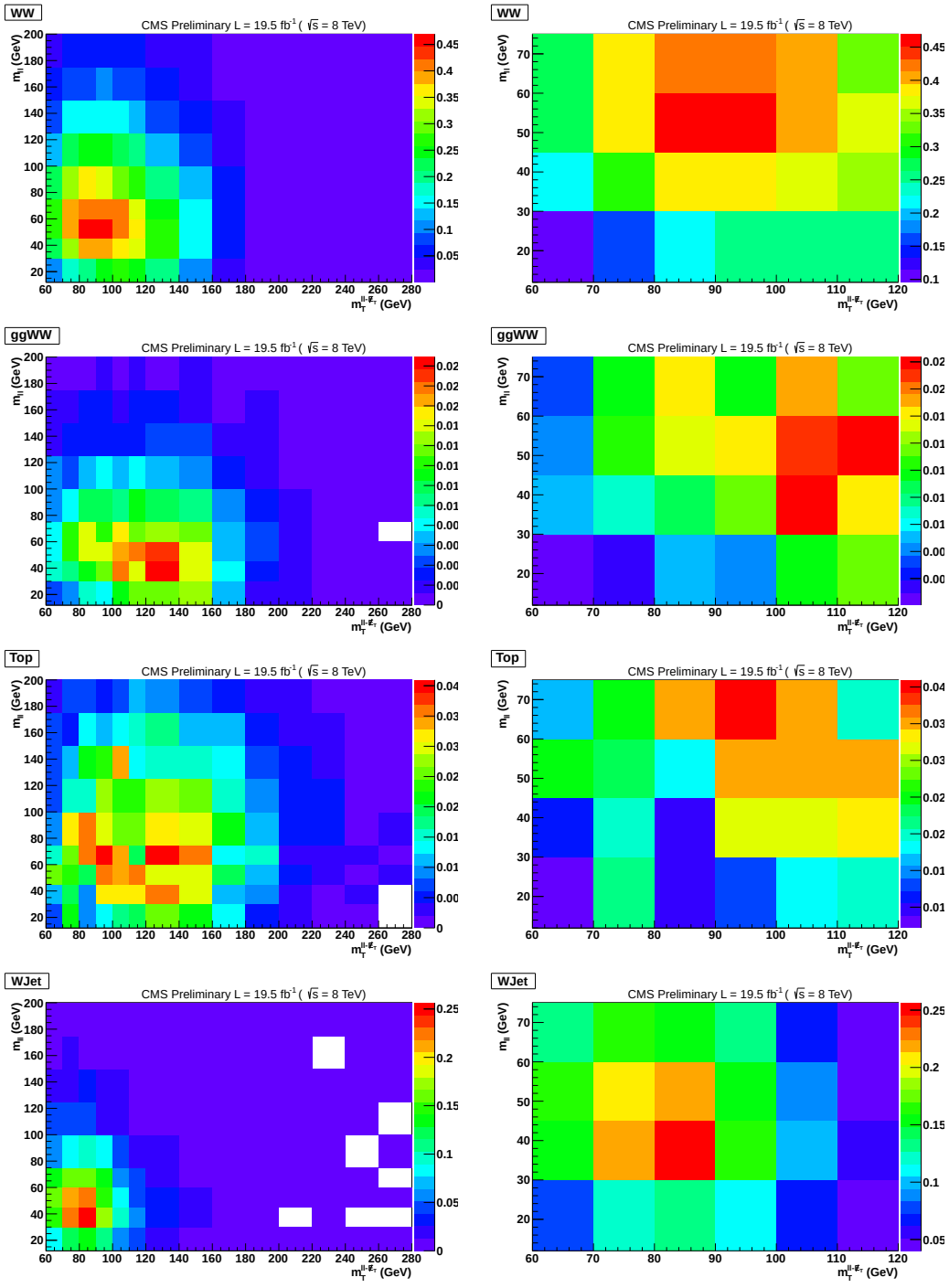

Figure A.2.: 2D ($m_{\ell\ell}$,m_{T}) distributions used as inputs for the shape analysis for $\mathbf{q\bar{q} \rightarrow WW}$, $\mathbf{gg \rightarrow WW}$, $\mathbf{tt/tW}$ and **W+jets** backgrounds in the **0-jet eμ** channel. The selection and the binning correspond to those used for the low mass analysis up to $m_{\mathrm{H}} = 250$ GeV. The plots on the right side are a close-up view of the signal-like region (for low Higgs masses). All the plots are normalized to a unit integral and the z-axis is scaled to the maximum of each given plot.

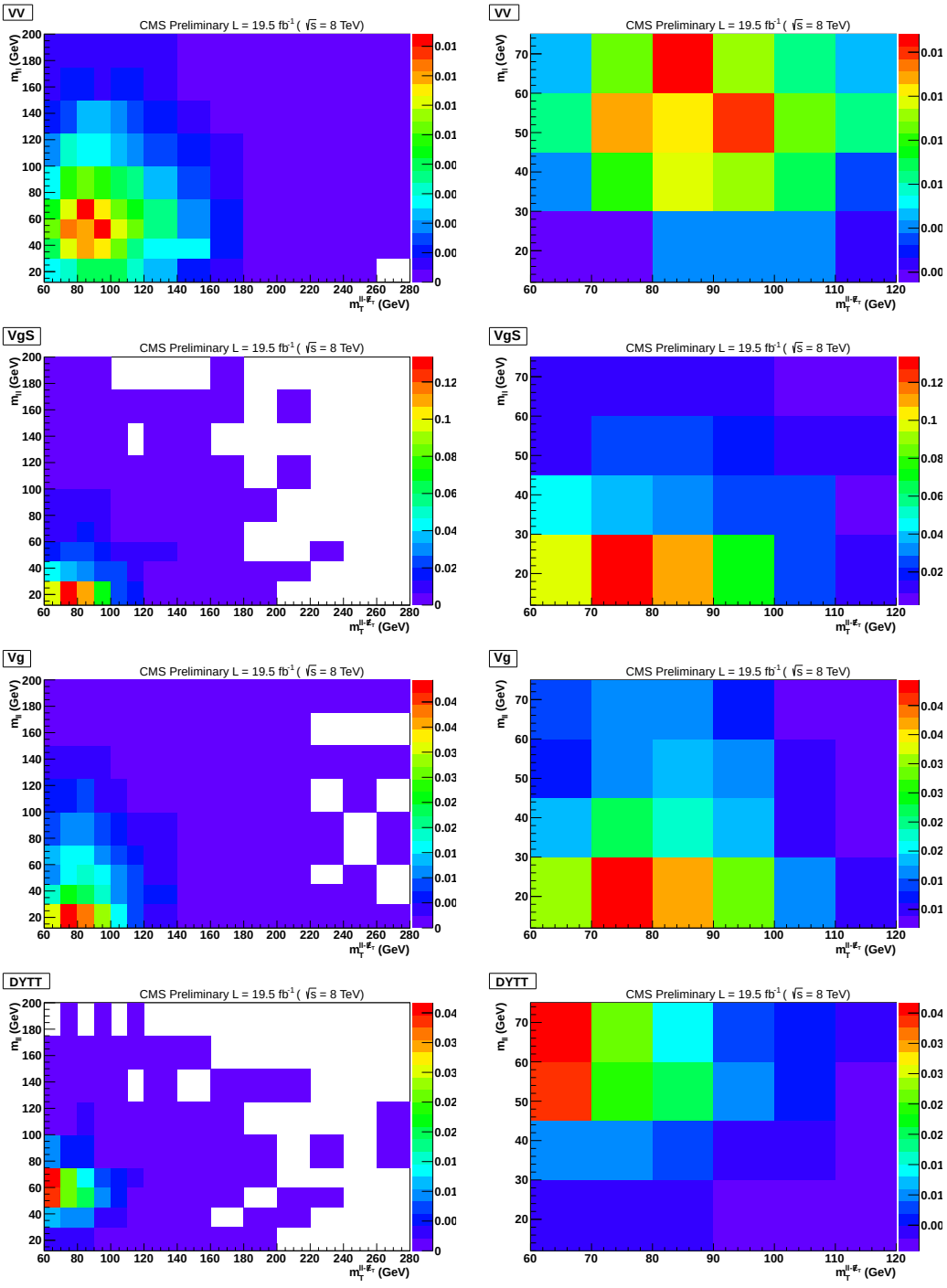

Figure A.3.: 2D ($m_{\ell\ell}$,m_{T}) distributions used as inputs for the shape analysis for **WZ/ZZ**, **W+γ^***, **W+γ** and **Z/$\gamma^{(*)}$ $\rightarrow$ $\tau\tau$** backgrounds in the **0-jet eμ** channel. The selection and the binning correspond to those used for the low mass analysis up to $\mathrm{m_H}$ = 250 GeV. The plots on the right side are a close-up view of the signal-like region (for low Higgs masses). All the plots are normalized to a unit integral and the z-axis is scaled to the maximum of each given plot.

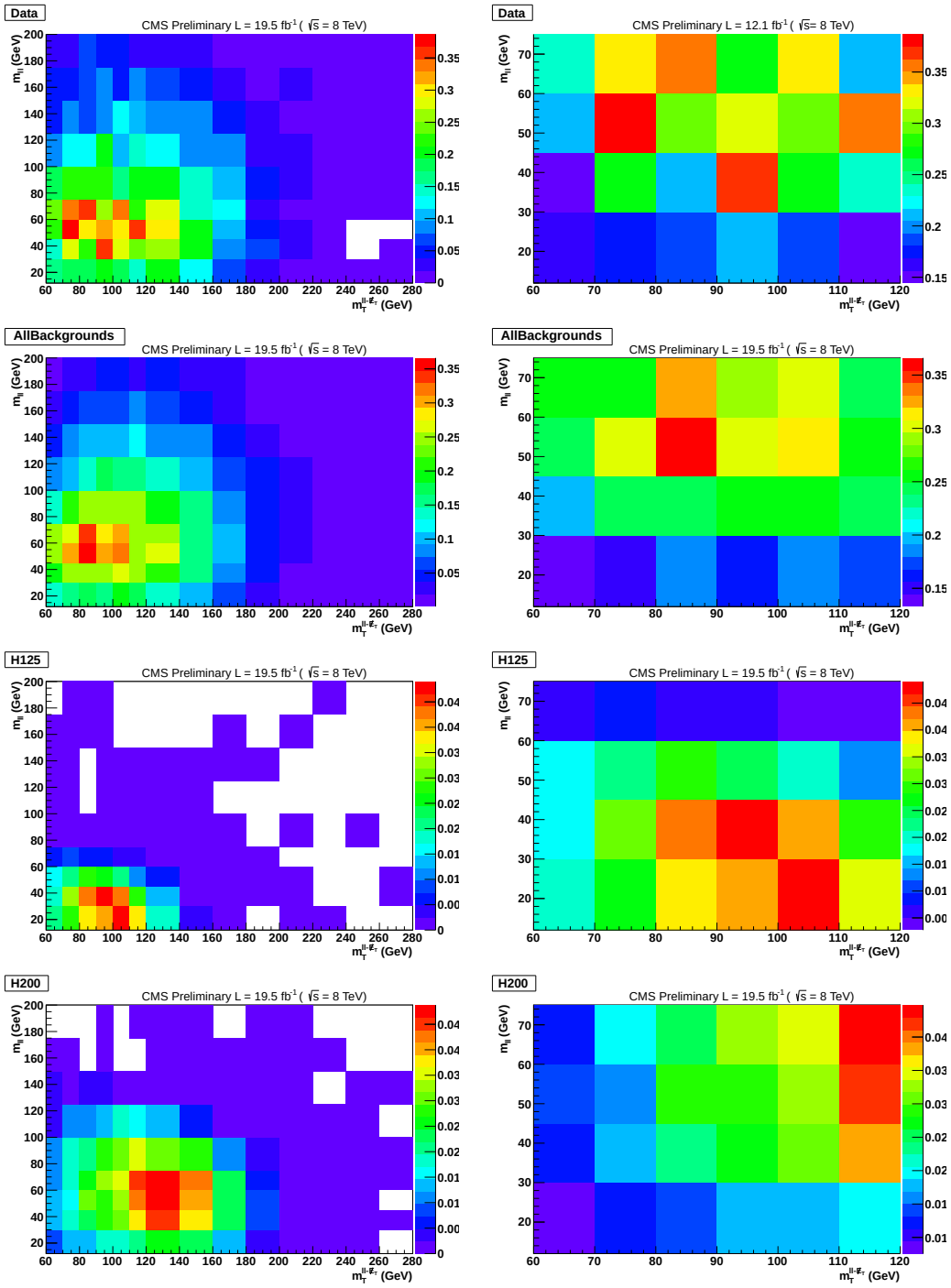

Figure A.4.: 2D ($m_{\ell\ell}$,m_{T}) distributions used as inputs for the shape analysis for **data**, **sum of backgrounds** and **signal** at $m_{\mathrm{H}} = 125$ GeV and $m_{\mathrm{H}} = 200$ GeV in the **1-jet eμ** channel. The selection and the binning correspond to those used for the low mass analysis up to $m_{\mathrm{H}} = 250$ GeV. The plots on the right side are a close-up view of the signal-like region (for low Higgs masses). All the plots are normalized to a unit integral and the z-axis is scaled to the maximum of each given plot.

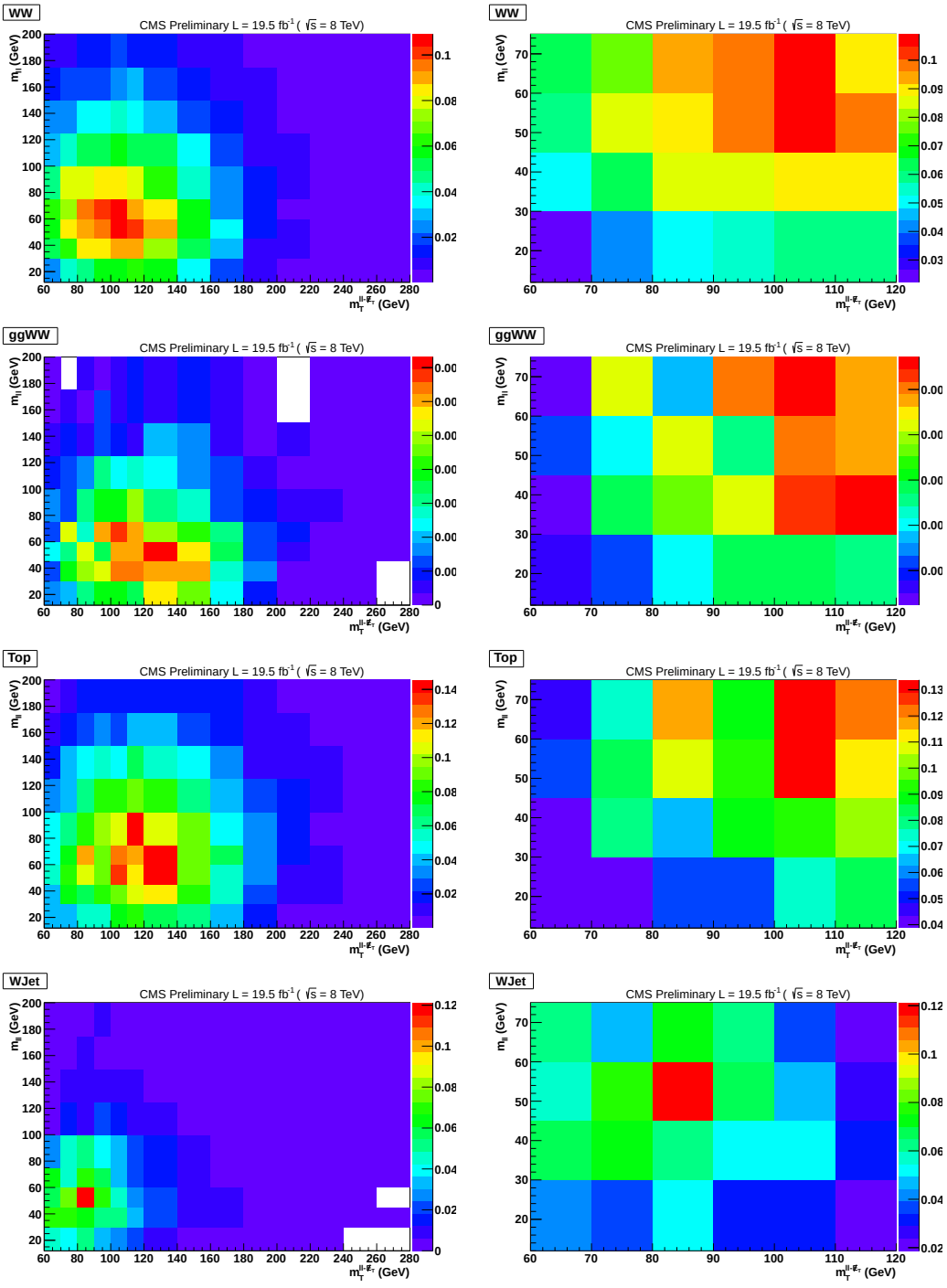

Figure A.5.: 2D ($m_{\ell\ell}$,m_{T}) distributions used as inputs for the shape analysis for $\mathbf{q\bar{q} \rightarrow WW}$, $\mathbf{gg \rightarrow WW}$, **tt/tW** and **W+jets** backgrounds in the **1-jet eμ** channel. The selection and the binning correspond to those used for the low mass analysis up to $m_{\mathrm{H}} = 250$ GeV. The plots on the right side are a close-up view of the signal-like region (for low Higgs masses). All the plots are normalized to a unit integral and the z-axis is scaled to the maximum of each given plot.

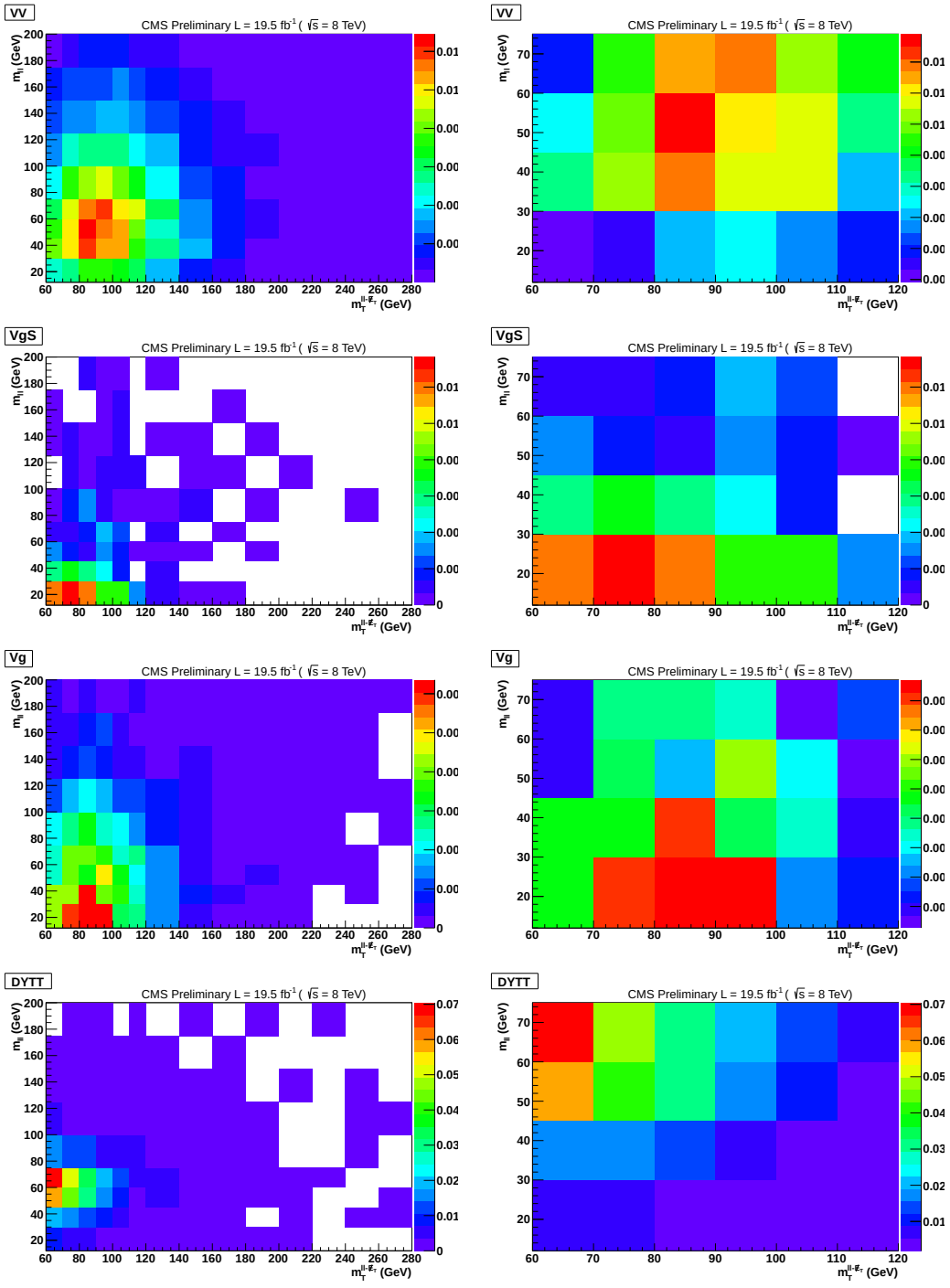

Figure A.6.: 2D ($m_{\ell\ell}$,m_{T}) distributions used as inputs for the shape analysis for **WZ/ZZ**, **W+γ^***, **W+γ** and **Z/$\gamma^{(*)}$ $\rightarrow$ $\tau\tau$** backgrounds in the **1-jet eμ** channel. The selection and the binning correspond to those used for the low mass analysis up to $\mathrm{m_H}$ = 250 GeV. The plots on the right side are a close-up view of the signal-like region (for low Higgs masses). All the plots are normalized to a unit integral and the z-axis is scaled to the maximum of each given plot.

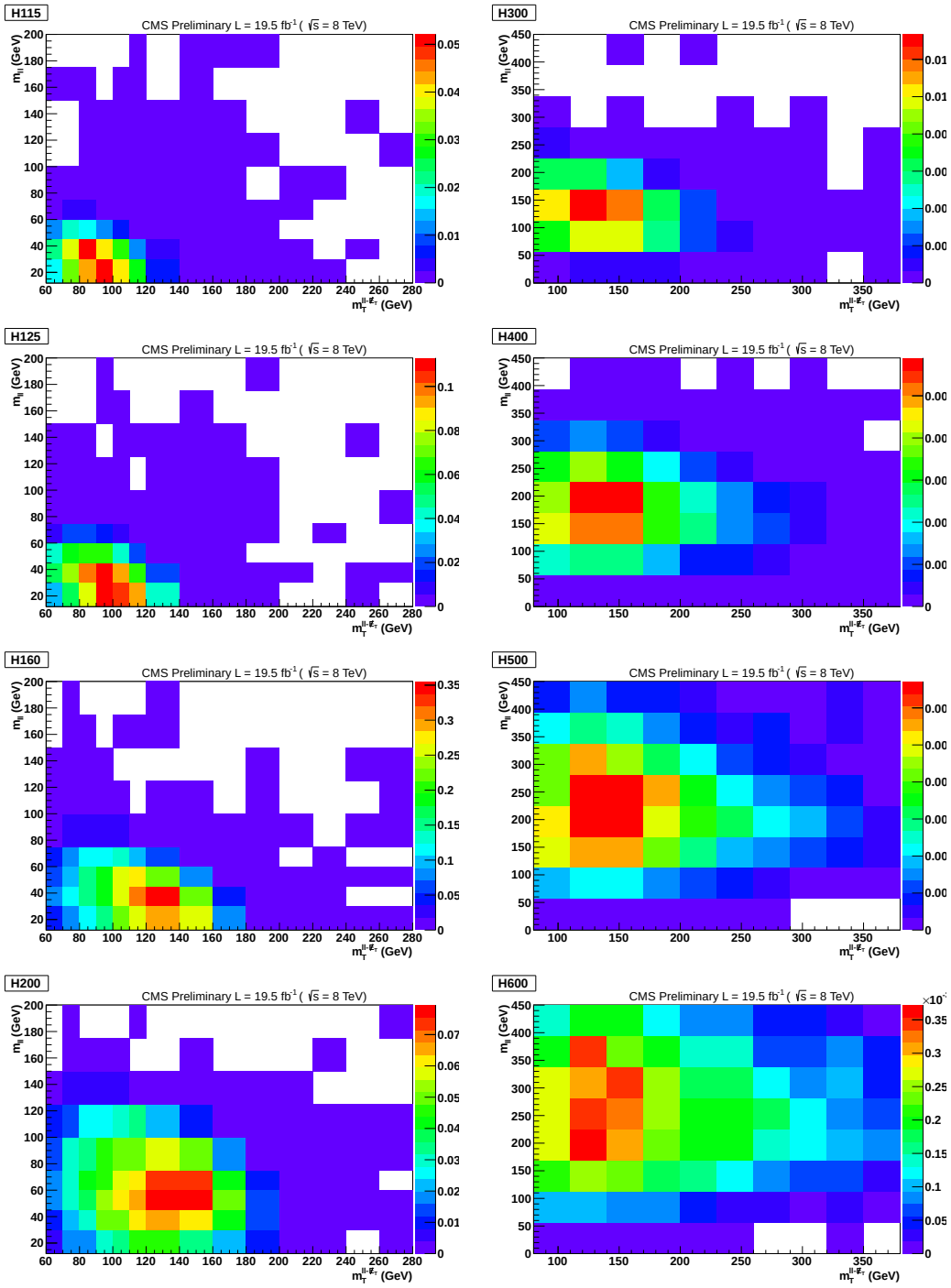

Figure A.7.: 2D ($m_{\ell\ell}$,m_{T}) distributions of the **signal** for the low mass shape analysis at $m_{\mathrm{H}} = \{115, 125, 160, 200\}$ GeV and for the high mass shape analysis at $m_{\mathrm{H}} = \{300, 400, 500, 600\}$ GeV in the **0-jet eμ** channel. The selection and the binning depend on the Higgs mass. The low mass analysis is used up to $\mathrm{m_H}$ = 250 GeV, while the high mass analysis is used for $\mathrm{m_H} > 250$ GeV. All the plots are normalized to a unit integral and the z-axis is scaled to the maximum of each given plot.

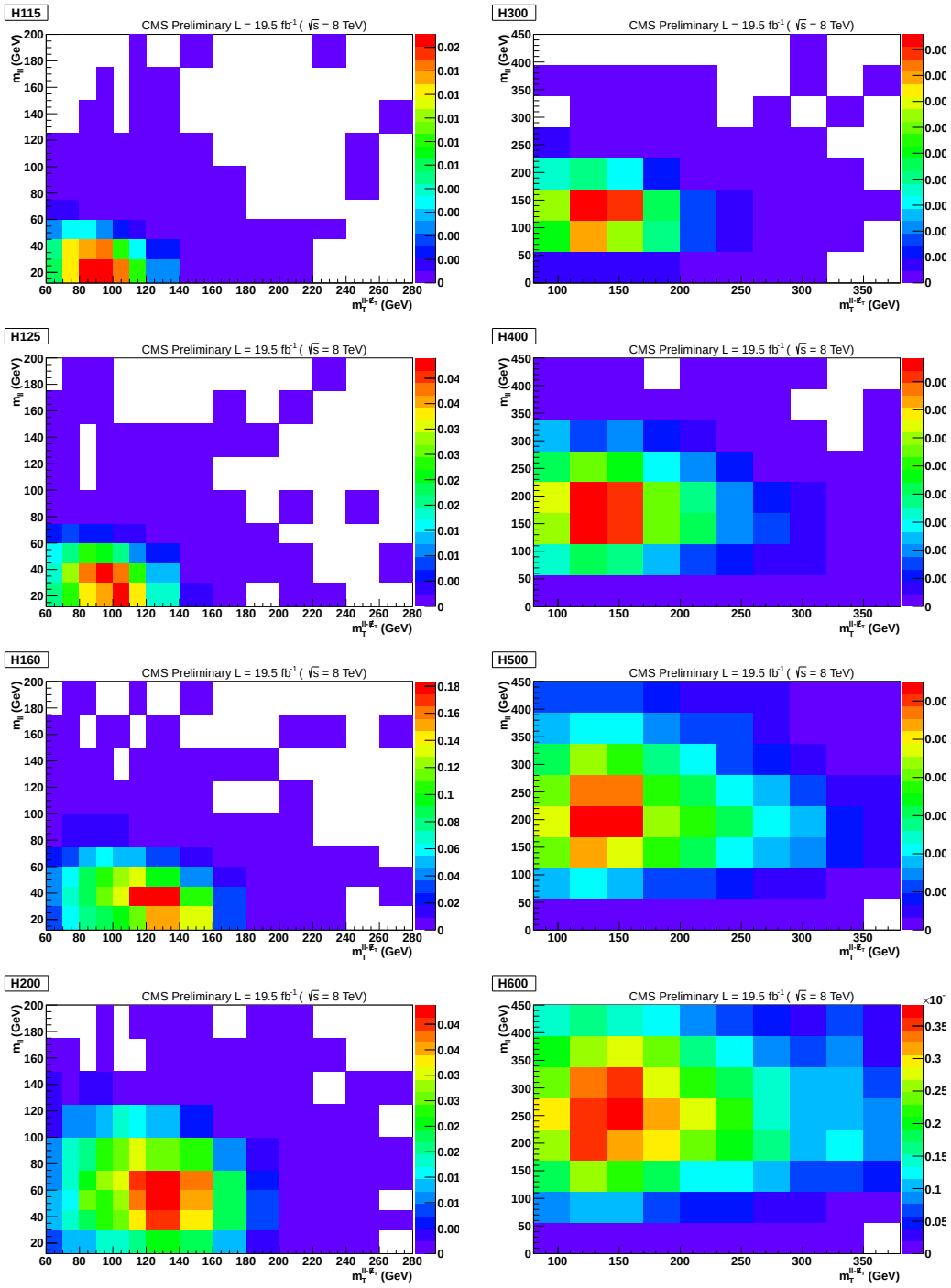

Figure A.8.: 2D ($m_{\ell\ell}$,m_{T}) distributions of the **signal** for the low mass shape analysis at $m_{\mathrm{H}} = \{115, 125, 160, 200\}$ GeV and for the high mass shape analysis at $m_{\mathrm{H}} = \{300, 400, 500, 600\}$ GeV in the **1-jet eμ** channel. The selection and the binning depend on the Higgs mass. The low mass analysis is used up to m_{H} = 250 GeV, while the high mass analysis is used for $m_{\mathrm{H}} > 250$ GeV. All the plots are normalized to a unit integral and the z-axis is scaled to the maximum of each given plot.

Appendix B.

Limits and significance tables separate for the 2011 and 2012 dataset

B.1. Cut-based results

The expected and observed upper limits for the full cut-based analysis, separate for $\sqrt{s} = 7$ TeV and $\sqrt{s} = 8$ TeV are tabelized, together with the significances for the background-only hypothesis to account for the excess in units of standard deviations (sd) in Table B.1 and Table B.2 for $\sqrt{s} = 7$ TeV and $\sqrt{s} = 8$ TeV, respectively.

B.2. Shape-based results

The full shape-based analysis result consists of the combination of the analyses of the shape-based different-flavor final state with the cut-based same-flavor final state and is tabelized in Table B.3 and Table B.4 for $\sqrt{s} = 7$ TeV and $\sqrt{s} = 8$ TeV, respectively.

Table B.1.: Expected and observed **cut-based** upper limits on the $H \to W^+ W^-$ production cross section relative to the SM prediction, and the expected and observed significances for the background-only hypothesis to account for the excess in units of standard deviations, for all the lepton-flavor final states and 0- and 1-jet categories combined using **4.9 fb^{-1} of $\sqrt{s}$ = 7 TeV data**.

Higgs mass [GeV]	Observed limits	Median limits	68% Range	95% Range	Observed significance	Expected significance
110	8.48	6.19	[4.35, 8.93]	[3.23, 12.60]	0.82	0.36
115	4.01	2.98	[2.10, 4.32]	[1.55, 6.07]	0.71	0.73
120	2.47	1.84	[1.30, 2.64]	[0.98, 3.69]	0.76	1.15
125	1.69	1.16	[0.83, 1.65]	[0.62, 2.31]	0.99	1.80
130	1.33	0.86	[0.61, 1.23]	[0.46, 1.70]	1.03	2.41
135	1.05	0.66	[0.47, 0.94]	[0.35, 1.30]	1.11	3.07
140	0.70	0.53	[0.38, 0.76]	[0.29, 1.05]	0.59	3.63
150	0.53	0.39	[0.28, 0.56]	[0.21, 0.78]	0.94	4.76
160	0.28	0.21	[0.15, 0.31]	[0.12, 0.43]	0.00	7.81
170	0.24	0.23	[0.16, 0.33]	[0.12, 0.46]	0.00	7.39
180	0.27	0.32	[0.23, 0.46]	[0.17, 0.64]	0.00	5.39
190	0.32	0.48	[0.34, 0.69]	[0.26, 0.96]	0.00	3.61
200	0.55	0.70	[0.49, 1.00]	[0.37, 1.40]	0.00	2.66
250	0.70	1.05	[0.74, 1.52]	[0.55, 2.13]	0.00	1.79
300	1.31	1.70	[1.20, 2.45]	[0.89, 3.41]	0.00	1.15
350	1.29	1.44	[1.01, 2.09]	[0.75, 2.96]	0.00	1.37
400	1.30	1.48	[1.04, 2.14]	[0.78, 3.00]	0.00	1.31
450	1.39	1.68	[1.18, 2.42]	[0.88, 3.42]	0.00	1.18
500	1.70	2.09	[1.47, 3.06]	[1.09, 4.38]	0.00	0.98
550	2.46	2.70	[1.86, 4.02]	[1.37, 5.93]	0.00	0.81
600	3.31	3.48	[2.35, 5.37]	[1.71, 8.27]	0.00	0.68

Table B.2.: Expected and observed **cut-based** upper limits on the $H \to W^+ W^-$ production cross section relative to the SM prediction, and the significances for the background-only hypothesis to account for the excess in units of standard deviations, for all the lepton-flavor final states and 0- and 1-jet categories combined using **19.5 fb^{-1} of $\sqrt{s} = 8$ TeV data**.

Higgs mass [GeV]	Observed limits	Median limits	68% Range	95% Range	Observed significance	Expected significance
110	7.56	3.89	[2.71, 5.64]	[2.04, 7.84]	2.09	0.57
115	3.67	1.91	[1.34, 2.75]	[1.01, 3.81]	2.13	1.14
120	1.91	1.14	[0.81, 1.62]	[0.60, 2.23]	1.71	1.86
125	1.40	0.82	[0.58, 1.15]	[0.43, 1.57]	1.79	2.56
130	1.10	0.61	[0.43, 0.86]	[0.32, 1.18]	1.94	3.37
135	0.87	0.46	[0.33, 0.65]	[0.25, 0.89]	2.12	4.30
140	0.68	0.38	[0.27, 0.53]	[0.20, 0.72]	2.03	5.12
145	0.57	0.32	[0.23, 0.44]	[0.17, 0.61]	2.03	5.90
150	0.48	0.25	[0.18, 0.35]	[0.14, 0.48]	2.51	7.01
155	0.37	0.20	[0.15, 0.28]	[0.11, 0.38]	2.34	8.18
160	0.24	0.13	[0.09, 0.18]	[0.07, 0.24]	2.23	10.31
170	0.21	0.13	[0.10, 0.19]	[0.08, 0.26]	1.61	9.57
180	0.35	0.20	[0.14, 0.28]	[0.11, 0.38]	0.00	7.72
190	0.57	0.34	[0.25, 0.48]	[0.19, 0.66]	1.64	5.27
200	0.80	0.47	[0.34, 0.67]	[0.25, 0.92]	1.70	4.08
250	1.28	0.90	[0.64, 1.29]	[0.48, 1.77]	1.19	2.27
300	1.09	0.93	[0.66, 1.32]	[0.49, 1.83]	0.18	2.15
350	0.80	0.76	[0.54, 1.08]	[0.40, 1.52]	0.08	2.58
400	0.76	0.74	[0.53, 1.06]	[0.40, 1.48]	0.09	2.57
450	0.66	0.81	[0.58, 1.15]	[0.43, 1.60]	0.00	2.28
500	0.82	1.07	[0.76, 1.54]	[0.57, 2.17]	0.00	1.76
550	1.32	1.39	[0.98, 2.04]	[0.73, 2.95]	0.00	1.46
600	1.70	1.84	[1.27, 2.78]	[0.93, 4.13]	0.00	1.16

Table B.3.: Expected and observed **shape-based** upper limits on the $H \to W^+ W^-$ production cross section relative to the SM prediction, and the expected and observed significances for the background-only hypothesis to account for the excess in units of standard deviations, for all the lepton-flavor final states and 0- and 1-jet categories combined using **4.9 fb^{-1} of $\sqrt{s}$ = 7 TeV data**.

Higgs mass [GeV]	Observed limits	Median limits	68% Range	95% Range	Observed significance	Expected significance
110	9.99	4.55	[3.22, 6.56]	[2.39, 9.20]	2.72	0.48
115	5.23	2.32	[1.65, 3.37]	[1.22, 4.71]	2.72	0.90
120	3.10	1.41	[1.00, 2.03]	[0.75, 2.84]	2.56	1.47
125	1.83	0.88	[0.62, 1.26]	[0.47, 1.76]	2.28	2.35
130	1.27	0.65	[0.46, 0.93]	[0.34, 1.30]	2.01	3.16
135	0.97	0.50	[0.36, 0.71]	[0.27, 1.00]	1.99	4.05
140	0.74	0.41	[0.29, 0.59]	[0.22, 0.81]	1.94	4.84
150	0.47	0.30	[0.21, 0.42]	[0.16, 0.59]	1.49	6.55
160	0.28	0.18	[0.13, 0.26]	[0.10, 0.36]	1.34	9.99
170	0.24	0.20	[0.14, 0.28]	[0.11, 0.40]	0.60	9.13
180	0.22	0.27	[0.19, 0.39]	[0.15, 0.55]	0.00	6.77
190	0.33	0.41	[0.29, 0.59]	[0.22, 0.82]	0.00	4.65
200	0.54	0.59	[0.42, 0.85]	[0.31, 1.20]	0.00	3.31
250	0.94	0.85	[0.60, 1.23]	[0.45, 1.72]	0.37	2.31
300	1.75	1.32	[0.93, 1.91]	[0.70, 2.68]	0.76	1.50
350	1.12	1.04	[0.73, 1.51]	[0.54, 2.14]	0.18	1.94
400	1.13	1.08	[0.76, 1.57]	[0.57, 2.22]	0.12	1.82
450	1.39	1.31	[0.92, 1.92]	[0.68, 2.72]	0.15	0.00
500	1.77	1.71	[1.18, 2.52]	[0.87, 3.66]	0.10	0.00
550	2.58	2.16	[1.46, 3.29]	[1.05, 4.92]	0.43	0.00
600	2.72	2.88	[1.91, 4.53]	[1.36, 7.04]	0.00	0.00

Table B.4.: Expected and observed **shape-based** upper limits on the $H \to W^+ W^-$ production cross section relative to the SM prediction, and the significances for the background-only hypothesis to account for the excess in units of standard deviations, for all the lepton-flavor final states and 0- and 1-jet categories combined using **19.5 fb^{-1} of $\sqrt{s} = 8$ TeV data**.

Higgs mass [GeV]	Observed limits	Median limits	68% Range	95% Range	Observed significance	Expected significance
110	6.28	2.24	[1.60, 3.22]	[1.20, 4.50]	3.42	0.93
115	3.19	1.14	[0.81, 1.62]	[0.61, 2.26]	3.55	1.80
120	1.81	0.66	[0.47, 0.94]	[0.35, 1.30]	3.31	3.09
125	1.27	0.44	[0.32, 0.63]	[0.24, 0.87]	3.50	4.62
130	0.91	0.32	[0.23, 0.45]	[0.17, 0.62]	3.58	6.41
135	0.75	0.25	[0.18, 0.35]	[0.14, 0.49]	3.91	8.09
140	0.61	0.21	[0.15, 0.29]	[0.11, 0.40]	3.93	9.70
145	0.51	0.17	[0.13, 0.25]	[0.10, 0.34]	3.82	11.39
150	0.40	0.15	[0.11, 0.21]	[0.09, 0.30]	3.34	12.54
155	0.33	0.13	[0.09, 0.18]	[0.07, 0.24]	3.28	14.22
160	0.22	0.09	[0.07, 0.13]	[0.05, 0.18]	3.28	17.66
170	0.23	0.10	[0.08, 0.15]	[0.06, 0.20]	2.45	15.14
180	0.26	0.15	[0.11, 0.21]	[0.08, 0.29]	1.83	11.08
190	0.36	0.24	[0.17, 0.33]	[0.13, 0.46]	1.23	7.89
200	0.37	0.31	[0.22, 0.44]	[0.17, 0.62]	0.00	6.31
250	0.81	0.57	[0.40, 0.82]	[0.30, 1.15]	1.22	3.62
300	0.72	0.61	[0.43, 0.88]	[0.32, 1.23]	0.40	3.34
350	0.47	0.52	[0.37, 0.76]	[0.27, 1.07]	0.00	3.99
400	0.39	0.52	[0.37, 0.75]	[0.27, 1.05]	0.00	3.97
450	0.40	0.62	[0.44, 0.89]	[0.33, 1.24]	0.00	3.10
500	0.74	0.85	[0.60, 1.24]	[0.45, 1.75]	0.00	2.23
550	1.45	1.08	[0.75, 1.60]	[0.55, 2.34]	0.75	1.84
600	1.73	1.46	[1.00, 2.25]	[0.72, 3.40]	0.34	1.50

Bibliography

[1] M. E. Peskin and D. V. Schroeder, *An Introduction to quantum field theory*, Westview Press (1995).

[2] F. Halzen and A. D. Martin, *Quarks and Leptons: an introductory course in modern particle physics*, John Wiley & Sons (1984).

[3] Particle Data Group, *Review of Particle Physics*, Phys.Rev. **D86**, 010001 (2012).

[4] C.-N. Yang and R. L. Mills, *Conservation of Isotopic Spin and Isotopic Gauge Invariance*, Phys.Rev. **96**, 191 (1954).

[5] H. D. Politzer, *Reliable Perturbative Results for Strong Interactions?*, Phys.Rev.Lett. **30**, 1346 (1973).

[6] D. J. Gross and F. Wilczek, *Ultraviolet Behavior of Nonabelian Gauge Theories*, Phys.Rev.Lett. **30**, 1343 (1973).

[7] S. Glashow, *Partial Symmetries of Weak Interactions*, Nucl.Phys. **22**, 579 (1961).

[8] S. Weinberg, *A Model of Leptons*, Phys.Rev.Lett. **19**, 1264 (1967).

[9] A. Salam, *Weak and electromagnetic interactions in Elementary particle theory: relativistic groups and analyticity*, Proceedings of the eighth Nobel symposium , 367 (1968).

[10] Particle Data Group, *Review of particle physics*, J.Phys. **G37**, 075021 (2010).

[11] T. Nakano and K. Nishijima, *Charge Independence for V-particles*, Progress of Theoretical Physics **10**, 581 (1953).

[12] K. Nishijima, *Charge Independence Theory of V Particles*, Progress of Theoretical Physics **13**, 285 (1955).

[13] M. Gell-Mann, *The Interpretation of the New Particles as Displaced Charged Multiplets*, Il Nuovo Cimento **4**, 848866 (1956).

[14] Y. Nambu, *Quasiparticles and Gauge Invariance in the Theory of Superconductivity*, Phys.Rev. **117**, 648 (1960).

[15] J. Goldstone, *Field Theories with Superconductor Solutions*, Nuovo Cim. **19**, 154 (1961).

[16] J. Goldstone, A. Salam, and S. Weinberg, *Broken Symmetries*, Phys.Rev. **127**, 965 (1962).

[17] F. Englert and R. Brout, *Broken Symmetry and the Mass of Gauge Vector Mesons*, Phys.Rev.Lett. **13**, 321 (1964).

[18] P. W. Higgs, *Broken Symmetries and the Masses of Gauge Bosons*, Phys.Rev.Lett. **13**, 508 (1964).

[19] G. Guralnik, C. Hagen, and T. Kibble, *Global Conservation Laws and Massless Particles*, Phys.Rev.Lett. **13**, 585 (1964).

[20] I. Brock, Physics of and with leptons, `http://www-zeus.physik.uni-bonn.de/~brock/feynman/vtp_ws0506/`.

[21] Q. Ho-Kim and X. Pham, *Elementary Particles and Their Interactions: Concepts and Phenomena*, Springer (1998).

[22] P. W. Anderson, *Plasmons, Gauge Invariance, and Mass*, Phys.Rev. **130**, 439 (1963).

[23] G. 't Hooft, *Renormalizable Lagrangians for Massive Yang-Mills Fields*, Nucl.Phys. **B35**, 167 (1971).

[24] Gargamelle Neutrino Collaboration, *Observation of Neutrino Like Interactions Without Muon Or Electron in the Gargamelle Neutrino Experiment*, Phys.Lett. **B46**, 138 (1973).

[25] C. Prescott *et al.*, *Parity Nonconservation in Inelastic Electron Scattering*, Phys.Lett. **B77**, 347 (1978).

[26] UA1 Collaboration, *Further Evidence for Charged Intermediate Vector Bosons at the SPS Collider*, Phys.Lett. **B129**, 273 (1983).

[27] UA1 Collaboration, *Experimental Observation of Lepton Pairs of Invariant Mass Around 95-GeV/c**2 at the CERN SPS Collider*, Phys.Lett. **B126**, 398 (1983).

[28] B. Einhorn, *The Standard Model Higgs Boson: Selections and Comments*, Current Physics - Sources and Comments Vol. 8, Elsevier Science (1991).

[29] N. Cabibbo, L. Maiani, G. Parisi, and R. Petronzio, *Bounds on the Fermions and Higgs Boson Masses in Grand Unified Theories*, Nucl.Phys. **B158**, 295 (1979).

[30] M. Lindner, *Implications of Triviality for the Standard Model*, Z.Phys. **C31**, 295 (1986).

[31] T. Hambye and K. Riesselmann, *Matching conditions and Higgs mass upper bounds revisited*, Phys.Rev. **D55**, 7255 (1997).

[32] LEP Working Group for Higgs boson searches, ALEPH Collaboration, DELPHI Collaboration, L3 Collaboration, OPAL Collaboration, *Search for the standard model Higgs boson at LEP*, Phys.Lett. **B565**, 61 (2003).

[33] CDF Collaboration, D0 Collaboration, *Higgs Boson Studies at the Tevatron*, Phys.Rev. **D88**, 052014 (2013).

[34] ALEPH Collaboration, CDF Collaboration, D0 Collaboration, DELPHI Collaboration, L3 Collaboration, OPAL Collaboration, SLD Collaboration, LEP Electroweak Working Group, Tevatron Electroweak Working Group, SLD Electroweak and Heavy Flavour Groups, *Precision Electroweak Measurements and Constraints on the Standard Model*, unpublished (2010), 1012.2367.

[35] H. G. Veltman, *The process f anti-f* $\to W_L W_L$, Phys.Rev. **D43**, 2236 (1991).

[36] The LEP Electroweak Working Group, `http://lepewwg.web.cern.ch/LEPEWWG/`.

[37] Gfitter Group, *Status of the global fit to electroweak precisions data*, PoS **ICHEP2010**, 570 (2010).

[38] ATLAS Collaboration, *ATLAS high-level trigger, data acquisition and controls: Technical design report*, (2003).

[39] LHC Higgs Cross Section Working Group, *Handbook of LHC Higgs Cross Sections: 1. Inclusive Observables*, CERN Report No. CERN-2011-002 (2011).

[40] LHC Higgs Cross Section Working Group, *Handbook of LHC Higgs Cross Sections: 2. Differential Distributions*, CERN Report No. CERN-2012-002 (2012).

[41] H. Georgi, S. Glashow, M. Machacek, and D. V. Nanopoulos, *Higgs Bosons from Two Gluon Annihilation in Proton Proton Collisions*, Phys.Rev.Lett. **40**, 692 (1978).

[42] A. Denner, S. Heinemeyer, I. Puljak, D. Rebuzzi, and M. Spira, *Standard Model Higgs boson branching ratios with uncertainties*, Eur.Phys.J.C **71**, 1753 (2011).

[43] A. Djouadi, *The Anatomy of electro-weak symmetry breaking. I: The Higgs boson in the standard model*, Phys.Rept. **457**, 1 (2008).

[44] CMS Collaboration, *Observation of a new boson at a mass of 125 GeV with the CMS experiment at the LHC*, Phys.Lett. **B716**, 30 (2012).

[45] ATLAS Collaboration, *Observation of a new particle in the search for the Standard Model Higgs boson with the ATLAS detector at the LHC*, Phys.Lett. **B716**, 1 (2012).

[46] CMS Collaboration, *Combination of standard model Higgs boson searches and measurements of the properties of the new boson with a mass near 125 GeV*, CERN Report No. CMS-PAS-HIG-13-005 (2013).

[47] ATLAS Collaboration, *Updated coupling measurements of the Higgs boson with the the ATLAS detector using up to 25* fb^{-1} *of proton-proton collision data*, CERN Report No. ATLAS-CONF-2014-009 (2014).

[48] L. Landau, *On the angular momentum of a two-photon system*, Dokl.Akad.Nauk Ser.Fiz. **60**, 207 (1948).

[49] C.-N. Yang, *Selection Rules for the Dematerialization of a Particle Into Two Photons*, Phys.Rev. **77**, 242 (1950).

[50] ATLAS Collaboration, *Measurements of the properties of the Higgs-like boson in the two photon decay channel with the ATLAS detector using 25* fb^{-1} *of proton-proton collision data*, CERN Report No. ATLAS-CONF-2013-012 (2013).

[51] CMS Collaboration, *Properties of the Higgs-like boson in the decay H to ZZ to 4l in pp collisions at sqrt s =7 and 8 TeV*, CERN Report No. CMS-PAS-HIG-13-002 (2013).

[52] L. Evans and P. Bryant, *LHC Machine*, JINST **3**, S08001 (2008).

[53] H. Schopper, *LEP: a historical introduction*, Philos. Trans. R. Soc. Lond. **A 336**, 179 (1991).

[54] CMS Collaboration, *The CMS experiment at the CERN LHC*, JINST **3**, S08004 (2008).

[55] ATLAS Collaboration, *The ATLAS Experiment at the CERN Large Hadron Collider*, JINST **3**, S08003 (2008).

[56] ALICE Collaboration, *The ALICE experiment at the CERN LHC*, JINST **3**, S08002 (2008).

[57] LHCb Collaboration, *The LHCb Detector at the LHC*, JINST **3**, S08005 (2008).

[58] M. Ferro-Luzzi, *LHC Operation - as viewed from the Experiments*, Chamonix 2012 Workshop on LHC Performance, France , 35 (2011).

[59] M. Ferro-Luzzi, *Review of 2011 LHC run from the experiments perspective*, Chamonix 2012 Workshop on LHC Performance, France , 38 (2012).

[60] CMS Collaboration, Cms luminosity - public results, `https://twiki.cern.ch/twiki/bin/view/CMSPublic/LumiPublicResults`.

[61] CMS Collaboration, *CMS physics: Technical design report volume 1: Detector Performance and Software*, CERN-LHCC-2006-001 (2006).

[62] R. Brun and F. Rademakers, *ROOT: An object oriented data analysis framework*, Nucl.Instrum.Meth. **A389**, 81 (1997).

[63] GEANT4 Collaboration, *GEANT4: A Simulation toolkit*, Nucl.Instrum.Meth. **A506**, 250 (2003).

[64] S. Cucciarelli, M. Konecki, D. Kotlinski, and T. Todorov, *Track reconstruction, primary vertex finding and seed generation with the Pixel Detector*, CERN Report No. CMS-NOTE-2006-026 (2006).

[65] W. Adam, B. Mangano, T. Speer, and T. Todorov, *Track Reconstruction in the CMS tracker*, CERN Report No. CMS-NOTE-2006-041 (2006).

[66] R. Fruhwirth, W. Waltenberger, and P. Vanlaer, *Adaptive Vertex Fitting*, CERN Report No. CMS-NOTE-2007-008 (2007).

[67] R. Fruhwirth, *Application of Kalman filtering to track and vertex fitting*, Nucl.Instrum.Meth. **A262**, 444 (1987).

[68] R. Kalman, *A New Approach to Linear Filtering and Prediction Problems*, Transactions of the ASME-Journal of Basic Engineering **82 Series D**, 35 (1960).

[69] CMS Collaboration, *CMS Tracking Performance Results from early LHC Operation*, Eur.Phys.J. **C70**, 1165 (2010).

[70] CMS Collaboration, *Tracking and Primary Vertex Results in First 7 TeV Collisions*, CERN Report No. CMS-PAS-TRK-10-005 (2010).

[71] T. Sjostrand, S. Mrenna, and P. Z. Skands, *A Brief Introduction to PYTHIA 8.1*, Comput.Phys.Commun. **178**, 852 (2008).

[72] CMS Collaboration, *Vertex reconstruction at the CMS experiment*, Journal of Physics: Conference Series **110**, 092009 (2008).

[73] K. Rose, *Deterministic annealing for clustering, compression, classification, regression and related optimization problems*, Proceedings of the IEEE **86**, 2210 (1998).

[74] CMS Collaboration, *Particle-Flow Event Reconstruction in CMS and Performance for Jets, Taus, and MET*, CERN Report No. CMS-PAS-PFT-09-001 (2009).

[75] CMS Collaboration, *Commissioning of the Particle-Flow reconstruction in Minimum-Bias and Jet Events from pp Collisions at 7 TeV*, CERN Report No. CMS-PAS-PFT-10-002 (2010).

[76] CMS Collaboration, *Particle-flow commissioning with muons and electrons from J/Psi and W events at 7 TeV*, CERN Report No. CMS-PAS-PFT-10-003 (2010).

[77] M. Cacciari, G. P. Salam, and G. Soyez, *The Anti-k(t) jet clustering algorithm*, JHEP **0804**, 063 (2008).

[78] M. Cacciari and G. P. Salam, *Pileup subtraction using jet areas*, Phys.Lett. **B659**, 119 (2008).

[79] CMS Collaboration, *Determination of Jet Energy Calibration and Transverse Momentum Resolution in CMS*, JINST **6**, P11002 (2011).

[80] CMS Collaboration, *Jet Performance in pp Collisions at 7 TeV*, CERN Report No. CMS-PAS-JME-10-003 (2010).

[81] B. P. Roe *et al.*, *Boosted decision trees as an alternative to artificial neural networks for particle identification*, Nuclear Instruments and Methods in Physics Research Section A **543**, 577 (2005).

[82] CMS Collaboration, *Pileup Jet Identification*, CERN Report No. CMS-PAS-JME-13-005 (2013).

[83] S. Baffioni *et al.*, *Electron reconstruction in CMS*, Eur.Phys.J. **C49**, 1099 (2007).

[84] H. Bethe and W. Heitler, *On the Stopping of fast particles and on the creation of positive electrons*, Proc.Roy.Soc.Lond. **A146**, 83 (1934).

[85] CMS Collaboration, *Performance of CMS muon reconstruction in pp collision events at* $\sqrt{s} = 7$ *TeV*, JINST **7**, P10002 (2012).

[86] CMS Collaboration, *Identification of b-quark jets with the CMS experiment*, JINST **8**, P04013 (2013).

[87] CMS Collaboration, *Algorithms for b Jet identification in CMS*, CERN Report No. CMS-PAS-BTV-09-001 (2009).

[88] CMS Collaboration, *Search for the standard model Higgs boson decaying to a W pair in the fully leptonic final state in pp collisions at* $\sqrt{s} = 7$ *TeV*, Phys.Lett. **B710**, 91 (2012).

[89] CMS Collaboration, *Measurement of Higgs boson production and properties in the WW decay channel with leptonic final states*, JHEP **1401**, 096 (2014).

[90] S. Frixione, P. Nason, and C. Oleari, *Matching NLO QCD computations with Parton Shower simulations: the POWHEG method*, JHEP **0711**, 070 (2007).

[91] G. Passarino, *Higgs Interference Effects in* $gg \to ZZ$ *and their Uncertainty*, JHEP **1208**, 146 (2012).

[92] S. Goria, G. Passarino, and D. Rosco, *The Higgs Boson Lineshape*, Nucl.Phys. **B864**, 530 (2012).

[93] N. Kauer and G. Passarino, *Inadequacy of zero-width approximation for a light Higgs boson signal*, JHEP **1208**, 116 (2012).

[94] LHC Higgs Cross Section Working Group, *Handbook of LHC Higgs Cross Sections: 3. Higgs Properties*, CERN Report No. CERN-2013-004 (2013).

[95] N. Kauer, *Signal-background interference in $gg \to H \to VV$*, PoS **RADCOR2011**, 027 (2011).

[96] J. M. Campbell, R. K. Ellis, and C. Williams, *Gluon-Gluon Contributions to W+ W- Production and Higgs Interference Effects*, JHEP **1110**, 005 (2011).

[97] J. Alwall, M. Herquet, F. Maltoni, O. Mattelaer, and T. Stelzer, *MadGraph 5 : Going Beyond*, JHEP **1106**, 128 (2011).

[98] T. Binoth, M. Ciccolini, N. Kauer, and M. Kramer, *Gluon-induced W-boson pair production at the LHC*, JHEP **0612**, 046 (2006).

[99] T. Sjostrand, S. Mrenna, and P. Z. Skands, *PYTHIA 6.4 Physics and Manual*, JHEP **0605**, 026 (2006).

[100] H.-L. Lai *et al.*, *Uncertainty induced by QCD coupling in the CTEQ global analysis of parton distributions*, Phys.Rev. **D82**, 054021 (2010).

[101] H.-L. Lai *et al.*, *New parton distributions for collider physics*, Phys.Rev. **D82**, 074024 (2010).

[102] J. M. Campbell and R. Ellis, *MCFM for the Tevatron and the LHC*, Nucl.Phys.Proc.Suppl. **205-206**, 10 (2010).

[103] D. Barge, C. Campagnari, S. Gessner, and D. Kovalskyi, *Study of photon conversion rejection at CMS*, CERN Report No. CMS-NOTE-2009-159 (2009).

[104] A. Massironi, *Search for a Higgs Boson in the $H \to W^+W^- \to \ell^+\nu\ \ell^-\overline{\nu}$ channel at CMS*, PhD thesis, University of Milano-Bicocca (2013).

[105] G. Cerati *et al.*, *A multivariate approach for Drell-Yan rejection in the $H \to W^+W^-$ analysis*, CERN Report No. CMS-NOTE-2012-210 (2012).

[106] CMS Collaboration, *Measurement of the W^+W^- Cross section in pp Collisions at $\sqrt{s} = 7$ TeV and Limits on Anomalous $WW\gamma$ and WWZ couplings*, Eur.Phys.J. **C73**, 2610 (2013).

[107] CMS Collaboration, *Measurement of W+W- and ZZ production cross sections in pp collisions at sqrt(s) = 8 TeV*, Phys.Lett. **B721**, 190 (2013).

[108] L. L. Iglesias, *Search for the standard model Higgs boson in the $H \to WW \to 2l2\nu$ with the CMS experiment*, PhD thesis, Universidad de Oviedo (2013).

[109] CMS Collaboration, Standard Model Cross Sections for CMS, CMS Generator Group Twiki, 2010.

[110] M. Selvaggi, *Search for a Brout-Englert-Higgs Boson decaying to $W^+W^- \to \ell^+\nu\ \ell^-\overline{\nu}$ with the CMS experiment*, PhD thesis, University of Antwerp (2012).

[111] M. Bluj, A. Burgmeier, T. Fruboes, G. Quast, and M. Zeise, *Modelling of $\tau\tau$ final states by embedding τ pairs in $Z \to \mu\mu$ events.*, CERN Report No. CMS-NOTE-2011-020 (2011).

[112] R. C. Gray, C. Kilic, M. Park, S. Somalwar, and S. Thomas, *Backgrounds To Higgs Boson Searches from $W\gamma^* \to l\nu l(l)$ Asymmetric Internal Conversion*, unpublished (2011), 1110.1368.

[113] M. Dittmar and H. K. Dreiner, *h0 → W+ W- → lepton+ lepton- lepton-neutrino anti-lepton-neutrino as the dominant SM Higgs search mode at the LHC for M(h0) = 155-GeV - 180-GeV*, (1996).

[114] I. W. Stewart and F. J. Tackmann, *Theory Uncertainties for Higgs and Other Searches Using Jet Bins*, Phys.Rev. **D85**, 034011 (2012).

[115] S. Xie, *Search for the Standard Model Higgs Boson Decaying to Two W Bosons at CMS*, PhD thesis, Massachusetts Institute of Technology (2012).

[116] ATLAS and CMS Collaborations, *Procedure for the LHC Higgs boson search combination in summer 2011*, CERN Report No. ATL-PHYS-PUB-2011-011, CMS-NOTE-2011-005 (2011).

[117] CMS Collaboration, *Combined results of searches for the standard model Higgs boson in pp collisions at $\sqrt{s} = 7$ TeV*, Phys.Lett. **B710**, 26 (2012).

[118] A. L. Read, *Presentation of search results: The CL(s) technique*, J.Phys. **G28**, 2693 (2002).

[119] T. Junk, *Confidence level computation for combining searches with small statistics*, Nucl.Instrum.Meth. **A434**, 435 (1999).

[120] CMS Collaboration, *Observation of a new boson with mass near 125 GeV in pp collisions at $\sqrt{s}$ = 7 and 8 TeV*, JHEP **1306**, 081 (2013).

[121] CMS Collaboration, *Combination of standard model Higgs boson searches and measurements of the properties of the new boson with a mass near 125 GeV*, CERN

Report No. CMS-PAS-HIG-13-005 (2013).

[122] J. Ellis and D. S. Hwang, *Does the 'Higgs' have Spin Zero?*, JHEP **1209**, 071 (2012).

[123] S. Bolognesi *et al.*, *On the spin and parity of a single-produced resonance at the LHC*, Phys.Rev. **D86**, 095031 (2012).

[124] S. Bolognesi, Y. Gao, and A. V. Gritsan, JHU generator, `http://www.pha.jhu.edu/spin/`.

[125] CMS Collaboration, *Constraints on the Higgs boson width from off-shell production and decay to ZZ to llll and llvv*, CERN Report No. CMS-PAS-HIG-14-002 (2014).

List of Abbreviations

$E_{\mathrm{T}}^{\mathrm{miss}}$	Missing Transverse Energy
$\mathrm{t\bar{t}H}$	Associated Higgs Production with a top pair
ALICE	A Large Ion Collider Experiment
ATLAS	A Toroidal LHC Apparatus
BDT	Boosted Decision Tree
BEH boson	Brout-Englert-Higgs boson or in short Higgs boson
BEH field	Brout-Englert-Higgs field
BPTX	Beam Pick-up Timing for the Experiments
BSC	Beam Scintillator Counters
CC	Charged Current
CERN	European Organization for Nuclear Research
CL	Confidence Level
CMS	Compact Muon Solenoid
CMSSW	CMS Software
CSC	Cathode Strip Chambers
CTF	Combinatorial Track Finder
DA	Deterministic Annealing
DQM	Data Quality Management
DT	Drift Tubes
DY	Drell-Yan ($\mathrm{Z} + \mathrm{jets}$)
ECAL	Electromagnetic Calorimeter
EM	Electromagnetism
ggH	Higgs gluon-gluon fusion
GSF	Gaussian Sum Filter
GT	Global Trigger
GWS	Glashow-Weinberg-Salam
HB	Hadron Barrel
HCAL	Hadron Calorimeter

HE	Hadron Endcaps
HF	Hadron Forward
HLT	High Level Trigger
HO	Hadron Outer Barrel
IP	Impact Parameter
L1 trigger	Level-1 trigger
LEP	Large Electron Positron collider
LHC	Large Hadron Collider
LHCb	LHC Beauty experiment
LHCOPN	LHC Optical Private Network
LO	Leading Order
MC	Monte Carlo
MET	Missing Transverse Energy
MET	Missing Transverse Energy
min-proj.$E_{\mathrm{T}}^{\mathrm{miss}}$	min(proj.trk $E_{\mathrm{T}}^{\mathrm{miss}}$, proj.PF $E_{\mathrm{T}}^{\mathrm{miss}}$)
NC	Neutral Current
NLO	Next-To-Leading Order
NNLO	Next-To-Next-To-Leading Order
p-p collisions	proton-proton collisions
PD	Primary Dataset
PDF	Parton Distribution Function
PF	Particle Flow
PF$E_{\mathrm{T}}^{\mathrm{miss}}$	Particle-Flow based Missing Transverse Energy
POWHEG	NLO Monte Carlo generator
proj.$E_{\mathrm{T}}^{\mathrm{miss}}$	Projected Missing Transverse Energy
PS	Proton Synchrotron
PSB	Proton Synchrotron Booster
PU	Pile-Up
PYTHIA	LO Monte Carlo generator
Q	Charge
QCD	Quantum Chromodynamics
QED	Quantum Electrodynamics
QFT	Quantum Field Theory
qqH	Higgs Vector-Boson Fusion
RPC	Resistive Plate Chambers
RT	Regional Triggers

SC	Supercluster
SM	Standard Model
SPS	Super-Proton Synchrotron
TCHE	Track Counting High Efficiency
TCHP	Track Counting High Purity
TEC	Tracker Outer Disks
TIB	Tracker Inner Barrel
TID	Tracker Inner Disk
TOB	Tracker Outer Barrel
TPG	Trigger Primitive Generator
trk$E_{\mathrm{T}}^{\mathrm{miss}}$	Missing Transverse Energy calculated with charged particles
TTC	Timing, Trigger and Control system
VBF	Vector Boson Fusion
WH	Associated Higgs Production with a W boson
WLCG	Worldwide LHC Computing Grid
Y	Hypercharge
ZH	Associated Higgs Production with a Z boson

Acknowledgements

In the first place I would like to thank my supervisor, Nick van Remortel, for giving me the opportunity to perform a PhD in the first place and for supporting me during these past three years. Thank you for the experience, for the interesting discussions and for the friendly atmosphere. Thanks for everything!

A special thanks goes to my colleague Xavier Janssen, who kickstarted me in the Higgs analysis world, showed me around in CERN, guided me into the Higgs to WW subgroup and the Latinos working group, and connected me with a lot of CMS colleagues in general. Thank you for all the technical help and your insight in the Higgs field. Your dedication and motivation kept me sharp and really motivated me during our countless working nights on the verge of the discovery of the new boson. I would also like to thank my second office mate, Sara Alderweireldt, for the help, discussions, fun and friendship. Next, I would like to give a special thanks to all the members of the particle physics group at the University of Antwerp. You provided a nice work environment!

The work presented here would not have been possible without the help and excellent cooperation with several CMS colleagues, in specific the colleagues from the Latinos group, with whom I directly worked since the start of my PhD on this analysis. I am really grateful that I was able to be part of the group! I would also like to thank all the scientists I have had a chance to work with, brought together by our common interest in the Higgs field. It was nice working with all of you!

Furthermore, I would like to thank Inge van Hooydonk for sharing her linguistic feeling by proofreading this work.

I am grateful to my parents Rita Laenen and Michel Luyckx, for giving me the opportunity to study physics and for their unconditional support. Lastly I would like to thank my sister Evi and all my friends, especially Cynthia, for always being present and for all the nice moments in my spare-time.

Thank you all !

Samenvatting

De wetten van de natuur kunnen op microscopisch niveau geformuleerd worden met behulp van fundamentele elementaire deeltjes. Jarenlang onderzoek en steeds krachtigere versnellers hebben geleid tot de ontwikkeling van het standaardmodel, een kwantumveldentheorie gebaseerd op symmetriebehoud. Deze theorie beschrijft de dynamica van de elementaire deeltjes en de fundamentele interacties. Materie wordt beschreven als een samenstelling van twaalf fermionen die interageren door de uitwisseling van vectorbosonen, de dragers van de fundamentele interacties: het elektromagnetisme en de sterke en de zwakke kernkracht.

Ondanks haar capaciteit om verschillende experimentele resultaten met grote precisie succesvol te voorspellen, is de theorie van het standaardmodel nog steeds niet volledig begrepen. Los van de gravitationele interactie, die momenteel niet beschreven wordt door het standaardmodel, blijven vele vragen nog steeds onbeantwoord. Hoe kunnen de vele parameters van dit standaardmodel theoretisch worden verklaard? Waarom zijn de fermionen gegroepeerd in exact drie generaties? En waar komt de massa van de deeltjes vandaan vermits alle deeltjes massaloos zouden moeten zijn wegens het behoud van de fundamentele symmetrieën welke verantwoordelijk zijn voor het bestaan van de drie interacties? Deze laatste vraag staat bekend als het probleem van de elektrozwakke symmetriebreking. Een oplossing voor dit probleem werd in 1964 gevonden door Brout, Englert, Higgs, Guralnik, Hagen en Kibble. In hun voorgesteld mechanisme ontstaat de massa van een deeltje door zijn interactie met een extra veld, genaamd het Brout-Englert-Higgs (BEH) veld. Het fundamentele deeltje geassocieerd met dit veld, het BEH boson of kortweg het Higgs boson, is het deeltje waar deeltjesfysici afgelopen decennia uitvoerig naar hebben gezocht en komende decennia nog steeds een grote aandacht aan zullen schenken. De studie van de elektrozwakke symmetriebreking, het Brout-Englert-Higgs mechanisme, en de studie van de signatuur van deze theorie, het Higgs boson, worden beschouwd als een van de belangrijkste onderwerpen van de moderne fysica.

De grootste en meest krachtige versneller, aangewend binnen deze zoektocht, is momenteel de Large Hadron Collider (LHC), gesitueerd te CERN in Genève. De LHC laat bundels van relativistische protonen frontaal op elkaar botsen met een maximale massamiddelpuntsenergie van 14 TeV. De LHC, operationeel sinds 2009, is omringd door verschillende experimenten, waaronder het Compact Muon Solenoid (CMS) experiment, waar het onderzoek van deze thesis werd verricht. Een van de belangrijke korte termijn doelstellingen van het CMS experiment is de ontdekking van het Higgs boson door de overblijfselen van de botsingen te bestuderen. De productie van het Higgs boson aan de LHC is echter een zeer zeldzaam proces. Het Higgs boson kan verder afhankelijk van zijn massa, die niet theoretisch bepaald kan worden, vervallen in verschillende eindtoestanden. Het CMS experiment is ontworpen om een maximale gevoeligheid te bieden aan al deze mogelijke eindtoestanden. Het experiment heeft in 2011 6.1 fb^{-1} data verzameld aan een massamiddelpuntsenergie van 7 TeV en in 2012 23.3 fb^{-1} aan een massamiddelpuntsenergie van 8 TeV.

Op 4 juli 2012 kondigden zowel de ATLAS als de CMS collaboratie de observatie van een nieuw deeltje aan, een waarneming onafhankelijk van elkaar waarbij het deeltje telkens in overeenstemming is met het Higgs boson. De massa van het gevonden deeltje bedraagt 125 GeV en leidde tot de uitreiking van de Nobel Prijs voor F. Englert and P. Higgs voor het opstellen van hun Brout-Englert-Higgs mechanisme welke de verschillende elementaire deeltjes voorziet van massa.

Deze thesis omvat een gedetailleerde beschrijving van de theoretische en experimentele activiteiten omtrent een van de belangrijke vervalkanalen dat bijgedragen heeft tot de ontdekking van het Higgs boson: De meting van het Brout-Englert-Higgs boson via het vervalkanaal naar twee W bosonen in de volledig leptonische eindtoestand gebruik makende van de CMS detector bij de LHC. De gepresenteerde resultaten zijn gebaseerd op de volledige 2011 en 2012 dataset.